

# Geodätisch-geophysikalische Arbeiten in der Schweiz

(Fortsetzung der Publikationsreihe  
«Astronomisch-geodätische Arbeiten in der Schweiz»)

herausgegeben von der

Schweizerischen Geodätischen Kommission  
(Organ der Akademie der Naturwissenschaften Schweiz)

**Einhundertzweiter Band**  
**Volume 102**

**Single-frequency**  
**RTK GNSS positioning**

Zhenzhong SU

2019

Adresse der Schweizerischen Geodätischen Kommission:

ETH Zürich  
Institut für Geodäsie und Photogrammetrie  
Eidg. Technische Hochschule Zürich  
8093 Zürich  
Switzerland

Internet: <http://www.sgc.ethz.ch>

ISBN 978-3-908440-50-5

Redaktion des 102. Bandes:  
Dr. Z. Su, J. Müller-Gantenbein, Prof. A. Geiger, Prof. M. Rothacher  
Druck: Print-Atelier ADAG, Zürich

## VORWORT

Obwohl die Satellitenpositionierung zu einem Standardverfahren geworden ist, tauchen immer wieder neue Fragestellungen und ungelöste Problematiken auf. Insbesondere sind real-time Lösungen hoher Genauigkeit mit low-cost Einfrequenzempfängern nach wie vor nicht einfach zu bewerkstelligen. Für Warnsysteme besteht ein Bedarf an Echtzeitverfahren, die mit sehr kurzer Latenzzeit die überwachten Parameter zur Verfügung stellen können. Bei Hangrutschen geht es um die schnelle Bestimmung der Rutschgeschwindigkeit. Da die Genauigkeit unter anderem von der Dauer der Beobachtung abhängt, ist es eine Herausforderung eine Genauigkeitssteigerung bei gleichzeitiger Reduktion der Beobachtungszeit zu erreichen. Das dazu geeignete Verfahren: RTK. Real Time Kinematic GNSS (Globales Satellitennavigationssystem) Positionierung basiert auf der Auswertung von ‚Phasemessungen‘ und braucht immer eine Referenzstation (differentielle Positionierung). Um ‚cm-Genauigkeiten‘ zu erreichen, müssen die sogenannten GNSS-Phasemehrdeutigkeiten gelöst und fixiert werden. Dies allerdings ist eine der Hauptschwierigkeiten bei low-cost ein-frequenz Systemen. Allerdings ist die Methode vielversprechend, um kommerziell genutzte Drohnen, selbstfahrende Autos und Landwirtschaftsmaschinen präzise zu navigieren.

Herrn Su ist es gelungen, die beschriebenen Hindernisse weitgehend zu überwinden und eine Lösung zu präsentieren, die sowohl beim Geomonitoring als auch bei Fahrzeugen eingesetzt werden kann. Auch die schnell wachsende Drohnencommunity interessiert sich für Herrn Sus Lösung, die er, nunmehr im Rahmen von Fixposition, einem Spin-off der ETH, weiter operationalisiert und nutzbar macht.

Das ursprüngliche Geomonitoring-Projekt 'x-sense' wurde im Rahmen des SNF Forschungsprogramms 'Nano-Tera' gefördert und betraf die 'Technische Informatik und Kommunikation' der ETH Zürich, die 'Geodäsie und Photogrammetrie', ETH Zürich sowie die 'Physische Geographie' der Uni Zürich. Als Partner beteiligt waren auch Gamma Remote Sensing und das BAFU.

Die vorliegende Untersuchung reiht sich in die Arbeiten zum Geomonitoring des Institutes für Geodäsie und Photogrammetrie der ETH Zürich und der Schweizerischen Geodätischen Kommission (SGK) ein. Wir danken dem Verfasser, Herrn Su, für seinen Beitrag zur schnellen Positionierung mit low-cost Geräten. Dem SNF mit seinem 'Nano-Tera'-Forschungsprogramm gebührt Dank für die anfängliche Teilfinanzierung und Unterstützung, genauso wie dem BAFU für die finanzielle und technische Hilfeleistung.

Der SCNAT danken wir für die Übernahme der Druckkosten.

**Prof. Dr. Alain Geiger**  
Institut für Geodäsie und Photogrammetrie  
ETH Zürich

**Prof. Dr. Markus Rothacher**  
ETH Zürich  
Präsident der SGK

## PREFACE

Bien que le positionnement par satellites soit devenu un procédé usuel, de nouvelles questions ainsi que des problèmes non résolus surviennent constamment. En particulier des solutions, en temps réel et de hautes précisions obtenues à l'aide de récepteurs mono-fréquence bon marchés, ne sont pas aisées à obtenir. Pour des systèmes d'avertissements il existe une nécessité d'avoir des méthodes en temps réels qui peuvent fournir les paramètres de surveillance recherchés avec un court temps d'attente. Pour les glissements de terrains, par exemple, il s'agit de la détermination des vitesses de glissements. Parmi d'autres problèmes existe aussi celui de l'augmentation de la précision en réduisant les temps d'observations car cette précision dépend de ce dernier.

Le procédé approprié pour ce problème est le positionnement par RTK (Real Time Kinematic GNSS, ou Système global de navigation) qui est basé sur l'évaluation des mesures de la phase (phase-measurements). Cependant ce système requiert une station fixe de référence. (Positionnement différentiel). Afin d'obtenir une précision centimétrique, les ambiguïtés de phases doivent être résolues et fixées. Ceci est une, parmi d'autres difficultés majeures, rencontrée avec l'utilisation des récepteurs bon marché à une fréquence. Cependant cette méthode est prometteuse pour la navigation commerciale utilisant des drones, pour les automobiles autonomes et pour les machines agricoles.

Monsieur Su a été largement capable de surmonter ces obstacles et a présenté une solution qui peut être utilisée en géo-surveillance ainsi que pour les véhicules. Avec une croissance rapide, la communauté des utilisateurs de drones est intéressée par la solution proposée par monsieur Su. Celui-ci est en train de rendre sa solution opérationnelle au travers d'une « Spin-Off » de L'EPF-Z, nommée « Fixposition ».

Le projet original de géo-surveillance « x-sense » a été financé dans le cadre du programme de recherche «Nano-Tera de la SNST et a concerné l'institut de technique de l'information et de communication de même que de l'institut de géodésie et Photogrammétrie tous deux de l'EPF-Z, et aussi l'institut de géographie physique de l'université de Zürich. L'entreprise Gamma Remote Sensing ainsi que le FOEN ont aussi été des partenaires de ce projet.

La présente étude est une partie du travail de géo-surveillance de l'institut de Géodésie et Photogrammétrie de l'EPF-Z et de la commission suisse de géodésie. Nous remercions monsieur Su pour sa contribution au positionnement rapide par système bon marché. La SNF avec son programme de recherche « Nano-Tera » mérite nos remerciements pour le financement initial partiel de ce projet ainsi que pour son support. Nos remerciements vont aussi au FOEN pour son aide financière et pour son assistance technique. De même nous remercions la SCNAT pour avoir pris à sa charge les coûts de l'impression de ce fascicule.

**Prof. Dr. Alain Geiger**  
Institut de Géodésie et Photogrammétrie  
ETH Zürich

**Prof. Dr. Markus Rothacher**  
ETH Zürich  
Président de la CGS



## FOREWORD

Although satellite positioning has become a standard procedure, new questions and unsolved problems keep cropping up. In particular, real-time solutions of high accuracy with low cost single frequency receivers are still not easy to accomplish. For warning systems, there is a need for real-time methods that can provide the monitored parameters with very short latency. Landslides are about quickly determining the sliding speed. Among other things, since the accuracy depends on the duration of the observation, it is a challenge to increase the accuracy while reducing the observation time. The appropriate procedure for this end: RTK. Real Time Kinematic GNSS (Global Navigation Satellite System) positioning is based on the evaluation of 'phase measurements' and always needs a reference station (differential positioning). In order to achieve 'cm accuracies', the so-called GNSS phase ambiguity must be solved and fixed. However, this is one of the major difficulties with low-cost single-frequency systems. However, the method is promising to precisely navigate commercially used drones, self-driving cars and agricultural machinery.

Mr. Su has been able to largely overcome the described obstacles and present a solution that can be used in both geo-monitoring and vehicles. The fast-growing drone community is also interested in Mr. Su's solution, which he is now further operationalizing and making use of, as part of Fixposition, a spin-off of the ETH.

The original geo-monitoring project 'x-sense' was funded within the framework of the SNSF research program 'Nano-Tera' and concerned the 'Technical Informatics and Communication' of ETH Zurich, 'Geodesy and Photogrammetry', ETH Zurich and 'Physical Geography' of the University of Zurich. The partners involved were Gamma Remote Sensing and the FOEN.

The present study is part of the geo-monitoring work of the Institute of Geodesy and Photogrammetry of the ETH Zurich and the Swiss Geodetic Commission (SGK). We thank the author, Mr. Su, for his contribution to rapid positioning with low-cost devices. The SNSF, with its 'Nano Tera' research program, deserves thanks for the initial partial funding and support, as well as the FOEN for financial and technical assistance.

We thank the SCNAT for taking over the printing costs. This investigation represents a further master piece in the series of geo-monitoring research of the Institute of Geodesy and Photogrammetry and the Swiss Geodetic Commission (SGC).

Thanks go to the author, Fabian Neyer, for his valuable contribution to geodetic geo-monitoring. We thank the SNSF who, through its program 'Nano-Tera', strongly supported this work as well FOEN, whose financial and technical support is greatly appreciated. Thanks are given to the Swiss Academy of Sciences for covering the printing costs of this volume.

**Prof. Dr. Alain Geiger**  
Institute of Geodesy and Photogrammetry  
ETH Zurich

**Prof. Dr. Markus Rothacher**  
ETH Zurich  
President of SGC



## Abstract

Real Time Kinematic (RTK) GNSS positioning is a carrier-phase differential positioning technique depending upon the fixing of the carrier phase integer ambiguities to ensure cm-level positioning accuracy. It is up to now the most viable technique to achieve cm-level accuracy for kinematic positioning in post-processing mode and particularly in real time mode. (Odijk 2014) discussed RTK and Precise Point Positioning (PPP) techniques for single-frequency case. It is suggested that instantaneous ambiguity fixing is achievable for single-frequency multi-constellation RTK, but single-frequency PPP integer ambiguity fixing is more challenging due to the need of additional information like satellite hardware phase biases and ionospheric corrections. Thus, single-frequency RTK GNSS positioning is the most feasible technique to achieve centimeter-level high precision positioning in real time using low-cost single-frequency GNSS antennas and receivers. It is a promising technique, which answers the growing high-precision navigation demand from industrial drones, self-driving cars and automated farming in which low-cost is crucial to democratize its application.

Compared to the expensive geodetic GNSS receivers and antennas, low-cost single-frequency GNSS antennas and receivers do have some limitations in their performances like larger measurement variance and less suppression of multipath errors. In this thesis, the variances of code and carrier phase measurements of the single-frequency antenna and u-blox receiver are analyzed through computing the empirical standard deviation of code and carrier phase residuals in zero baseline tests and short-baseline tests. Multiplying the obtained variances with a proper weighting function of the measurements, a realistic stochastic model is constructed. The author proposes a mixed weighting function, where both C/N0 and satellite elevation angle are taken into account to better dilute the multipath error's effect. The antenna C/N0 pattern is modeled using measurements of geostationary satellites and this pattern is used as the input to the proposed mixed weighting function. The results show that the proposed weighting function can well detect and down-weight the multipath contaminated carrier phase measurements and leads to better RTK positioning accuracy. The author has also estimated the phase center variations of the Trimble Bullet III antenna by processing the GNSS measurements collected from 4 sessions with the antenna pointing to 0°, 90°, 180° and 270°. Applying the estimated antenna phase center variations to RTK processing indeed reduces the systematic trend and biases/offsets in the carrier-phase residuals. Finally, by comparing the GPS-only RTK solution with GPS + BeiDou and GPS + GLONASS solution, the results indicate that using more satellites from additional constellations can significantly increase the ratio of ambiguity-fixed to ambiguity-float solutions in single-frequency RTK GNSS positioning.



# Zusammenfassung

Real Time Kinematic (Echtzeitkinematisch, RTK) GNSS (Globales Satellitennavigationssystem) Positionierung ist eine trägerphasen-basierte, differentielle Positionierungstechnik, die durch das Fixieren der GNSS-Phasenmehrdeutigkeit Positionierungsgenauigkeit im cm-Bereich garantiert. Bis jetzt ist es die gebräuchlichste Methode um, im Post-Processing aber vor allem auch in Echtzeit, cm-Genauigkeit für kinematische Positionierung zu erreichen.

(Odijk 2014) diskutiert RTK und Precise Point Positioning (PPP) Methoden für den Fall basierend auf einer einzelnen GNSS Frequenz. Es wird erklärt, dass instantanes Festlegen der Phasenmehrdeutigkeit mit Einfrequenz, multi-constellation RTK möglich sei. Das Bestimmen der Phasenmehrdeutigkeitszahl im Einfrequenz PPP Modus sei allerdings aufgrund der Notwendigkeit von zusätzlichen Informationen wie (satellite hardware phase bias) und Ionosphärenkorrekturen anspruchsvoller. Folglich ist Einfrequenz RTK GNSS Positionierung, in Verbindung mit kostengünstigen Einfrequenz GNSS Antennen und Receivern, die passendste Methode für cm-genaue Positionierung in Echtzeit. Als Antwort auf die wachsende Nachfrage für hochpräzise Navigation kommend von kommerziell genutzten Drohnen, selbstfahrenden Autos und autonomen Landwirtschaftsmaschinen, ist es eine vielversprechende Methode.

Im Vergleich zu kostspieligen geodätischen GNSS Empfängern und Antennen, haben günstige Einfrequenz-GNSS-Antennen und –Empfänger Einschränkungen in ihrer Leistungsfähigkeit wie erhöhte Messvarianzen und schlechtere Unterdrückung von «Multipath»-Fehlern. In dieser Dissertation werden die Messvarianzen von Code und Trägerfrequenz einer Einfrequenz-Antenne und einem Empfänger der Firma Ublox durch berechnen der empirischen Standardabweichung der Code- und Trägerfrequenz-Residuen in zero-baseline und short-baseline Tests analysiert. Durch Multiplikation der erhaltenen Varianzen mit einer angemessenen Gewichtungsfunktion wird ein realistisches stochastisches Modell erstellt. Der Autor schlägt eine gemischte Gewichtungsfunktion vor in welcher C/N0 und Satelliten-Elevationswinkel berücksichtigt werden um die Effekte der Multipath-Fehler zu minimieren. Die C/N0-Charakteristiken werden durch Messung der Signale von geostationären Satelliten modelliert. Diese Charakteristiken dienen als Eingangsvariablen für die vorgeschlagene Gewichtungsfunktion. Es konnte gezeigt werden, dass diese Gewichtungsfunktion die multipath-kontaminierten Trägerfrequenz-Messungen gut detektieren, die entsprechenden Satellitensignale herabstufen kann und so zu einer verbesserten RTK Positionierungsgenauigkeit führt. Ebenso hat der Autor die Phasenzentrumsabweichungen der Trimble Bullet III Antenne abgeschätzt. Dazu wurden die GNSS-Signale von 4 Messreihen mit Antennenausrichtung 0°, 90°, 180° und 270° verarbeitet. Wie postuliert, reduziert das Anwenden der geschätzten Antennen-Phasenzentrumsabweichungen in der RTK-Verarbeitung den systematischen Trend und die Abweichungen in den Trägerfrequenz-Residuen. Abschliessend wurde durch den Vergleich der reinen GPS-RTK-Lösung mit den resultierenden Lösungen bei Benutzung von GPS + BeiDou und GPS + GLONASS gezeigt, dass das Verarbeiten zusätzlicher Satellitensignale von zusätzlichen GNSS-Konstellationen eine

signifikante Verbesserung des Verhältnisses von ambiguity-fixed zu ambiguity-float RTK-Lösungen bei der Einfrequenz-RTK-GNSS-Positionierung ermöglichen kann.

# Content

Abstract .....	i
Zusammenfassung.....	iii
<b>Chapter 1</b> Introduction .....	10
1.1 A short overview of GNSS positioning techniques .....	10
1.2 Motivation .....	12
1.3 Objectives and outline of this thesis .....	12
1.4 State of the art.....	13
<b>Chapter 2</b> GNSS fundamentals .....	15
2.1 Mathematical model of GNSS positioning .....	15
Functional model.....	15
Stochastic model .....	18
2.2 Extended Kalman Filter for RTK GNSS positioning .....	19
EKF with static model .....	22
EKF with kinematic model .....	23
2.3 GNSS measurement errors .....	24
Satellite orbit and clock errors .....	24
Phase wind-up effects .....	26
2.4 Carrier-to-noise density ratio .....	27
Noise power density $N_0$ .....	28
Received carrier power .....	28
Parameters affecting the measured $C/N_0$ .....	29
$C/N_0$ as indicator of receiver measurement precision.....	30
The $C/N_0$ estimator in a GNSS receiver.....	31
2.5 Multipath .....	33
Multipath categories .....	33
Code multipath.....	34
Carrier-phase multipath .....	35
Spectral analysis of the multipath through $C/N_0$ .....	37
Unique feature of multipath .....	43
Mitigate the multipath by sidereal stacking of the coordinates for a static station.....	47
<b>Chapter 3</b> Single-frequency receivers and antennas .....	48

3.1	Zero baseline test of low-cost single frequency receivers and antennas .....	48
3.2	Receiver clock .....	51
	The effect of the receiver clock adjustment on positioning .....	56
3.3	Carrier-to-noise density ratio measurements .....	61
3.4	Receiver measurements precision .....	63
	Least square variance component estimation .....	66
	Results and analysis.....	69
<b>Chapter 4</b>	<b>Empirical antenna <math>C/N_0</math> pattern modelling using geostationary satellites .....</b>	<b>75</b>
4.1	The motivation of using geostationary satellites .....	75
4.2	Methodology .....	77
4.3	Measuring campaign with the BeiDou C05 satellite .....	79
4.4	Measuring campaign with the SBAS 136 satellite .....	83
<b>Chapter 5</b>	<b>Relative antenna phase center variation estimation of a low-cost single-frequency antenna .....</b>	<b>89</b>
5.1	Antenna mean phase center and phase center variations .....	89
5.2	Current state.....	91
5.3	Data collection and processing strategy.....	91
5.4	Results.....	95
	Estimated relative antenna PCV with 1 session's data.....	95
	Investigation of the antenna PCV influence on daily static positioning.....	97
	Investigation of the antenna PCV influence on 2-hour static positioning .....	100
	Investigation of the antenna PCV influence on kinematic positioning .....	104
	Estimated relative antenna PCV with 4 sessions' data.....	104
	Investigation of the antenna PCV influence on RTK positioning.....	107
5.5	Conclusions.....	113
<b>Chapter 6</b>	<b><math>C/N_0</math>- and elevation-based observation weighting model .....</b>	<b>115</b>
6.1	Existing observation weighting approaches.....	115
6.2	Proposed mixed weighting function.....	118
6.3	Comparing different weighting approaches.....	120
6.4	Benefits of applying MWF in RTK positioning .....	123
<b>Chapter 7</b>	<b>RTK positioning with Dual GNSS constellations .....</b>	<b>128</b>
7.1	GPS+BeiDou .....	128
7.2	GPS+GLONASS .....	131



The additional SD reference ambiguity term .....	131
The inter-frequency biases.....	132
GPS+GLONASS RTK .....	133
<b>Chapter 8</b> Conclusions and Outlook.....	139
8.1 Conclusions .....	139
8.2 Outlook .....	140
Appendix A Mathematical derivation of phase wind-up .....	142
Appendix B Proof of the first and second derivative of carrier-phase multipath error over the phase shift in NLOS signal. ....	146
Appendix C u-blox Evaluation kit to u-blox modules mapping list .....	148
Appendix D CPGF linear combination jumps .....	149
Appendix E Statistics of the DD code and carrier phase residuals in a zero baseline test with two u-blox M8P receiver modules and one Trimble Bullet III antenna.....	154
Appendix F Plots of SD carrier-phase residuals for the RTK processing with and without the estimated rover antenna PCV corrections .....	156
Appendix G From the X-Sense project to the low-cost RTK GNSS receiver prototype....	158
References.....	160

# Abbreviations

<b>BDS</b>	Chinese BeiDou navigation satellite System
<b>DD</b>	double-differenced
<b>EBW</b>	Elevation Based Weighting
<b>EGNOS</b>	European Geostationary Navigation Overlay Service
<b>EKF</b>	Extended Kalman Filter
<b>GEO</b>	GEostationary
<b>GLONASS</b>	Russian GLObal Navigation Satellite System
<b>GNSS</b>	Global Navigation Satellite System
<b>GPS</b>	American Global Positioning System
<b>IFB</b>	Inter-Frequency Biases
<b>IGS</b>	International GNSS Service
<b>KF</b>	Kalman Filter
<b>LNA</b>	Low-Noise Amplifier
<b>LSA</b>	Least Squares Adjustment
<b>LSVCE</b>	Least-Square Variance Component Estimation
<b>MEO</b>	Medium Earth Orbit
<b>MPC</b>	Mean Phase Center
<b>MWF</b>	Mixed Weighting Function
<b>O-C</b>	observed-minus-computed
<b>PCO</b>	Phase Center Offset
<b>PCV</b>	Phase Center Variation
<b>PPS</b>	Precise Positioning Service
<b>PRN</b>	PseudoRandom Noise
<b>RMS</b>	Root Mean Square
<b>RTS</b>	Real Time Service
<b>RTK</b>	Real Time Kinematic
<b>SB</b>	Short Baseline
<b>SD</b>	Single-differenced

<b>SPP</b>	Single Point Positioning
<b>SPS</b>	Standard Positioning Service
<b>TMF</b>	Tropospheric Mapping Function
<b>ZB</b>	Zero Baseline

# Chapter 1 Introduction

## 1.1 A short overview of GNSS positioning techniques

Global Navigation Satellite Systems (GNSS) are space-based radio positioning systems providing 24-hour 3 dimensional (3D) position, velocity and time information to suitably equipped users anywhere on, near or even off the surface of earth (e.g., low earth orbit satellites) (Hofmann-Wellenhof, Lichtenegger and Wasle 2008). Unlike other navigation sensors, like cameras, LIDARs (Light Detection and Ranging), and radars, providing only relative positioning and navigation to the users, a GNSS unit as the most important navigation system in a vehicle, supplies its absolute coordinates on earth in a unified global coordinate frame. Nowadays, the GNSS system is enriched by more and more satellites from the American Global Positioning System (GPS), European Galileo system, Chinese BeiDou navigation satellite System (BDS) and the Russian Globalnaya Navigatsionnaya Sputnikovaya Sistema (GLONASS), leading to better coverage and reliability.

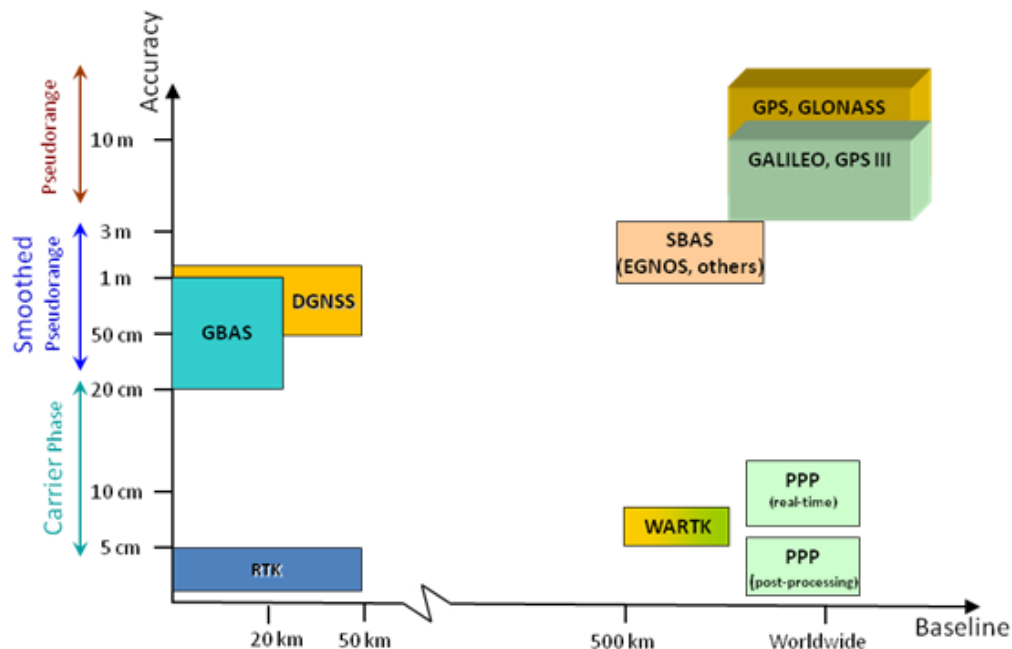


Figure 1 Accuracy comparison of GNSS positioning techniques (source: ESA Navipedia<sup>1</sup>)

The first navigation satellite of the GPS, a Block-I satellite, was launched in 1978 (Hegarty and Chatre 2008). Since then, getting the 3D position of an object on earth becomes possible using a

<sup>1</sup> Web link: [http://www.navipedia.net/index.php/GNSS\\_Augmentation](http://www.navipedia.net/index.php/GNSS_Augmentation)

GPS device. In the past decades, a tremendous amount of work has been done to improve the accuracy and reliability of GNSS positioning. The user position accuracy has been brought down from 8-60 m (95% confidential interval) provided by the Standard Positioning Service (SPS) using C/A-code on GPS L1 signal only, or 6-20 m by the Precise Positioning Service (PPS) using P-code on the GPS L1 and L2 signals (Kelly 2006), to 1-10 m when the code-based Differential GNSS (DGNSS) techniques and various augmentation systems are used. And then the accuracy is improved to sub-meter level by processing the phase-smoothed code ranges and further to centimeter level as the advance of carrier-phase based techniques, like PPP and RTK positioning. Figure 1 gives a good overview of the positioning accuracy of various kinematic GNSS positioning techniques (only kinematic positioning techniques are of interest to the discussion in this thesis).

Centimeter-level positioning accuracy is feasible by using RTK or PPP techniques. With standard PPP, this is typically reached in a post-processing mode taking into account the most precise final orbits and clock products as well as a prior correction. Nowadays, using the real time product (with 25s data latency) provided by Real Time Service of the International GNSS Service (IGS), the real-time PPP can also reach centimeter-level positioning accuracy after convergence time. (Elsobeiey and Al-Harbi 2016) presented the performance of the real-time kinematic PPP solution with average Root Mean Squares (RMS) of 16cm, 9cm and 23cm in East, North and Up components for 12 stations. Nevertheless, (Chassagne 2012) and (Elsobeiey and Al-Harbi 2016) indicate that the main drawback of the PPP technique is the long convergence time, more than 30 minutes, before the PPP solution can reach a positioning accuracy below 10cm.

In contrast, with the RTK technique, centimeter-level accuracy is achievable very quickly, even instantaneously, when sufficient satellites are observed, especially on short baselines with distance less than 10 km (Chassagne 2012), (Odolinski and Odijk 2014).

On the one side the cm-level accuracy of real time positioning and navigation is needed more than ever, coming from the growing demand for high precision in geo-monitoring, unmanned aerial vehicles, self-driving, automated farming and autonomous robotics. On the other side, the price of such devices is expected to drop to an affordable level to enable ubiquitous high precision navigation and location services. The single-frequency RTK GNSS positioning is answering such demands with its cm-level real time positioning accuracy and the cost-effectiveness, typically 5-100 Euros per GNSS module/chip (Weston and Schwieger 2014). Even though the market will eventually push down the price of dual-frequency or even triple-frequency GNSS modules, the single-frequency RTK GNSS positioning would still keep its position in less reliability-demanding but cost-sensitive applications, while multi-frequency RTK GNSS will serve more safety-critical applications.

## 1.2 Motivation

The first motivation of this study comes from the task of establishing a real-time and post-processed high-precision GNSS positioning system using low-cost GNSS antennas and consumer-grade GNSS receivers to monitor rock falls and landslides in the Swiss alpine area. It is the sub-system of a wireless sensor connected network in the X-sense project<sup>2</sup>, started in 2011. The real-time epoch-wise positions of the study targets with an expected accuracy at centimeter-level is achieved by the author of this thesis using RTK GNSS processing of the live GNSS raw data stream, developed on top of the open-source program library RTKLIB (Takasu 2009), (Takasu 2013). It has been operational since 2012. The post-processed GNSS daily static positions with an accuracy at millimeter-level is achieved by Dr. Philippe Limpach through automated batch processing of the collected GNSS data, developed on top of the Bernese GNSS Software (Dach, et al. 2007), (Limpach, Geiger and Su 2013). Single-frequency Trimble Bullet III antennas and u-blox LEA-6T GNSS receiver modules are used in this project.

The second motivation is the strong demand for a low-cost RTK solution coming from the growing markets in unmanned aerial vehicles, autonomous cars and precision agriculture. This clear market demand even influenced the industry. Consumer GNSS manufactures, traditionally only focusing on the high-volume, low-accuracy (meter-level accuracy) GNSS market, are paying attention to the growing high-precision GNSS market now. For example, the consumer GNSS receiver module provider u-blox has already provided the raw carrier-phase observations in its GNSS timing modules (LEA-5T, NEO/LEA-6T, NEO/LEA-7T and NEO/LEA-M8T) for a few years and recently released its new RTK module NEO-M8P. The jointly established company SAPCORDA by Bosch, Geo++, Mitsubishi Electric and u-blox, which aims to bring high-precision GNSS positioning services to the mass market, also verified the importance of the low-cost, high-precision GNSS navigation for the future. Until there is a significant price drop in the hardware costs for multi-frequency GNSS devices, the single-frequency RTK GNSS positioning technique is the most practical solution for low-cost high-precision GNSS navigation.

A description of how the single-frequency RTK GNSS system developed in the project X-Sense evolves into a low-cost RTK GNSS receiver prototype is given in Appendix G.

## 1.3 Objectives and outline of this thesis

The goal of this thesis is to improve the performance of single-frequency RTK GNSS positioning. The author has investigated the dominating errors in single-frequency RTK GNSS positioning using low-cost receivers and antennas. Then these errors have been quantified, modeled, or

---

<sup>2</sup> <http://www.nano-tera.ch/pdf/sheets/X-Sense.pdf>

diluted through observation weighting and finally, the RTK performance is improved by using more GNSS constellations.

After the introduction in **Chapter 1**, the GNSS fundamentals are given in **Chapter 2**. The connection between multipath and carrier-to-noise density ratio is also presented in **Chapter 2**. Then the differences between a low-cost u-blox receiver and a geodetic-grade Javad receiver are discussed, and the precision of code and carrier phase measurement from a low-cost antenna and receiver are estimated based on zero baseline and short-baseline tests in **Chapter 3**. The two important characteristics of a GNSS antenna are the gain pattern and the stability of the phase center. An approach to estimate the low-cost antenna  $C/N_0$  pattern using geostationary satellites is given in **Chapter 4**. The relative antenna phase center variations of the low-cost antenna is estimated and adapted as correction into RTK process to quantify its influence on RTK positioning in **Chapter 5**. Then the estimated antenna  $C/N_0$  pattern for the Trimble Bullet III antenna is used in the  $C/N_0$  and elevation based mixed weighting function to construct a more realistic stochastic model for the code and phase measurements in **Chapter 6**. In **Chapter 7**, the benefit of using additional GNSS constellations is presented with two examples, the single-epoch ambiguity fixing with a combination of GPS+BeiDou measurements for static stations and the combined GPS+GLONASS RTK positioning for a kinematic station. Finally the conclusions are made in **Chapter 8**.

## 1.4 State of the art

RTK GNSS positioning is a carrier-phase differential positioning technique depending on the fixing of the carrier phase integer ambiguities to ensure cm-level positioning accuracy. It is up to now the most viable technique to achieve cm-level accuracy for kinematic positioning in the post-processing mode and particularly in the real-time mode. In case of single-frequency GNSS positioning, RTK is the only feasible way to reach cm-level position accuracy in real-time. Whereas single-frequency PPP cannot use the ionosphere-free linear combination to eliminate the ionospheric errors, which is an essential step for PPP solutions, in order to achieve high accuracy. (Odijk 2014) discussed RTK and PPP techniques for single-frequency case. It is suggested that instantaneous ambiguity fixing is achievable for the single-frequency multi-constellation RTK, but single-frequency PPP integer ambiguity fixing is much more challenging due to the need of additional information like satellite hardware phase biases and ionospheric corrections.

On the development of the functional model of single-frequency RTK GNSS positioning, (Carcanague 2012) extended the functional model by Doppler measurements and proposed a Doppler weighting scheme where both velocity of the antenna and  $C/N_0$  are used to weight the Doppler measurements. In (Carcanague, Julien, et al. 2013), they used a  $C/N_0$  dependent weighting function proposed by (Aminian 2011) in an adapted RTK algorithm where GLONASS

carrier phase inter-channel biases are calibrated to achieve single-frequency RTK positioning with GPS and GLONASS constellations.

Unlike the rather well-established and thoroughly studied functional model of GNSS positioning (i.e., observation equations), the knowledge of the stochastic model is still insufficient. A stochastic model is represented by the co-variance matrix of the observations in the GNSS observation equation. A co-variance matrix equals to a multiplication of the variances and the weighting functions of the measurements. (Odolinski and Teunissen 2017) applied the Least-squares variance component estimation (Teunissen and Amiri-Simkooei 2008) to estimate the code and phase variances in a short-baseline setup to formulate a realistic stochastic model. Empirical analysis of the influences of survey-grade, high-quality patch, low-quality patch and smartphone-quality GNSS antennas on the antenna gain, residuals of double-differenced phases as well as a performance evaluation of the carrier-phase differential GNSS positioning using a smartphone antenna were done in (Pesyna, Heath and Humphreys 2014). Studies on the weighting functions include (Euler and Goad 1991), (Jin and de Jong 1996) and (Collins and Langley 1999), who studied different types of elevation-dependent weighting of GNSS code and carrier phase measurements, (Collins and Langley 1999), (Brunner, Hartinger and Troyer 1999), (Hartinger and Brunner 1999) and (Luo 2013) who studied the various  $C/N_0$ -based GNSS observational weighting functions. (Wieser and Brunner 2000) had further extended the  $C/N_0$  based weighting approach with a Danish method to reduce the influence of outliers.

Also other studies on the topic of using low-cost GPS for monitoring tasks were done by (Glabsch, et al. 2010), (Heunecke, Glabsch and Schuhbäck 2011), (Zhang, Stange and Schwieger 2012). Especially, (Zhang 2016) and (Zhang and Schwieger 2013) have studied the quality of low-cost GPS receivers for monitoring through time and spatial correlation analysis.



# Chapter 2 GNSS fundamentals

## 2.1 Mathematical model of GNSS positioning

The mathematical model of GNSS positioning consists of functional and stochastic components (Luo 2013). The functional model describes the deterministic relation between the GNSS observations and the unknown parameters (to be estimated) while the stochastic model describes the uncertainty and correlations of the observations.

### Functional model

The general functional model for single-frequency GNSS of the zero-difference GNSS observation equations for phase and code are formulated as:

$$L_k^i = \varrho_k^i + c \cdot \delta^i - c \cdot \delta_k - I_k^i + T_k^i + \lambda \cdot N_k^i + e_{pcv}^i + e_{pcv_k} + \xi_{L_k} + \varepsilon_{L_k}^i + \varphi_{PWD_k}^i + e_L \quad (2-1)$$

$$P_k^i = \varrho_k^i + c \cdot \delta^i - c \cdot \delta_k + I_k^i + T_k^i + e_{pcv}^i + e_{pcv_k} + \xi_{P_k} + \varepsilon_{P_k}^i + e_P \quad (2-2)$$

where the superscript  $i$  stands for satellite  $i$  and subscript  $k$  stands for receiver  $k$ , following the convention from (Dach, et al. 2007): using superscript to denote satellites and subscript to denote receivers.

- $L$  is the carrier-phase measurements (in meters) of satellite  $i$  measured by receiver  $k$
- $\varrho$  is the geometric distance between the satellite  $i$  and the receiver  $k$
- $\delta^i$  is the clock error of the satellite  $i$
- $c$  is the speed of light
- $\delta_k$  is the clock error of the receiver  $k$
- $I$  is the frequency dependent ionospheric delay
- $T$  is the tropospheric delay
- $\lambda$  is the wavelength of carrier-phase (in this dissertation, only the L1 carrier-phase with frequency of 1,575.42 MHz is of interest)
- $N$  is the integer ambiguity of carrier-phase
- $e_{pcv}^i$  is the PCV of the transmitting antenna on satellite  $i$
- $e_{pcv_k}$  is the PCV of the receiving antenna of receiver  $k$
- $\xi_L$  and  $\xi_P$  are the instrumental phase and code delays respectively
- $\varepsilon_L$  and  $\varepsilon_P$  are the multipath errors in carrier-phase and code pseudoranges
- $\varphi_{PWD}$  is the Phase Wind Up
- $e_L$  and  $e_P$  are the white noises in carrier-phase and code measurements
- $P$  is the code pseudorange measurement

In general the PPP method can use the formula (2-1) and (2-2) as the functional model.

The desired coordinates of the receiver and the satellite position are implicitly contained in the geometric distance (Euclidean distance):

$$\rho_k^i = \sqrt{(X^i - X_k)^2 + (Y^i - Y_k)^2 + (Z^i - Z_k)^2} = \|\vec{r}^i - \vec{r}_k\| \quad (2-3)$$

$\vec{r}^i = (X^i, Y^i, Z^i)$  is the position vector of the satellite  $i$  at the phase center of the transmitting antenna and  $\vec{r}_k = (X_k, Y_k, Z_k)$  is the position vector of the receiving antenna phase center, both in the Earth-Center Earth-Fixed (ECEF) coordinate system. The satellite position can be computed using the broadcasted navigation data (Spilker Jr 1996) in real time.

As  $\rho_k^i$  is a nonlinear expression in the coordinates of the receiving antenna, a linearization is done by applying Taylor's theorem where Equation (2-3) is approximated by its 1<sup>st</sup>-order Taylor polynomial:

$$\begin{aligned} \rho_k^i &= \sqrt{(X^i - X_{k0})^2 + (Y^i - Y_{k0})^2 + (Z^i - Z_{k0})^2} \\ &\quad + \frac{-(X^i - X_{k0})}{\sqrt{(X^i - X_{k0})^2 + (Y^i - Y_{k0})^2 + (Z^i - Z_{k0})^2}} dX_k \\ &\quad + \frac{-(Y^i - Y_{k0})}{\sqrt{(X^i - X_{k0})^2 + (Y^i - Y_{k0})^2 + (Z^i - Z_{k0})^2}} dY_k \\ &\quad + \frac{-(Z^i - Z_{k0})}{\sqrt{(X^i - X_{k0})^2 + (Y^i - Y_{k0})^2 + (Z^i - Z_{k0})^2}} dZ_k \end{aligned} \quad (2-4)$$

The subscript 0 is used to denote the initial values;  $dX_k, dY_k$  and  $dZ_k$  are the unknown corrections to the initial values. To simplify the notation, we write formula (2-4) as

$$\rho_k^i = \rho_{k0}^i + \frac{-(X^i - X_{k0})}{\rho_{k0}^i} dX_k + \frac{-(Y^i - Y_{k0})}{\rho_{k0}^i} dY_k + \frac{-(Z^i - Z_{k0})}{\rho_{k0}^i} dZ_k \quad (2-5)$$

$$\rho_k^i = \rho_{k0}^i + e_{kX}^i dX_k + e_{kY}^i dY_k + e_{kZ}^i dZ_k \quad (2-6)$$

The geometric interpretation of  $e_{kX}^i, e_{kY}^i$  and  $e_{kZ}^i$  are the projections of the unit vector  $e_k^i$  onto the X, Y and Z axes. They are the elements in the design matrix  $\mathbf{A}$  of the GNSS observation equation when it is written in vector and matrix notation:

$$\underbrace{\begin{bmatrix} L_k^1 - \varrho_{k0}^1 \\ \vdots \\ L_k^i - \varrho_{k0}^i \\ \vdots \\ L_k^m - \varrho_{k0}^m \end{bmatrix}}_{L_k} = \underbrace{\begin{bmatrix} e_{kX}^1 & e_{kY}^1 & e_{kZ}^1 \\ \vdots & \vdots & \vdots \\ e_{kX}^i & e_{kY}^i & e_{kZ}^i \\ \vdots & \vdots & \vdots \\ e_{kX}^m & e_{kY}^m & e_{kZ}^m \end{bmatrix}}_A \underbrace{\begin{bmatrix} dX_k \\ dY_k \\ dZ_k \end{bmatrix}}_{X_k} + c \cdot \underbrace{\begin{bmatrix} \delta^1 - \delta_k \\ \vdots \\ \delta^i - \delta_k \\ \vdots \\ \delta^m - \delta_k \end{bmatrix}}_{dt_k} + \lambda \cdot I_m \cdot \underbrace{\begin{bmatrix} N_k^1 \\ \vdots \\ N_k^i \\ \vdots \\ N_k^m \end{bmatrix}}_{N_k} + E_L \quad (2-7)$$

We use  $E_L$  to denote the remaining aforementioned error terms in carrier-phase measurements and  $I_m$  is an identity matrix with  $m$  rows and  $m$  columns. Written in matrix and vector notation:

$$L_k = AX_k + c \cdot dt_k + \lambda \cdot I_m \cdot N_k + E_L \quad (2-8)$$

$$P_k = AX_k + c \cdot dt_k + E_P \quad (2-9)$$

In RTK GNSS positioning, the satellite clock error is obtained from the navigation data and the receiver clock error is estimated along with the position of the rover using the code measurements in a first step, and then they cancel out when forming Double-Differenced (DD) observation equations.

A typical RTK GNSS positioning is based on the DD observations, formed firstly between two receivers, and then between two satellites. The vector and matrix notations of the linearized DD GNSS observations read:

$$L_{kg}^{ij} = AX_{kg} + \lambda \cdot I_m \cdot N_{kg}^{ij} + E_{L_{kg}}^{ij} \quad (2-10)$$

$$P_{kg}^{ij} = AX_{kg} + E_{P_{kg}}^{ij} \quad (2-11)$$

Now  $E_{L_{kg}}^{ij}$  and  $E_{P_{kg}}^{ij}$  denote the vector containing the DD errors of carrier-phase and code measurements respectively. Assuming satellite 1 is the reference satellite used to form differences with other satellite, the matrix A becomes

$$A = \begin{bmatrix} e_{kgX}^{12} & e_{kgY}^{12} & e_{kgZ}^{12} \\ \vdots & \vdots & \vdots \\ e_{kgX}^{1i} & e_{kgY}^{1i} & e_{kgZ}^{1i} \\ \vdots & \vdots & \vdots \\ e_{kgX}^{1m} & e_{kgY}^{1m} & e_{kgZ}^{1m} \end{bmatrix}$$

with

$$e_{kgX}^{12} = (e_{kX}^1 - e_{gX}^1) - (e_{kX}^2 - e_{gX}^2)$$

and the same equality applies to  $e_{kgY}^{12}$  and  $e_{kgZ}^{12}$ . The position vector  $X_{kg}$  stands for the baseline vector between the two receivers. However, the carrier-phase ambiguities are handled at the Single-Difference (SD) level in software like RTKLIB (Takasu 2013). The linearized GNSS observation equation for the single-frequency RTK positioning is:

$$L_{kg}^{ij} = AX_{kg} + \lambda \cdot I_m \cdot D \cdot N_{kg}^i + E_{L_{kg}}^{ij} \quad (2-12)$$

$$P_{kg}^{ij} = AX_{kg} + E_{P_{kg}}^{ij} \quad (2-13)$$

with

$$D = \begin{bmatrix} 1 & -1 & 0 & \dots & 0 \\ 1 & 0 & -1 & \dots & 0 \\ \vdots & \vdots & \vdots & \ddots & \vdots \\ 1 & 0 & 0 & \dots & -1 \end{bmatrix}$$

$L_{kg}^{ij}$  and  $P_{kg}^{ij}$  are the vectors of the DD carrier-phase and code measurements.  $N_{kg}^i$  is the vector of the SD carrier-phase ambiguities. The approximation due to the linearization (reflected by matrix  $A$ ) of the GNSS observation equations is compensated by iterative Least Square Adjustment (LSA). Such iterative processing is used mostly by software designed for post-processing.

For real-time processing, such as RTK GNSS positioning in this thesis, the nonlinear GNSS observation equations:

$$L_{kg}^{ij} = f(X_{kg}) + \lambda \cdot I_m \cdot D \cdot N_{kg}^i + E_{L_{kg}}^{ij} \quad (2-14)$$

$$P_{kg}^{ij} = f(X_{kg}) + E_{P_{kg}}^{ij} \quad (2-15)$$

where  $f(\cdot)$  denotes a nonlinear function, are handled by the extended Kalman filter which will be discussed in chapter 2.2.

### Stochastic model

The stochastic model is represented by the covariance matrix whose diagonal elements are the variances and the off-diagonal elements are the co-variances of the GNSS observations. Non-differenced GNSS observations are considered to be independent leading to zeros in the off-diagonal elements of the covariance matrix. The covariance matrix for measurements at zero-difference level, which could be used as the stochastic model of PPP, shall be

$$Q_L = \sigma_0^2 * P^{-1} = \begin{bmatrix} (\sigma_k^1)^2 & 0 & \dots & 0 \\ 0 & (\sigma_k^2)^2 & \dots & \vdots \\ \vdots & \vdots & \vdots & \vdots \\ 0 & 0 & \dots & (\sigma_k^m)^2 \end{bmatrix} \quad (2-16)$$

$$Q_P = C \cdot Q_L \quad (2-17)$$

where  $Q_L$  and  $Q_P$  are the notations for the covariance matrices of carrier-phase and code measurements at zero-difference level,  $\sigma_0^2$  is the variance of unit weight for carrier-phase observations,  $P$  is the symmetric positive-definite weight matrix and  $C$  is the scale factor between

the phase variances and code variances. Applying the error propagation theorem, one can get the covariance matrices at DD level:

$$Q_{LDD} = \begin{bmatrix} (\sigma_k^1)^2 + (\sigma_g^1)^2 + (\sigma_k^2)^2 + (\sigma_g^2)^2 & \dots & (\sigma_k^1)^2 + (\sigma_g^1)^2 \\ \vdots & \ddots & \vdots \\ (\sigma_k^1)^2 + (\sigma_g^1)^2 & \dots & (\sigma_k^1)^2 + (\sigma_g^1)^2 + (\sigma_k^m)^2 + (\sigma_g^m)^2 \end{bmatrix} \quad (2-18)$$

$$Q_{PDD} = C \cdot Q_{LDD} \quad (2-19)$$

In matrix  $Q_{LDD}$ , the diagonal entries are filled by the variance sums of all four involved measurements and the non-diagonal entries are filled by the variance sums of only the two measurements from the reference satellite.

In real data processing they are empirically determined and most GNSS software provide an input interface or internally fix these values. For example, the Bernese GPS software sets 1 mm<sup>2</sup> (default value) for  $\sigma_0^2$ , 10,000 for the scale factor  $C$  and uses an elevation-dependent weighting function to construct  $P$ . These settings are justified for GNSS data collected by geodetic grade antennas and receivers, but not appropriate for GNSS data from low-cost single-frequency antennas and receivers. A new set of values is estimated through a short-baseline test presented in Chapter 3.3. Incorrect weights of observations can result in a biased estimate of the variance of unit weight, thus leading to wrong values of the formal error of the estimated parameters (see (Xu 2013) and (Koch 1999)).

A realistic stochastic model of the GNSS measurements consists of three critical parts as indicated in formula (2-16) and (2-17): a realistic precision of the GNSS measurements, a realistic scale factor between code and phase measurements and a proper weighting approach to account for the varying uncertainty of the GNSS measurements.

## 2.2 Extended Kalman Filter for RTK GNSS positioning

The Kalman Filter (KF), named after Rudolf Emil Kalman, is the most widely implemented algorithm for real-time or near real-time positioning and navigation applications. It has become an essential part of modern navigation systems (Grewal, Andrews and Bartone 2013), because it is an extremely effective and versatile procedure for combining noisy measurements to estimate the state of a system with uncertain dynamics. The KF algorithm is derived based on the optimality criterion of least-squares unbiased estimation of the state vector with optimal weight, using all available data information (Chui and Chen 2009).

Depending on the continuity of the measurements, the KF is categorized into continuous-time KF and discrete-time KF. Most KF implementations use the discrete implementation (even when the system modeled is actually continuous), because measurements are almost always obtained at discrete points in time (Gibbs 2011). This is exactly the case for a GNSS positioning system where

the GNSS measurements to be processed are generated by receivers at discrete measurement epochs. Henceforth, the KF mentioned in this thesis means the discrete-time KF.

The KF is the optimal estimator for a linear system. However, as stated before, the GNSS observation equation in the measurement model is nonlinear. Stanley F. Schmidt proposed Extended Kalman Filter (EKF) where the linearization technique of using partial derivatives evaluated at the current time and estimated state variable is applied in KF (Grewal and Andrews 2015) and (Schmidt 1981). Since then the EKF is used as the de facto standard for any nonlinear processing such as GNSS positioning.

The KF or EKF consists of two parts: a system dynamic model and a measurement model (Gleason and Gebre-Egziabher 2009). The system dynamic model describes the transformation of the state vector over time whereas the measurement model describes the relationship between the state and the measurements. The system dynamic model is given by (Gibbs 2011) as:

$$X_i = f(X_{i-1}) + U_i + W_i \quad (2-20)$$

where

- $X_i$  is the state vector at current time epoch  $i$
- $f(X_{i-1})$  contains the state transition from previous to current epoch
- $U_i$  is the control input vector at current time epoch
- $W_i$  is the system noise

For RTK GNSS positioning, the control input vector is not present in the formula, thus we have the system dynamic model as:

$$X_i = f(X_{i-1}) + W_i \quad (2-21)$$

where the state vector  $X$  contains the rover position (relative to the reference), carrier-phase ambiguities and possibly other parameters, like velocity of the rover or tropospheric delay, depending on the dynamics and the GNSS data processing strategy  $P$  is very often used to denote the co-variance matrix of the state vector  $X$ .

The measurement model for RTK GNSS positioning is exactly the functional model in formula (2-14) and (2-15). The notation is converted into the notation in KF convention as:

$$Y_i = h(X_i) + V_i \quad (2-22)$$

where

- $Y_i$  is the measurement vector at time epoch  $i$
- $V_i$  is the measurement error vector
- $h(X_i)$  is a function presenting the relation between measurement vector and state vector

Accordingly, the covariance matrix of  $Y_i$ , the DD measurements (see formulas (2-18) and (2-19)), are denoted as  $R_i$  in the convention of KF.

The EKF allows both models to be nonlinear and uses the fully nonlinear model to propagate the state vector and to connect it to the measurements. However, a linearization by means of partial derivatives on  $f(X_{i-1})$  and  $h(X_i)$  is needed to propagate the co-variance matrix of the state vector and the gain matrix.

The design matrix  $H_i$  is usually used to denote the partial derivatives of  $h(X_i)$  and the transition matrix  $F_i$  denotes the partial derivative of  $f(X_{i-1})$  with respect to the state variables:

$$H_i = \frac{\partial h(X_i)}{\partial X}; F_i = \frac{\partial f(X_{i-1})}{\partial X}$$

According to (Takasu 2013), the exact EKF formulation of the RTK processing in RTKLIB for short baselines is summarized as:

### The propagation of the system dynamic model

$$X_i(-) = F_i \cdot X_{i-1}(+) \quad (2-23)$$

$$P_i(-) = F_i \cdot P_{i-1}(+) \cdot F_i^T + W_{i-1} \quad (2-24)$$

where  $F_i$  is a constant matrix due to the simple linear dynamic model one has in RTK GNSS positioning.

### The measurement model and its update

$$Y_i = f(X_i(-)) + V_i \quad (2-25)$$

$$X_i(+) = X_i(-) + K_i \cdot (Y_i - f(X_i(-))) \quad (2-26)$$

$$P_i(+) = (I - K_i \cdot H_i) \cdot P_i(-) \quad (2-27)$$

$$K_i = P_i(-) \cdot H_i^T \cdot (H_i \cdot P_i(-) \cdot H_i^T + R_i)^{-1} \quad (2-28)$$

where  $(-)$  denotes variables before update and  $(+)$  denotes variables after update. The state vector reads,

$$X = (Xp, Xv, Xa)^T$$

where  $Xp$  is the vector containing the three components of the rover positions,  $Xv$  is the velocity vector of the rover (not used in this thesis because all data are collected in low dynamic motions) and  $Xa$  is the vector of carrier phase ambiguities to be estimated. Because only short baselines ( $\leq 5$  km) are of interest to this thesis, the other parameters like tropospheric and ionospheric delays are excluded from the state vector.

As (Takasu 2013) pointed out, the RTKLIB employs EKF to compute the positioning solution in all modes: DGPS/DGNSS, static, kinematic, moving-baseline modes and PPP. The only exception is the single point positioning (SPP) mode, which relies on an iterated weighted LSA.

The static model and the kinematic model in an EKF used for RTK GNSS positioning are demonstrated with the data from the shake table experiment provided by (Häberling 2015). A brief description of the experiment setup is given here. The GNSS rover receiver is mounted on a one-axis shake table (Figure 2) where inductive sensors provide the “true” motion.



Figure 2 Shake table (Häberling 2015)

The shake table is actuated by motors to generate movements. A Javad Sigma-G3TA receiver and a Javad GrAnt-G3T antenna are used to collect the GNSS data with 100 Hz. The baseline distance between rover and reference station is 5.5m. For more details please refer to Chapter 6 of (Häberling 2015).

### **EKF with static model**

In the EKF with a static model, the position  $Xp$  of rover antenna phase center in the state vector and its covariance matrix  $Pp$  propagate from previous epoch  $i - 1$  to current epoch  $i$  as:

$$\begin{aligned} Xp_i &= Xp_{i-1} \\ Pp_i &= Pp_{i-1} \end{aligned} \tag{2-29}$$



The other parameters in the state vector propagate as indicated in (2-23) to (2-28).

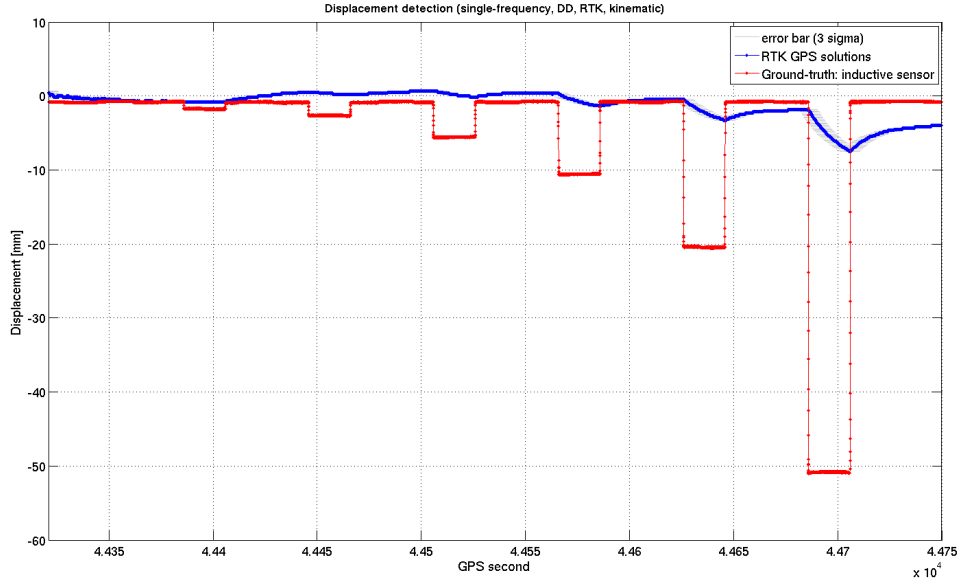


Figure 3 The epoch-wise rover positions processed with static model (blue) compared to the ground truth: inductive sensor (red);

Figure 3 shows the epoch-wise positions of the rover GNSS antenna mounted on the shake table computed using an EKF with a static model. In the figure, blue points represent the displacements computed from GPS and the red points represent the displacement measured by the inductive sensor. The grey bar is indicating the 3 sigma of the GPS position, which is too small to be visible in this figure.

The results shown in the figure indicate that using an EKF with a static model, the computed GPS positions do not coincide with the real antenna movement. Even though they have the trend to approach to real position, the difference between the real positions and the GPS positions are large.

### EKF with kinematic model

In the EKF with a kinematic model, the position of the rover antenna phase center in the state vector and its covariance matrix propagate from previous epoch  $i - 1$  to current epoch  $i$  as:

$$\begin{aligned} Xp_i &= Xp_{i-1} \\ Pp_i &= a^2 \cdot I \end{aligned} \quad (2-30)$$

where  $I$  is an identity matrix and  $a$  is set to 30 meters which allows a geometric change of rover antenna's position by 30 meters from one epoch to the next.

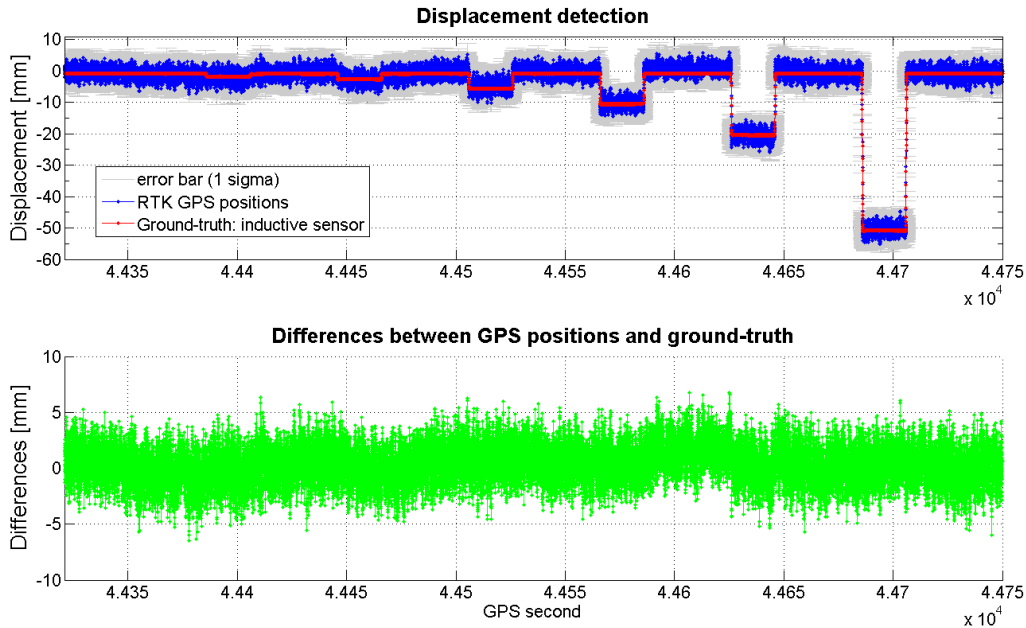


Figure 4 The epoch-wise rover positions processed with static model (blue) comparing to the ground truth: inductive sensor (red); The differences are plotted in green.

Figure 4 shows that using the EKF with a kinematic model, the computed GPS positions coincide well with the real antenna movement. The differences between the GPS positions and the ground truth are within  $\pm 5$ mm. This result tells that the EKF with a kinematic model is the right processing model for RTK positioning of low speed objects studied in this thesis.

### 2.3 GNSS measurement errors

This thesis focuses on the RTK GNSS positioning for short baselines, where except multipath and un-modeled phase center corrections of the low-cost single-frequency antenna, the remaining GNSS measurement errors are assumed to cancel out by double-differences. However, the satellite orbit and clock errors and the phase wind-up effects are still explained in this chapter for clarification because they are not well documented by literature. For more information on other GNSS measurement errors like ionospheric delays and tropospheric delays please refer to GNSS text books like (Hofmann-Wellenhof, Lichtenegger and Wasle 2008).

#### Satellite orbit and clock errors

Even though the real-time satellite orbit and clock corrections to the broadcast ephemeris are available as part of the Real Time Service (RTS)<sup>3</sup> products provided by IGS<sup>4</sup>, most real-time GNSS positioning systems still use only the broadcast ephemeris due to the constraints of data link and

<sup>3</sup><http://www.igs.org/rts>

<sup>4</sup> <http://www.igs.org/>

data latency. Therefore, the satellite orbit and clock errors discussed here refer to the differences between the broadcast satellite orbits and clocks, and their true values.

From formulas (2-5) and (2-7), we see that the satellite orbital error influences the geometric distance term and the design matrix. Moving the satellite clock error term to the geometric distance term as well, we get:

$$L_k^i - (\varrho_{k0}^i + \Delta \varrho_{k0}^i + c \cdot \delta^i) = \left( e_X^{ik} + \frac{\Delta X^i}{\varrho_{k0}^i} \right) dX_k + \left( e_Y^{ik} + \frac{\Delta Y^i}{\varrho_{k0}^i} \right) dY_k + \left( e_Z^{ik} + \frac{\Delta Z^i}{\varrho_{k0}^i} \right) dZ_k \quad (2-31)$$

The same expression applies to the observation equation of code pseudoranges. The left side of the equation is the so-called observed-minus-computed (O-C) term. As one can see, both satellite orbit and clock errors influence directly the O-C term in a non-difference observation equation. Even though the exact values of the errors are not easy to quantify, the Signal-In-Space Ranging Errors (SISREs) can describe the statistical uncertainty of the modeled pseudorange due to the satellite orbit and clock errors. According to the latest report of (Montenbruck, Steigenberger and Hauschild 2015), the global average SISREs for individual constellations amount to  $0.7 \pm 0.02$  m (GPS),  $1.5 \pm 0.1$  m (BDS),  $1.6 \pm 0.3$  m (Galileo) and  $1.9 \pm 0.1$  m (GLONASS), based on the analysis of one year's data collected from 2013 to 2014. These values represent the uncertainties induced by the satellite orbit and clock errors to the O-C measurements in a non-differential GNSS processing:

$$\sigma_{SISRES} = \sqrt{\sigma_{orb}^2 + \sigma_{clk}^2} \quad (2-32)$$

The total uncertainty induced by both orbit and clock errors is 0.7 m for GPS, so the projected orbit errors  $\Delta X^i$ ,  $\Delta Y^i$  and  $\Delta Z^i$  on the three coordinate axes are much smaller than 0.7 m. Taking the nominal value of 20200 km for the satellite altitude  $\varrho_{k0}^i$ , the  $\frac{\Delta X^i}{\varrho_{k0}^i}$ ,  $\frac{\Delta Y^i}{\varrho_{k0}^i}$  and  $\frac{\Delta Z^i}{\varrho_{k0}^i}$  terms are less than  $0.3 \times 10^{-8}$ . Such small values can be ignored compared to the  $e_X^{ik}$ ,  $e_Y^{ik}$ , and  $e_Z^{ik}$  with values in the range of (-1, 1).

For RTK processing, the satellite clock errors completely cancel out by the differencing between receivers. However, the satellite orbit errors remain in the differenced measurements even though they are considerably reduced. A handy rule of thumb to obtain the approximate impact of unmodelled satellite orbit errors on the baseline estimation is given in (Dach, et al. 2007):

$$\Delta l \approx \frac{l}{\rho} \cdot \Delta O \quad (2-33)$$

where  $\Delta l$  is the error in the baseline coordinates,  $l$  is the baseline length in km,  $\Delta O$  is the satellite orbit error and  $\rho$  is the geometric distance between the satellite antenna and the receiving antenna.

(Luo 2013) has used formula (2-33) with  $\rho = 25,000$  km, and  $\Delta O = 1$  m as the value of broadcast satellite orbit errors and his results show that for short baselines with distances up to 10 km, the induced errors in the baseline coordinate estimation due to the broadcast satellite orbit errors are below 0.4 mm. This leads to the conclusion that the satellite orbit and clock errors are negligible in a short baseline RTK processing.

### **Phase wind-up effects**

Phase Wind-Up (PWD) is a bias in GNSS carrier-phase caused by rotation of either the satellite transmitting antenna or the receiving antenna. First studies of the PWD effect on the phase and amplitude of the observed signal at linearly and circularly polarized receiving antennas was done by (Cannon 1964) and on Doppler range-rate measurements by (Marini 1971) and (Marini 1972). The GNSS community started to pay attention to this effect in the 1990s, back to when it was still called phase wrap-up.

The PWD is directly related to the polarization of GNSS carrier-phase, thus a short introduction of the signal polarization is given here. All GNSS transmit Right-Hand Circularly Polarized (RHCP)<sup>5</sup> signals. For the GPS signals, the signal ellipticity is said being better than 1.8 dB for L1 and 3.2 dB for L2 (GPS-ICD 2012). (BDS-ICD 2013) shows that all BDS signal polarization ellipticities are no worse than 2.9 dB, whereas (GLONASS-ICD 2008) shows the elliptic coefficient of GLONASS signal not to be worse than 0.7 dB for both L1 and L2 sub-bands. (Galileo-ICD 2015) indicates only that the signal is RHCP without information about its ellipticity. Since the ellipticity is quite small, we assume the signals to be perfectly circular polarized in the following analysis.

The GNSS receiving antenna is designed to receive RHCP signals and reject Left-Hand Circularly Polarized (LHCP) signals. But even well-designed GNSS antennas will exhibit a small, nonzero LHCP response in addition to the desired RHCP response (Dorsey, et al. 2006). However, (Beyerle 2009) shows that the assumption of GNSS signals to be purely RHCP signals is well justified, because the error in PWD introduced by this approximation is at sub-millimeter level.

A circularly polarized signal can be generated by combining two linearly polarized signals with equal amplitude: one in the horizontal and the other in the vertical plane but shifted by 90° in phase (see Figure 5). So a RHCP antenna can be conveniently modelled by cross dipoles (Tetewsky and Mullen 1996).

As the phase wind-up is not taken into account in the RTK solution, the details and mathematical derivations are moved to Appendix A.

---

<sup>5</sup> For a RHCP wave, the thumb of the right hand points in the propagation direction in the far field, while the wave's electric field rotates in the same direction of the curled fingers.

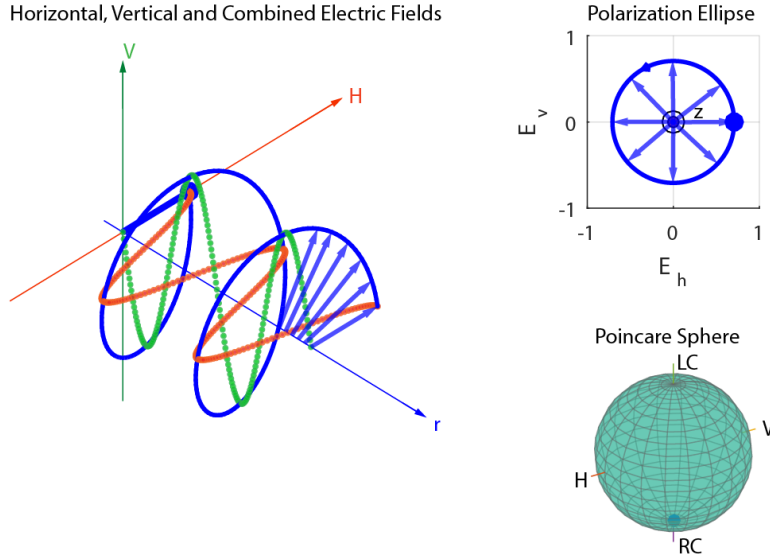


Figure 5 Illustration of the Electric Field of a RHCP signal<sup>6</sup>

(left) Electric Fields: red and black represent the vertical and horizontal components, blue represents the combined field; (right upper) Polarization Ellipse: Z is the signal propagation direction, pointing out of the paper;  $E_v$  and  $E_h$  are the electric fields in vertical and horizontal components; Blue circle present the rotation of the electric vector; (right lower) Poincare Sphere: LC stands for LHCP, RC stands for RHCP

## 2.4 Carrier-to-noise density ratio

Besides the basic observables, like code pseudoranges, carrier-phases and Doppler frequencies, modern GNSS receivers also output the signal strength, in terms of carrier-to-noise density ratio ( $C/N_0$ ) or signal-to-noise ratio (SNR). These two terms are regularly used interchangeably however they have fundamental differences.

In (Hofmann-Wellenhof, Lichtenegger and Wasle 2008), the  $C/N_0$  is defined as the ratio of the received carrier power  $P_r$  to the noise power per unit bandwidth  $N_0$ , whereas, SNR refers to the ratio of the signal power  $P$  to the noise power  $N$  in a given bandwidth:

$$C/N_0 = 10 \log_{10} \frac{P_r}{N_0} \text{ [dBHz]} \quad (2-34)$$

$$SNR = 10 \log_{10} \frac{P}{N} \text{ [dB]} \quad (2-35)$$

with,

$$N_0 = kT = -228.6T \text{ [WHz}^{-1}\text{]} \quad (2-36)$$

<sup>6</sup> The figure is plotted by Matlab using codes: `fv = [1; -i]; helperPolarizationView(fv);`

$$N = N_0 B_r [W] \quad (2-37)$$

$T$  is the temperature equivalent in Kelvin (K) and  $k$  is the Boltzmann constant in  $\text{dBWK}^{-1}\text{Hz}^{-1}$ .  $B_r$  is the front-end bandwidth, which is usually the noise equivalent bandwidth of the last filter stage in the receiver's radio-frequency front-end (Joseph 2010).  $P_r$  is the received carrier power.

In theory, the received carrier power  $P_r$  and noise power density  $N_0$  are both independent of the acquisition, the tracking algorithms and the front-end bandwidth of the receiver. Thus (Badke 2009) suggested that compared to SNR,  $C/N_0$  provides a better metrics for analyzing GNSS receiver performance because in  $C/N_0$  the bandwidth of the receiver is eliminated. In a latter chapter of this thesis, we are going to take advantage of this  $C/N_0$  feature to construct the stochastic model of the GNSS measurements in RTK processing.

### Noise power density $N_0$

Different from the simplified expression of  $N_0$  given in (2-36) that only depends on temperature,  $N_0$  is in fact related to the noise figure  $F_{LNA}$  of the Low-Noise Amplifier (LNA), the gain  $G_c$  of the cable and filter that precede the LNA, and the antenna temperature  $T_A$  due to noise received from the sky plus ground radiation. Its expression is given in the unit of  $\text{dBWHZ}^{-1}$  in (Misra and Enge 2011) as:

$$N_0 = 10 \log_{10} k \left( T_A + 290 \left( \frac{F_{LNA}}{G_c} - 1 \right) \right) [\text{dBWHZ}^{-1}] \quad (2-38)$$

The value for  $F_{LNA}$  is 2.09 (3.2dB) for the u-blox LEA-5T, LEA-6T and 2.95 (4.7dB) for the u-blox LEA-M8T receiver modules according to their data sheets (u-blox AG 2011), (u-blox AG 2010) and (u-blox AG 2016). With a typical value of  $T_A = 100$  K and  $G_c = 0.8$ , the noise power density for LEA 5T&6T and LEA-M8T are  $-201.1 \text{ dBWHZ}^{-1}$  and  $-199.2 \text{ dBWHZ}^{-1}$  respectively, calculated with formula (2-50). Given this differences, the measured  $C/N_0$  values by LEA-M8T will be 1.9 dBHz lower than those of the previous modules. Nevertheless, for a fixed receiver type under the same antenna temperature, the noise power density is usually considered as a constant parameter.

### Received carrier power

Even though  $C/N_0$  is bandwidth-independent, the measured  $C/N_0$  is influenced by other parameters related to the received carrier power  $P_r$  which is given in (Misra and Enge 2011) as:

$$P_r = \frac{A_E G_T G_R}{L_A L_R} \cdot \frac{P_T}{4\pi R^2} [\text{watts}] \quad (2-39)$$

with

$$A_E = \frac{\lambda^2}{4\pi}$$

$$R = -R_E \sin el + \sqrt{R_E^2 (\sin^2 el - 1) + R_{SV}^2}$$

$$R_E \approx 6371 \times 10^3 \text{ m}$$

$$R_{SV} \approx 26,560 \times 10^3 \text{ m}$$

where  $P_T$  is the power at the satellite antenna input which is given as 14.3 dBW on L1 C/A signal in Table 2 of (Aparicio, et al. 1996). The  $\frac{1}{4\pi R^2}$  accounts for the path loss, where  $R$  is the distance between satellite and receiver computed from the earth radius  $R_E$ ,  $R_{SV}$  is the distance from satellite to earth center, and  $el$  is the satellite elevation angle at the user.  $A_E$  stands for the effective area of the receive antenna.  $G_T$  is the gain of the transmitting antenna and  $G_R$  is the gain of the receiver antenna.  $L_A$  is the signal power loss due to atmosphere attenuation and  $L_R$  denotes the signal power loss in the receiver.

Among these parameters,  $A_E$  (for a specific signal with a constant wavelength),  $L_A$  (typical 0.5 dB) and  $L_R$  (for a specific type of receiver) are constants, while the rest are variables depending on  $el$  directly or indirectly, e.g.,  $G_T$  depends directly on the nadir angle which can be transferred to the elevation angle.

### Parameters affecting the measured C/N<sub>0</sub>

Besides the aforementioned parameters, multipath effects will also change the received carrier power measured by the receiver antenna. Therefore, we can summarize the parameters affecting the measured C/N<sub>0</sub> in the following formula using decibels:

$$C/N_0 = (10 \log_{10} P_T + 10 \log_{10} A_E - 10 \log_{10} L_A - 10 \log_{10} L_R - N_0)_{cst} + 10 \log_{10} G_T + 10 \log_{10} G_R - 10 \log_{10} (4\pi R^2) - M \quad [dBHz] \quad (2-40)$$

All the constant terms in  $( )_{cst}$  are treated as constant parameters regarding a specific GNSS signal and receiver type. Except for the multipath interference, the rest of the parameters is depending on the satellite elevation  $el$ .

A closed-form formula of  $G_T$  is derived from (Misra and Enge 2011) as:

$$G_T = \frac{2}{1 - \cos \alpha} \quad (2-41)$$

where  $\alpha$  is the nadir angle.

The nadir angle is linked to satellite elevation angle by:

$$\sin \alpha = \frac{R_E \sin(el + 90^\circ)}{R_{SV}} \quad (2-42)$$

Thus,

$$G_T = \frac{2}{1 - \sqrt{1 - \left(\frac{R_E \cos el}{R_{SV}}\right)^2}} \quad (2-43)$$

So the last two un-modelled parameters affecting  $C/N_0$  are receiver antenna gain pattern  $G_R$  and multipath. It is essential to separate and model these two parameters' influences on measured  $C/N_0$  before using it to construct the stochastic model of GNSS measurements. We will come back to this point at Chapter 4.

### **C/N<sub>0</sub> as indicator of receiver measurement precision**

The direct link of the  $C/N_0$  value to the precision of the receiver's code pseudoranges and carrier-phase measurements is given by (Langley 1997):

$$\sigma_{DLL} = \lambda_c \sqrt{\frac{\alpha B_L}{c/n_0} \left[1 + \frac{2}{T \cdot c/n_0}\right]} \quad (2-44)$$

$$\sigma_{PLL} = \frac{\lambda}{2\pi} \sqrt{\frac{B_P}{c/n_0} \left[1 + \frac{1}{2 \cdot T \cdot c/n_0}\right]} \quad (2-45)$$

with

$$c/n_0 = 10^{0.1 \cdot C/N_0}$$

The  $\sigma_{DLL}$  stands for the jitter of the Delay Lock Loop (DLL) or code-tracking loop,  $\alpha$  is the dimensionless DLL discriminator correlator factor;  $B_L$  is the equivalent code loop noise bandwidth in Hz;  $T$  is the predetection integration time in seconds;  $\lambda_c$  is the wavelength of the PseudoRandom Noise (PRN) code (293.05 meters for the C/A-code);  $B_P$  is the carrier loop noise bandwidth in Hz;  $\lambda$  is the wavelength of the carrier (19.03 cm for L1).

One has to notice that thermal noise is the only error being considered in the above two formulas. They are exactly the thermal noise jitters for the DLL and the PLL given in (Ward, Betz and Hegarty 2006).

Approximated formula which are justified for moderate to strong signals with  $C/N_0$  larger than 35 dBHz are also given in (Langley 1997):

$$\sigma_{DLL} = \lambda_c \sqrt{\frac{\alpha B_L}{c/n_0}} \quad (2-46)$$

$$\sigma_{PLL} = \frac{\lambda}{2\pi} \sqrt{\frac{B_P}{c/n_0}} \quad (2-47)$$



Under ideal observational conditions where the receiver thermal noise is the only measurement noise, the jitter of the DLL and the PLL is equivalent to the precision (or standard deviation) of the receiver code and carrier-phase measurements, respectively.

### The C/N<sub>0</sub> estimator in a GNSS receiver

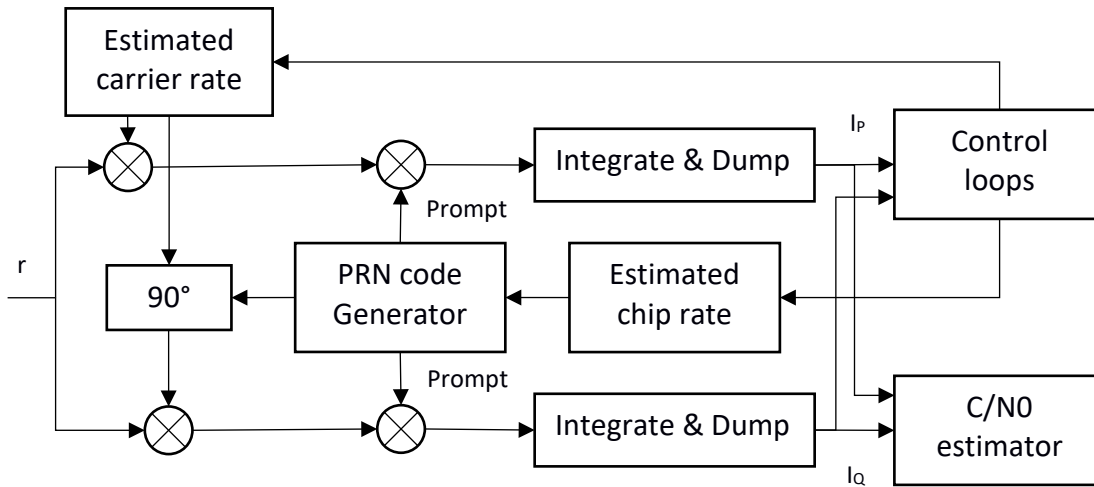


Figure 6 Position of the C/N<sub>0</sub> estimator in a typical GNSS receiver architecture (Kútik and Orejas 2012)

According to (Falletti, Pini and Presti 2011) and (Kútik and Orejas 2012), the position of the C/N<sub>0</sub> estimator in a GNSS receiver is located right after the correlator block and before the carrier tracking loop in the receiver architecture as illustrated in Figure 6.  $r$  is the down-converted digital signal. (Ward, Betz and Hegarty 2006) gives a more detailed description of the computation steps illustrated in Figure 7. The prompt In-phase ( $c$ ) and Quadra-phase ( $Q_p$ ) signals are integrated and dumped with  $K$  samples ( $K=20$  for a 1ms correlator) over the pre-detection integration time  $DT$ , which is typically 20 ms for GPS L1 C/A code. The meaning of “integrate” is clear, namely the cumulative sum of the input signals refers to the  $\sum_K(\cdot)$  operator in Figure 7. The term dump refers to the abrupt discharge of the capacitor (Singh and Sapre 2007) indicated by the switch symbol in Figure 7. From computational aspect, the integration and dumping process calculates the cumulative sum of the  $K$  samples from the input signals over a period defined by  $DT$ . After that, the cumulative sum is squared (corresponding to the  $(\cdot)^2$  operator) over a period of  $K$  times  $DT$  separately for I and Q signals. Then they are summed up to get the power envelope of the signal and passed through a Low Pass Filter (LPF). The output from the LPF is an estimate of the carrier power  $C$ . The noise power density  $N_0$  is obtained from the averaged Q component of the noise samples  $Q_N$  (corresponding to the  $\frac{1}{K}\sum_K(\cdot)$  operator), multiplied by a scale factor, squared and passed through the LPF. Finally, an estimation of C/N<sub>0</sub> is computed by dividing the carrier power by the noise power.

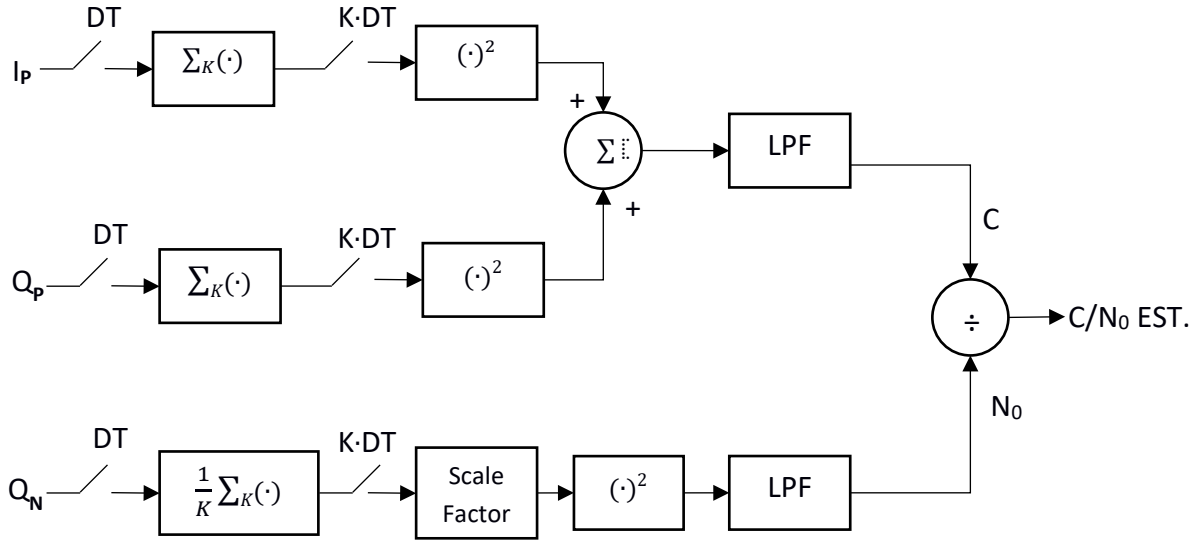


Figure 7 Basic C/N<sub>0</sub> meter in a receiver (Ward, Betz and Hegarty 2006)

Figure 7 describes one possible algorithm for the C/N<sub>0</sub> estimation in the GNSS receivers, which is almost equivalent to the formula given in (Badke 2009), where the carrier power is computed using the I signals and the Noise power density is estimated using the Q signals:

$$C = \frac{2 \cdot \overline{I_{ACC}^2}}{(f_s \cdot \tau)^2} \quad (2-48)$$

$$N_0 = \frac{2 \cdot \overline{Q_N^2}}{f_s \cdot \tau \cdot NBW} \quad (2-49)$$

$$C/N_0 = \frac{\overline{I_{ACC}^2}}{\overline{Q_N^2}} \cdot \frac{NBW}{f_s \tau} \quad (2-50)$$

where  $\overline{I_{ACC}^2}$  and  $\overline{Q_{ACC}^2}$  are the averages of the squares of accumulated I<sub>p</sub> and Q<sub>p</sub>, respectively;  $f_s$  is the analog to the digital sampling frequency and  $\tau$  is the integration time; The NBW stands for the noise bandwidth.

Other algorithms implemented in the GNSS receiver to compute C/N<sub>0</sub> are the Real Signal – Complex Noise (RSCN), the Beaulieu's method (BL), the Signal-to-Noise Variance (SNV), the Moment Method (MM) and the Narrowband-Wideband Power Ratio (NWPR) method (see (Muthuraman and Borio 2010) and (Dierendonck 1995)). (Falletti, Pini and Presti 2010) has compared the computational complexity and looked into the effect of phase noise on the C/N<sub>0</sub> estimation in these algorithms. The BL and MM algorithms are unbiased with respect to the residual phase error but they require more computation steps than the other algorithms.

Depending on the algorithm implemented in a GNSS receiver, the C/N<sub>0</sub> values may vary from one receiver type to another.

## 2.5 Multipath

Up-to-date, multipath is still considered to be the major error source that limits the accuracy of cm-level positioning, because it is a site-specific effect which is hard to model and cannot be eliminated by differential processing. Traditionally, multipath is defined as multiple signals arriving at the GNSS antenna by different paths, one direct path and a set of indirect paths, including signals resulting from reflection, diffraction<sup>7</sup> and scattering. For the reflected multipath, this thesis discusses only the specular reflection, which generates systematic errors in GNSS observables while the diffuse reflection on rough surfaces produces noise-like signals and is generally uncorrelated with time (Braasch 1996).

### Multipath categories

GNSS receiver measures the direct Line-of-Sight (LOS) signal plus the indirect Non-Line-of-Sight (NLOS) signals. The later ones are the cause of multipath in GNSS and wireless telecommunication fields. It includes the following three subcategories:

- Reflected signals: signals reflected from a smooth surface
- Diffracted signals: signals deviating from their direct paths upon interaction with on obstacles
- Scattering signals: signals travelling through objects of sizes similar to the signal wavelength, e.g., tree leaves

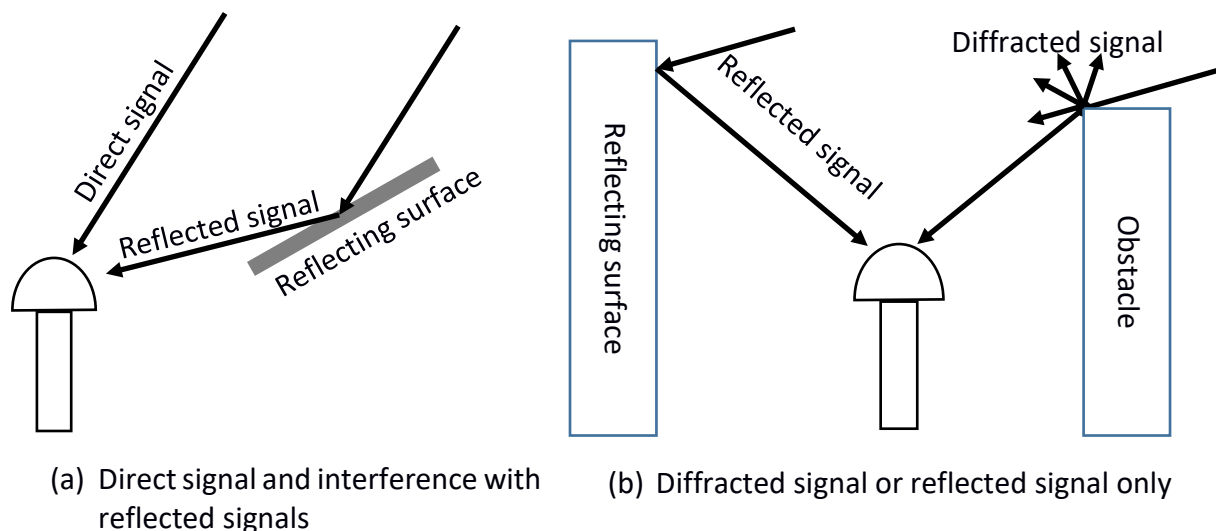


Figure 8 Illustration of multipath (a) type I: a composite of LOS and NLOS signals (b) type II: only NLOS signals

---

<sup>7</sup> We refer to the definition of diffraction by Collins dictionary: a deviation in the direction of a wave at the edge of an obstacle in its path.

The multipath shall be further categorized into:

- Multipath type I: Multipath error caused by the interference of the LOS and the NLOS signals
- Multipath type II: Multipath error caused by only the NLOS signals, while the LOS signals are blocked completely. This is type of multipath can cause larger errors in both, the code and carrier-phase measurements. Unlike the type I multipath, it can cause carrier-phase errors larger than a quarter of the wavelength because it depends only on the additional path length travelled by the NLOS signal.

(Brunner, Hartinger and Troyer 1999) and (Hartinger and Brunner 1999) have studied the signal diffraction effects which are belonging to multipath of type II and proposed  $C/N_0$  based observation weighting methods, SIGMA- $\epsilon$  and SIGMA- $\Delta$ . (Wieser and Brunner 2000) have further investigated the limitation of these two methods and proposed an extended model with a Danish method to reduce the influence of outliers.

### Code multipath

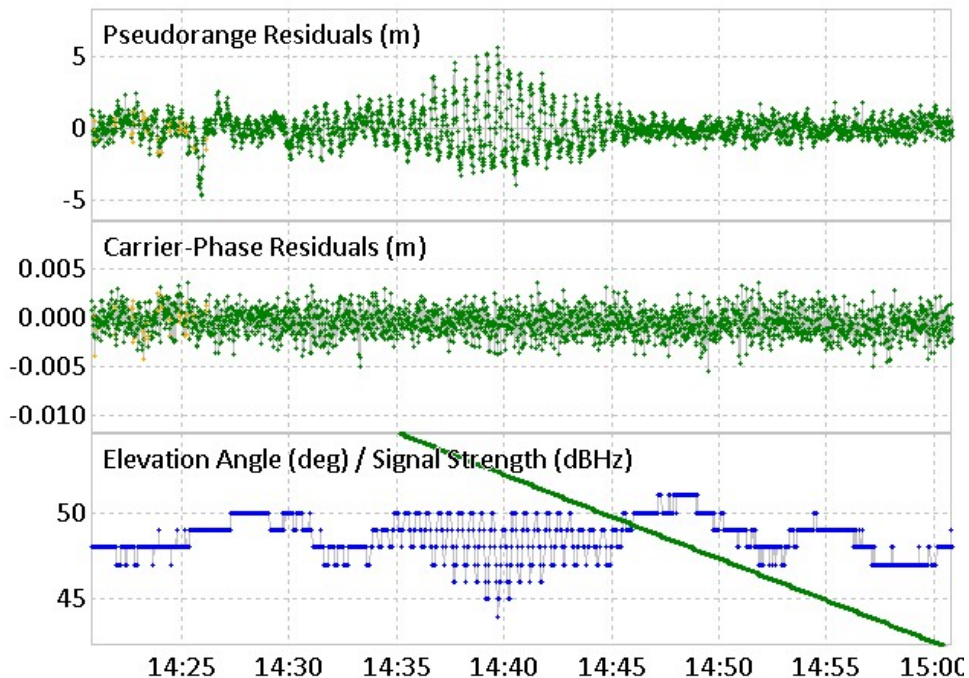


Figure 9 Short-delay multipath in the signal from GPS satellite G27 (data collected on the roof of HPV ETH Honggerberg in a zero baseline experiment)

(Misra and Enge 2011) point out that one important characteristics of multipath is that: if the delay of the multipath is less than 1.5 PRN code chip lengths (around 439.5 meters for C/A code), so-called short-delay multipath, the internally generated receiver signal will partially correlate with it. If the delay is greater than 1.5 chips, so-called long-delay multipath, the correlation power will be negligible. Receivers with the Multipath Estimating Delay-Lock-Loop (MEDLL)

implemented, can mitigate the long-delay multipath as showed in (Townsend, Wiebe and Jakab 2000).

An example of multipath present in the code pseudorange measurements is given in Figure 9. Clear oscillations are both seen in the time series of the  $C/N_0$  and SD code residuals from 14:35 to 14:45. Note that the satellite elevation angle for this period is rather high, varying from  $55^\circ$  to  $48^\circ$ . This data set is collected in a zero baseline test where one antenna is connected to one geodetic-grade Javad receiver and a low-cost u-blox receiver through a signal splitter. The Javad receiver has much stronger compression on the code multipath than the u-blox one, thus the residuals of the single-differenced code (between two receivers) plotted in Figure 9 show clearly the code multipath effect.

### Carrier-phase multipath

Several publications have shown the feasibility to create carrier-phase multipath corrections using  $C/N_0$  values. These studies are based on a simple multipath model in which only a single NLOS signal is present and a ground reflection with a small surface tilting angle  $g$  (see Figure 11) is assumed (Bilich, Larson and Axelrad 2008).

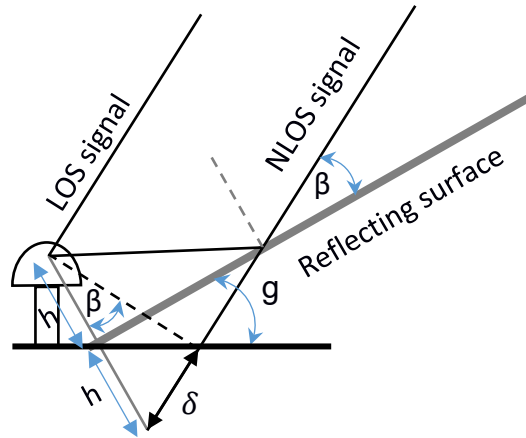


Figure 10 illustration of ground reflection

$$\begin{aligned}
 S &= S_{LOS} + S_{NLOS} = A \cos \varphi + \alpha A \cos(\varphi + \theta) \\
 &= \alpha_M A \cos(\varphi + \theta_M)
 \end{aligned}
 \tag{2-51}$$

With

$$\alpha_M = \sqrt{1 + \alpha^2 + 2\alpha \cos \theta}
 \tag{2-52}$$

$$\theta_M = \arctan \frac{\alpha \sin \theta}{1 + \alpha \cos \theta}
 \tag{2-53}$$

where  $S$  stands for the composite signal measured by the receiver;  $S_{LOS}$  is the direct LOS signal,  $S_{NLOS}$  denotes the NLOS signal;  $A$  is the amplitude of the direct signal;  $\alpha$  is the scale factor due to

reflection, diffraction or scattering;  $\varphi$  is the phase of the direct signal and  $\theta$  is the extra phase shift of the NLOS signal with respect to the direct signal.  $\theta_M$  stands for the carrier phase multipath in phase.

In order to obtain the extreme value of  $\theta_M$ , we take the first derivative of  $\theta_M$  with respect to  $\theta$  and set the derivative equal to zero:

$$\frac{d\theta_M}{d\theta} = \frac{\alpha \cos\theta + \alpha^2}{(1 + \alpha \cos\theta)^2 + \alpha^2 \sin^2\theta} = 0 \quad (2-54)^8$$

As one can see, the denominator is always larger than zero. The only way to make the equality hold is to set the numerator equal to zero.

$$\alpha \cos\theta + \alpha^2 = 0$$

Thus, according to the extreme value theorem, when

$$\theta = \arccos(-\alpha) \quad (2-55)$$

Thus

$$\begin{aligned} \cos\theta &= -\alpha \\ \sin\theta &= \sqrt{1 - \alpha^2} \end{aligned}$$

If the second derivative is negative, the carrier-phase multipath error  $\theta_M$  has the maximum value  $\theta_{M_{\max}}$ .

$$\begin{aligned} \frac{d^2\theta_M}{d\theta^2} &= \frac{\alpha \sin\theta (\alpha^2 - 1)}{(1 + 2\alpha \cos\theta + \alpha^2)^2} \\ &= \frac{\alpha (\alpha^2 - 1) \sqrt{1 - \alpha^2}}{(1 - \alpha^2)^2} \\ &= \frac{-\alpha}{\sqrt{1 - \alpha^2}} \end{aligned} \quad (2-56)$$

Since  $\alpha$  is the ratio of the amplitudes of the LOS and NLOS signal, its value is in-between zero and one.  $\frac{d^2\theta_M}{d\theta^2}$  is always smaller than zero and thus  $\theta_M$  indeed has a maximum value when (2-55) holds true. Replacing  $\theta$  in formula (2-53) by (2-55), the maximum carrier-phase multipath error is derived as

$$\theta_{M_{\max}} = \arctan \frac{\alpha \sqrt{1 - \alpha^2}}{1 - \alpha^2} = \arctan \frac{\alpha}{\sqrt{1 - \alpha^2}} \quad (2-57)$$

The  $\frac{\alpha}{\sqrt{1 - \alpha^2}}$  is monotonically increasing function with  $\alpha \in (0, 1)$  and reaches the positive infinite when  $\alpha = 1$  (see Figure 11). The arctan function also monotonically increases, thus  $\theta_{M_{\max}}$

---

<sup>8</sup> Proof of the equality refers to Appendix A

reaches its maxim value  $90^\circ$  when  $\alpha = 1$ . Therefore, the largest carrier-phase multipath error is a quarter of the carrier wavelength, which is 4.8 cm for the GPS L1 signal.

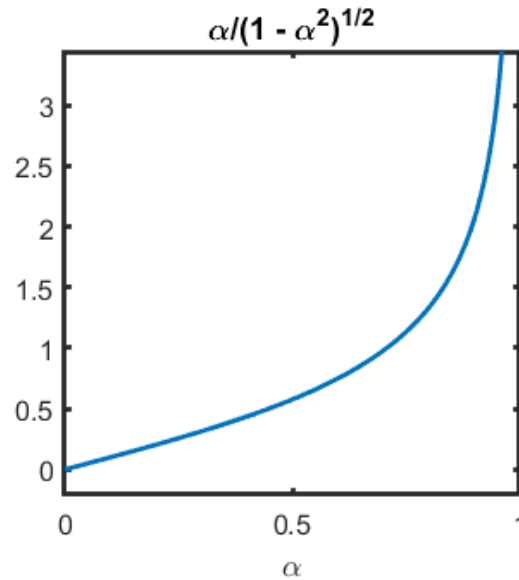


Figure 11 Plot of the function  $\alpha / (1 - \alpha^2)^{1/2}$

### Spectral analysis of the multipath through $C/N_0$

*Create carrier-phase multipath correction through Fourier transfer of the  $C/N_0$  values*

The phase shift  $\theta$  relates to the  $C/N_0$  values as:

$$a \cdot CNR = (\alpha_M A)^2 = A^2 + \alpha^2 A^2 + 2\alpha A^2 \cos\theta \quad (2-58)$$

with

$$CNR = 10^{\frac{C/N_0}{10}}$$

where  $a$  is a scale factor. The  $A^2$  and  $\alpha^2 A^2$  terms contribute as an offset while the  $2\alpha A^2 \cos\theta$  term contributes to the oscillation of the signal strength  $CNR$  due to the  $\cos\theta$  term. Therefore, by analyzing the spectral parameters of the  $C/N_0$  values, one can extract the frequency and amplitude content of the oscillations in  $C/N_0$  induced by multipath signals, e.g., (Axelrad, Comp and MacDoran 1994).

As an example, the  $C/N_0$  values of satellite G27 measured by the u-blox receiver in the Zero Baseline (ZB) test in Chapter 3 is analyzed by Fourier transform. The  $C/N_0$  values in the time domain is plotted in Figure 12 and the Fourier transformed  $C/N_0$  values in the frequency domain are plotted in log-log scale in Figure 13. A spike at 0.033 Hz in the log-log scale plot indicates that an oscillation signal with a period of 30s exists in the  $C/N_0$  time series, which is verified by the enlarged  $C/N_0$  plot in the interval 5000 to 5600 second in the time domain (Figure 14).

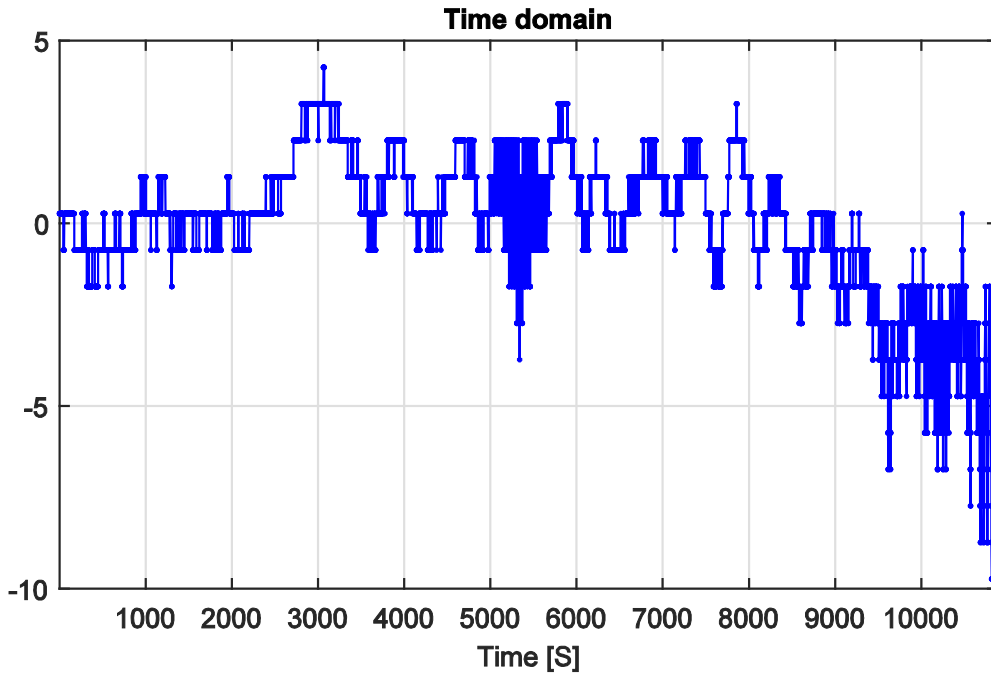


Figure 12 The  $C/N_0$  time series of satellite G27 measured by the u-blox receiver module with mean value removed.

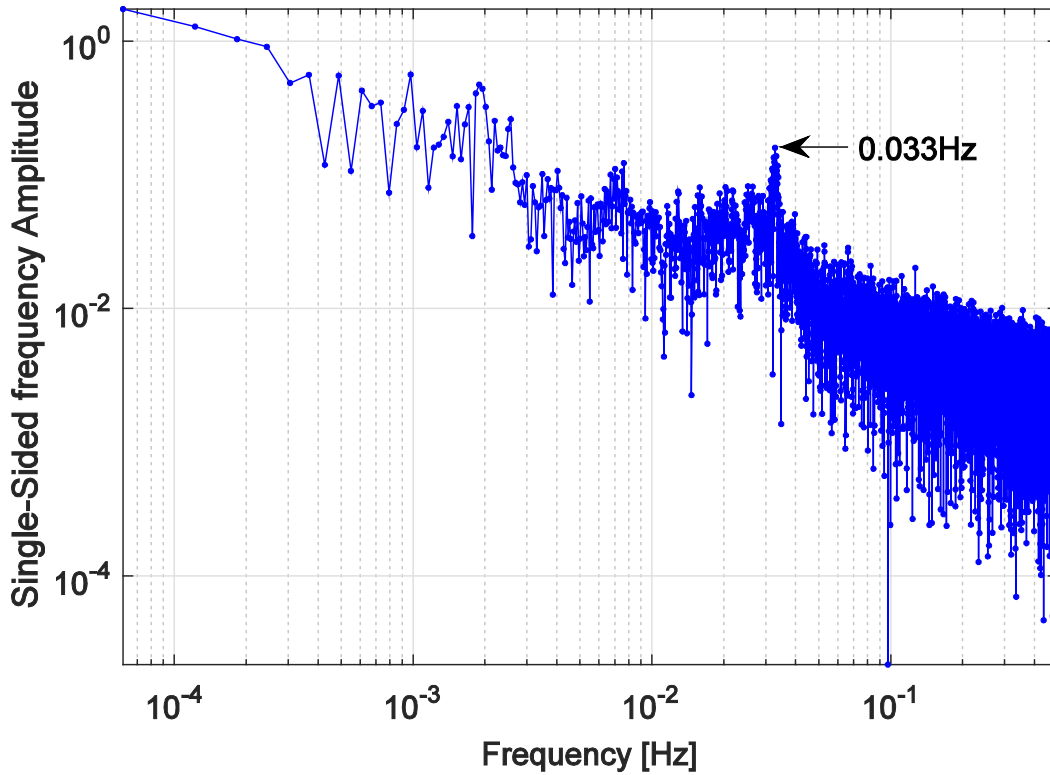


Figure 13 The Fourier transform of the  $C/N_0$  time series (with mean value removed)



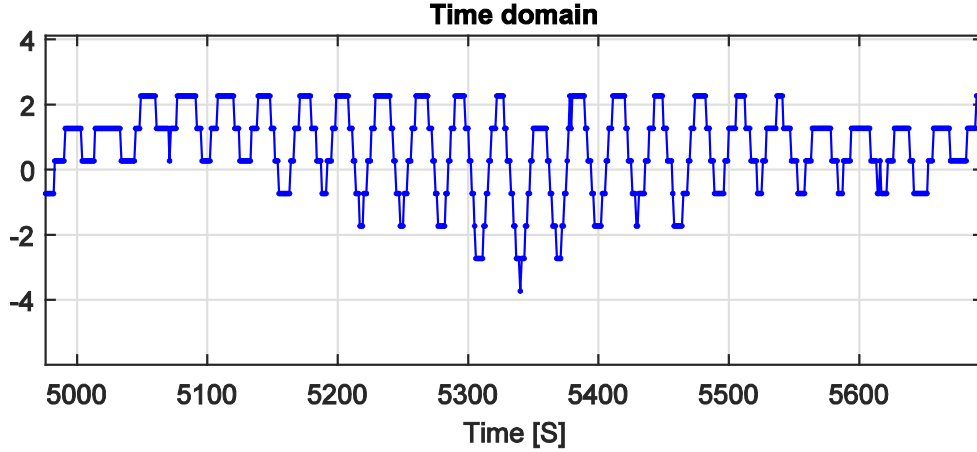


Figure 14 The oscillations with a 30 second period in the C/N<sub>0</sub> time series

In (Rost and Wanninger 2009), the author derived a direct relation among the signal strength oscillation, the carrier-phase multipath and the antenna height as follows.

$$\theta_M = -\arcsin\left(\frac{d\alpha_M}{d\theta}\right) \quad (2-59)$$

Then one can extend the derivative  $\frac{d\alpha_M}{d\theta}$  to

$$\theta_M = -\arcsin\left(\frac{d\alpha_M}{dt} / \frac{d\theta}{dt}\right) \quad (2-60)$$

The phase shift  $\theta$  in the reflected signal from a flat ground can be calculated based on its relation to the antenna height  $h$  as illustrated in Figure 11.

The extra travel path  $\delta$  is obtained as:

$$\delta = 2h\sin\beta = 2h\sin(el + \gamma) \quad (2-61)$$

Given that

$$\theta = \frac{\delta}{\lambda} \cdot 2\pi$$

One has

$$\theta = \frac{4\pi h}{\lambda} \sin(el + \gamma) \quad (2-62)$$

Thus,

$$\frac{d\theta}{dt} = \frac{4\pi h}{\lambda} \cos(el + \gamma) \frac{del}{dt} \quad (2-63)$$

The rate of elevation change can be easily computed from the broadcast ephemeris. When one knows the antenna height and the  $\gamma$  angle, the time derivative of  $\theta$  becomes available. Now the

only unknown term in (2-60) is the time derivative of  $\alpha_M$ . As indicated by formula (2-58), even though the  $C/N_0$  values are proportional to  $\alpha_M$ , there is no direct connection because normally the proportionality factor  $N_0$  is not unknown. However, by removing the trend in the  $C/N_0$  time series and applying the Fourier transform, the frequency of the  $C/N_0$  time series is obtained.

$$X(f) = \mathcal{F}\{\delta_{CNR}\} \quad (2-64)$$

where  $\delta_{CNR}$  is the CNR without the trend (the trend  $A$  is usually modeled by a polynomial fitting). Applying the time derivative to (2-58) on both side,

$$\frac{d\delta_{CNR}}{dt} \propto \frac{d\alpha_M}{dt}$$

Then utilizing the differentiation property of Fourier transforms, one has:

$$\mathcal{F}\left(\frac{d\alpha_M}{dt}\right) \propto \mathcal{F}\left(\frac{d\delta_{CNR}}{dt}\right) = i2\pi f X(f) \quad (2-65)$$

Finally, by an inverse Fourier transform, the time derivative of  $\alpha_M$  is calculated and used to compute the carrier-phase multipath error  $\theta_M$ , which can be used to directly correct the carrier-phase measurements.

#### *Wavelet analysis based carrier-phase multipath modeling*

The Fourier transform can tell which frequency of oscillation exists in the  $C/N_0$  time series, but cannot tell when or where it happens. A better method is proposed by (Bilich, Larson and Axelrad 2008): the wavelet analysis which detects the non-stationary content of multipath induced oscillations in both, frequency and scale (time domain). Compiling the formula from (Georgiadou and Kleusberg 1988) as the complete mathematical model of carrier-phase measurements with multiple NLOS signals:

$$S = S_{LOS} + \sum_i S_{NLOS}^i = A \cos \varphi + \sum_i \alpha_i A \cos(\varphi + \theta_i) \quad (2-66)$$

where  $i$  stands for the index of the  $i$ th NLOS signal.

The important information hidden in equation (2-66) is that the NLOS signals are time-varying signals with limited periods. To be more precise, the time argument shall be added to the expression:

$$S(t) = S_{LOS}(t) + \sum_i S_{NLOS}^i(t) \quad (2-67)$$

$$\text{with } S_{NLOS}^i(t) = \begin{cases} 0 & \text{when } t \notin (t_0^i, t_p^i) \\ \alpha_i A \cos(\varphi(t) + \theta_i(t)) & \text{when } t \in (t_0^i, t_p^i) \end{cases}$$

$(t_0^i, t_p^i)$  is the interval of the  $i$ th multipath signals

Compared to a Fourier transform, which decomposes a signal into only the frequency domain, the wavelet analysis breaks up a signal into shifted and scaled versions of the original (or mother) wavelet (Misiti, et al. 2009), in both the time and frequency domain. The drawback of a Fourier transform is that it assumes that the constituent sinusoidal signals are stationary and have an infinite duration. This is against the nature of a multipath signal which is nonstationary (Daubechies 1990) as you see from (2-67). On the other hand, a wavelet is a waveform of limited duration and has a zero mean, making wavelet transforms well-suited for multipath analysis. (Bilich and Larson 2007) have shown that it also provides better time-frequency localization than windowed Fourier transforms in the development of signal strength power spectral mapping. The mathematical representation of a continuous wavelet transform is:

$$C(s, p) = \int_{-\infty}^{\infty} f(t)\psi(s, p, t)dt \quad (2-68)$$

where  $C(s, p)$  is the wavelet coefficient which is a function of scale  $s$  and position  $p$ ,  $f(t)$  denotes the original signal in time domain  $t$ ,  $\psi(s, p, t)$  is the wavelet function which can be selected from a broad set of wavelet families, like Haar, Daubechies, Symlets and others. More details on how to model carrier-phase multipath using the wavelet analysis of signal strength please read (Bilich, Larson and Axelrad 2008) and (Bilich and Larson 2007).

As an example, the wavelet analysis of the same  $C/N_0$  time series of satellite G27 as plotted in Figure 12 is given in Figure 15. The chosen wavelet function is the Morlet wavelet as suggested in (Meyers, Kelly and O'Brien 1993):

$$\psi(t) = \pi^{-1/4} e^{-i\omega_0 t} e^{-t^2/2} \quad (2-69)$$

The amplitudes of the transferred signals with wavelet scales from 1 to 64 are plotted in the middle of Figure 15. The dominating scales are indicated by the two bright zones: one with scales from 33 to 17 located at 5000 to 6000 and the other one with scales from 61 to 17 located at 10000 to 11000. The dominating scale with maximum amplitude is found to be 32, corresponding to 0.025 Hz in frequency, plotted in the bottom of Figure 15. To show it more clearly, a zoom of the plot from 5000 to 6000 is given in Figure 16.

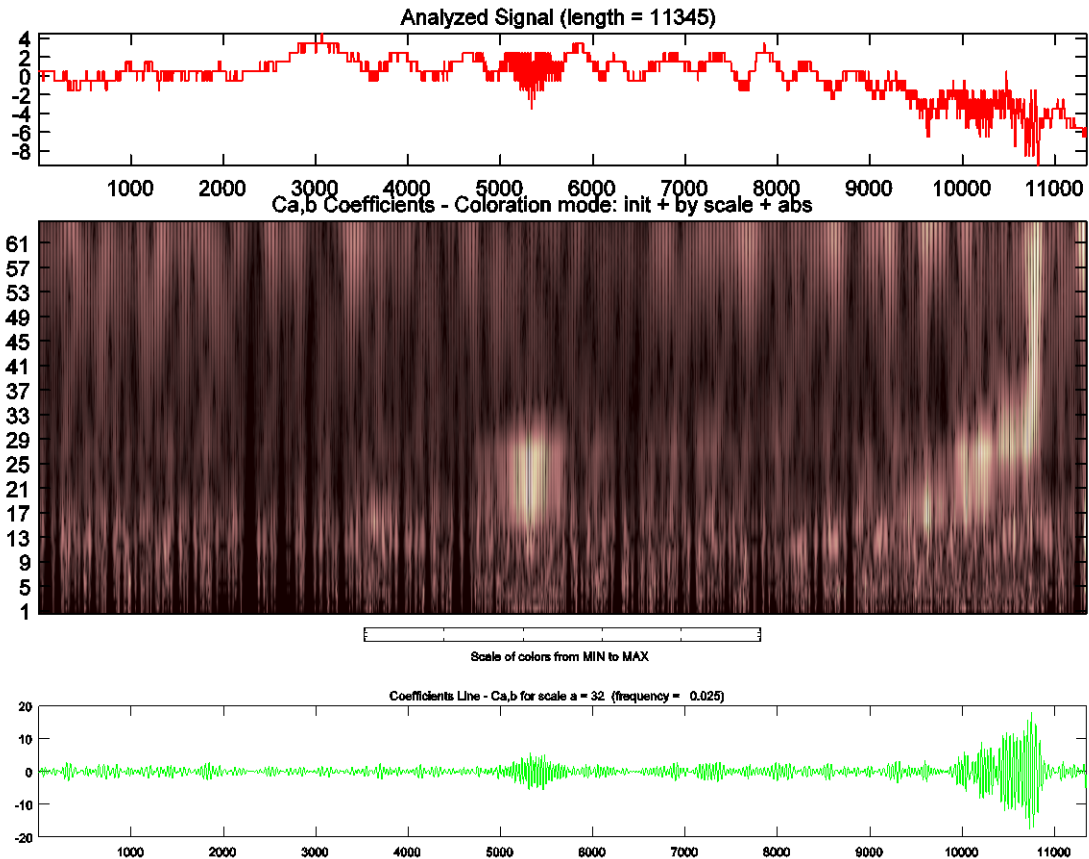


Figure 15 Wavelet analysis of the C/Notime series (mean value removed)

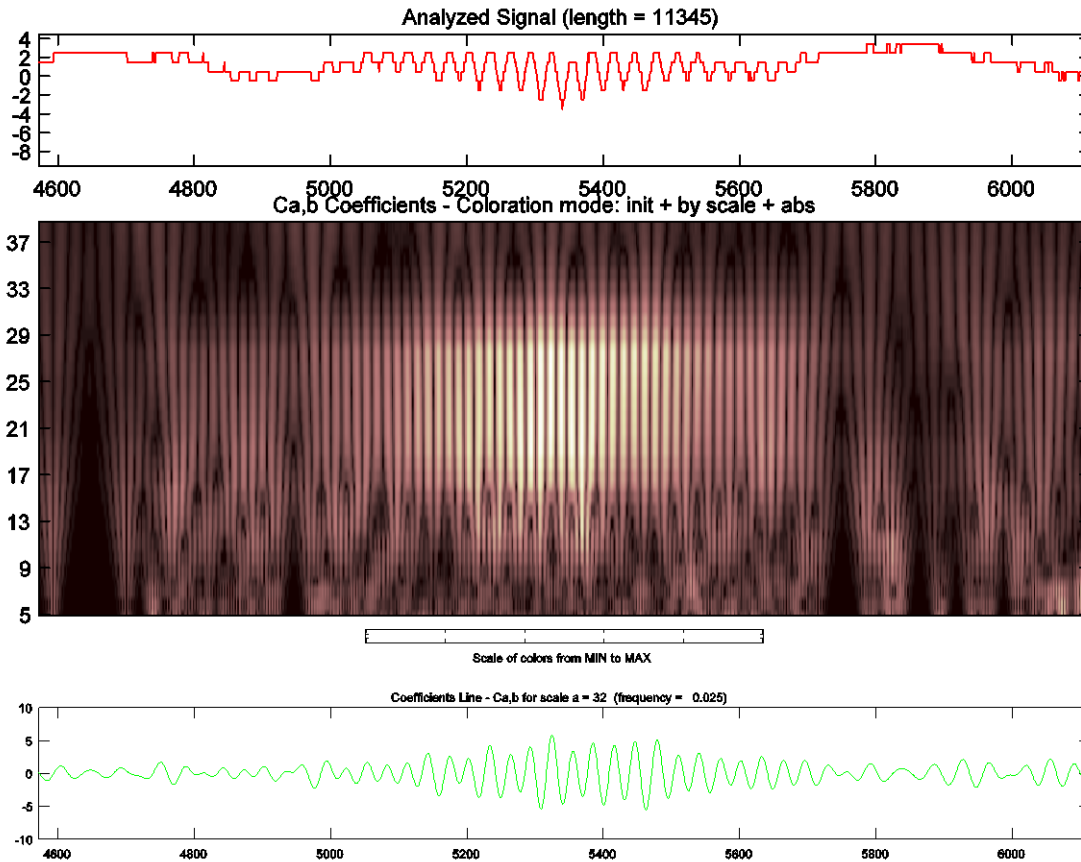


Figure 16 Zoom in of the wavelet analysis plot

### Unique feature of multipath

The multipath possesses the following 4 features:

- 1. Effects on all three coordinate components**

Take the big coordinate variations from 12:30 to 13:30 (marked by red and light-blue in Figure 17) as an example. It is known that for this time interval the signal of satellite 32 is contaminated by multipath effects (mostly the type II multipath), and it can be seen that the coordinates differ from the true values in all three components.

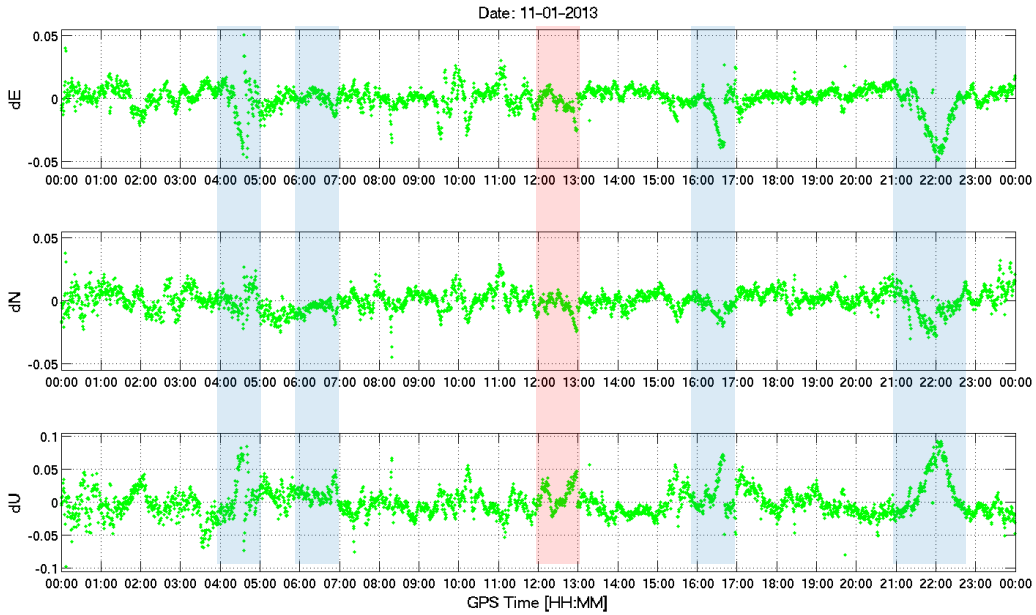


Figure 17 Coordinate deviations in East, North and Up component of station RGo1

## 2. $C/N_0$ signature

The cause of the big coordinate deviations marked by red in Figure 17 are the big carrier-phase residuals from GPS satellite 32, which is coupled with a big reduction of its  $C/N_0$  values (see Figure 18).

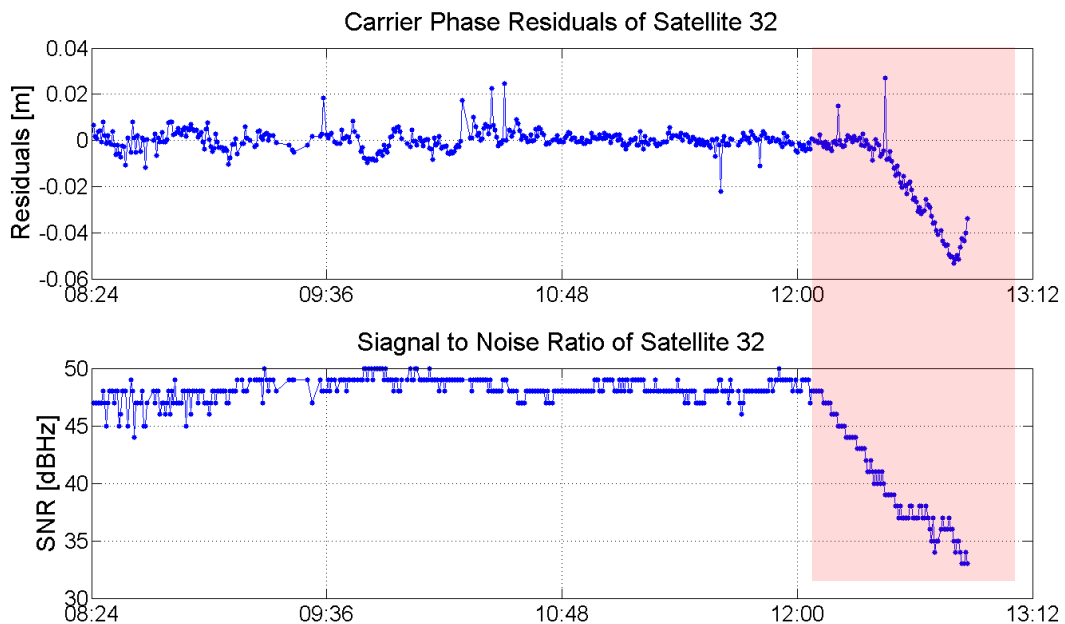


Figure 18 Single-difference carrier-phase residuals and the  $C/N_0$  values of satellite G32 (type II multipath)

## 3. Sidereal repetition

By comparing the carrier-phase residuals of three adjacent days, a sidereal repetition is seen in Figure 19, where one see that a 226 second shift exists in the time series plot of the carrier phase residuals from Day 1 to Day 2 and from Day 2 to Day 3.

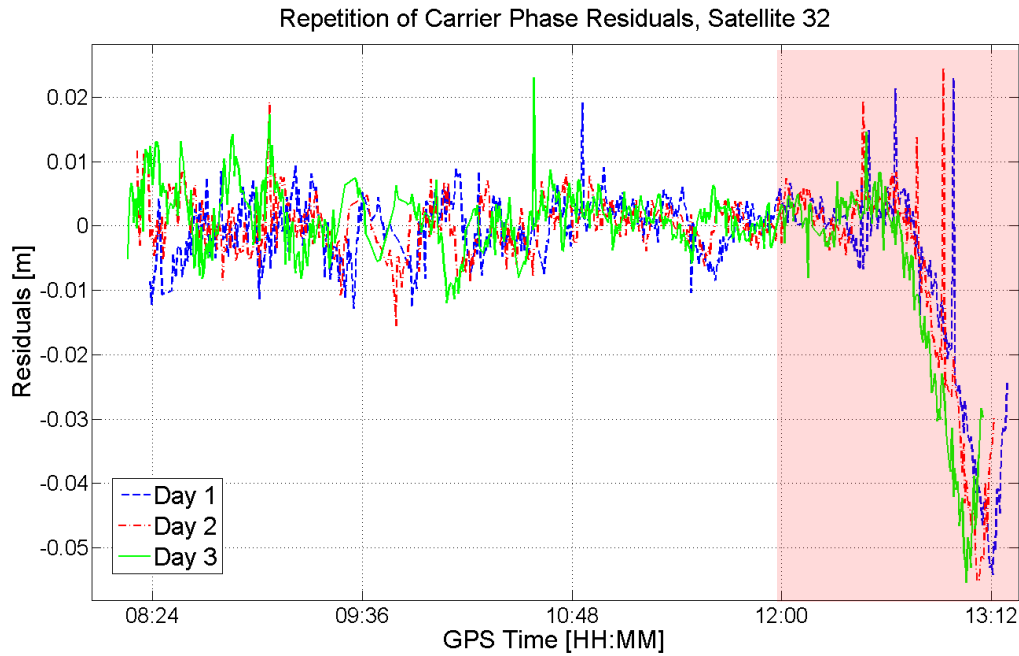


Figure 19 Sidereal repetition of the carrier-phase multipath

In general, the satellite geometry repeatability is assumed to be one sidereal day, namely 23 hours 56 minutes and 4 seconds. However, the actual repeat period is slightly different from satellite to satellite and from day to day. Methods to calculate the correct repeat period based on broadcast ephemeris, post-processed GPS orbits and local geometry were proposed by (Axelrad, Larson and Jones 2005).

Here, a new method called time shift cross-correlation is presented in this contribution. We cross correlate the SD carrier-phase residuals of a specific satellite between two days. An optimized time shift between these two days is estimated under the principle of maximum likelihood.

$L_i^{k,m}$  ... carrier phase residual of satellite  $k$  at epoch  $i$  on day  $n$

$L_i^{k,n}$  ... carrier phase residual of satellite  $k$  at epoch  $i$  on day  $m$

Correspondingly,

$T_i^{k,m}$  ... GPS time stamp of  $L_i^{k,m}$

$T_i^{k,n}$  ... GPS time stamp of  $L_i^{k,n}$

A time shift cross-correlation is implemented by the following steps:

a) Time matching between vector  $[T_1^{k,m} \dots T_i^{k,m}]$  and  $[T_1^{k,n} \dots T_i^{k,n}]$  plus a time shift  $(m - n) \cdot T_{repeat}$ . We say  $T_i^{k,m} \rightarrow T_j^{k,n}$  when  $T_i^{k,m} = T_j^{k,n} + (m - n)T_{repeat} + e$ , where  $e$  is a small value at the millisecond level to account for the clock jumps in low-cost receivers.

b) Compute the RMS of the matching carrier-phase residual differences.

$$\Delta L_{RMS} = \sqrt{\frac{1}{n} \sum_1^l (L_i^{k,m} - L_j^{k,n})^2}$$

where  $l$  is the number of matched pairs.

c) Step a and b are repeated with different  $T_{repeat}$  values. The  $T_{repeat}$  that generates the smallest RMS of residual differences is the maximum likely correct repeat period of this satellite.

To make it easy to read, we list  $T_{shift} = T_{solar} - T_{repeat}$  where  $T_{solar} = 24 \text{ hours}$ . The computed  $T_{shift}$  for all satellites are listed in Table 1 below.

Table 1 Time difference between solar day and the GPS satellite repeat period

<b>PRN</b>	<b>1</b>	<b>2</b>	<b>3</b>	<b>4</b>	<b>5</b>	<b>6</b>	<b>7</b>	<b>8</b>	<b>9</b>	<b>10</b>	<b>11</b>
$T_{shift}$	226	226	256	286	285	226	226	285	286	285	200
<b>PRN</b>	<b>12</b>	<b>13</b>	<b>14</b>	<b>15</b>	<b>16</b>	<b>17</b>	<b>18</b>	<b>19</b>	<b>20</b>	<b>21</b>	<b>22</b>
$T_{shift}$	226	286	226	226	226	225	226	226	226	226	225
<b>PRN</b>	<b>23</b>	<b>24</b>	<b>25</b>	<b>26</b>	<b>28</b>	<b>29</b>	<b>30</b>	<b>31</b>	<b>32</b>		
$T_{shift}$	226	226	255	226	226	226	226	226	226		

One can see from the results shown in Table 1, 20 of the GPS satellites repeat its orbit every 23 hours 56 minutes 14 seconds ( $T_{shift} = 226$ ), including satellite 32 as plotted in Figure 19. However, the other satellites have different repeat periods which one has to pay attention to when using this feature to model or mitigate multipath errors.

#### 4. Site specific

The multipath errors depend on the locations of the reflecting surfaces or the obstacles. Therefore, it is highly site-specific. Even two stations close to each other may have a different multipath environment.

Based on the 4 features above, one can differentiate the multipath effects from other GNSS errors.



## Mitigate the multipath by sidereal stacking of the coordinates for a static station

In short baseline processing, the deviation of the kinematic coordinates from the true values is mainly due to multipath, the dominating GNSS signal error source remaining in the double-difference measurements. And from the estimated satellite repeat period, all are close to a sidereal day (see Table 1). Therefore, a method to mitigate the multipath effects and improve the coordinate's accuracy is proposed based on sidereal stacking of the kinematic coordinates over multiple days.

The baseline between station RD01 (as reference) and RG01(as rover) is processed by RKT processing. The kinematic coordinates of RG01 are used to conduct the sidereal stacking. From 3 up to 100 days were chosen as the time interval for sidereal stacking. 7 days is found to be the best period, which generates the smallest RMS. The multipath template at coordinate level is derived from the 7 day sidereal stacking, plotted in Figure 20. Then it is used to correct the coordinates of a consecutive (denoted as raw data in the figure). The corrected kinematic coordinates are improved, reducing the standard deviation by 5.1 mm in the East, 2.4 mm in the North and 9.7 in the Up component.

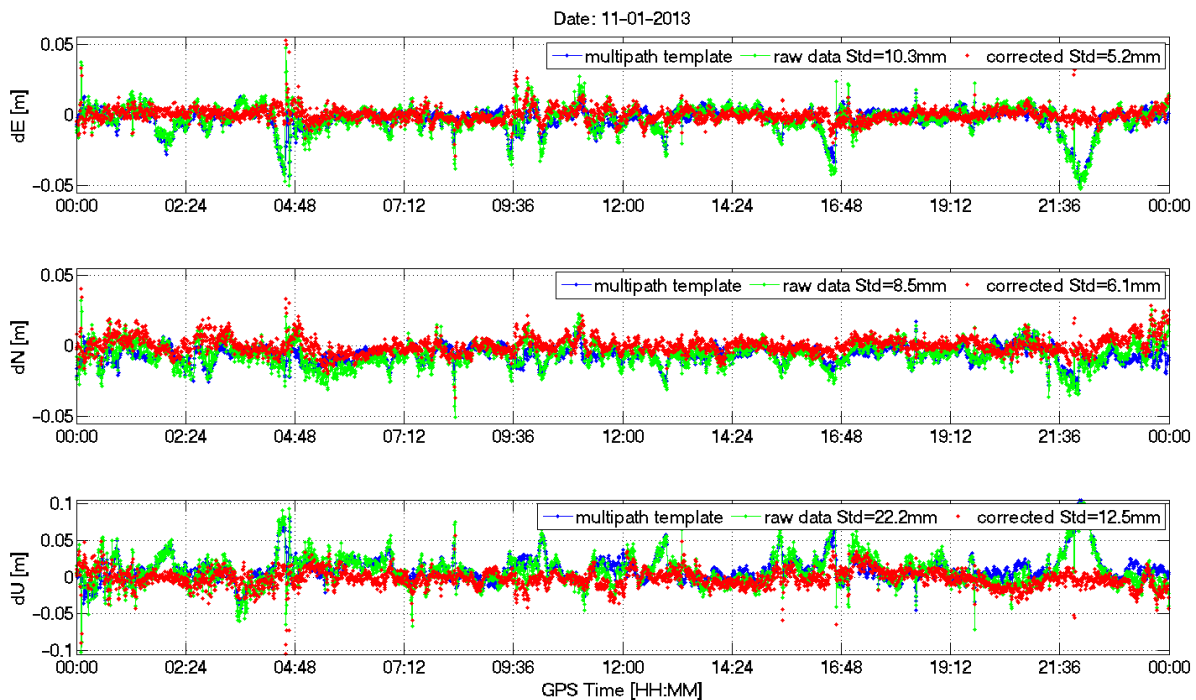


Figure 20 Sidereal stacking of 7 days kinematic coordinates

This method is practical to mitigate the multipath effects directly on the kinematic coordinates of static stations. However, it will not work for a moving station because the observation environment is changing all the time.

## Chapter 3 Single-frequency receivers and antennas

Single-frequency receivers and antennas are mostly low-cost ones. (Carcanague, Julien, et al. 2013) discussed the differences between low-cost and high-end GNSS receivers, among which I compile the following:

- Front-end filter quality and bandwidth: high-end receivers use wide-band and expensive SAW<sup>9</sup> filters, while low-cost receivers use narrow-band filters to limit the sampling frequency.
- Local oscillator stability: more stable Oven Controlled crystal Oscillators (OCXO) are used in high-end receivers and Temperature Compensated crystal Oscillators (TCXO) are used in low-cost receivers. A TCXO receiver clock is far below 100 Euros but drifts (the difference to true time) much faster than an OCXO clock (see Figure 24 and Figure 25).
- Local clock steering: high-end receivers designed for RTK typically use clock steering techniques, to keep their clock offset synchronized within a few ten nanoseconds of GPS time. Most low-cost receivers do not do that but simply adjust when the difference is close to one millisecond. This has to be paid special attention to for GNSS moving baseline or Multi-GNSS Attitude applications (Rothacher and Willi 2017).
- Signal processing techniques: high-end receivers use patented multipath mitigation techniques, whereas low-cost receivers are prone to multipath effect.
- Measurement selectivity: high-end receivers are generally more selective in terms of measurement quality.
- Measurement precision: the typical carrier-phase and code precision of a high-end receiver on L1 is around 0.2 mm and 2 cm, respectively (Leica Geosystems AG 2008), while a low-cost receiver's carrier-phase precision is in the range of 2 mm to 3 mm. The carrier-phase precision is equivalent to the zero-difference jitter of the carrier-phase phase-locked loop (Häberling 2015).

In this chapter, the author investigates the low-cost single-frequency receivers and antennas via ZB and short baseline tests.

### 3.1 Zero baseline test of low-cost single frequency receivers and antennas

In a ZB test, the double-differenced code and carrier-phase measurements present the noise characteristics, because the signals come from the same antenna and go to two different receivers after the signal splitter, i.e., all the common errors cancel out by double differencing

---

<sup>9</sup> SAW filter: Surface Acoustic Wave filter

except the receiver-dependent noises. The experiment setup of the ZB test is shown in Figure 21. The instruments and data information are summarized in Table 2.

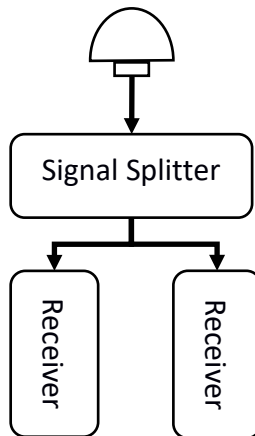


Figure 21 A zero baseline setup

Table 2 Experiment setup of zero baseline test

	Antenna	Receiver	Date	Sampling rate
Test 1	Trimble bullet III	u-blox 5T; u-blox 5T	03/10/2013	1 Hz
Test 2	Trimble bullet III	Javad Sigma-G3TAJ; u-blox 5T	04/10/2013	1 Hz

The differences of processed kinematic coordinates to true antenna coordinates are plotted in Figure 23 and Figure 22.

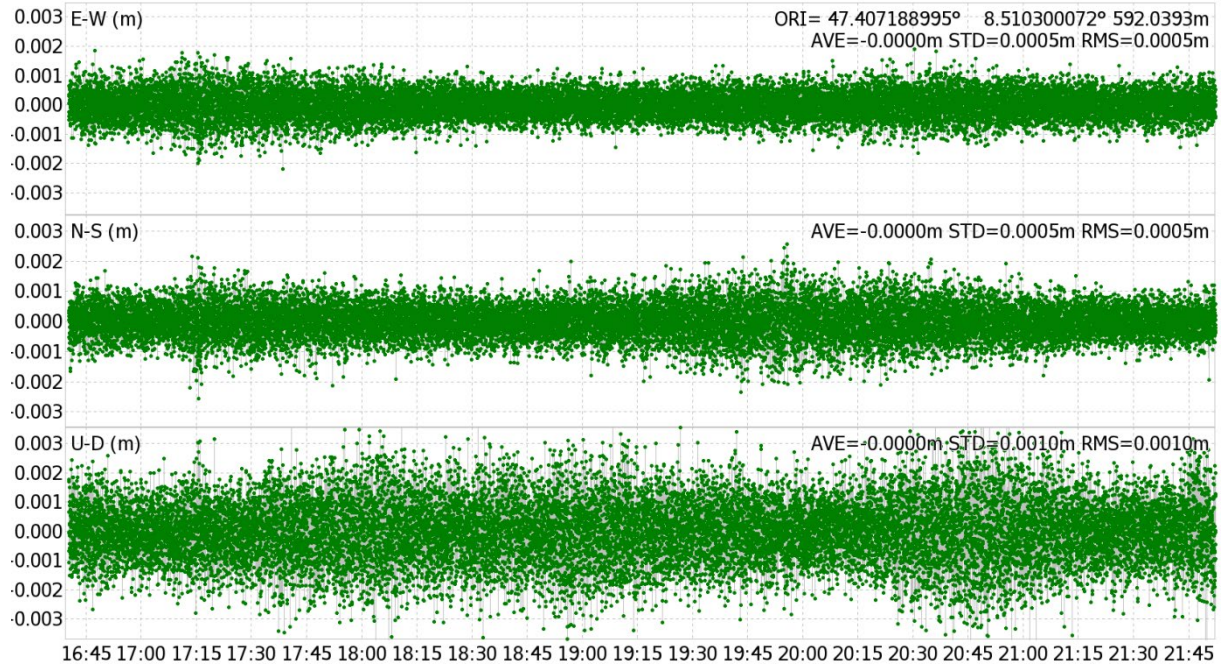


Figure 22: Kinematic coordinates of the zero baseline test with two u-blox-5T receiver modules

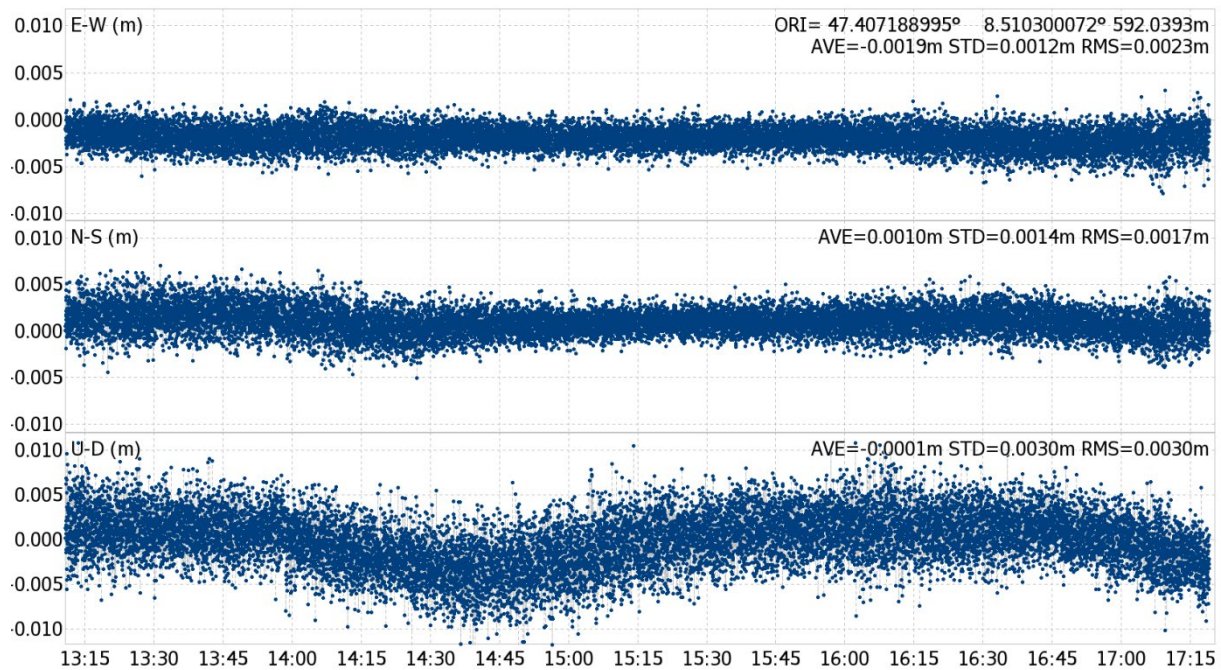


Figure 23: Kinematic coordinates of the zero baseline test with one u-blox-5T receiver module and one Javad receiver

The statistics of the computed kinematic coordinates from the two tests are listed in Table 3.

Table 3 Statistics of the kinematic coordinates

	Receiver	Mean [mm]			STD [mm]			RMS error[mm]		
		E	N	U	E	N	U	E	N	U
Test 1	u-blox 5T; u-blox 5T	0	0	0	0.5	0.5	1	0.5, 0.5, 1		
Test 2	Javad sigma; u-blox 5T	-1.9	1	0.1	1.2	1.4	3	2.3, 1.7, 3		

The Mean, STD and RMS error are defined as:

$$Mean = \bar{x} = \frac{1}{n} \sum_{i=1}^n x_i$$

$$STD = \sqrt{\frac{1}{n-1} \sum_{i=1}^n (x_i - \bar{x})^2}$$

$$RMS = \sqrt{\frac{1}{n} \sum_{i=1}^n (x_i - x_{real})^2}$$

where  $x_{real}$  stands for the real coordinates of the antenna phase center.

The processed kinematic positions, which are computed from the data measured by the same type of receivers, are two times more accurate than those with different receivers. Because the receiver-dependent errors in different type of receivers, like receiver clock errors, are remaining in the double-differenced measurements. This explains why in Test 2 the accuracies of the computed positions are worse than those of Test 1. And in Test 2, clear trend is seen in the kinematic coordinate time series, indicating the existence of systematic errors.

### 3.2 Receiver clock

As mentioned in the beginning of this Chapter, Low-cost single-frequency GNSS receivers like u-blox receiver modules employ the TCXO (see in

Table 4) according to "u-blox GNSS module overview". This means the u-blox receiver should have larger clock error than the Javad receiver which uses OCXO.

Table 4 u-blox receiver clock

Receivers	Oscillator	Short Term Stab.
u-blox NEO-M8P	TCXO	1s: 1e-9 10s: 5e-10 100s: 5e-10
u-blox LEA-6T	TCXO	
u-blox LEA-5T	TCXO	

The receiver clock errors of the u-blox receiver and the Javad receiver are both estimated by SPP approach using code measurements from the data collected in Test 2. The clock errors are represented by receiver clock offsets and drifts which are visualized from Figure 24 to Figure 26. The clock offset is estimated along with the coordinate parameters in a standard SPP process using code measurements, whereas the clock drift is computed as the first order time derivative of the estimated clock offset.

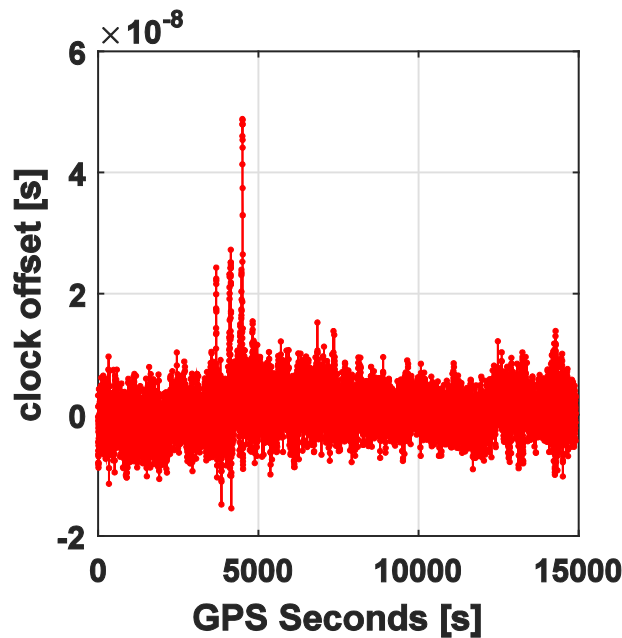


Figure 24 Receiver clock offsets of Javad sigma receiver



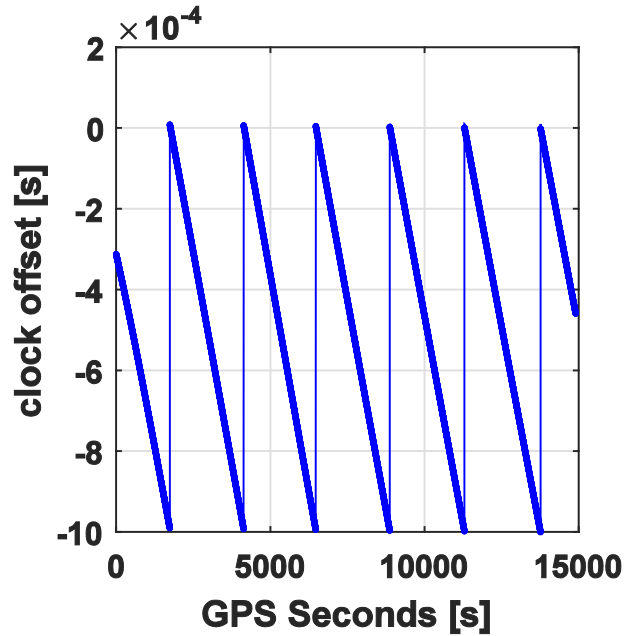


Figure 25 Receiver clock offsets of ublox 5T receiver

One can see that the low-cost single-frequency receiver’s clock offset is at the  $10^{-4}$  second level while the high-end receiver’s clock offset is at the  $10^{-8}$  second level. As mentioned at beginning of this chapter, low-cost u-blox receivers adjust their receiver clock to keep its difference to real GPS time within less than 1 millisecond (see Figure 25) because no clock steering is implemented like in the high-end Javad receiver.

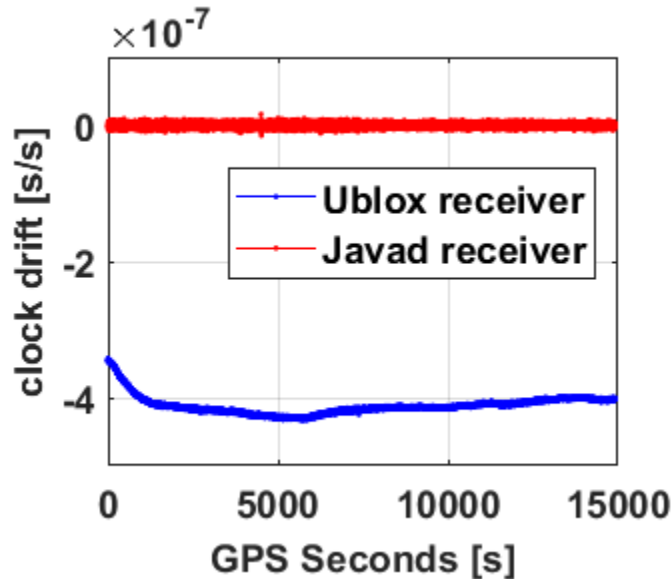


Figure 26 Receiver clock drifts of ublox and Javad receivers

Moreover, two low-cost receivers of the same type might adjust their clocks at different epochs. By processing the data collected in Test 1, one can see the two u-blox 5T receivers clocks have their 1 ms clock error jumps (caused by the clock adjustment) at different epochs (see Figure 27).

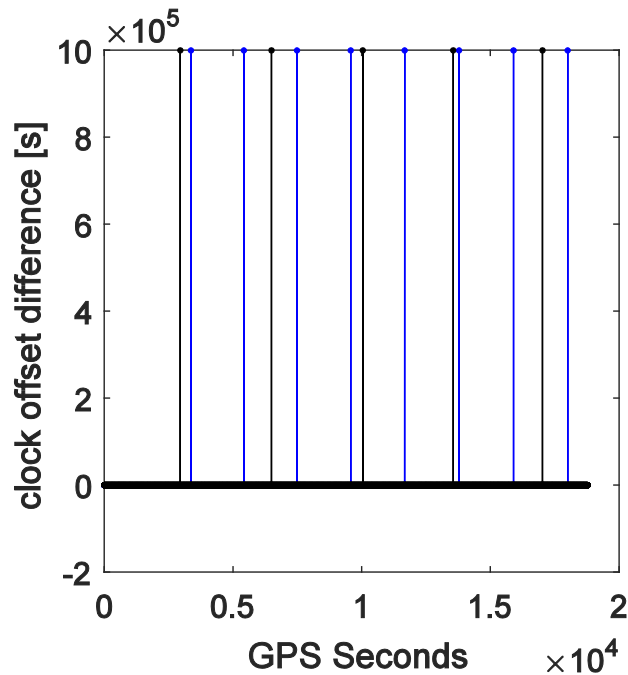


Figure 27 The 1 ms receiver clock error jumps of the rover (blue) and the reference receiver (black), vertical axis is the difference of receiver clock offset between two epochs (unit: seconds), horizontal axis is the GPS seconds since the first epoch

However, the results from the newer u-blox M8T and u-blox M8P do not show any clock adjustment in the two hours data plotted in Figure 29, because they are designed for RTK positioning and might have implemented the clock steering internally.



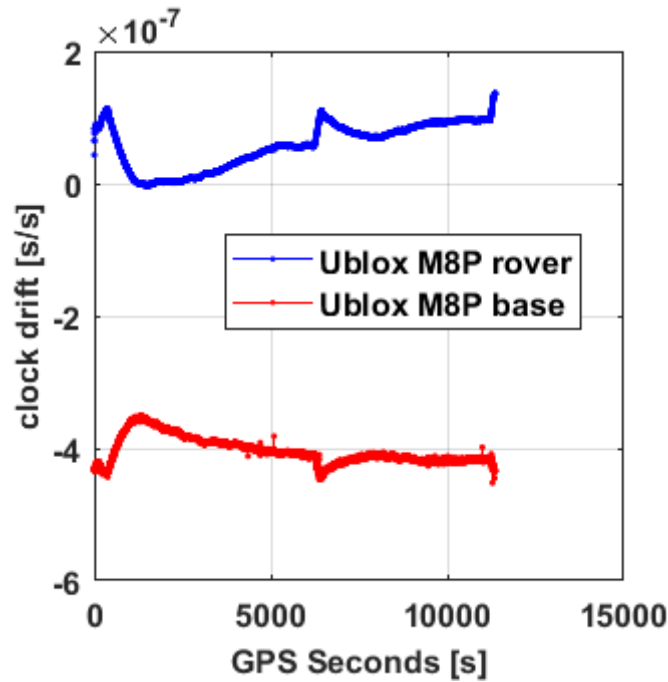


Figure 28 Estimated receiver clock drifts in ublox-M8P

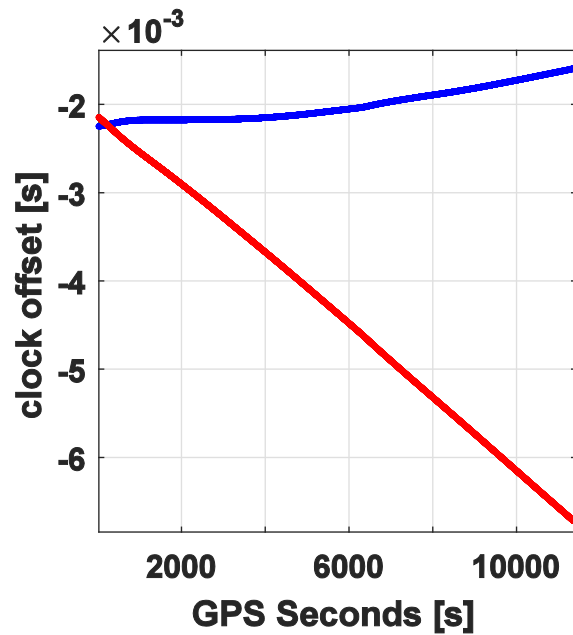


Figure 29 Estimated receiver clock offsets in ublox-m8p

Care must be taken to properly detect and account for the receiver clock offset in low-cost receivers, prior to incorporating measurements into a GNSS data processing, because it is related to at least the following four aspects:

- Computing GNSS signal transmit time

- Time-matching of the measurements between two receivers in a differential GNSS processing
- Tagging user positions
- Correcting the measurements

If the receiver adjusts the measurements using the real-time-derived receiver clock offsets, the consistency of code, phase and time-stamp (measurement epoch) must be maintained as suggested in (Gurtner 2007), especially for those receivers conducting the 1ms clock adjustment. This 1ms clock adjustment is not only seen in u-blox 5T but also u-blox LEA-6T used in X-sense project. One example is given in Figure 30.

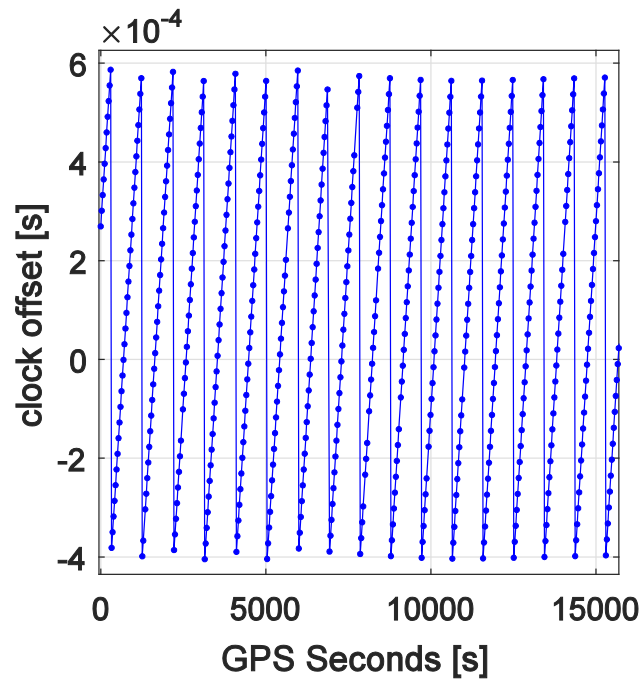


Figure 30 Estimated receiver clock offset  
(Receiver: u-blox LEA-6T; Station RG01 in X-sense project; Date: 13/01/2013)

### The effect of the receiver clock adjustment on positioning

To better explain receiver clock error influence, one writes the observation equations as:

$$L_k^i = \rho_k^i(t^t, t_r) + c \cdot \delta^i - c \cdot \delta_k + \lambda \cdot N_k^i + e \quad (3-1)$$

$$P_k^i = \rho_k^i(t^t, t_r) + c \cdot \delta^i - c \cdot \delta_k + e \quad (3-2)$$

The above equations ignore the GNSS signal errors except for the satellite clock and receiver clock errors to concentrate the discussion on the receiver clock adjustment effect.

$$t^t = t_r - P_k^i/c \quad (3-3)$$

where  $t^t$  is the signal transmitting time and  $t_r$  is the receiving time.

When a clock adjustment occurs, at least the code measurements have to be corrected consistently by the 1 ms jumps applied to the receiving time. Otherwise the wrong signal transmitting time will cause a satellite position errors of up to 4 meters (results from 1ms error in time with respect to a satellite velocity at 4 km/s).

Even worse is that the clock adjustment does not happen at the same time in reference and rover receivers (see Figure 27) when using low-cost single-frequency receivers. This causes big trouble to those RTK processing which saves phase ambiguities at the single-difference level (between receivers), because the clock adjustment appears as cycle-slips (or discontinuities) in the carrier phase ambiguities (see equation (3-4)). In Figure 33 this effect is visualized based on the data collected from u-blox LEA-6T modules used in the X-sense project.

$$L_{kg}^i = \varrho_{kg}^i(t^t, t_r) - c \cdot \delta_{kg} + \lambda \cdot N_{kg}^i + e \quad (3-4)$$

The clock error term  $\delta_{kg}$ , stays in the above SD carrier phase measurements. Whenever a clock adjustment happens at either rover or reference receiver, the huge value shall be handled properly: e.g., identifying and removing from SD carrier phases, considering they are common errors to all satellites.

Consistent carrier-phase ambiguities are important for a reliable and accurate RTK solution whereas discontinuities in the carrier-phase ambiguities, like cycle-slips, lead to an overhead of ambiguity integers re-estimations.

The 1ms receiver clock adjustment induces a change of 1,576,458.22 cycles in the L1 carrier phase:

$$\delta_k \cdot \frac{c}{\lambda} = 1ms \times 3 \times 10^8 m/s \div 0.1903m = 1576458.22 \text{ [cycles]}$$

To better explain this large phase cycle jump caused by the receiver clock adjustment, a Code-Phase linear combination between the code and carrier-phase is formed as:

$$P - L = 2I + \lambda N + \varepsilon_L + \varepsilon_P + e \quad (3-5)$$

where  $I$  is the ionospheric delay,  $N$  is the carrier phase ambiguity. The phase multipath is denoted as  $\varepsilon_L$  and the code multipath as  $\varepsilon_P$ .  $e$  represents the white noise.

This linear combination was mentioned as geometry-free model in (Teunissen 1997). Therefore, this code minus phase linear combination in (3-5) converted into cycles, is named code phase geometry-free (CPGF) linear combination by the author in this thesis and denote by

$$L_{CPGF} = \frac{P - L}{\lambda} \text{ [cycles]} \quad (3-6)$$

As the Ionospheric delay in mid-latitude is in general a low-frequency error, the CPGF linear combination can be used to estimate the high-frequency code multipath when there is no

receiver clock adjustment. The  $L_{CPGF}$  of satellite G27 for the Javad and ublox receivers in the ZB test are plotted in Figure 31. One can clearly see that in this dataset the low-cost u-blox 5T receiver has less code multipath suppression than the high-end Javad receiver.

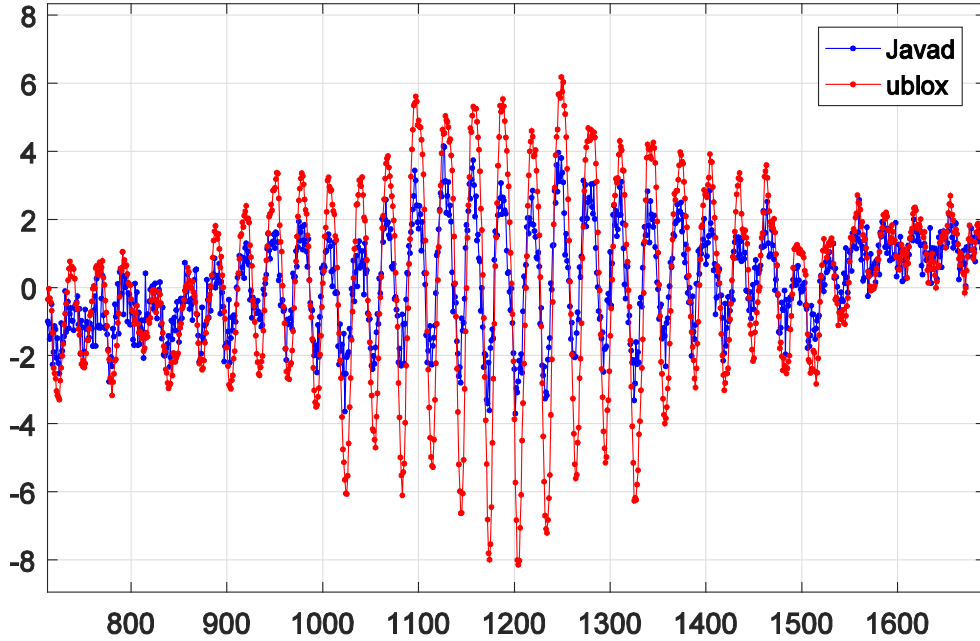


Figure 31 Code multipath of satellite G27 in Javad and u-blox receivers in zero baseline test; Vertical axis is code multipath in meters; Horizontal axis is GPS time in seconds

When forming single differences between two receivers in a short baseline, the ionospheric delay  $I$  is negligible; the phase multipath  $\varepsilon_L$  is at centimeter level but the code multipath  $\varepsilon_P$  is at meter level, thus dominating the error budget apart from the phase ambiguities on the left side of (3-7)

$$L_{CPGF}^{SD} = N + \frac{\varepsilon_L}{\lambda} + \frac{\varepsilon_P}{\lambda} + \frac{e}{\lambda} \quad [cycles] \quad (3-7)$$

where  $SD$  denotes the single difference between receivers.

This  $L_{CPGF}^{SD}$  is the simplest approach to get an initial estimation of the SD carrier-phase ambiguities when the receiver clock adjustments are corrected in the code and carrier phase measurements consistently. The new u-blox M8 modules stop to do receiver clock adjustments (at least not seen within 3 hours) and even if there is an adjustment, it is consistently corrected in the code and carrier phase measurements. One can see this from Figure 32 as an example.

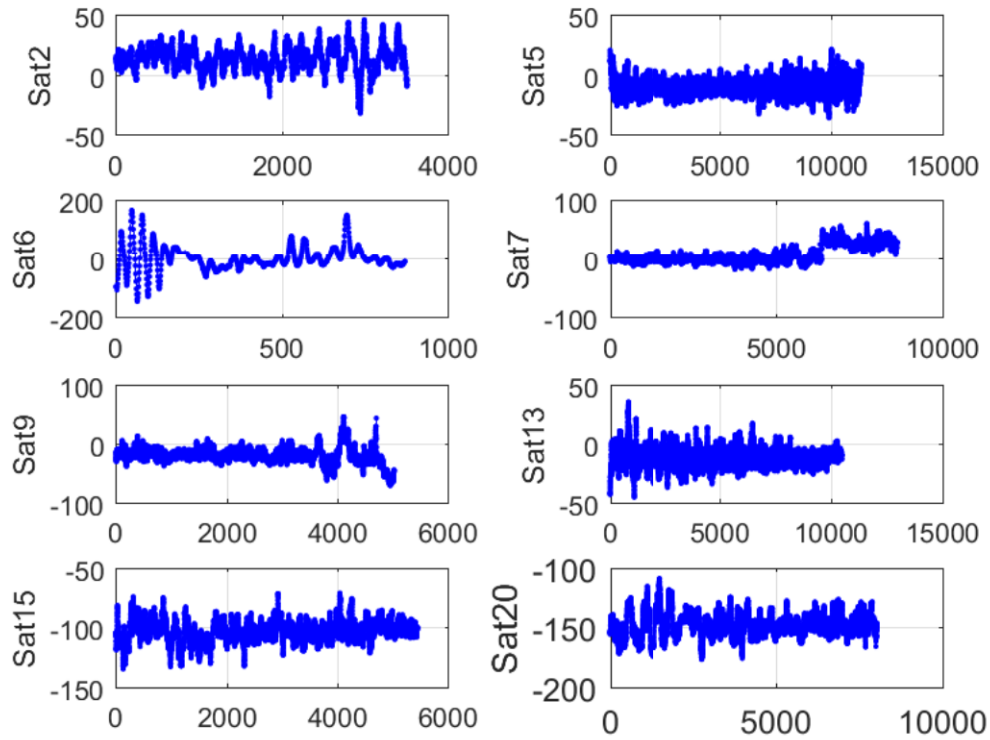


Figure 32 SD CPGF linear combination of 8 satellites formed from two u-blox M8P receivers; baseline length is 1.6 m

However, this was not the case with the older receiver modules, e.g., LEA-6T. The inconsistent adjustments regarding this clock jumps in LEA-6T is visualized by plotting the  $L_{CPGF}^{SD}$  in Figure 33 (only the first 4 satellites are plotted. For the plots of all the 32 satellites, please go to Appendix D).

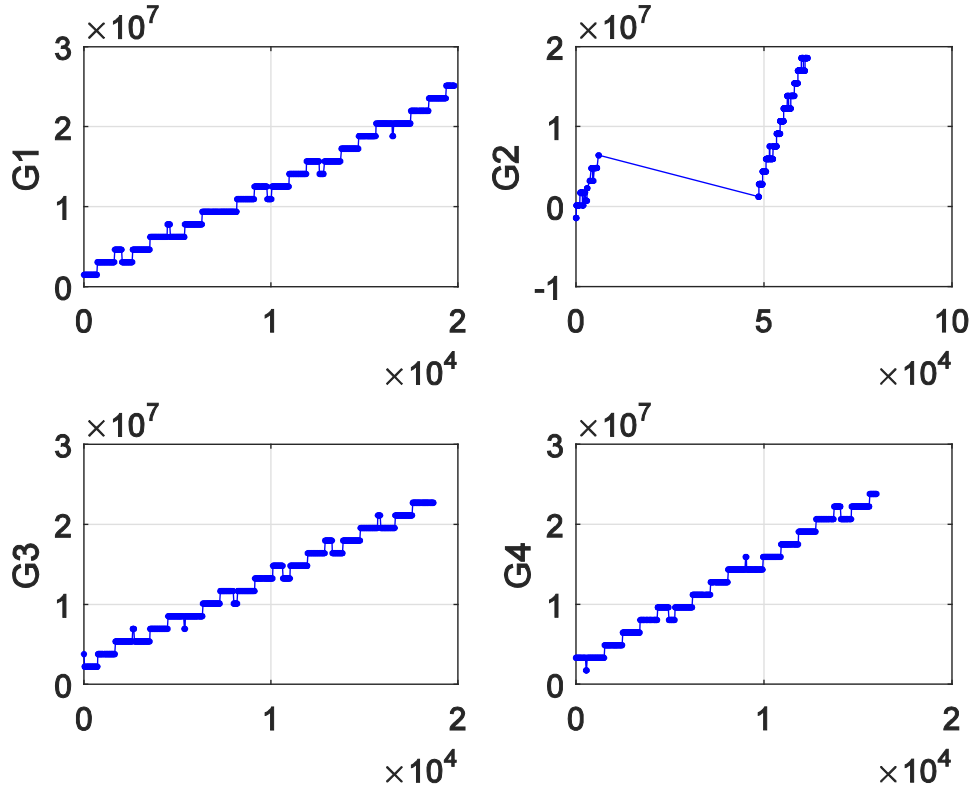


Figure 33 SD CPGF linear combination; Horizontal axis is GPS time in second (Receiver: u-blox LEA-6T; Station RG01 in X-sense project; Date: 13/01/2013)

Those cycle slips in the CPGF combination in Figure 33 equal to exactly the 1 ms clock jumps when converting the cycle changes to light traveling time.

To make a conclusion that those phase cycle slips (common to all satellites) in the above data from the u-blox 5T and 6T receiver modules are caused exactly by the receiver clock adjustments, one has to also check whether they happen at the same time. To do so, we compare the difference of  $L_{CPGF}^{SD}$  in time as in (3-8) to the estimated receiver clock offsets in time domain. The time series of the two values are plotted in Figure 34.

$$dL_{CPGF}^{SD}(t_{i+1}) = L_{CPGF}^{SD}(t_{i+1}) - L_{CPGF}^{SD}(t_i) \quad (3-8)$$

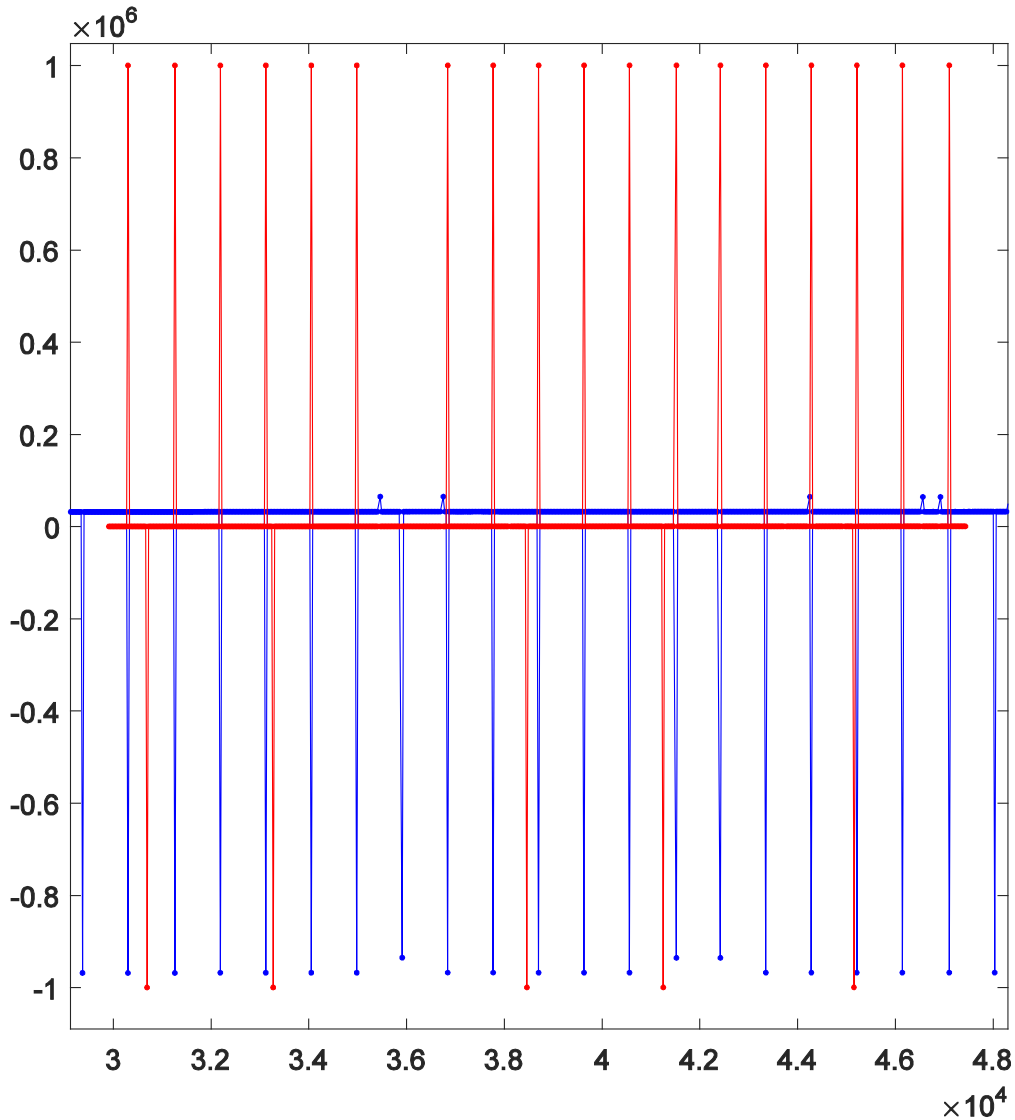


Figure 34 Vertical axis is time in ns; Horizontal axis is GPS time second; Blue is the estimated receiver clock offsets and Red is the  $dL_{CPGF}^{SD}$  of satellite G32 converted to light travel time

It is found that the positive  $dL_{CPGF}^{SD}$  jumps in satellite G32 happen exactly at the same time when the rover receiver's 1ms receiver clock offset adjustments occur; and the 5 negative  $dL_{CPGF}^{SD}$  jumps are caused exactly by the receiver clock offset adjustments of the reference receiver. These finds justify the conclusion we wanted to make before.

### 3.3 Carrier-to-noise density ratio measurements

To see the differences in the  $C/N_0$  values measured by a low-cost single frequency receiver compared to a high-end Javad receiver, the  $C/N_0$  values of GPS satellite G11 (which has the

longest arc in this specific dataset) are plotted together with its satellite elevation angle in Figure 35.

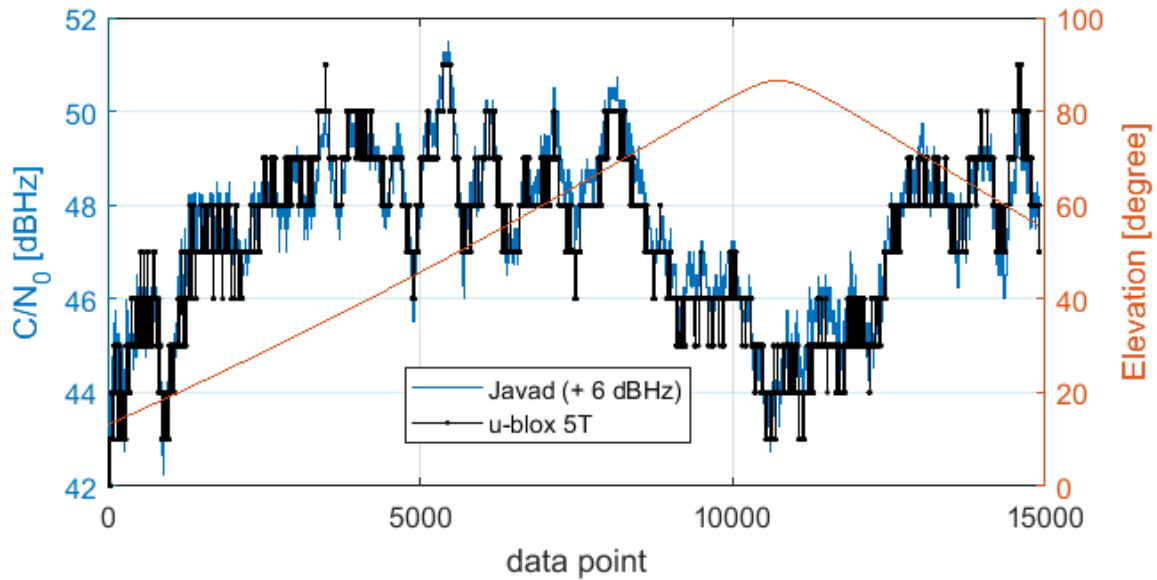


Figure 35 The  $C/N_0$  time series of satellite G11 measured by a Javad (shifted by 6 dBHz) and a u-blox 5T receiver in a zero baseline test;

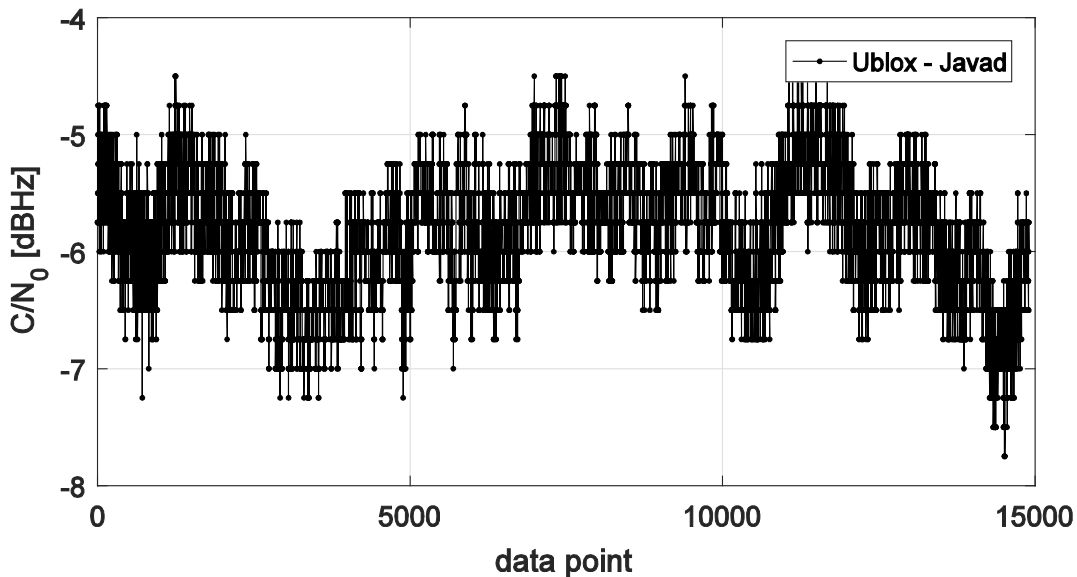


Figure 36 The  $C/N_0$  difference of satellite G11 between a Javad and a u-blox 5T receiver

The first difference is that the low-cost u-blox 5T receiver outputs only integer  $C/N_0$  values<sup>10</sup> while the Javad receiver outputs  $C/N_0$  values with a resolution of 0.25 dBHz. The second

<sup>10</sup> It is possible to get the same level of  $C/N_0$  resolution by accessing to the TRK\_MEAS message however throughout of this thesis, only the RXM-RAW or RXM-RAWX message are used.



difference is a 6 dBHz offset between the two C/N<sub>0</sub> time series, which is computed from the mean of the differences between the two time series (see Figure 36). After adding 6 dBHz to the C/N<sub>0</sub> of the Javad, a good agreement between the two receivers is visible in Figure 35 and made evident by their cross correlation in Figure 37. The correlations of other satellites have their pick at 0 second, too.

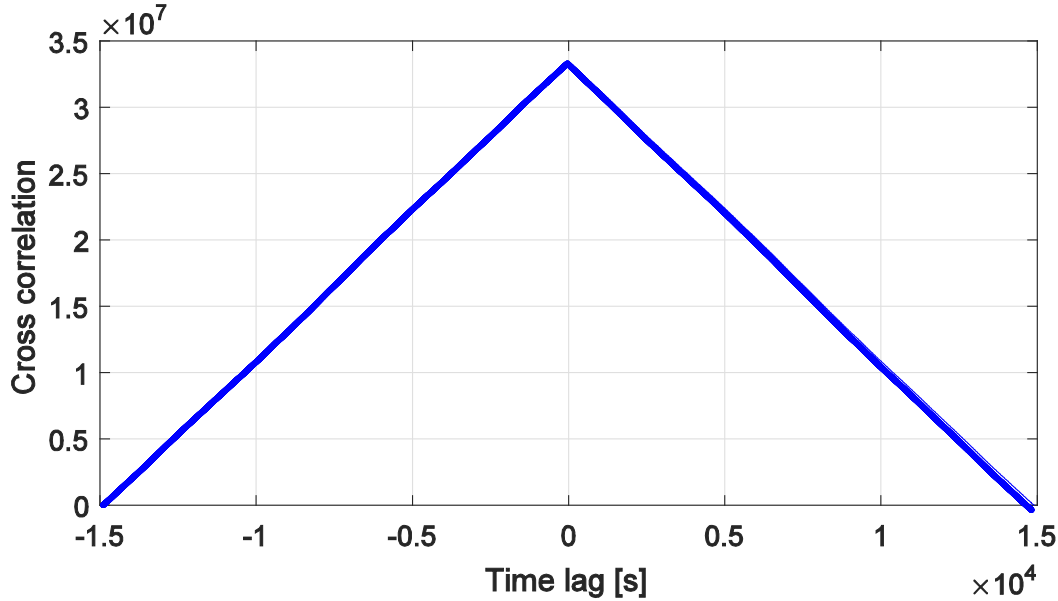


Figure 37 Cross correlation of the two C/N<sub>0</sub> time series measured by a Javad and a u-blox 5T receiver in a zero baseline test

### 3.4 Receiver measurements precision

A zero baseline test is traditionally used to assess the measurement noise characteristics of a GNSS receiver, because all common errors in the measurements cancel out in the double-difference processing (Gopi 2005). The remaining errors are attributable to random noise and receiver biases. In case of using the same type of receiver, the receiver biases, including P1-C1 code differential bias for single frequency receivers, are expected to be eliminated in the DD measurements so that the standard deviation of the code and phase residuals will present the precision of the receiver's code and phase measurements (Bossler, et al. 2002).

The GNSS data collected during the above ZB test is processed by the RTK software in a kinematic model with a 10° satellite elevation mask, with 100% of carrier phase ambiguities fixed. The DD code residual (post-fit residuals after the carrier phase ambiguities have been fixed to integers)

$e_{P_{kg}^{ij}}$  and phase residuals  $e_{L_{kg}^{ij}}$  at one epoch read:

$$e_{L_{kg}^{ij}} = L_{kg}^{ij} - \rho_{kg}^{ij} - \lambda \cdot N_{kg}^{ij} \quad (3-9)$$

$$e_{P_{kg}^{ij}} = P_{kg}^{ij} - \rho_{kg}^{ij} \quad (3-10)$$

One can obtain an empirical stochastic model of code and phase measurements by analyzing their DD residuals.

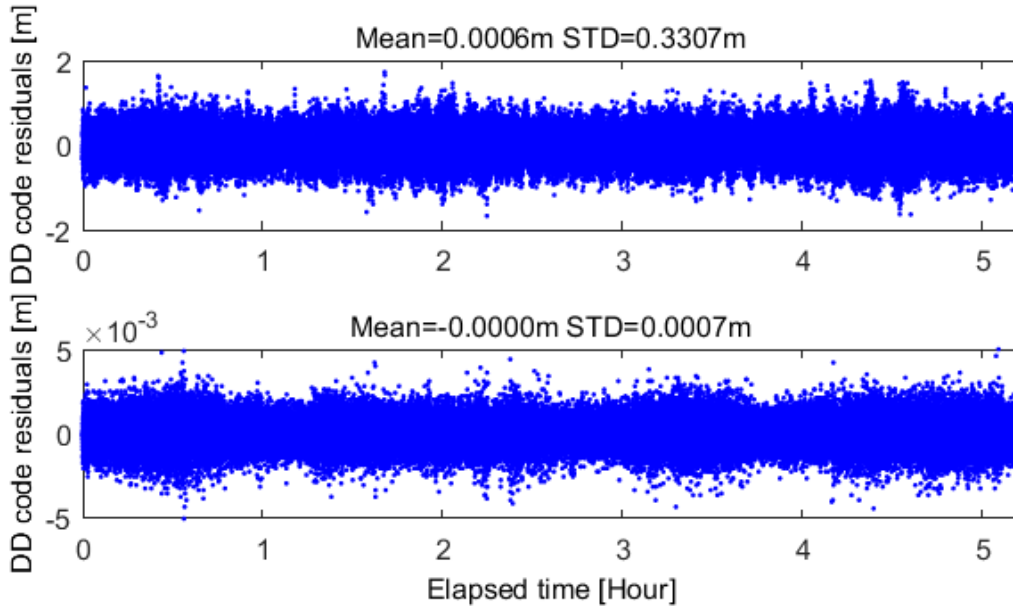


Figure 38 Time series of the DD code and phase residuals (zero baseline of two u-blox 5T receivers)

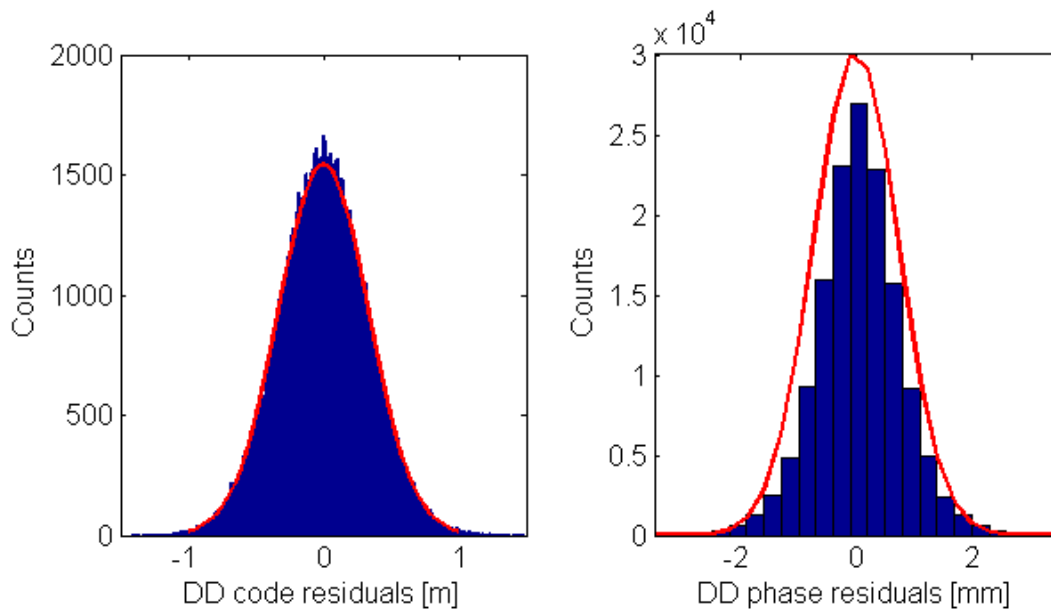


Figure 39 The histogram and normal distribution fit (red line) of the DD code and phase residuals (zero baseline of two u-blox 5T receivers)

After processing, the DD code and phase residuals have a standard deviation of 0.3307m and 0.0007m, respectively. These values are inconsistent with the multipath-corrected DD residuals presented in (Odolinski and Teunissen 2017). The time series of the DD residuals are visualized in Figure 38 and the histogram plots with the normal distribution fit are given in Figure 39. As one can see clearly from the two figures, the DD residuals data are symmetric, centered at 0 and fit well to the normal distribution. This verified the claim that only random noise is remaining in the DD processing of data from a ZB setup of two equal type receivers, however the estimated standard deviation of carrier phases looks too good to be true for such a low-cost receiver. This will be explained later and let's look at other basic statistics of the DD residuals, like the time correlation, at the beginning of this chapter.

To examine the time correlation in the DD residuals, their autocorrelation functions were calculated and are given in Figure 40 for the DD measurements between satellite G10 and reference satellite (the one having the highest elevation). The autocorrelation of the DD residuals of the carrier phase is 1 at time lag 0 by definition and is close to zero at other time lags, indicating that the DD residuals contains only white noises. However, time correlations are seen in the DD code residuals, which might be due to the temporal correlation in the code tracking loop implemented in the u-blox LEA 5T as well as in the NEO M8P receiver modules (for the analysis of NEO M8P please refer to Appendix F).

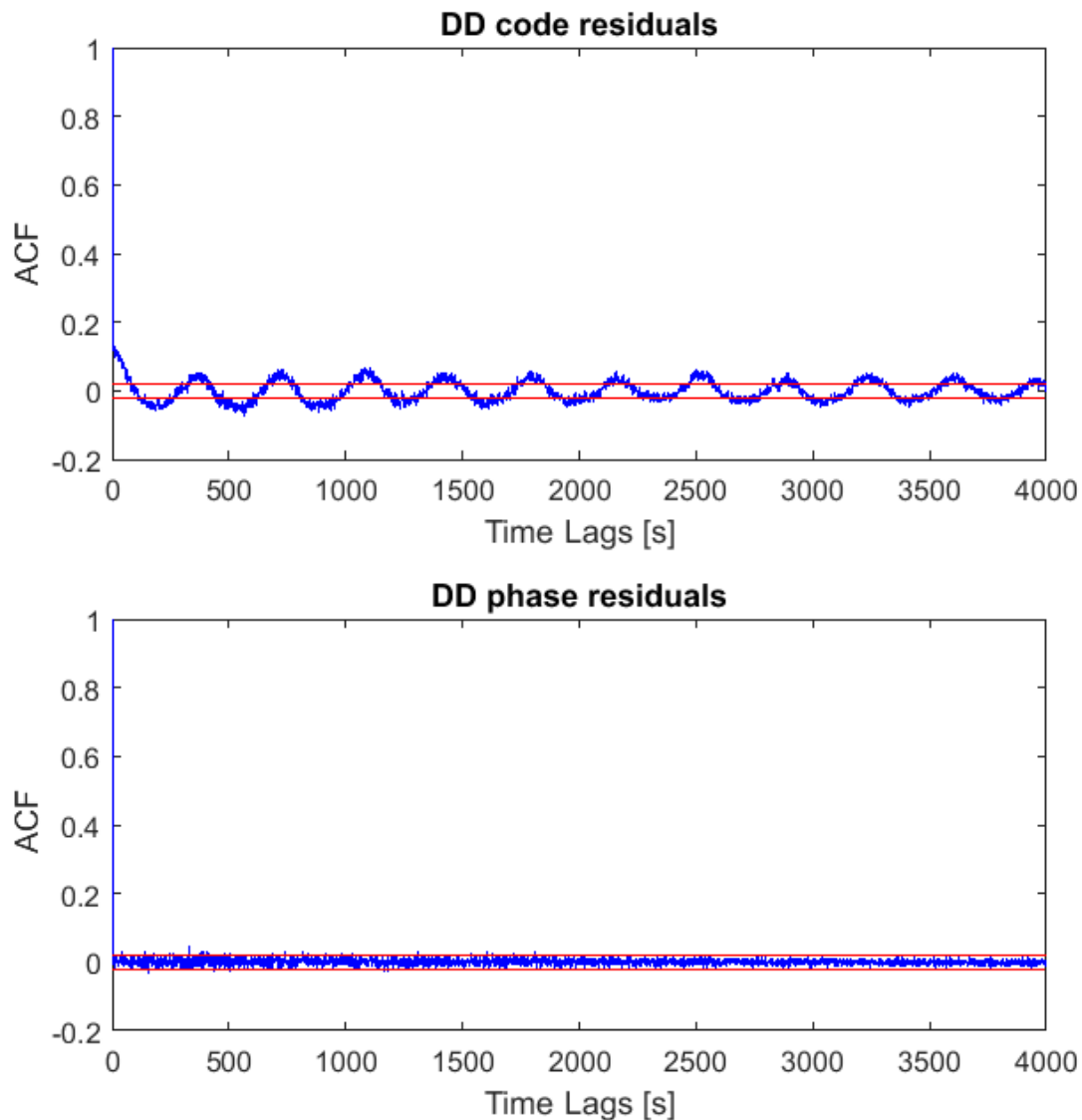


Figure 40 The sampled autocorrelation of the ZB DD code (top) and phase residuals (bottom); Red lines are the upper and lower bound with 95% confidence

### Least square variance component estimation

To obtain the precision of the code and phase measurements, a Least-Square Variance Estimation (LSVCE) is adapted and implemented on an epoch-by-epoch basis in the Kalman filter and then the mean of all the estimated epoch-wise variances is taken as the empirically estimated variance for the code and phase measurements.

The LSVCE was first proposed by (Helmert 1907) and recent development of LSVCE and its application in GNSS includes (Teunissen 1988) (Amiri-Simkooei 2007) and (Teunissen and Amiri-Simkooei 2008). Its implementation in a Kalman filter was done by (Wang 1997). (Wang, Gopaul

and Guo 2010) were using it for posteriori co-variance estimation in an adaptive Kalman filter and (Qian, Wang and Hu 2016) further developed it for a Kalman filter in a multi-sensor integrated navigation.

A rigorous form of the LSVCE given in (Teunissen 1988) and (Teunissen and Amiri-Simkooei 2008) is based on the linear model of the observation equations as:

$$E\{y\} = Ax, E\{(y - Ax)(y - Ax)^T\} = Q_{yy} \quad (3-11)$$

where  $y$  is the  $m \times 1$  dimension observation vector,  $A$  is the  $m \times n$  dimension full rank design matrix of the unknown parameter vector  $x$  with dimension  $1 \times n$ , and  $Q_{yy}$  is the co-variance matrix of the observations. In case the stochastic model of the observations is not available, one has two groups of unknowns: the parameter vector  $x$  and the co-variance matrix of the observations  $Q_{yy}$ . To estimate  $Q_{yy}$ , one has to eliminate the unknown parameter  $x$  by multiplying the matrix  $B^T$  to (3-11), with

$$B^T A = 0 \quad (3-12)$$

So that

$$E\{B^T y\} = 0, E\{B^T y y^T B\} = B^T Q_{yy} B \quad (3-13)$$

From the second equation of (3-13), a new linear equation with  $B^T y y^T B$  as observation vector and  $Q_{yy}$  as unknown is established. However, the construction of a non-zero matrix  $B$  is not trivial.

One example is that when  $A$  is an idempotent matrix, namely  $A \cdot A = A$ , one can construct the  $B^T$  matrix as  $B^T = I - A$ . The orthogonal projector  $P_A = A(A^T Q_y^{-1} A)^{-1} A^T Q_y^{-1}$  (Teunissen 2003) in the least square adjustment is such an idempotent matrix. One can find a matrix  $P_A^\perp = I - A(A^T Q_y^{-1} A)^{-1} A^T Q_y^{-1}$  which satisfies  $P_A P_A^\perp = 0$ . In general, the non-zero matrix  $B^T$  is in the null space of the matrix  $A$ .

To estimate the precision of GNSS measurements based on a ZB or a short baseline (SB) in this thesis, the observation residual vector  $v = y - Ax$ , containing the DD code and phase residuals, is directly available from the RTK processing of the zero or short baselines. The mean of the residuals equal to or is close to zero as one can see in previous analysis, thus the second equation in (3-11) is updated:

$$E\{v v^T\} = \begin{bmatrix} Q_{LDD} & Q_{LPDD} \\ Q_{LPDD} & Q_{PDD} \end{bmatrix} \quad (3-14)$$

where  $v$  has the dimension of  $m \times 1$  and  $v v^T$  has the dimension of  $m \times m$ .  $Q_{LDD}$  is the co-variance matrix of the DD carrier phase given in (2-18). The observation weighting function uses elevation based function:  $0.5 + 0.5/\sin^2(\text{el})$ .  $Q_{PDD}$  is the co-variance matrix of the DD code

measurements and  $Q_{LPDD}$  represents the correlation between the DD code and phase measurements. Equation (3-14) can be further developed:

$$vv^T = \begin{bmatrix} \sigma_L^2 \cdot P_{LDD}^{-1} & \sigma_{LP} \cdot K \\ \sigma_{LP} \cdot K & \sigma_P^2 \cdot P_{PDD}^{-1} \end{bmatrix} \quad (3-15)$$

and further decomposed

$$vv^T = \sigma_L^2 \begin{bmatrix} P_{LDD}^{-1} & 0 \\ 0 & 0 \end{bmatrix} + \sigma_P^2 \begin{bmatrix} 0 & 0 \\ 0 & P_{PDD}^{-1} \end{bmatrix} + \sigma_{LP} \begin{bmatrix} 0 & K \\ K & 0 \end{bmatrix} \quad (3-16)$$

where  $\sigma_L^2$  is the variance of non-differenced carrier phase,  $\sigma_P^2$  stands for the variance of non-differenced code and  $\sigma_{LP}$  represents the covariance between non-differenced code and carrier phase of the same satellite measured by the same receiver; matrix  $K$  has a 4 in diagonal and a 2 on non-diagonal positions as

$$K = \begin{bmatrix} 4 & \dots & 2 \\ \vdots & \ddots & \vdots \\ 2 & \dots & 4 \end{bmatrix}$$

By applying the  $vh$  operator to both sides of the equation, one gets a

$$vh(vv^T) = [vh \left( \begin{bmatrix} P_{LDD}^{-1} & 0 \\ 0 & 0 \end{bmatrix} \right), vh \left( \begin{bmatrix} 0 & 0 \\ 0 & P_{PDD}^{-1} \end{bmatrix} \right), vh \left( \begin{bmatrix} 0 & K \\ K & 0 \end{bmatrix} \right)] \cdot \begin{bmatrix} \sigma_L^2 \\ \sigma_P^2 \\ \sigma_{LP} \end{bmatrix} \quad (3-17)$$

where the  $vh$  operator stacks column-wisely the elements on and below the diagonal into one vector. Assuming the matrix  $Q$  is a symmetric square matrix with dimension  $m \times m$ , and  $q_{ij}$  is the element on the row  $i$  and column  $j$  with  $i > j$ :

$$vh(Q) = [ (q_{11}, \dots, q_{i1}, \dots, q_{m1}), \dots, (q_{jj}, \dots, q_{ij}, \dots, q_{mj}), \dots, q_{mm} ]^T$$

where, after the  $vh$  operation, one gets a vector with  $\frac{1}{2}m(m+1)$  rows.

Up to this step one has a new observation equation in (3-17), with  $vh(vv^T)$  as observation vector and the variances and covariance as parameters to be estimated. The least squares estimation of the parameters is done at every observation epoch and the mean of the estimated values over all epochs is taken as the final value.

Rewriting (3-17) into:

$$L_v = M \cdot X_\sigma$$

where,  $L_v$  has  $\frac{1}{2}m(m+1)$  rows and 1 column,  $M$  has  $\frac{1}{2}m(m+1)$  rows and 3 columns and  $X_\sigma$  is a 3 by 1 vector.

The least squares estimation of  $X_\sigma$  at epoch  $i$  is:

$$\hat{X}_\sigma(i) = (M^T M)^{-1} M^T L_v$$

$$\hat{X}_\sigma = \frac{\sum_i^n \hat{X}_\sigma(i)}{n} \quad (3-18)$$

A mean of the  $\hat{X}_\sigma(i)$  over all the epochs  $\hat{X}_\sigma$  is taken as the final value to represent the precision of the code and the phase as well as their correlation. The advantage of the above-proposed approach is that one can estimate the variance of code, the variance of phase, their correlation and even more parameters separately through properly constructing the equation.

To have a comparison, the posteriori variance of unit weight formula:

$$\hat{\sigma}_0^2 = \frac{v^T P v}{r} \quad (3-19)$$

is modified as

$$\hat{\sigma}_{LDD}^2 = \frac{v_{LDD}^T P_{LDD} v_{LDD}}{r_{LDD}} \text{ and } \hat{\sigma}_{PDD}^2 = \frac{v_{PDD}^T P_{PDD} v_{PDD}}{r_{PDD}} \quad (3-20)$$

where  $\hat{\sigma}_{LDD}^2$  and  $\hat{\sigma}_{PDD}^2$  represent the posteriori variance of unit weight for DD code and carrier phase respectively;  $r$  stands for the degree of freedom. These modified formulas are also known as the Förstner method (Yavuz, Baykal and Ersoy 2011).

In principle for GNSS data processing, one cannot separately calculate the  $\hat{\sigma}_{LDD}^2$  and  $\hat{\sigma}_{PDD}^2$  because the residuals of code and phase measurements are derived from a processing jointly influenced by code and phase measurements. Additionally, the degree of freedom is hard to define separately for the code and the carrier phase measurements. With the assumption of having fixed geometry and fixed carrier phase ambiguities in the zero baseline or short baseline, the author defined

$$r_{LDD} = r_{PDD} = \text{number of satellites}$$

Formula (3-20) is used to calculate the  $\hat{\sigma}_{LDD}^2$  and  $\hat{\sigma}_{PDD}^2$  over all epochs and the mean values are taken as the final variances of the code and phase measurements. They are compared to the value estimated by above LSVCE in (3-18).

## Results and analysis

We summarize the results using the above approach of estimated variances for three datasets in Table 5. The ZB data of two LEA-5T receiver modules is the same dataset used in previous analyses. The ZB data of two M8P receiver modules is collected from 3 hours of observations

with a 1s data sampling rate. The SB data of two M8P is collected from a 6m short baseline and 10 minutes of observations with a 1s data sampling rate.

The estimated phase standard deviation for the ZB of LEA-5T is close to that of the Trimble 4000SSI estimated on a zero baseline in (Amiri-Simkooei and Tiberius 2007). Both code and phase standard deviations for the ZB are close to the values estimated for Septentrio AsteRx1 single-frequency receivers in a zero baseline in (de Bakker, van de Marel and Tiberius 2009). The phase precision estimated for NEO-M8P from the SB equals to that of the EVK-M8T (with patch antenna) estimated in a SB in (Odolinski and Teunissen 2017) and the code standard deviation is slightly larger than the value in that paper.

The results show that there is no correlation between code and phase measurements in the zero baselines as one would expect. However, a correlation is seen in the results from the short baseline. It indicates that there are still external errors, like the multipath, remaining in the DD measurements and a proper model of these errors is still missing in the functional model.

One can obtain the scale factor between the code and phase noise through the above estimated values and apply it to the RTK process. In this thesis, 300 is used as the scale factor and 2mm is used as the precision of carrier phase measurements for all u-blox receivers, based on the estimated variances from the short baseline in Table 5.

Table 5 Variances of non-differenced code and phase measurements and their correlation

Baseline	Receivers	LSVCE			Posterior variance of unit weight	
		$\sigma_L$	$\sigma_P$	$\sigma_{LP}$	$\sigma_L$	$\sigma_P$
ZB	LEA-5T	0.21mm	109.4mm	0	0.23mm	112.2mm
ZB	NEO-M8P	0.14mm	82.3mm	0	0.163mm	69.3mm
SB	NEO-M8P	2mm	695.9mm	0.002	2mm	647.6mm



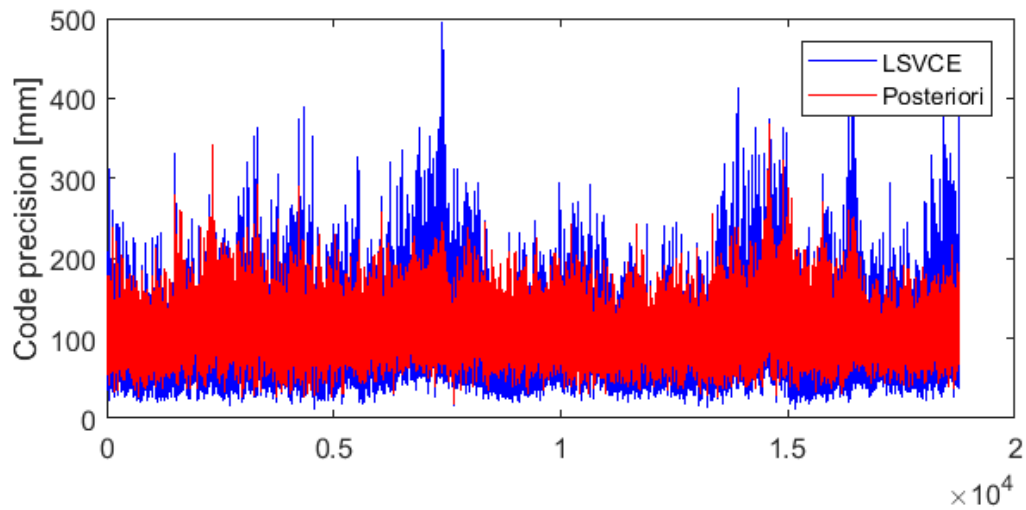
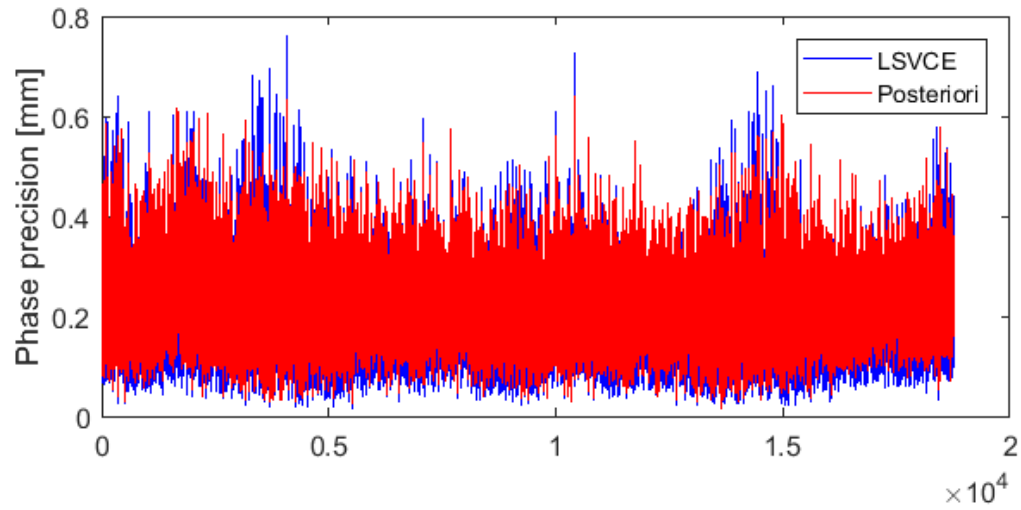


Figure 41 Phase and code precision (standard deviation) estimated by LSVCE and Posteriori variance of unit weight at every observational epoch (zero baseline with 2 LEA-5T); Horizontal axis is time in seconds

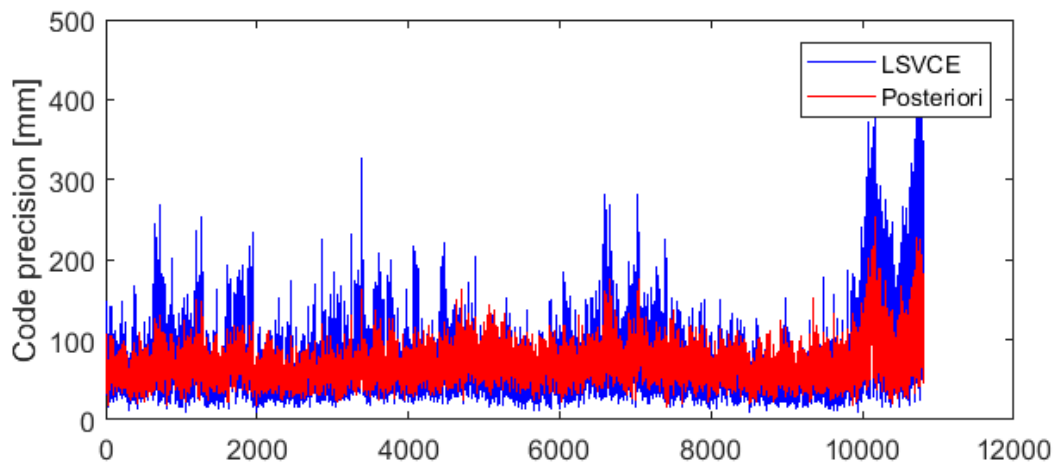
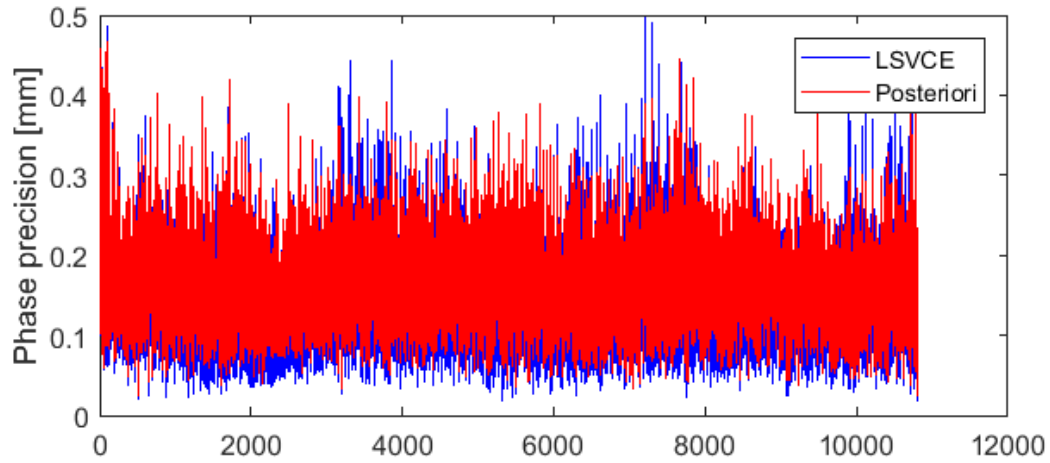


Figure 42 Phase and code precision (standard deviation) estimated by LSVCE and Posteriori variance of unit weight at every observational epoch (zero baseline with 2 NEO-m8p); Horizontal axis is time in seconds

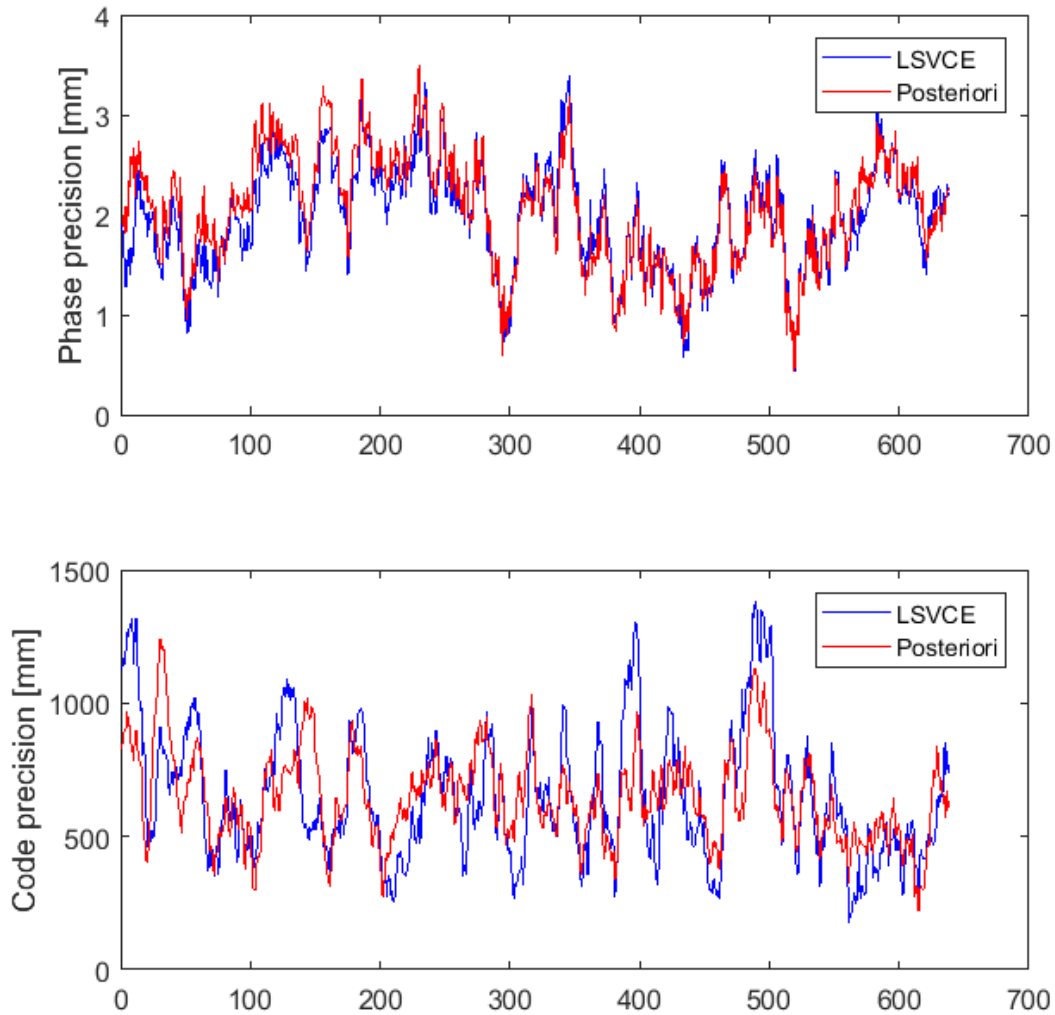


Figure 43 Phase and code precision (standard deviation) estimated by LSVCE and Posteriori variance of unit weight at every observational epoch (short baseline with 2 NEO-m8p); Horizontal axis is time in seconds

The estimated values from zero baselines are in general too optimistic as one can see from the results. Because the two receivers are connected to the same antenna and the signals measured by two receivers are effected by the same LNA and correlations exist as one can see as proof from the following paragraphs.

The variance of the DD residuals of the carrier phase will read:

$$\text{Var}(L_{kg}^{ij}) = \text{Var}(L_k^{ij} - L_g^{ij}) = \text{Var}(L_k^{ij}) + \text{Var}(L_g^{ij}) - 2\text{Cov}(L_k^{ij}, L_g^{ij}) \quad (3-21)$$

where  $L_{kg}^{ij}$  is the DD carrier phase,  $L_k^{ij}$  is the SD carrier phase between satellite  $i$  and satellite  $j$  measured by receiver  $k$ ,  $\text{Var}(\cdot)$  stands for variance and  $\text{Cov}(\cdot)$  stands for covariance. According to (de Bakker, van de Marel and Tiberius 2009) and (Gourevitch 1996), two receivers in a ZB setup are correlated as a result of being connected to the same antenna and LNA. Thus  $L_k^{ij}$  and  $L_g^{ij}$  are correlated and the correlation coefficient is connected to the covariance as:

$$\text{Corr}(L_k^{ij}, L_g^{ij}) = \frac{\text{Cov}(L_k^{ij}, L_g^{ij})}{\sigma_{L_k^{ij}} \cdot \sigma_{L_g^{ij}}} \quad (3-22)$$

where  $\sigma$  stands for the standard deviation and  $\text{Corr}(\cdot)$  is the notation of the correlation operation. Put the formula (3-22) into (3-21), one gets

$$\text{Var}(L_{kg}^{ij}) = \text{Var}(L_k^{ij}) + \text{Var}(L_g^{ij}) - 2 \cdot \sigma_{L_k^{ij}} \cdot \sigma_{L_g^{ij}} \cdot \text{Corr}(L_k^{ij}, L_g^{ij}) \quad (3-23)$$

Converting the variance of the SD measurements to zero difference ones and considering that there is no correlation between the satellites, we have

$$\begin{aligned} \text{Var}(L_k^{ij}) &= \text{Var}(L_g^{ij}) \text{Var}(L_k^i) + \text{Var}(L_k^j) = 2\sigma_L^2 \\ \sigma_{L_k^{ij}} \cdot \sigma_{L_g^{ij}} &= 2\sigma_L^2 \end{aligned} \quad (3-24)$$

where  $\sigma_L$  stands for the standard deviation of the zero difference carrier phases.

Substituting (3-24) into (3-23), one has the variance for both DD code and phase measurements as

$$\begin{aligned} \text{Var}(L_{kg}^{ij}) &= 4\sigma_L^2 - 4\sigma_L^2 \cdot \text{Corr}(L_k^{ij}, L_g^{ij}) = 4\sigma_L^2 [1 - \rho_{LNA}^{SD}] \\ \text{Var}(P_{kg}^{ij}) &= 4\sigma_P^2 [1 - \rho_{LNA}^{SD}] \end{aligned} \quad (3-25)$$

where  $\sigma_P$  stands for the standard deviation of zero difference code measurements,  $\rho_{LNA}^{SD}$  stands for the correlation of the SD measurements (between satellites) between two receivers due to common LNA. Note that in the co-variance matrix of DD measurements, the correlation goes into the non-diagonal element as well, namely in (2-18), instead of  $(\sigma_k^1)^2 + (\sigma_g^1)^2$  one has  $[1 - \rho_{LNA}^{SD}] \cdot [(\sigma_k^1)^2 + (\sigma_g^1)^2]$ .

It has been shown that the results from zero baselines are too optimistic whereas the results from short baselines may be contaminated by multipath. However, they can serve as the lower and upper boundaries for the realistic noise level of the measurements. The data from the SB setup listed in Table 5 and plotted in Figure 43 are collected with careful site selection to avoid multipath, thus the estimated standard deviations of zero difference code and phase measurements are used to represent the empirical measurements precision of u-blox M8T and M8P modules in this thesis.

# Chapter 4 Empirical antenna C/N<sub>0</sub> pattern modelling using geostationary satellites

## 4.1 The motivation of using geostationary satellites

Formula (2-40) in Chapter 2.4 outlines the different factors contributing to the C/N<sub>0</sub> measured by a GNSS receiver. For clarification, the non-constant parameters are again listed in Table 6 together with the closed-form formula and their typical values.

Table 6 Non-constant parameters affecting measured C/N<sub>0</sub>

Parameters [unit]	description	Typical values at $el$		
		5°	40°	90°
$G_T$ [dB]	$\frac{2}{1 - \sqrt{1 - (\frac{R_E \cos el}{R_{SV}})^2}}$	12.1	12.9	10.2
Path loss [dB/m <sup>2</sup> ]	$\frac{1}{4\pi(-R_E \sin el + \sqrt{R_E^2(\sin^2 el - 1) + R_{SV}^2})^2}$	-159.0	157.8	157.1
Multipath [dB]	Site specific	< 6		
$G_R$ for L1 [dBic*]	$G_T = f(el)$	-1	4	5

\* dBic the ratio of the energy amplification compared to an isotropic circularly polarized antenna.

The transmitting antenna gain pattern  $G_T$ , the path loss effects and the receiving antenna gain pattern  $G_R$ , on a specific satellite signal, all vary depending on the satellite elevation angle seen by the GNSS receiver. The typical value of 5 dBic for  $G_R$  at the elevation angle 90° refers to a peak gain of about 3dBic plus 2dB gain increased by using a ground plane suggested in (Panther 2012). The values at 5° and 40° are extrapolated based on the empirical C/N<sub>0</sub> pattern estimated in this chapter.

One may notice that using the closed-form formula (2-43) to calculate the gain of the transmitting antenna  $G_T$  will deliver higher values than the actual/typical values listed in Table 6, e.g.,  $G_T(el = 5^\circ) = 18.3 \text{ dB}$ . The reasons are given in Chapter 10 of (Misra and Enge 2011):

- There is additional loss in the transmit antenna suppressing the radiated power.
- The gain is tailored to compensate for the larger distance to the users at the edge of the earth.

Therefore, in practice one cannot use formula (2-43) but instead apply a linear interpolation with the typical values listed in Table 6, to account maximum for 2 dB  $C/N_0$  variations caused by  $G_T$ .

The two factors having the largest contributions to  $C/N_0$  values are the multipath (up to 6 dB) and the antenna gain pattern of the receiver antenna (up to 6 dBic for L1). Separating the receiver antenna gain pattern from the multipath will be very beneficial for applications which utilize the  $C/N_0$  variations to mitigate multipath for better positioning accuracy like (Comp and Axelrad 1998), or to detect snow depth like (Larson and Small 2016). In the spectral analysis of  $C/N_0$  time series it is also essential to remove the trend mainly determined by the receiver antenna's gain pattern, as done by (Bilich, Larson and Axelrad 2008) and (Rost and Wanninger 2009).

(Liu, et al. 2008) have attempted to analyze and model the  $C/N_0$  pattern of the receiver antenna using observed  $C/N_0$  from GPS Medium Earth Orbit (MEO) satellites. They showed that the time variation due to atmosphere is smaller than 1dB and pointed out that an in-depth study of the  $C/N_0$  influence by signal transmitting power and transmitting antenna gain pattern for various satellites should be undertaken. Moreover, a clear multipath effect is seen in the results which the authors have categorized it as  $C/N_0$  anomaly. Therefore, it is extremely difficult to tell the real cause of a  $C/N_0$  change measured from a MEO satellites because all the contributing factors are mixed up and hard to be separated.

A GEOstationary (GEO) satellite is a satellite at a circular orbit with an altitude of 35,786 km above the Earth's equator. It appears almost stationary for a user on earth as its orbital period is equal to the Earth's rotational period, even though a small north-south movement occurs due to dragging force of principal moment of inertia. (Steigenberger, et al. 2013) show the ground tracks of the GEO satellites from the BeiDou system, for which maneuvers in east-west are performed every 25 to 35 days and in north-south every 2 years. These small movements will lead to a maximum longitude variation of  $0.15^\circ$  and latitude of  $1.8^\circ$  (from the C05 satellite). Nevertheless, such small movements have almost no influence on the  $C/N_0$  measured by a receiver on the Earth for observational durations of one day.

The stationarity of a GEO satellite to a receiver on the Earth means constant satellite antenna gain and constant path loss. And multipath is a low frequency error, which can be avoided by good experiment design or rejected by a high-pass filter. Thus three of the four non-constant factors in Table 6 have been turned to constant, making it feasible to model the  $C/N_0$  pattern of the receiver antenna using the measured  $C/N_0$  values from GEO satellites.

Figure 44 demonstrates the complexity of the  $C/N_0$  time series from a GPS MEO satellite and the simplicity of that from the BeiDou GEO satellite C05.

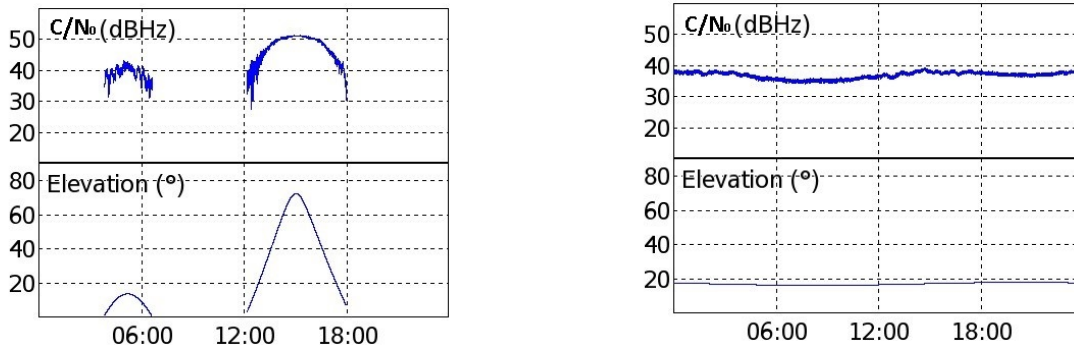


Figure 44  $C/N_0$  time series of a GPS MEO satellite (left) and a BDS GEO satellite C05 (right)

## 4.2 Methodology

As described before, when measuring the  $C/N_0$  values of a GEO satellite, the effect from the gain pattern of the receiver antenna can be separated from others. By tilting the receiver antenna, a profile of  $C/N_0$  values at different satellite elevation angles (seen from the receiver) is established. A rotating platform using the digital incremental encoders to measure and control the rotation actuated by the DC motor (details about the controller refer to (Ingenieurbüro M. Gysling Steuerung und Regeltechnik 1998)).



Figure 45 The rotating platform (with a Leica AR10 antenna connected to a Leica GR10 receiver)

An Xsens MTi IMU (Inertial Measurement Unit) is added to the rotating platform as an additional sensor to measure the attitude of the rotating bar. A control software in LabView is used to achieve automated actuation of the motor based on a predefined plan in which the angles to rotate at specific times are scheduled.

The Xsens is installed on the rotating bar where the GNSS antenna is mounted (see Figure 45) and the alignment of the Xsens is described graphically by Figure 46. The yaw and roll angles output by Xsens correspond to the azimuth and elevation angle of the rotating bar, respectively. An orientation performance of the Xsens MTi is given in Table 7. The roll angles of the antenna position measured by Xsens are, at a static condition, accurate to 0.5°, which is sufficient for the purpose of recording the pointing direction of the antenna boresight with respect to the fixed geostationary satellite.

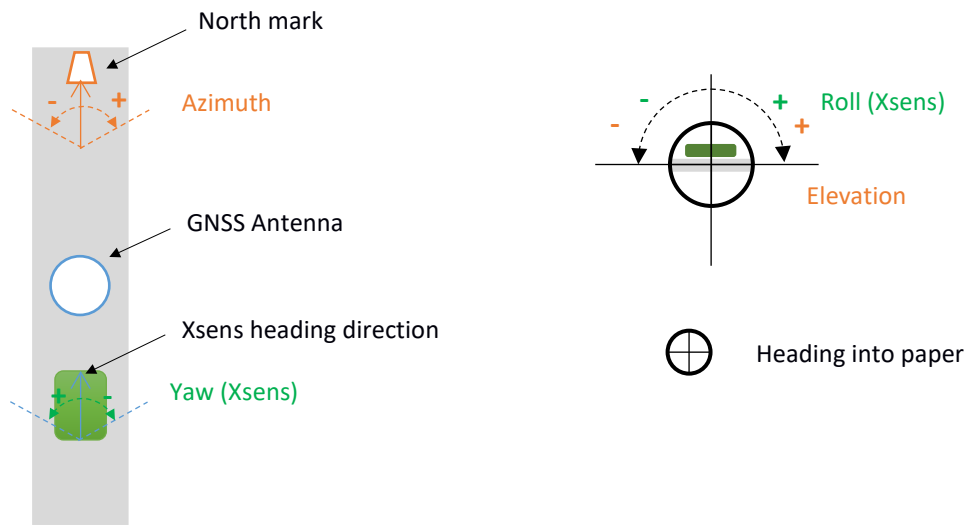


Figure 46 Alignment of the Xsens MTi on the rotating platform

Two measuring campaigns were conducted, one observes the C05 GEO satellite of the BeiDou system with a Leica AR10 antenna and a GR10 receiver; the other one measures the SES-5 (PRN 136) satellite of European Geostationary Navigation Overlay Service (EGNOS) with a low-cost Trimble Bullet III antenna and a u-blox LEA-M8T receiver module. From now on, S136 is used to denote the SES-5 geostationary satellite in this thesis. In both campaigns, the receiver antenna starts at the position with its boresight pointing towards the GEO satellite.



Table 7 Orientation performance specification of Xsens MTi  
(Xsens Technologies B.V. 2010)

Sensor	Xsens MTi
Range	All angles in 3D
Angular Resolution	0.05° RMS
Repeatability	0.2
Static Accuracy (roll/elevation)	0.5°
Static Accuracy (heading/azimuth)	1°
Dynamic Accuracy	2° RMS
Sampling frequency	max 256 Hz
Recommended sampling rate	100 or 200 Hz

### 4.3 Measuring campaign with the BeiDou C05 satellite

The only geostationary satellite of the BeiDou system visible in Switzerland is the C05 satellite at an azimuth angle of 122° and an elevation angle of 17° (see Figure 47). Figure 48 describes the antenna starting position and the rotating direction. The measurements start with the antenna's boresight (up direction) pointing towards the C05 satellite and stays for 5 minutes until it rotates to the next position. Then the rotating bar will move the antenna by 5 ° in the direction as illustrated in Figure 48 and stays for 5 minutes. This step is repeated until the antenna has conducted observations at every 5 degrees with antenna boresight rotating from 0° to 90° elevation angle with respect to the satellite C05. The roll angles of the antenna position recorded by the Xsens MTi are used to verify the antenna positions (see Figure 49). The roll angles will be converted to elevation angles in the antenna local frame by subtracting from 90°.

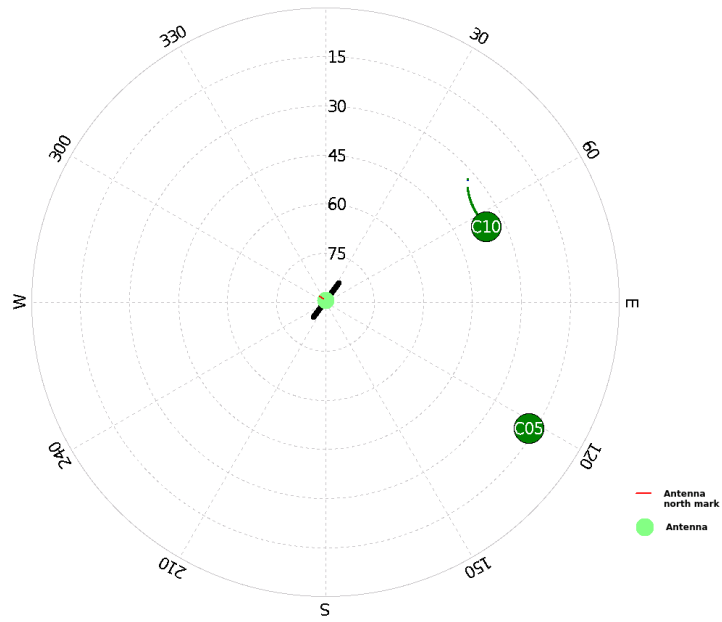


Figure 47 Skyplot of the BeiDou geostationary satellite C05;  
Azimuth: 122°; Elevation: 17°

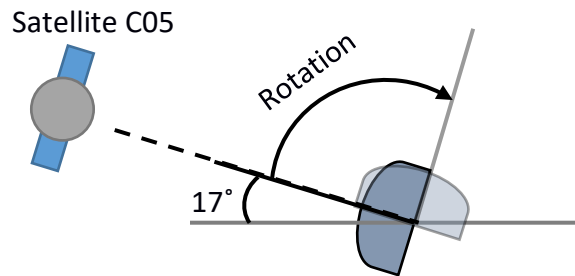


Figure 48 Illustration of the antenna starting position and the rotating direction for measuring the C05 satellite

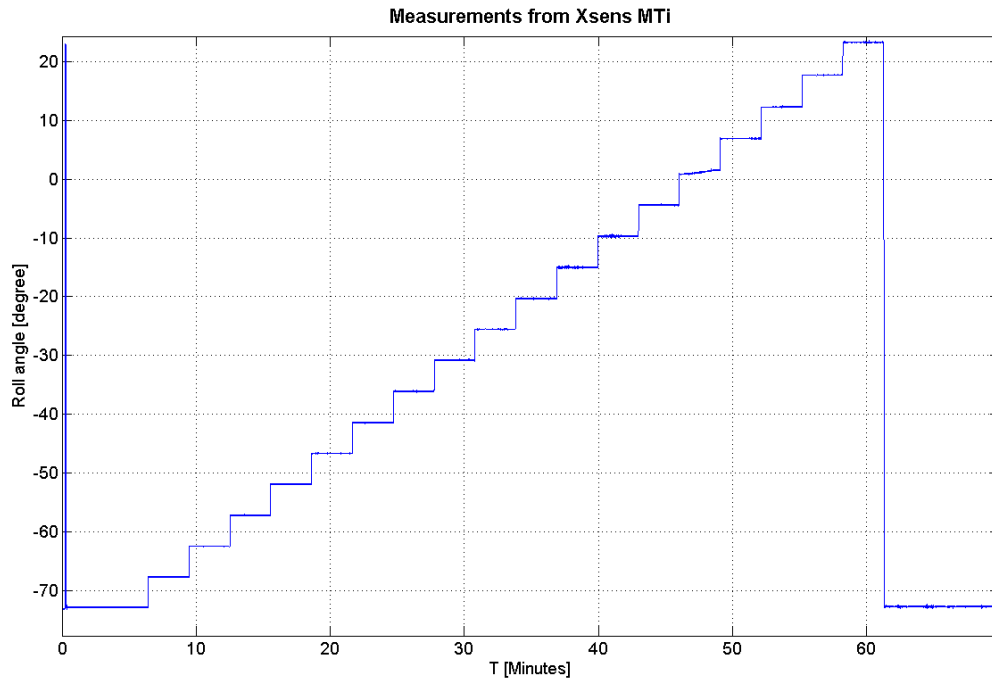
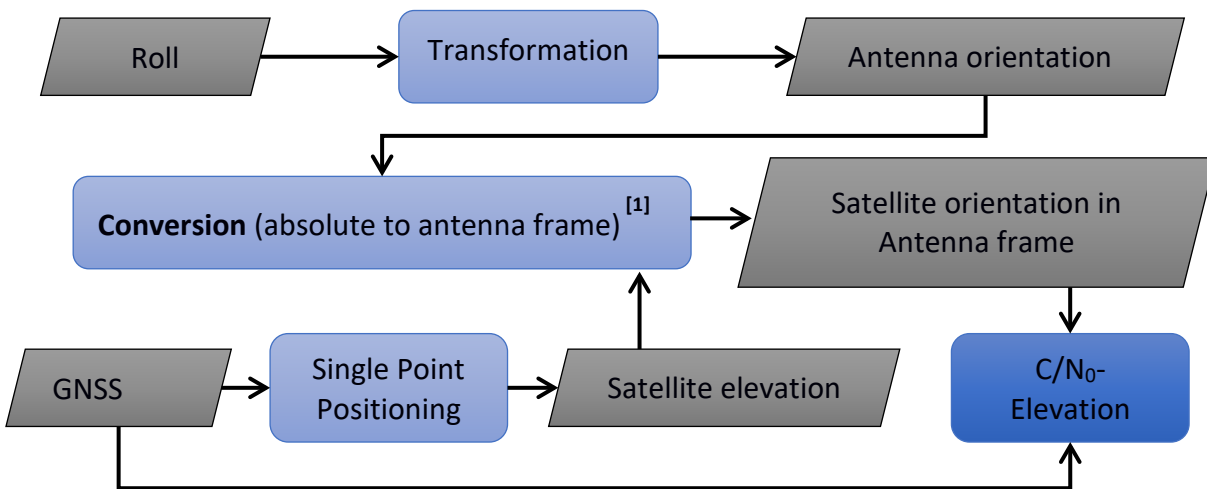


Figure 49 Roll angles of the antenna position measured by XSens MTi



[1] absolute frame – station topocentric frame: local north east and up

Figure 50 Flowchart of the empirical antenna gain pattern modeling

With the GNSS data collected with the antenna at all the positions and the recorded roll angles by Xsens MTi, the collected GNSS data including the C/N0 values are processed as described in Figure 50. The roll angles and satellite elevations are in the absolute frame, which is defined in

the station topocentric frame (North, East and Up). They are converted to the antenna frame, which is fixed with the antenna body. It is equivalent to a continuous GNSS signal scanning through the GNSS antenna to generate a set of  $C/N_0$  values depending only on the elevation-dependent antenna gain pattern.

*Results and analysis*

The observed  $C/N_0$  values during the antenna moving from one position to the next are all removed in order to exclude the error on the measured  $C/N_0$  induced by the antenna dynamic. The cleaned  $C/N_0$  time series are visualized below.

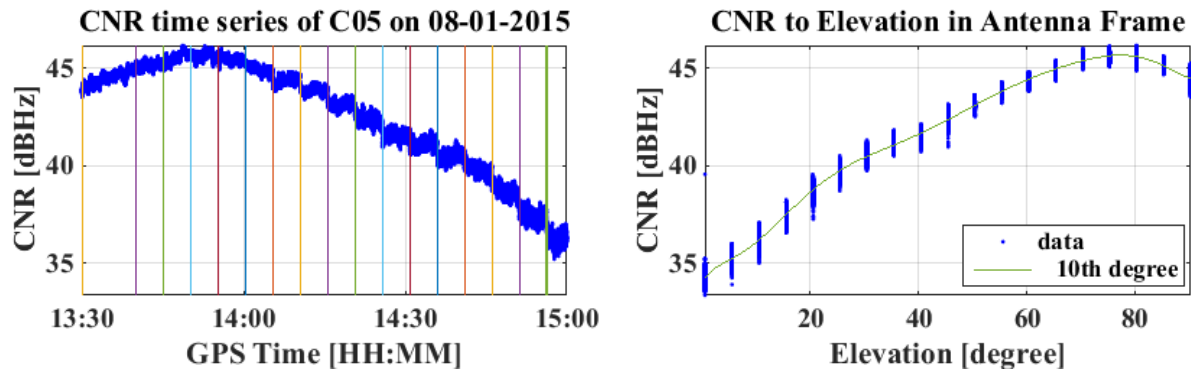


Figure 51 Plot of  $C/N_0$  time series (left) and  $C/N_0$  to elevation angles (right)

In the left picture, the  $C/N_0$  values are plotted with respect to the time stamps. Each vertical line indicates the epoch, where the antenna starts observations at a different position. In the right picture, the  $C/N_0$  values are plotted with respect to the satellite elevation angles. An antenna gain pattern with  $5^\circ$  resolution can be approximated from these values. One can see that the maximum  $C/N_0$  is measured at  $75^\circ$  elevation and the minimum value at  $0^\circ$ . Up to 10 dBHz difference exists between the maximum and minimum  $C/N_0$  values. The mean  $C/N_0$  values at each position/elevation are calculated and then a 10-degree polynomial is used to fit the data. An empirical antenna  $C/N_0$  pattern is obtained ( see Figure 52) by setting the mean  $C/N_0$  value at  $90^\circ$  elevation zero and compute the relative gain at other elevations. This empirical antenna  $C/N_0$  pattern can be used as a relative antenna gain pattern.

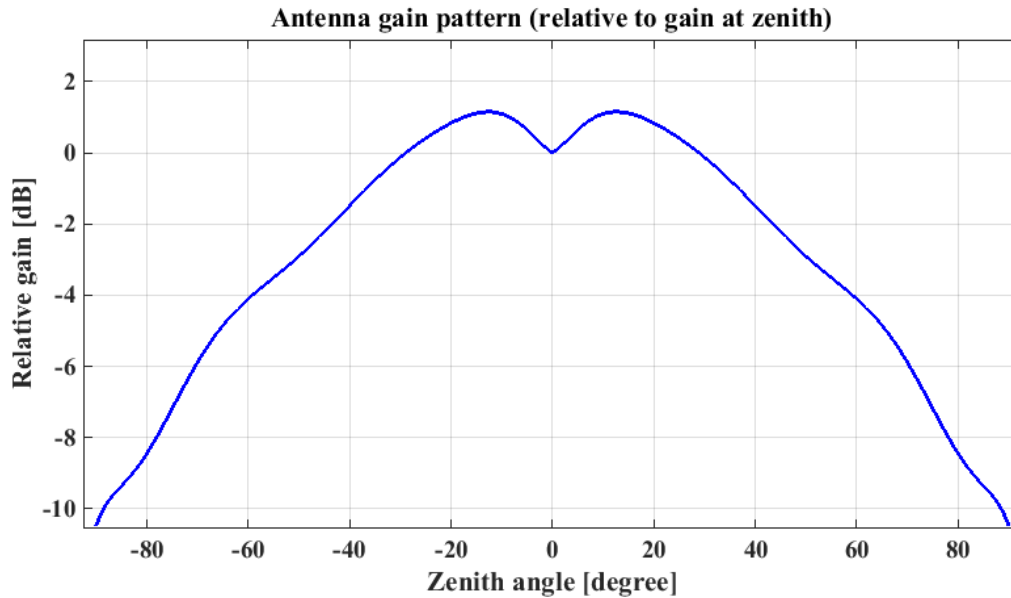


Figure 52 Antenna gain pattern derived from the experiment by 10-degree polynomial fits (center and scale x data) to the mean  $C/N_0$  values at each position

Besides modelling the antenna gain pattern, the results also demonstrated the feasibility of using high-end GNSS antennas for  $C/N_0$  based titling determination. One can see clearly in the  $C/N_0$  to elevation plot that the  $C/N_0$  values are well separated by each  $10^\circ$  elevation difference, especially at the low elevations.

#### 4.4 Measuring campaign with the SBAS 136 satellite



Figure 53 Trimble Bullet III antenna

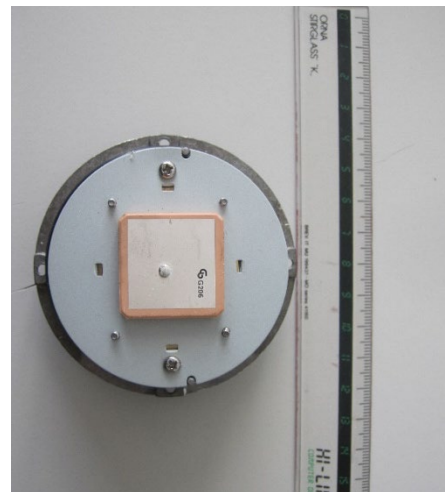


Figure 54 Trimble Bullet III antenna without radome

After obtaining the empirical antenna  $C/N_0$  pattern for the Leica AR10 antenna, the same procedure was applied using the low-cost single frequency antenna Trimble Bullet III (see Figure 53 and Figure 54) and the u-blox M8T receiver module.

However, the low-cost patch antenna and the u-blox M8T receiver deliver a much noisier observations of the BeiDou C05 satellite as shown in Figure 55. The  $C/N_0$  time series are collected from one stationary measurement setup (the antenna was kept stationary). The standard deviation is 1.29 dBHz and the range from maximum to minimum is 9 dBHz, which is close to the range of the Leica AR10 antenna's gain change. This large variation disqualifies the C05 satellite for modeling the low-cost antenna gain pattern. Moreover, the C05 satellite had up to 3 degrees' change in its elevation angle seen by the stationary antenna (based on the satellite elevation angle computed by code single point positioning).

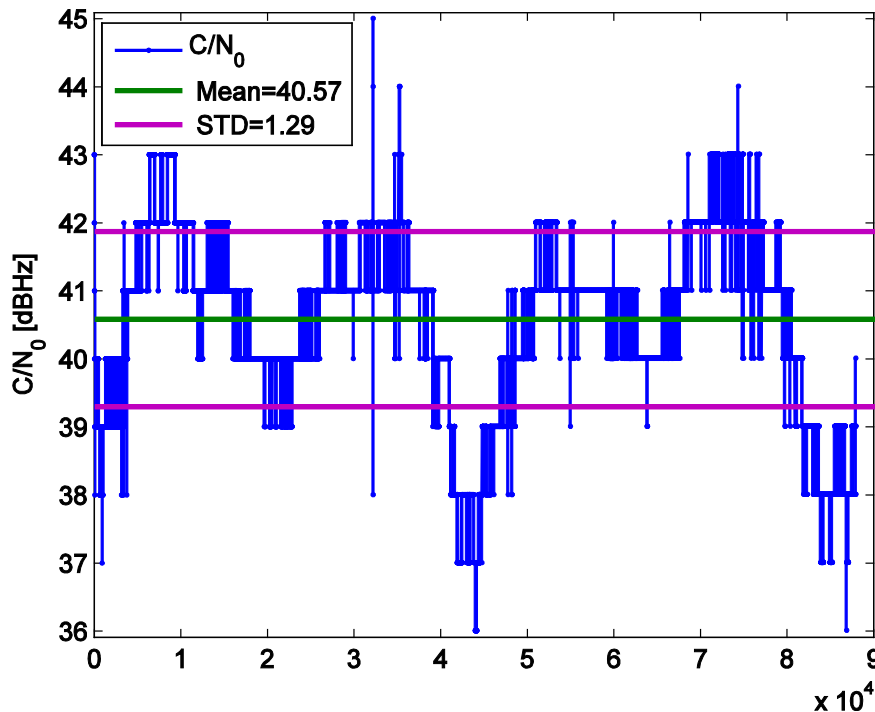


Figure 55  $C/N_0$  time series of the C05 satellite measured by a Trimble Bullet III antenna (stationary) and a u-blox M8T receiver module; Horizontal axis is the GPS time in second

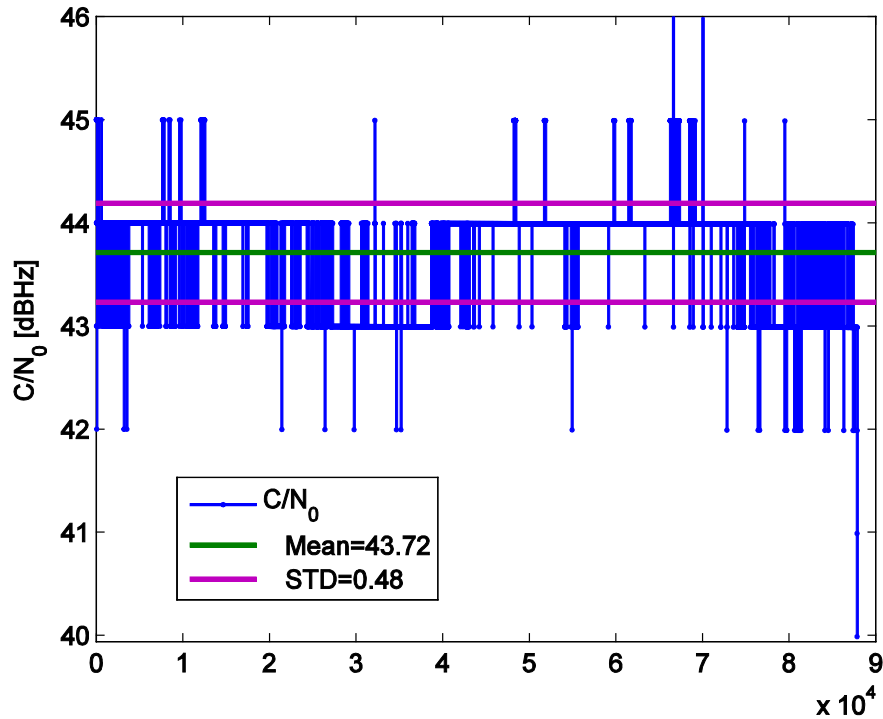


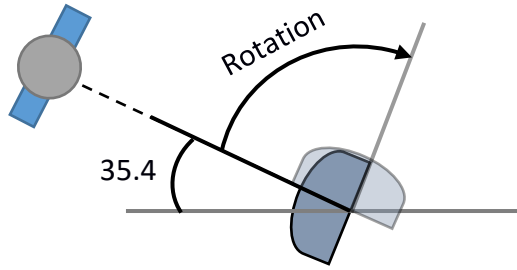
Figure 56  $C/N_0$  time series of the S136 satellite measured by a Trimble Bullet III antenna (stationary) and a u-blox M8T receiver module; Horizontal axis is the GPS time in second

Instead, the  $C/N_0$  of the S136 satellite shows higher mean values (3 dBHz higher), smaller dispersion (STD=0.48 dBHz) and much smaller variations. Excluding the last two points, the range from maximum to minimum value is only 3 dBHz. The satellite elevation angle is  $35.4^\circ$  and keeps unchanged during the whole observation period. These high consistencies make the satellite S136 a good candidate for modeling low-cost single frequency patch antenna's gain pattern. In addition, the high elevation angle of the S136 reduces the atmosphere attenuation and the risk of multipath effects on the observed  $C/N_0$  compared to the C05 satellite at a lower elevation of  $17^\circ$ . The same procedure, as described in Chapter 4.3, is repeated with the S136 satellite.

Two sets of data were collected with the antenna starting at the same position (boresight pointing towards S136 but rotating differently). Data set A was collected with antenna boresight moving away from the ground and the other towards the ground (see Figure 57).

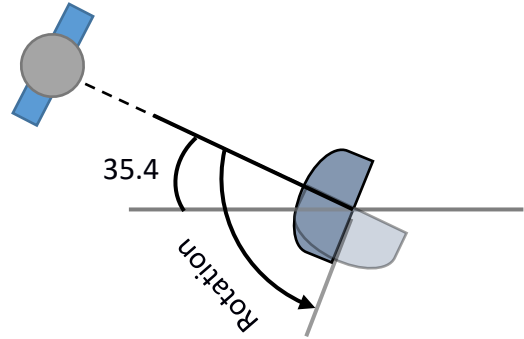
The mean value of the real valued  $C/N_0$  measurements at each antenna position was taken for the C05 satellite measured with a Leica antenna and receivers, because they are close to random variables with a Gaussian distribution and the mean represents the value of highest probability. Unfortunately, the u-blox M8T outputs only integer values for the measured  $C/N_0$ , thus a round-off error exists. For this reason, the median value is taken instead of the mean and the boxplot is used as a statistic tool to categorize the integer  $C/N_0$  values.

Satellite S136



(A)

Satellite S136



(B)

Figure 57 Illustration of the antenna starting position and the rotating direction for measuring the S136 satellite

The boxplot is a graph that depicts several statistics (Theus and Urbanek 2008). The upper extreme, lower extreme, median, upper hinge (Quartile) and lower Quartile are used to categorize the data samples in a statistical way. A illustration of the boxplot is given in Figure 58. The upper quartile is the middle number between the maximum and the median value of the data samples whereas the lower quartile is the middle number between the minimum and the median value. The range between upper and lower quartile is called InterQuartile Range (IQR). Then the upper and lower whiskers are defined as upper quartile plus 1.5 times IQR and lower quartile minus 1.5 times IQR, respectively. Any data out of this range are considered as outliers.



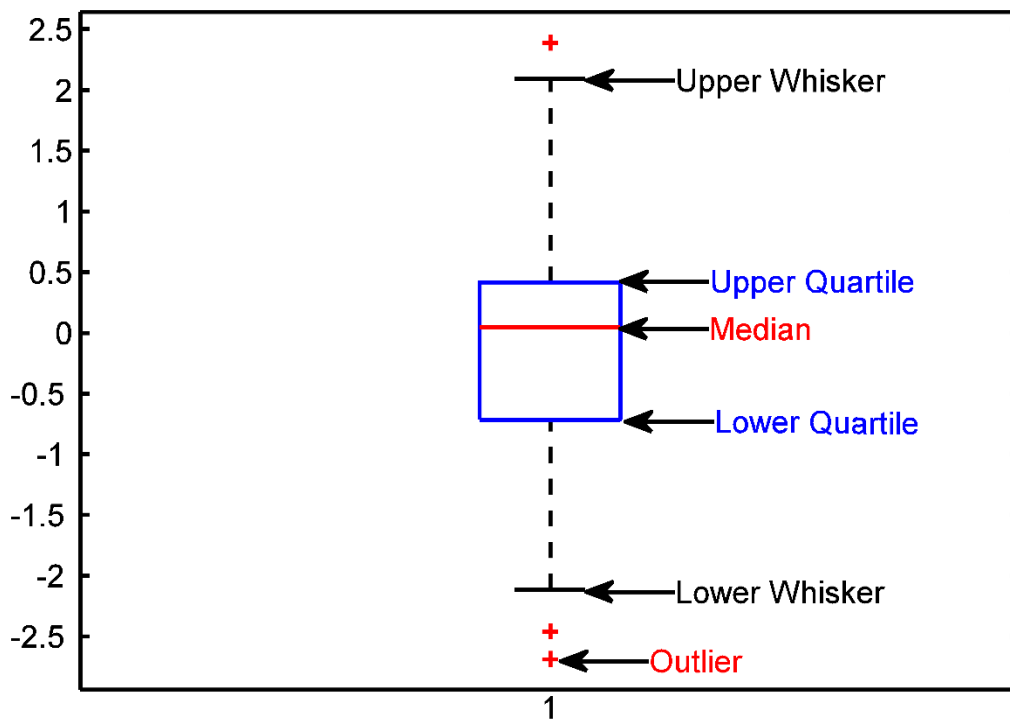


Figure 58 Illustration of the boxplot

The boxplot of data set A is given in Figure 59. The observed  $C/N_0$  values have a very high consistency at elevation angles of  $0^\circ$ ,  $20^\circ$ ,  $40^\circ$ ,  $50^\circ$ ,  $60^\circ$  and  $80^\circ$ . All  $C/N_0$  values are the same, except for few points that are different by 1 dBHz and detected as outliers. The  $C/N_0$  values measured at elevations  $10^\circ$ ,  $70^\circ$  and  $90^\circ$  have larger dispersion. However, the maximum differences are still smaller than 4 dBHz.

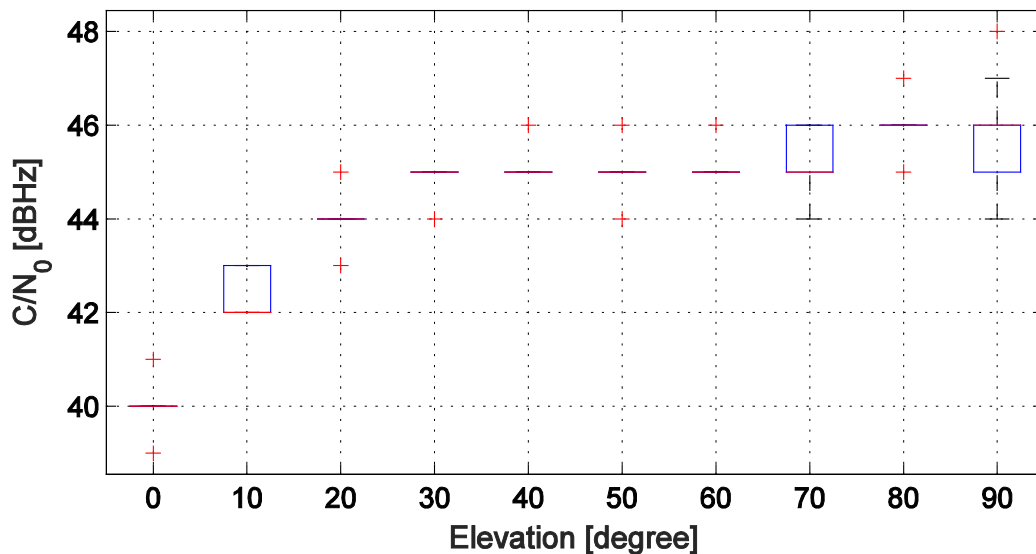


Figure 59 Boxplot of the  $C/N_0$  to elevation of the S136 satellite from data set A

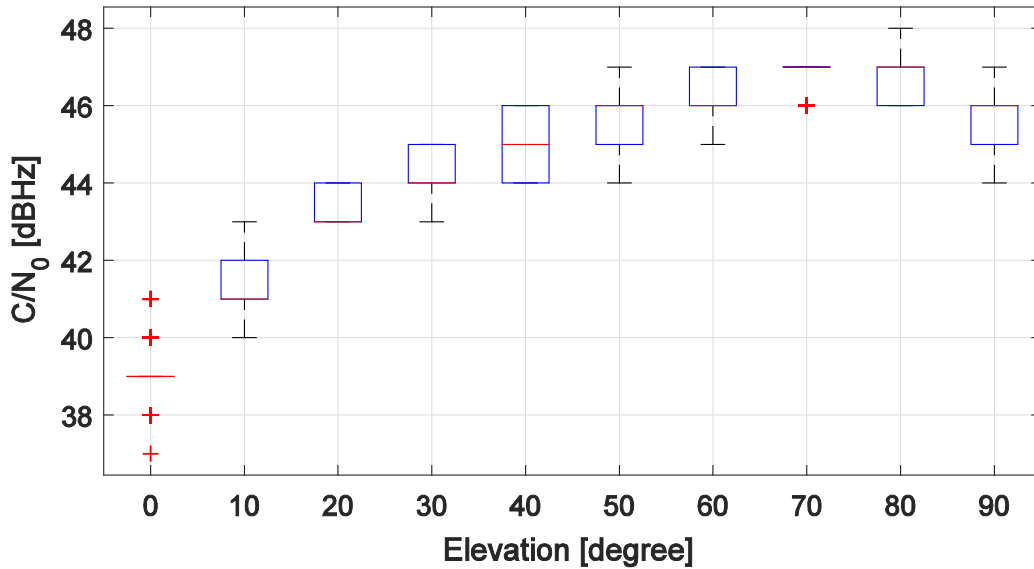


Figure 60 Boxplot of the  $C/N_0$  to elevation of the S136 satellite from data set B

The  $C/N_0$  values in data set B have a larger dispersion at all elevation angles, as one can see from Figure 60. Because the antenna boresight is directed towards the ground, any GNSS signal reflections from the ground can be easily received by the antenna. In contrast, the data set A has been collected with the antenna backside towards the ground, the antenna gain on the backside is very small so that the reflections are strongly mitigated.

Taking the median of the  $C/N_0$  values at each elevation from data set A, an empirical antenna relative  $C/N_0$  gain pattern (with respect to the boresight)  $G_r$  of the Trimble Bullet III is determined with a 10-degree resolution.

Table 8 Relative antenna gain for Trimble Bullet III

Elevation [degree]	0	10	20	30	40	50	60	70	80	90
Relative $C/N_0$ gain [dB]	-6	-4	-2	-1	-1	-1	-1	-1	0	0

Using a simple linear interpolation, the gain at any elevation angle can be calculated based on the values listed in Table 8. The computed gain can be used to remove  $C/N_0$  trend in the actually measured  $C/N_0$  contributed by the antenna gain.

# Chapter 5 Relative antenna phase center variation estimation of a low-cost single-frequency antenna

## 5.1 Antenna mean phase center and phase center variations

We assume the calculated mean GNSS receiver antenna position (the average of instantaneous antenna positions) to be a constant point called antenna mean phase center (MPC). In general, the antenna MPC differs from the geometric center of antenna. A reference point is marked on most geodetic grade antennas and the offset values from the reference point to the antenna MPC is called antenna Phase Center Offset (PCO). Figure 61 shows the antenna reference point and the phase centers for L1 and L2 frequencies of a Trimble TRM29659.00 antenna installed at the reference station ETHZ.

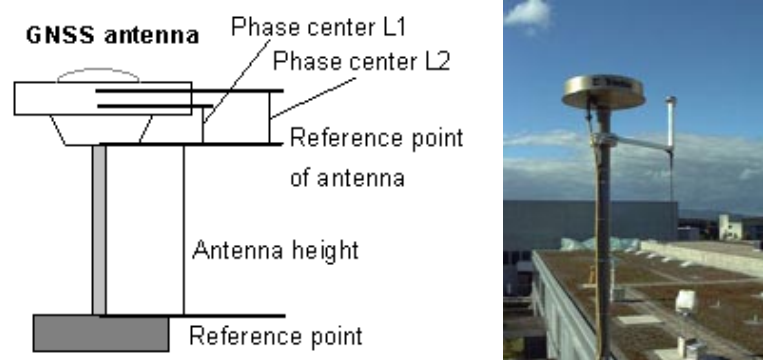


Figure 61: TRM29659.00 antenna of the reference station ETHZ (©AGNES, SWISSTOPO)

The electronic GNSS signals arriving at the receiver antenna from different azimuth and elevation angles do not meet at a point, instead their phase ends form a signal surface. The deviations between the phase ends of individual GNSS signals and the mean phase center (namely, the antenna phase center) is defined as the Phase Center Variations (PCV) as illustrated in Figure 62. (Geiger 1988) has discussed the analytic form of the PCV as an error function for different types of GNSS antennas and indicated that the PCV can directly be implemented as a distance correction to the GNSS measurements.

It is important to be aware of that the antenna PCV is bounded to the antenna MPC which was introduced as the known fix point when estimating the PCV. A different antenna PCV will be derived, if a different antenna MPC position is introduced in the PCV estimation processing, and the MPC deviation from its true value will go into the estimated PCV values.

One of the mathematical representations of the antenna PCV is the spherical harmonics function representation as used in (Rothacher, Schaer, et al. 1995):

$$PCV(\alpha, z) = \sum_{n=1}^{n_{max}} \sum_{m=0}^n P_{nm}(\cos z) (a_{nm} \cos m\alpha + b_{nm} \sin m\alpha) \quad (5-1)$$

Where the  $P_{nm}$  are normalized associated Legendre functions of degree  $n$  and order  $m$ ,  $a_{nm}$  and  $b_{nm}$  are the coefficients of the harmonic series to be estimated,  $\alpha$  is the azimuth and  $z$  is the zenith angle of the satellite line-of-sight. The maximum degree  $n_{max}$  is never smaller than the maximum order  $m_{max}$ .

An alternative is the tabular representation of the PCV, where discrete values are listed with respect to the satellite zenith and azimuth angles in a piece-wise linear way. This tabular representation is used in all the ANTEX files (Rothacher and Schmid 2010), e.g., the igs08.atx (see (Schmid, Dach, et al. 2016) for details) provided by the IGS.

The advantage of the mathematical representation is that it is physically more meaningful and one can get the exact PCV values at a specific elevation and azimuth angle from the spherical harmonics function. Using a maximum degree and order of 8 of the spherical harmonics functions, the resolution is  $180^\circ/8=22.5^\circ$  at zenith and  $360^\circ/(8 \times 2)=22.5^\circ$  in the azimuth direction. The number of unknown parameters ( $a_{nm}$  and  $b_{nm}$ ) in equation (5-1) is then 44.

Whereas for a typical tabular representation of size 19 x 73 (zenith ranging from  $90^\circ$  to  $0^\circ$  and azimuth from  $0^\circ$  to  $360^\circ$ , with  $5^\circ$  interval, the number of unknowns to be estimated is 1387. Therefore, using a spherical harmonics representation will lead to a smoother estimation of the PCV values. However, when coming to the step of applying the PCV as correction in the GNSS processing, it is practical to convert it to the tabular form which is more straightforward to apply as range corrections on the measurements.

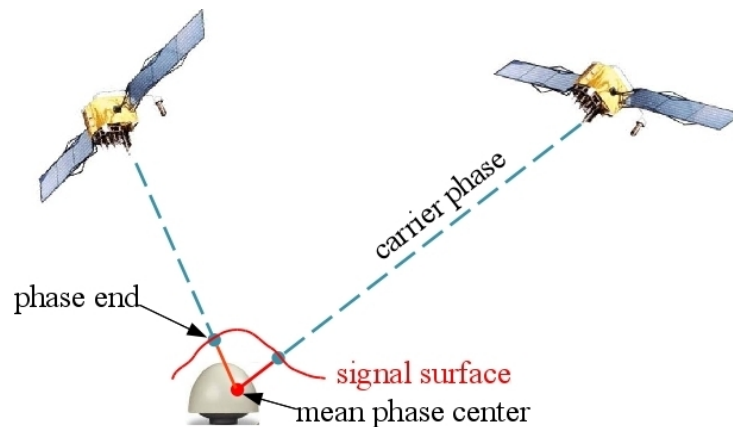


Figure 62: illustration of PCV

## 5.2 Current state

As already described in previous chapters, errors in GNSS measurements include, among others, the antenna PCVs for both, satellite and receiver. The satellite antenna PCVs are provided together with the satellite antenna PCOs in, e.g., igs08.atx file. Assuming that site-specific multipath is avoided by carefully choosing the observing location and using a choke ring antenna, then the only unmodeled error results from the receiver antenna PCV. In principle, when using the same type of antenna for rover and reference, the antenna PCVs are considered identical and are therefore eliminated by differencing as well. This is true for static stations but not for a moving rover whose antenna orientation is continuously changing.

Most of the geodetic-grade GNSS antennas are well calibrated and their PCV values are at millimeter level. The antenna PCO and PCV values are also available in igs08.atx. It provides the elevation- and azimuth-dependent absolute corrections estimated by the robot calibration. For more details about absolute and relative phase center corrections, please read (Schmid, Rothacher, et al. 2005) and (Rothacher and Mader 2002).

Unfortunately, no antenna calibrations are publically available for low-cost antennas like the Trimble Bullet III (see Figure 63), even though there are individual studies, like the antenna calibration of Trimble Bullet III, done in (Zhang 2016). Due to the dramatic price difference between the Trimble Bullet III antenna (< 100 Euro) and a geodetic antenna (>1000 Euro), we worried about the possible large variations in the antenna PCV. Thus, we developed a practical approach to estimate a low-cost single-frequency antenna PCV with respect to an absolutely calibrated reference antenna. The estimated relative antenna PCV reveals the antenna quality and is used to quantify its influence in RTK positioning.

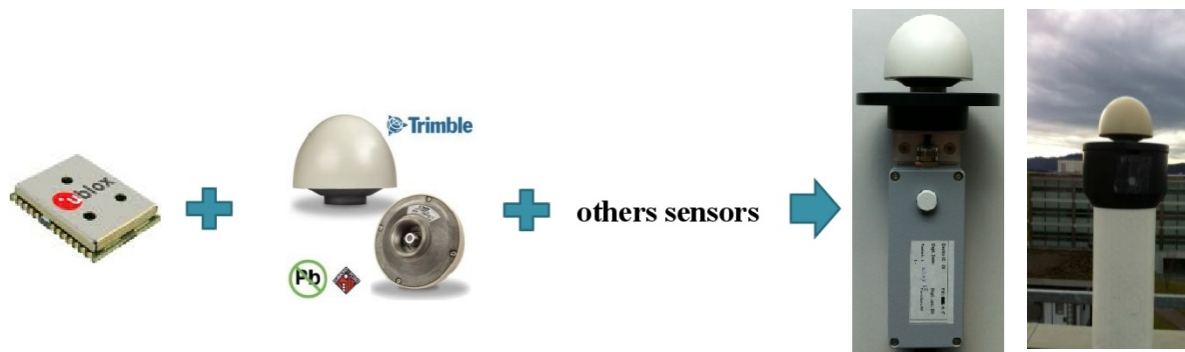


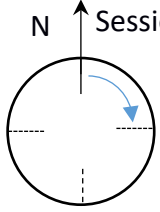
Figure 63: u-blox receiver module and Trimble Bullet III antenna in the X-Sense project (right) & setup for PCV estimation (left)

## 5.3 Data collection and processing strategy

The antenna PCVs are estimated under nearly zero baseline conditions and the reference antenna's absolute PCV values are assumed to be known. The rover station with low-cost

equipment is set up near the reference station ETHZ. The length of the baseline is 27 meters and DD observations are formed to eliminate common errors in the GNSS measurements. By carefully choosing the measurement site with no conductive obstructions above the antenna horizon, one can reduce the risk of massive multipath. However, on the roof of the HPV building, where the rover and the reference GNSS station are installed, multipath could still occur due to the metal boxes near the stations and the taller building HPP located in a north-east direction from 22° to 55°, with a maximum elevation angle at 27° seen from the receiver.

Table 9 Data collected for PCV estimation

	Session 1	Session 2	Session 3	Session 4	
	Antenna heading	N-E 0°	180°	90°	270°
	DOY <sup>11</sup> (at 2011)	186	188	193	196

4 sessions of data are collected, where the Trimble Bullet III antenna was rotated to 0°, 90°, 180° and 270° to the north. Each session lasted for 24 hours with a data sampling rate of 30s. The sky plot of the GNSS data collected during session 1 explains the reason to collect GNSS data with the antenna rotated to different azimuth angles.

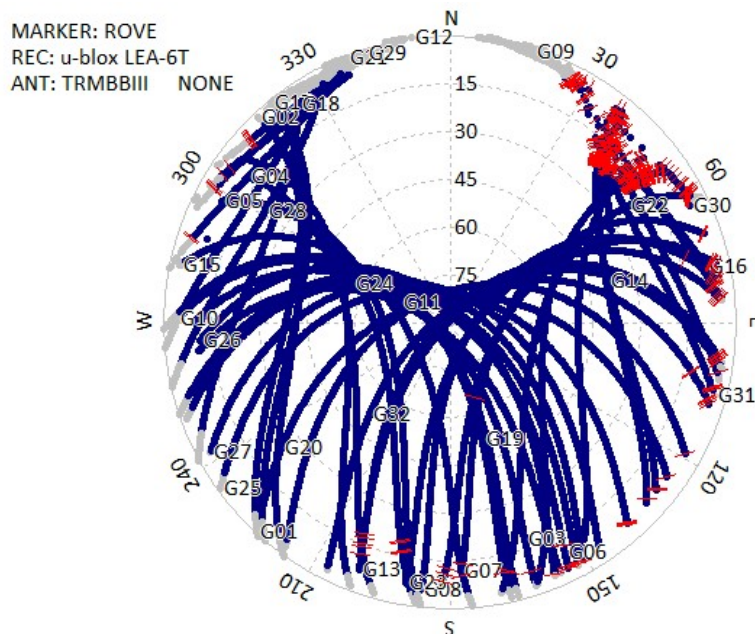


Figure 64 Sky plot of all the GPS satellites observed during session 1.

<sup>11</sup> DOY: Day of the Year

Each point in Figure 64 stands for an observed GPS satellite with its elevation and azimuth angle to the receiver marked in the polar coordinate system. The gray points are the observations below the 5° elevation mask. As one can see in the figure, there is a north hole in the sky plot, where no GPS satellites are available. However, to estimate the antenna PCV of the whole upper hemisphere, data collected from satellites with a full coverage of all azimuth angles is expected. A minimum of 2 sessions of observation data with the antenna pointing to north and 180° can fill up the north hole and guarantee a data set with full satellite coverage. To have more redundant observations, we conducted 4 observation sessions as described above. The tall building HPP causes a large amount of loss-of-lock events in the carrier-phase measurements marked by red in Figure 64, which is a clear evidence of multipath type II error for this area: the diffracted signals from the edge of the building were measured by the receivers.

The processing is based on the DD carrier-phase measurements which contain the DD geometric distance, the PCV of the rover and the reference antenna, the DD ambiguities and the remaining measurement errors:

$$L_{rb}^{ij} = \rho_{rb}^{ij} + \lambda \cdot N_{rb}^{ij} + PCV_{rov} - PCV_{ref} + e_{rb}^{ij} \quad (5-2)$$

where  $L_{rb}^{ij}$  is the DD carrier-phase measurements: first between rover and reference/base receiver and then between satellite  $i$ , and  $j$ ;  $\rho$  stands for the geometric distance between satellites and receivers;  $N$  is the phase ambiguity;  $e$  represents the remaining phase measurement errors; The last two terms are the PCV of the reference antenna and rover antenna. In our processing, the reference antenna's PCV is available from the igs08.atx file (for ETHZ) or from an absolute calibration by robot (for ETH2).

A Bernese Processing Engine (BPE) script "PCVEST" (see Figure 65) has been designed to automate the PCV estimation based on the Bernese Software 5.0. Figure 65 shows the flow chart of the PCV estimation procedure and the processing routines in the BPE.

In the first step, the MPC of the rover antenna is calculated from 24 hours of static observations. In the second step, the positions of both, the reference station and the rover are input as known parameters in the data processing. Using either a broadcast satellite ephemeris or a precise satellite orbit and clock correction file from the IGS final orbit products, the second term, the geometric distance  $\rho$  in equation (5-2), is precisely determined.

Then, the software will fix the phase ambiguities to integers along with the estimated rover coordinates and store them as known parameters in the first GPSEST<sup>12</sup> routine run of the designed BPE.

---

<sup>12</sup> A Bernese software routine/program to do parameter estimation based on least-square estimation.

Finally, formula (5-2) develops into an equation: with the PCV parameters, coefficients of spherical harmonics series  $a_{nm}$  and  $b_{nm}$ , on the right side; and the computed minus observed DD measurements on the left side, written in vector form as:

$$\Delta L = A \cdot [a_{1,0} \cdots a_{n,m} \ b_{1,0} \cdots b_{n,m}]^T + e \quad (5-3)$$

where  $A$  is the design matrix of the unknown parameters.

The above equation is solved by a least square adjustment in the second GPSEST routine run. The output is the set of estimated coefficients of the harmonics series in formula (5-1). The coefficients are stored in the Bernese format (see PHH file in (Dach, et al. 2007) ). Please notes that the Trimble Bullet III antenna is contained in neither the Bernese PCV file PCV.I08 nor in the ANTEX file igs.08. Its information has to be manually added up initialize the process.

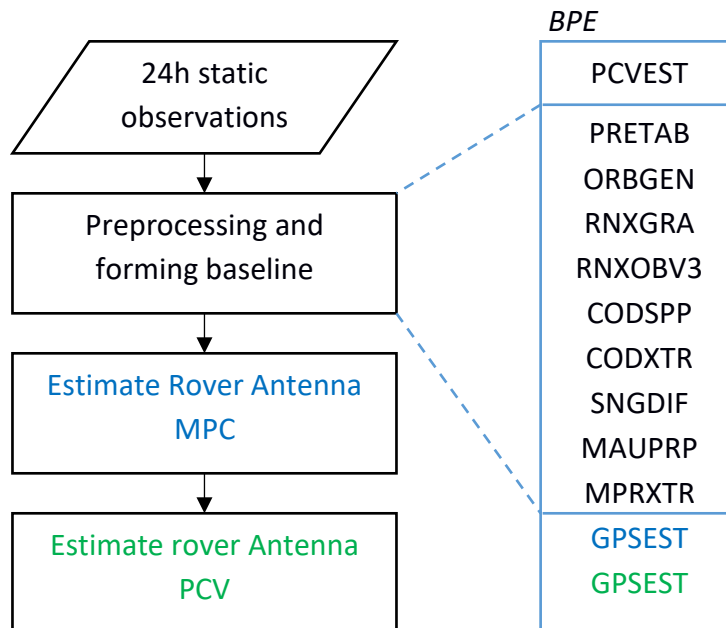


Figure 65 Procedures of PCV estimation with 1 session's data (left); The corresponding routines in the BPE (right)



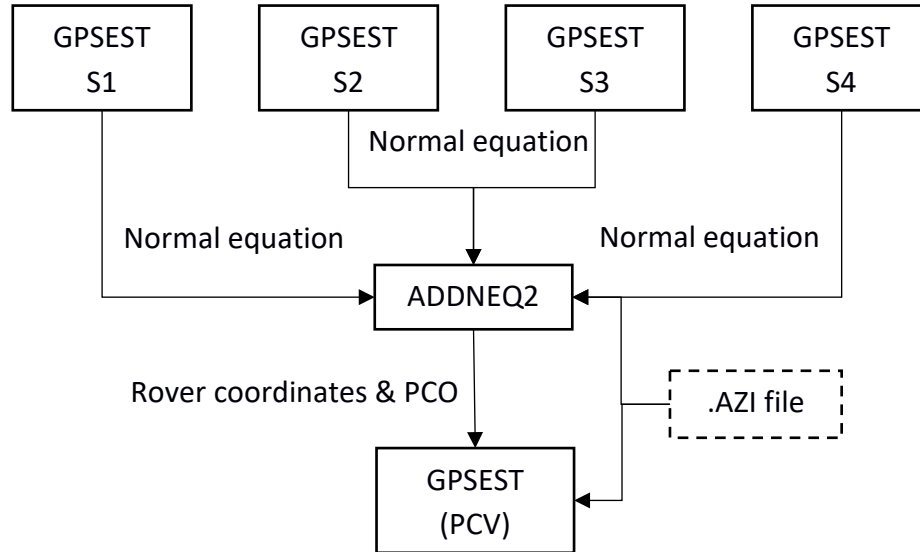


Figure 66: Procedures of PCV estimation using 4 sessions' data

Figure 66 describes the steps to estimate the antenna PCV with 4 sessions' data (Willi, et al. 2017). The same preprocessing steps as in the BPE PCVEST were done before each GPSEST on the top of Figure 66. Then in the GPSEST, instead of saving the estimated PCVs, the normal equations are saved as output. The normal equations from all four sessions together with the receiver antenna orientation file (.AZI file) are input to the program ADNEQ2<sup>13</sup> where the rover antenna coordinates and PCO parameters are estimated with data from all 4 sessions. After that, the estimated antenna coordinates and PCO are input to a last GPSEST run where the rover antenna's PCV are finally estimated.

## 5.4 Results

### Estimated relative antenna PCV with 1 session's data

The data collected during session 2 on DOY 188 is used to estimate the relative antenna PCV. Then the estimated PCV are used to correct the GPS data collected in the days (DOY 188 to 191) where the antenna position and orientation were kept the same.

<sup>13</sup> A Bernese software routine/program to compute multi-session solution from the combination of a set of single-session solutions.

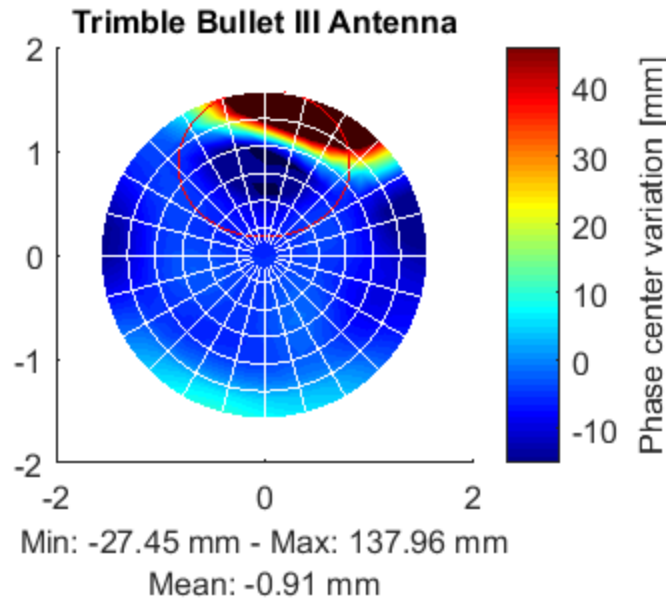


Figure 67 Estimated relative antenna PCV using 1 session's data ( without constrains), DOY188; the polar grid has a 15° resolution (each grid presents a 15° step for azimuth increments from 0° to 360° and for zenith increments from 90° (center) to 0° in the radial direction). The GPS data north hole is marked by the red circle.

The estimated antenna PCV is visualized in a polar coordinate system in Figure 67. The maximum PCV value is 137.96 mm, the minimum value is -27.45mm and the mean value is -0.91 mm. We can see that all the large values are located either inside the north hole or in the area, where the tall building HPP stands. In the other area, the PCV values are mostly with within 1 cm.

To exclude the influence of the north hole, a second processing is conducted, where a parameter constraining is applied to the PCV estimation by setting the a priori sigma to be 1 cm. The constraint on the antenna PCV is an absolute constraint. According to Chapter 7.5.4 of (Dach, et al. 2007) an absolutely constrained parameter is implemented by constraining the parameter improvement to zero using fictitious observations in the form:

$$p_i = 0 \quad (5-4)$$

with the weight

$$P_i = \frac{\sigma_0^2}{\sigma_i^2} \quad (5-5)$$

where  $\sigma_0^2$  is the a priori variance of unit weight and  $\sigma_i$  is the 1 cm a priori sigma you set to constrain the PCV parameter.

The estimated PCV constrained by the 1 cm a priori sigma is plotted in Figure 68. The maximum value is 46.80 mm, the minimum value is -15.78 and the mean is -0.45 mm. The figure shows that the large PCVs come from exactly the area where the tail building HPP is located (22° to 55° in the azimuth direction and 0° to 27° in the elevation direction). This is evidence that the carrier phase multipath (mostly the type II multipath: Only NLOS signals) caused by the tall building has contaminated the estimated PCV.

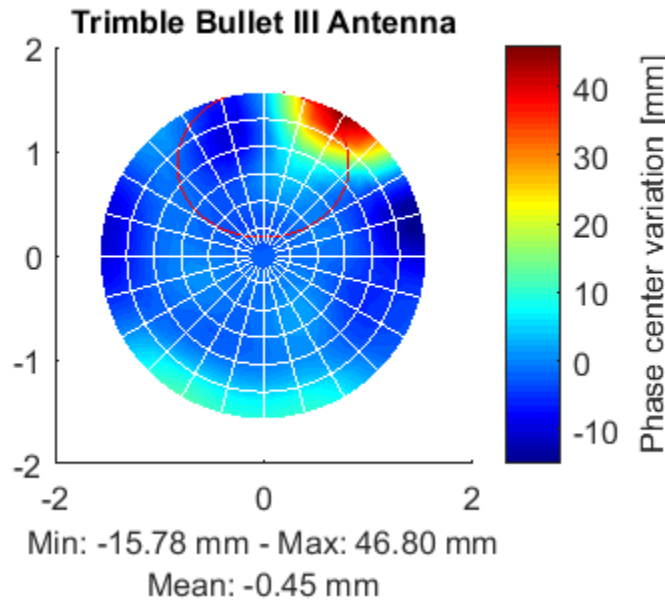


Figure 68 Estimated relative antenna PCV using 1 session's data (with constrains); DOY188

### Investigation of the antenna PCV influence on daily static positioning

The above estimated PCV (using only 1 observation session) is then applied as correction to the GNSS data collected in DOY 188, 189, 190 and 191 in a daily static positioning process (one position estimated out of 1 day's GNSS data). No differences are seen in the estimated coordinates, but the L1 DD carrier-phase residuals are decreased after applying the antenna PCV corrections. After applying the rover antenna PCV into the static daily positioning process, the mean RMS over all the DD carrier-phase residuals decreases by submillimeter. The improvements are due to both, the modeled multipath in the PCVs and the PCVs corrections. The RMS of the DD carrier-phase residuals of individual satellites are visualized by the Figure 69 to Figure 72.

Table 10 RMS of the mean DD carrier-phase residuals (over all satellites)

DOY	RMS (no PCV)	RMS (with PCV)
188	3.1 mm	2.9 mm
189	3.6 mm	3.4 mm
190	3.2 mm	3.1 mm
191	3.9 mm	3.6 mm

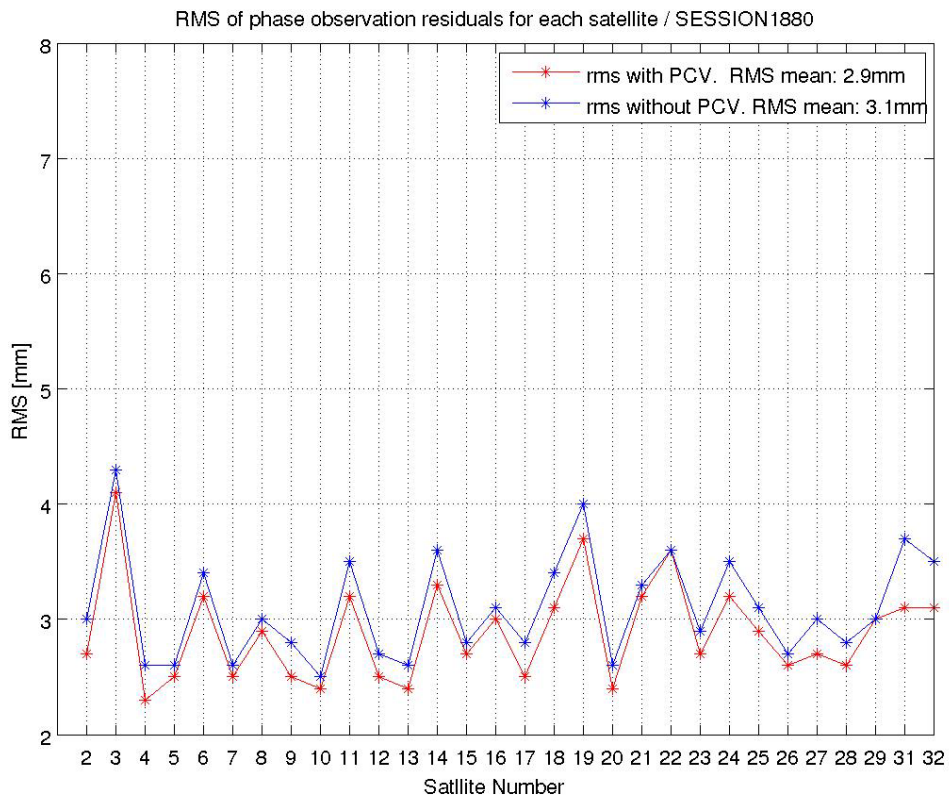


Figure 69 RMS of the DD carrier-phase residuals on individual satellites for DOY188

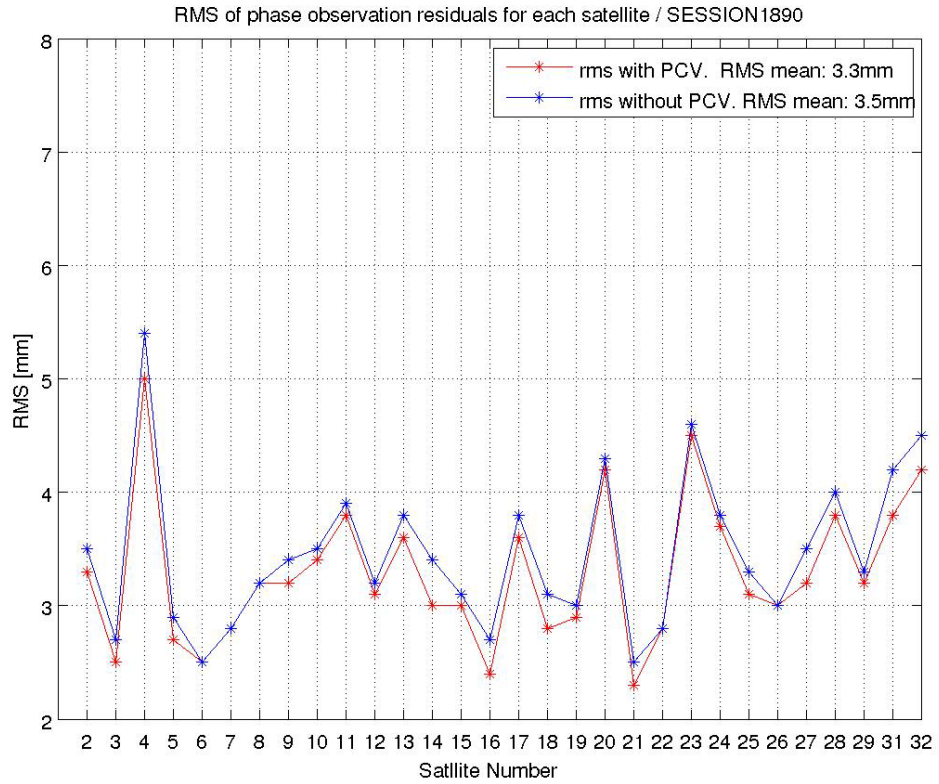


Figure 70 RMS of the DD carrier-phase residuals on individual satellites for DOY189

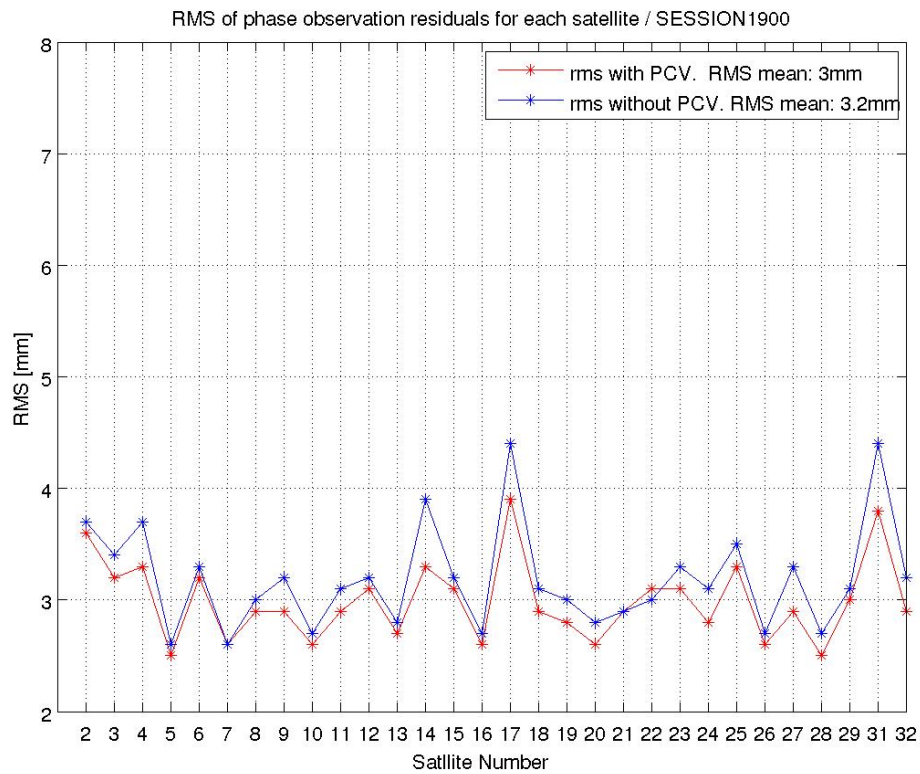


Figure 71 RMS of the DD carrier-phase residuals on individual satellites for DOY190

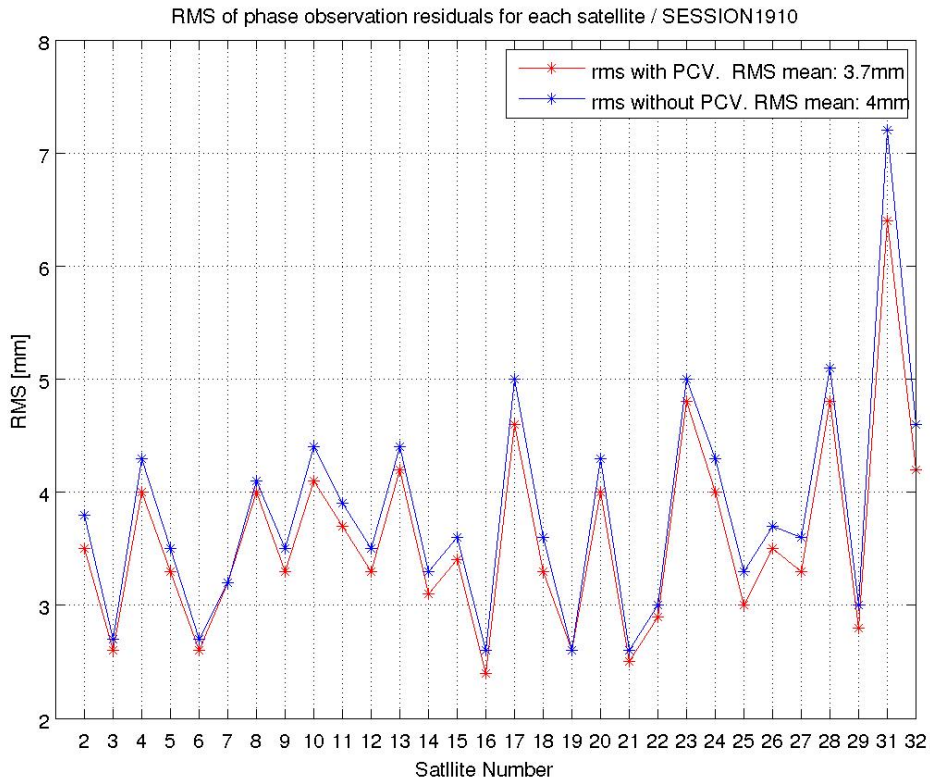


Figure 72 RMS of the DD carrier-phase residuals on individual satellites for DOY191

### Investigation of the antenna PCV influence on 2-hour static positioning

The influence of the PCV is more prominent for sub-daily coordinate resolution because of the satellite constellation change. To investigate the magnitude of the PCV influence, the estimated PCV for the rover antenna is applied to correct 2-hour GPS observations measured by the rover receiver. 2-hour solutions are calculated with and without using PCV corrections. Figure 73 to Figure 76 show that by using PCV corrections the calculated antenna positions are closer to the real value. Each point in the plots corresponds to a rover position calculated by 2 hours GPS observations. The position differences against real antenna position are plotted for North, East and Up. Numerical results are summarized in Table 11. The improvement comes mostly from the 2-hour static position estimated at 18:00 (see Figure 73 to Figure 76) which corresponds to the multipath caused by the tall building HPP.

Table 11 RMS of the mean 2-hour positions for DOY188 to DOY191

DOY188	RMS (no PCV)	RMS (with PCV)	Improvement
N	3.2 mm	1.6 mm	50%
E	2.2 mm	1.1 mm	50%
U	9.2 mm	5.1 mm	45%
DOY189	RMS (no PCV)	RMS (with PCV)	Improvement
N	2.6 mm	1.3 mm	50%
E	4.9 mm	1.6 mm	67%
U	6.2 mm	5.5 mm	11%
DOY190	RMS (no PCV)	RMS (with PCV)	Improvement
N	3.7 mm	3.0 mm	19%
E	4.9 mm	3.1 mm	37%
U	7.8 mm	5.1 mm	34%
DOY191	RMS (no PCV)	RMS (with PCV)	Improvement
N	3.6 mm	1.7 mm	36%
E	7.8 mm	1.7 mm	78%
U	7.7 mm	5.6 mm	27%



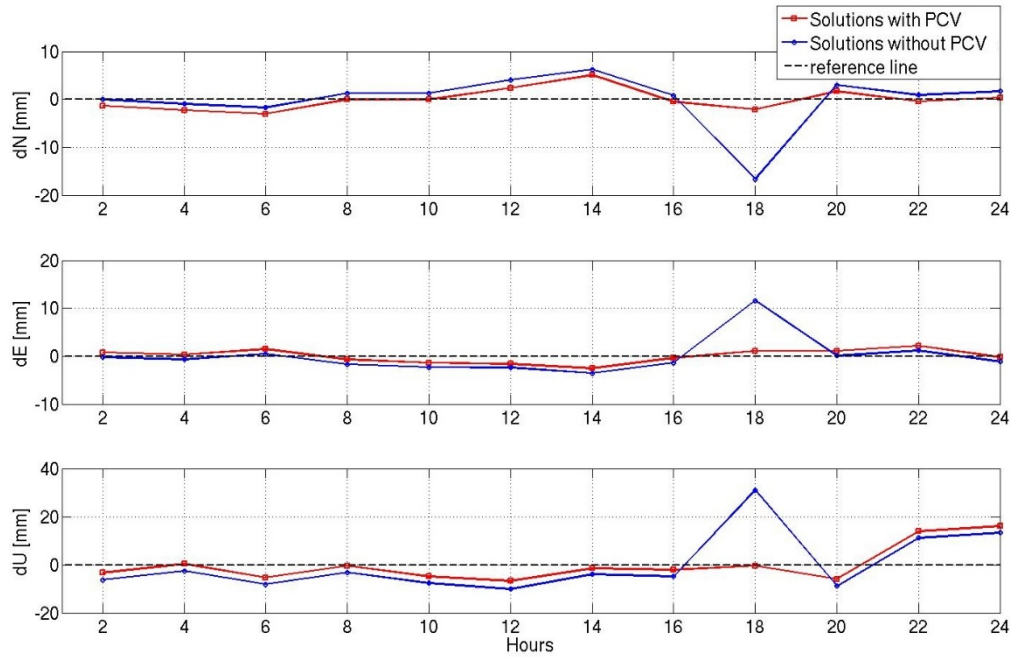


Figure 73 Position differences to true values of the 2-hour static solution for DOY188

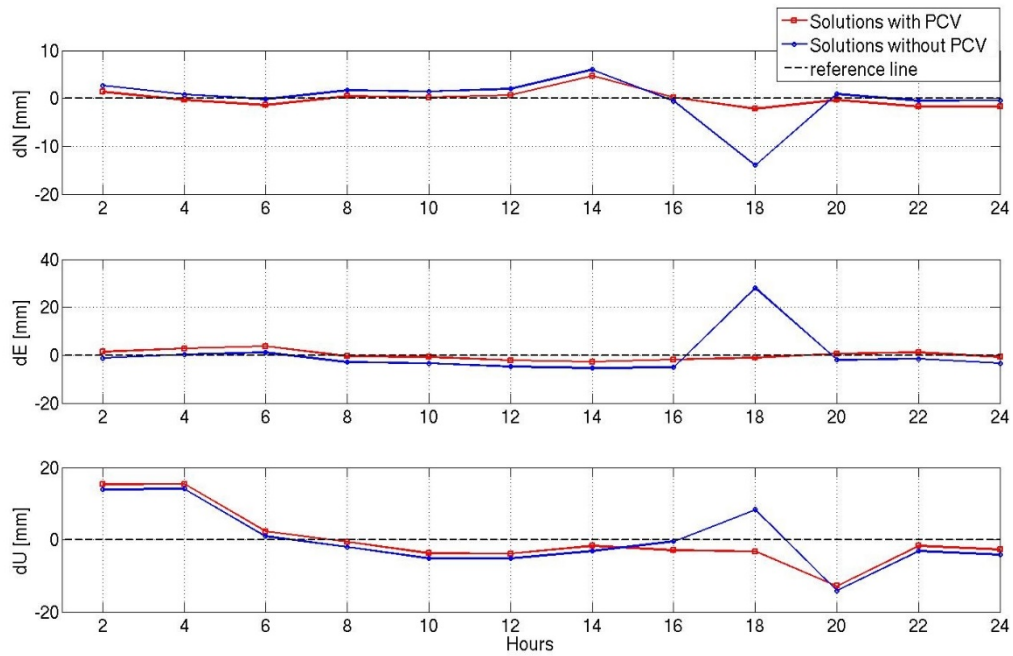


Figure 74 Position differences to true values of the 2-hour static solution for DOY189



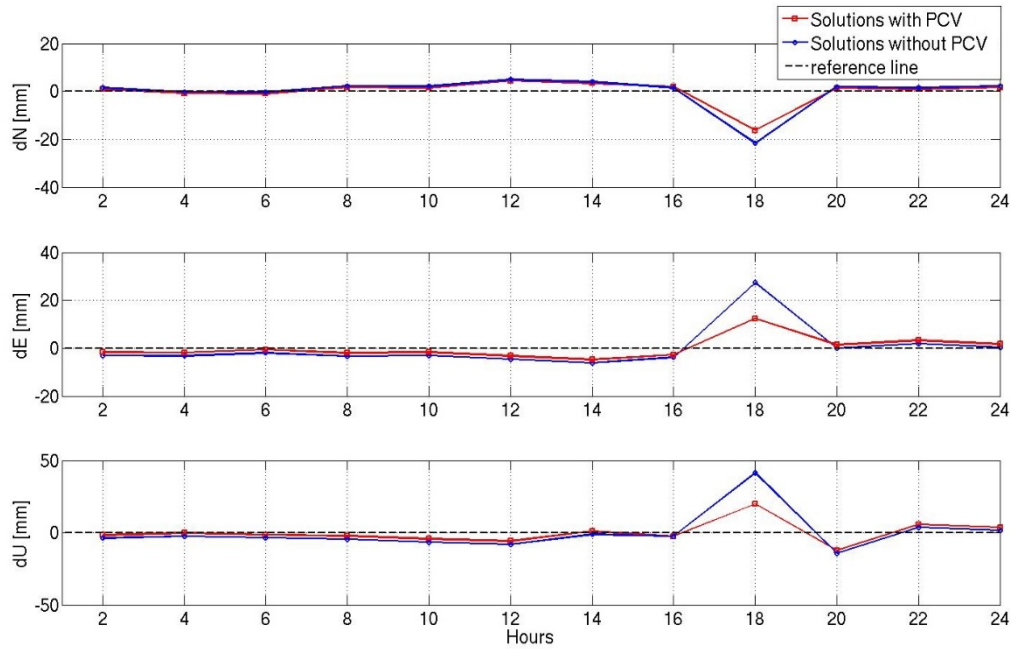


Figure 75 Position differences to true values of the 2-hour static solution for DOY190

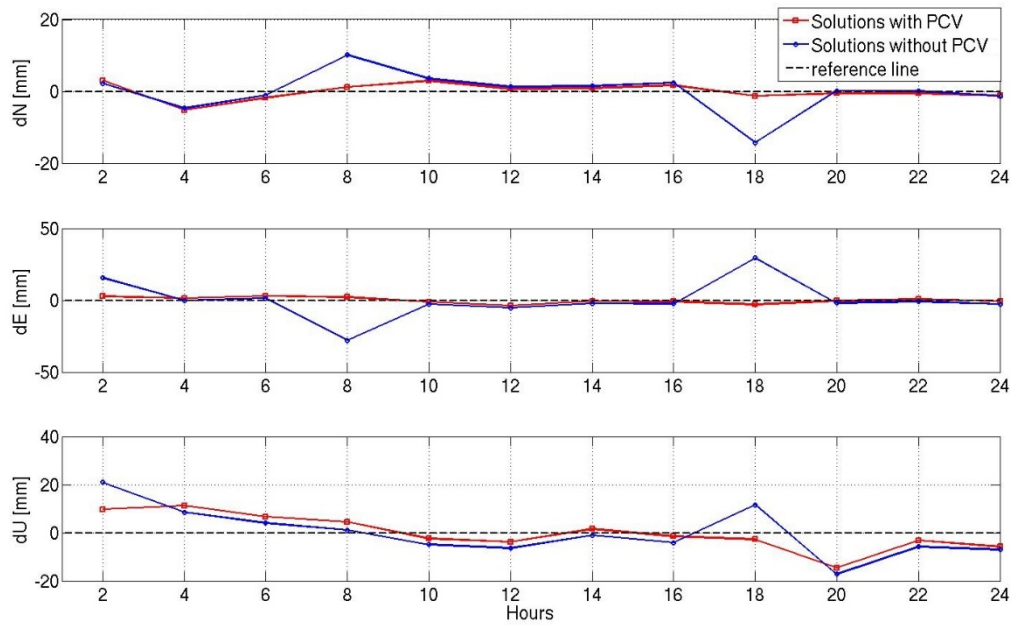


Figure 76 Position differences to true values of the 2-hour static solution for DOY191

### Investigation of the antenna PCV influence on kinematic positioning

Slight improvements in the kinematic positions are seen after applying the estimated rover antenna PCV to the kinematic processing with Bernese GPS software 5.0. The results show only submillimeter improvements in the RMS of the kinematic coordinates which are summarized in Table 12.

Table 12 RMS of kinematic positions

DOY188	RMS (no PCV)	RMS (with PCV)	Improvement [%]
N	4.5 mm	4.3 mm	2.2%
E	3.6 mm	3.5 mm	2.7%
U	5.8 mm	5.5 mm	5.2%
DOY189	RMS (no PCV)	RMS[mm] (with PCV)	Improvement [%]
N	5.1 mm	4.8 mm	5.9%
E	4.4 mm	4.3 mm	2.2%
U	6.3 mm	5.9 mm	6.3%
DOY190	RMS (no PCV)	RMS[mm] (with PCV)	Improvement [%]
N	5.5 mm	5.1 mm	7.3%
E	4.4 mm	4.4 mm	0.0%
U	6.7 mm	6.4 mm	4.5%
DOY191	RMS (no PCV)	RMS[mm] (with PCV)	Improvement [%]
N	5.5 mm	5.1 mm	7.3%
E	4.4 mm	4.4 mm	0.0%
U	6.7 mm	6.4 mm	4.5%

### Estimated relative antenna PCV with 4 sessions' data

To mitigate the multipath influence on the PCV estimation and cover up the missing data in the north hole, data from all 4 sessions with the antenna pointing to 4 different orientations are used together to estimate the rover relative antenna PCV pattern (recall Figure 66). For this estimation, we used ETH2 instead of ETHZ station. The ETH2 station is equipped with a TRMB59800.00 antenna, which has an absolute antenna PCV that was newly calibrated on 01/16/2015 by GEO++.

Figure 77 shows the estimated relative antenna PCV using 4 sessions' data. The maximum PCV is 10.26 mm and the minimum value is -5.90 mm. The magnitude of the PCV confirms that the 1 cm a priori sigma constraint we have applied for the PCV estimation with 1 session's data is appropriate. The pattern is quite symmetric along the azimuth direction. To better quantify the results, we converted the PCV represented by spherical harmonic to tabular PCV with azimuth ranging from 0° to 360° and zenith ranging from 0° to 90° by 5° increments (see Figure 78). The histogram of the tabular PCVs indicates that 97.6% of the PCV values are within  $\pm 6$  mm (see Figure 79).

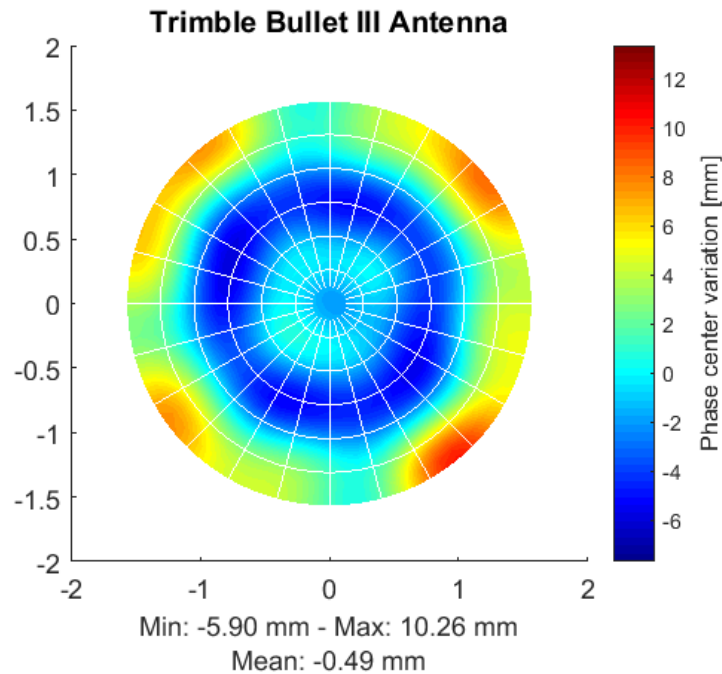


Figure 77 Estimated relative antenna PCV with 4 sessions' data with antenna pointing to north, south, east and west respectively.

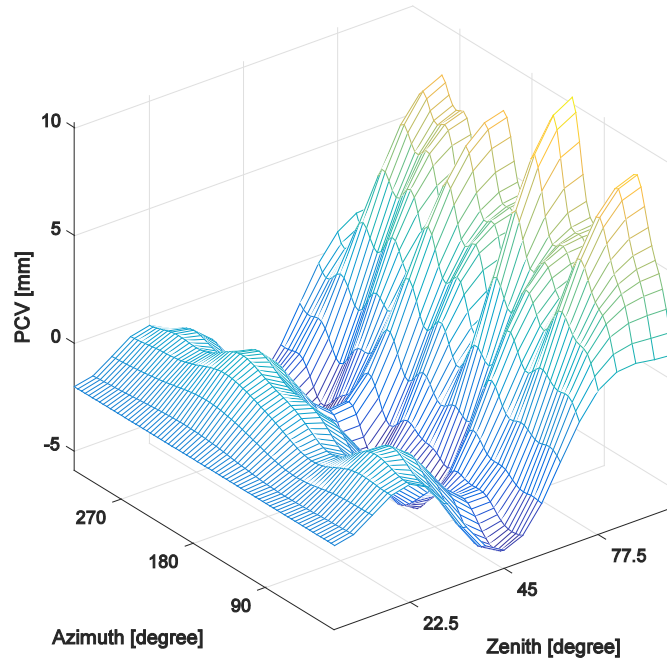


Figure 78 Tabular PCV values converted from the spherical harmonic representation

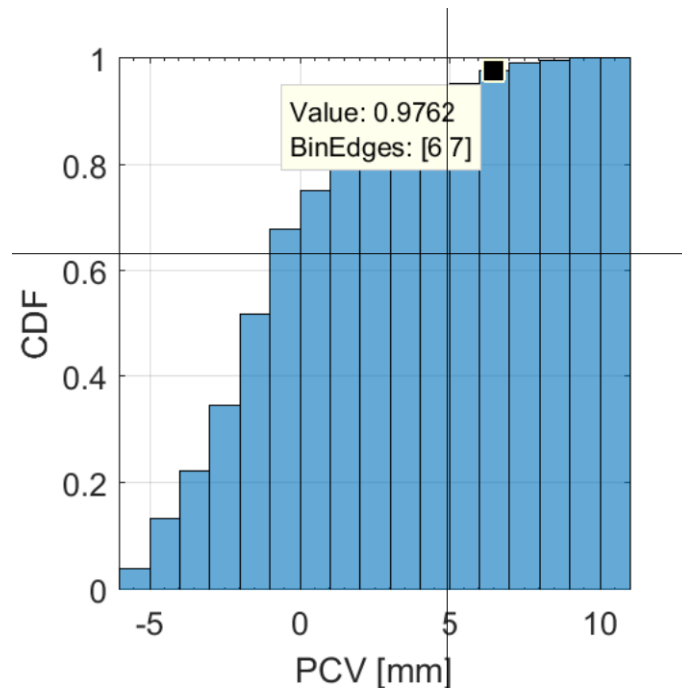


Figure 79 Histogram plot of the tabular PCV values; Y axis is the Cumulative distribution function; X axis is the PCV bin

## Investigation of the antenna PCV influence on RTK positioning

The receiver antenna PCV related functions in RTKLIB are extended to support azimuth- and elevation-dependent tabular PCVs, in order to investigate how much the receiver antenna PCV of such low-cost single-frequency antennas can influence the RTK positioning. When applying the PCV corrections, a two-dimensional linear interpolation is implemented to calculate the PCV values at a specific azimuth and elevation grid based on the PCV tabular values.

The difference between the kinematic positions processed by Bernese in previous chapters and the RTK positioning is, that the former one is estimated by a least squares adjustment, typical for post-processing, while the latter one is estimated by a Kalman filter for real-time processing.

### *Kinematic coordinates*

The computed kinematic positions with and without using the estimated rover antenna PCVs are plotted against the ground truths (the rover antenna MPC estimated during the PCV estimation using 4 sessions' data) in a topocentric coordinate system. The rate of integer ambiguity-fixed solutions is the same, 99.3%. The RMS and mean of the coordinate differences are summarized in Table 13. No improvement is seen in the East component and slight RMS reductions at sub-millimeters are seen in the North and Up components.

Table 13 RMS of kinematic position differences to the ground truth

DOY188	RMS (no PCV)	RMS (with PCV)	Improvement
E	4.8 mm	4.8 mm	0%
N	7.5 mm	6.8 mm	9.3%
U	16.4 mm	15.1 mm	7.9%

Table 14 Mean of kinematic position differences to the ground truth

DOY188	Mean (no PCV)	Mean (with PCV)	Difference
E	-0.4 mm	1.3 mm	-0.9 mm
N	-1.8 mm	-1.7 mm	-0.1 mm
U	-9.4 mm	-7.8 mm	-1.6 mm

The mean values of the kinematic position differences to the ground truth are listed in Table 14. Reduction of 1.6 mm in the Up component and 0.1 mm in the North component are seen. However, in the East component the mean value increases from -0.4 mm to 1.3 mm after applying the rover antenna PCV corrections.

The time series of the kinematic coordinates computed with and without rover antenna PCVs are plotted in Figure 80 and Figure 81. The differences between the two solutions are plotted in Figure 82. Even though applying the rover antenna PCV corrections does not improve the kinematic coordinates with respect to the ground truth, the difference between the two coordinates (with and without using the PCVs) are large. In the Up component the largest variation (from maximum to minimum) can reach 3.5 cm.

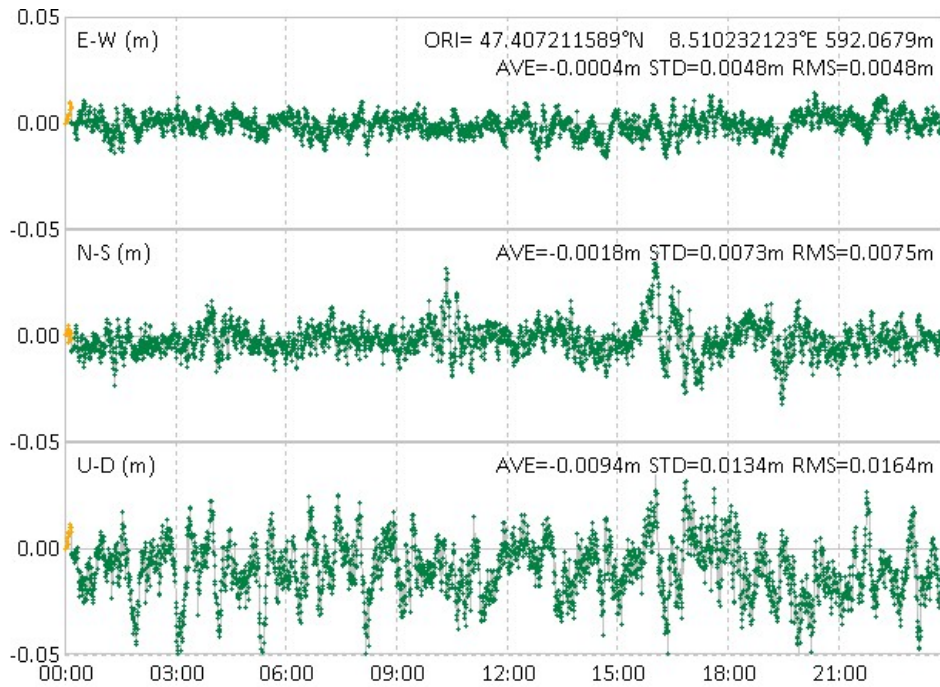


Figure 80 Differences of the kinematic positions (no PCV) to ground truth

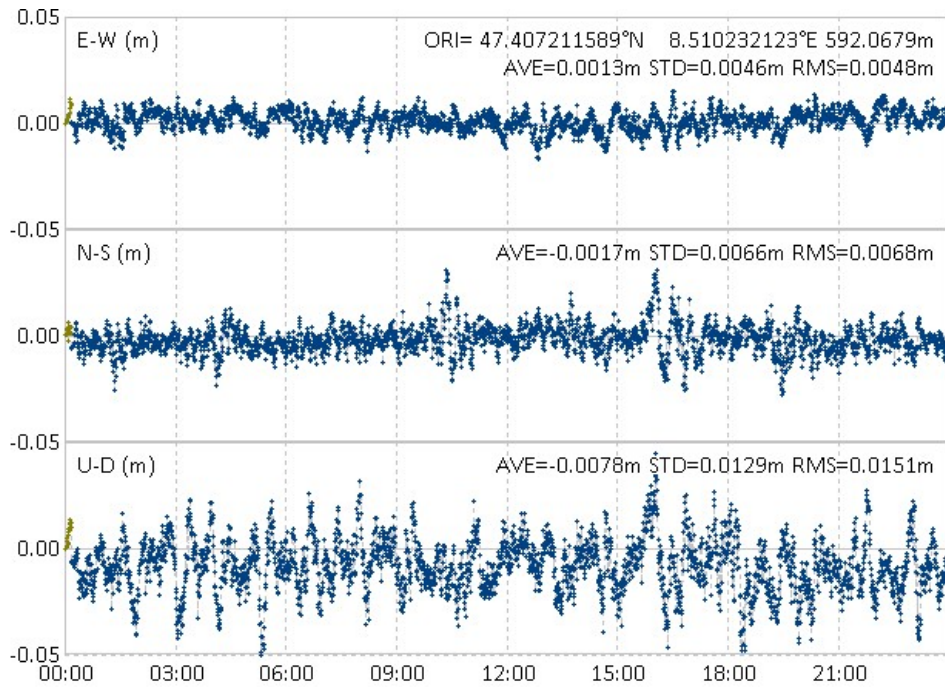


Figure 81 Differences of the kinematic positions (with PCV) to ground truth

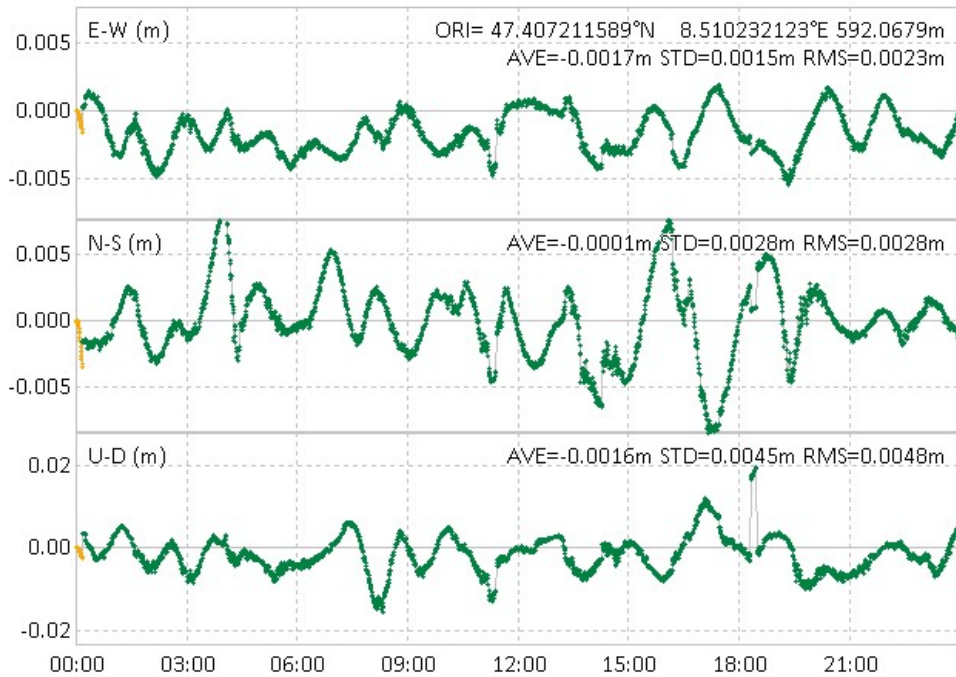


Figure 82 Differences between kinematic positions with and without using rover antenna PCV corrections

*Carrier-phase residuals*

The RMS values of the SD carrier phase residuals obtained by RTK processing with and without rover antenna PCV corrections are summarized in Figure 83. The mean RMS over all the satellites



reduces from 7.19 mm to 6.28 mm after applying the PCV corrections. The mean values of the SD carrier-phase residuals are summarized in Figure 84. The mean over the mean residuals of all satellites changes from -0.88 mm to -0.08 mm, which indicates a bias reduction because of taking the rover antenna PCVs into the RTK processing.

The largest RMS reductions are 3.16 mm from satellite G02 and 3.00 mm from satellite G07. Their time series are plotted in Figure 85 and Figure 86, where one can clearly see that the systematic trend in the SD carrier-phase residuals is removed to a large extent by the antenna PCV corrections. The mean changes from these two satellites are also those with the largest magnitude, which are 2.00 mm and 2.89 mm respectively. More plots of the SD carrier-phases are given in Appendix E.

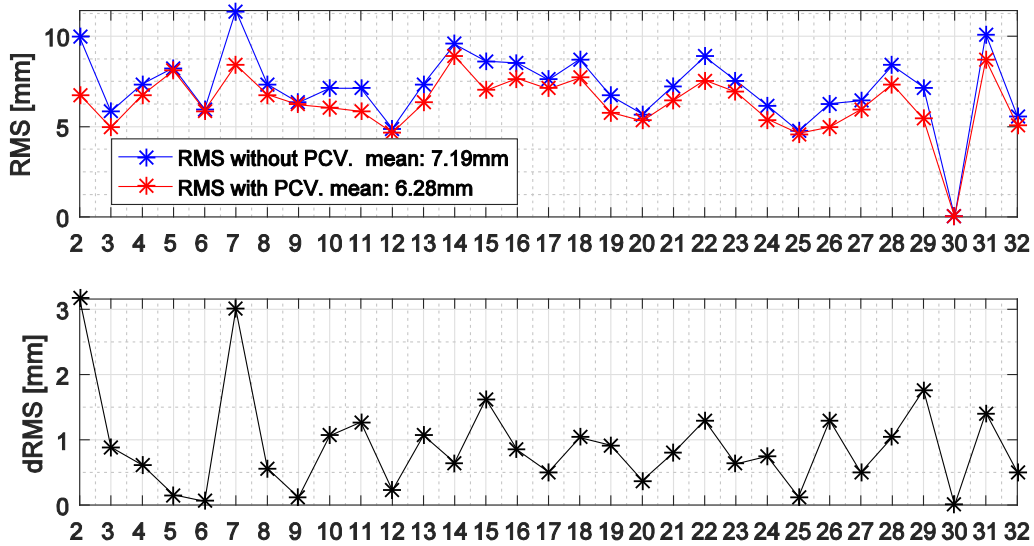


Figure 83 RMS (Top) and the RMS differences (Bottom) of SD carrier-phase residuals per satellite by RTK processing for DOY188



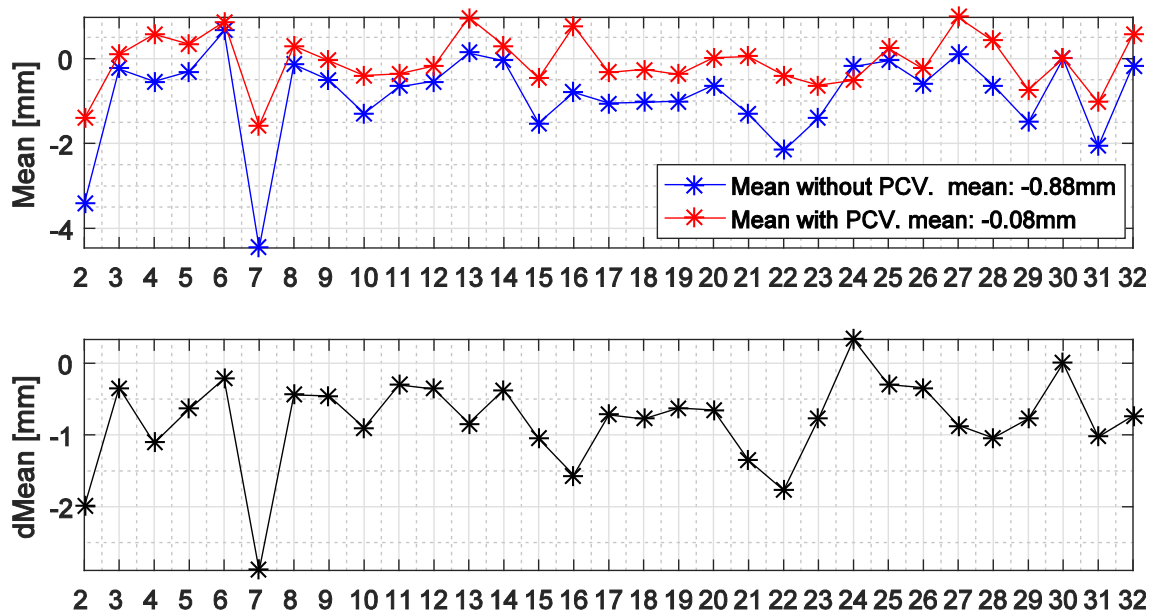


Figure 84 Mean (Top) and the Mean differences (Bottom) of SD carrier-phase residuals per satellite by RTK processing for DOY188

It has to be pointed out, that the satellite G30 has just two observations with only code measurements in the RTK processing. There were no carrier-phase measurements from the rover receiver. Thus, the zero RMS and zero Mean for satellite G30 does not indicate small residuals in carrier-phase but rather no measurements. Also for satellite 12, the code and carrier-phase measurements (whose SD residuals are larger than 100m) are excluded for the period from 11:12:30 to 11:15:00, which were detected as outliers by the Receiver Autonomous integrity Monitoring (RAIM) using code Single Point Positioning (SPP).

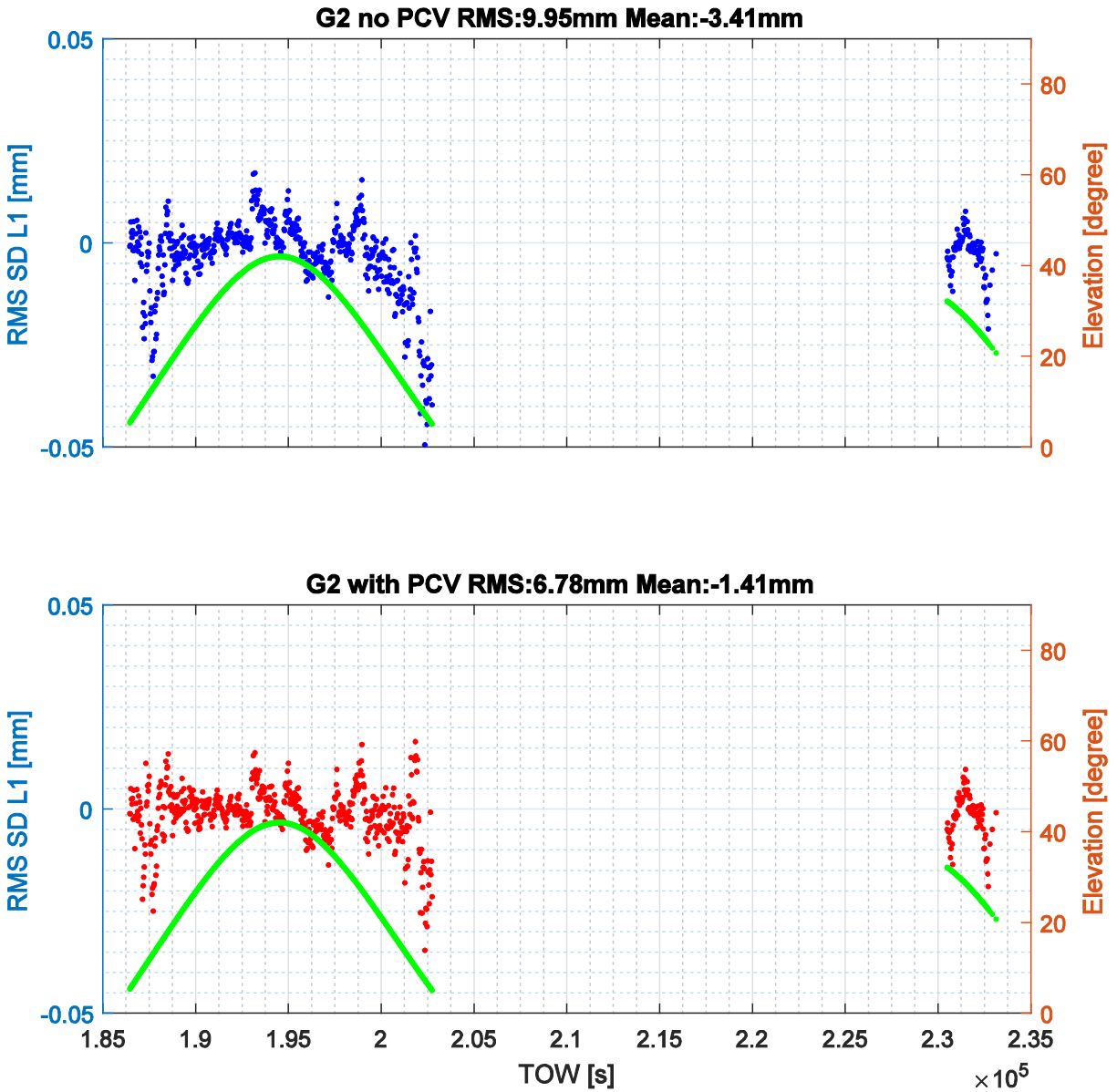


Figure 85 SD carrier-phase residuals by RTK processing of satellite G02 for DOY188

Please note that the SD carrier-phase residuals are converted from DD carrier phase residuals by assuming the reference satellite's SD carrier phase residuals to be zero.

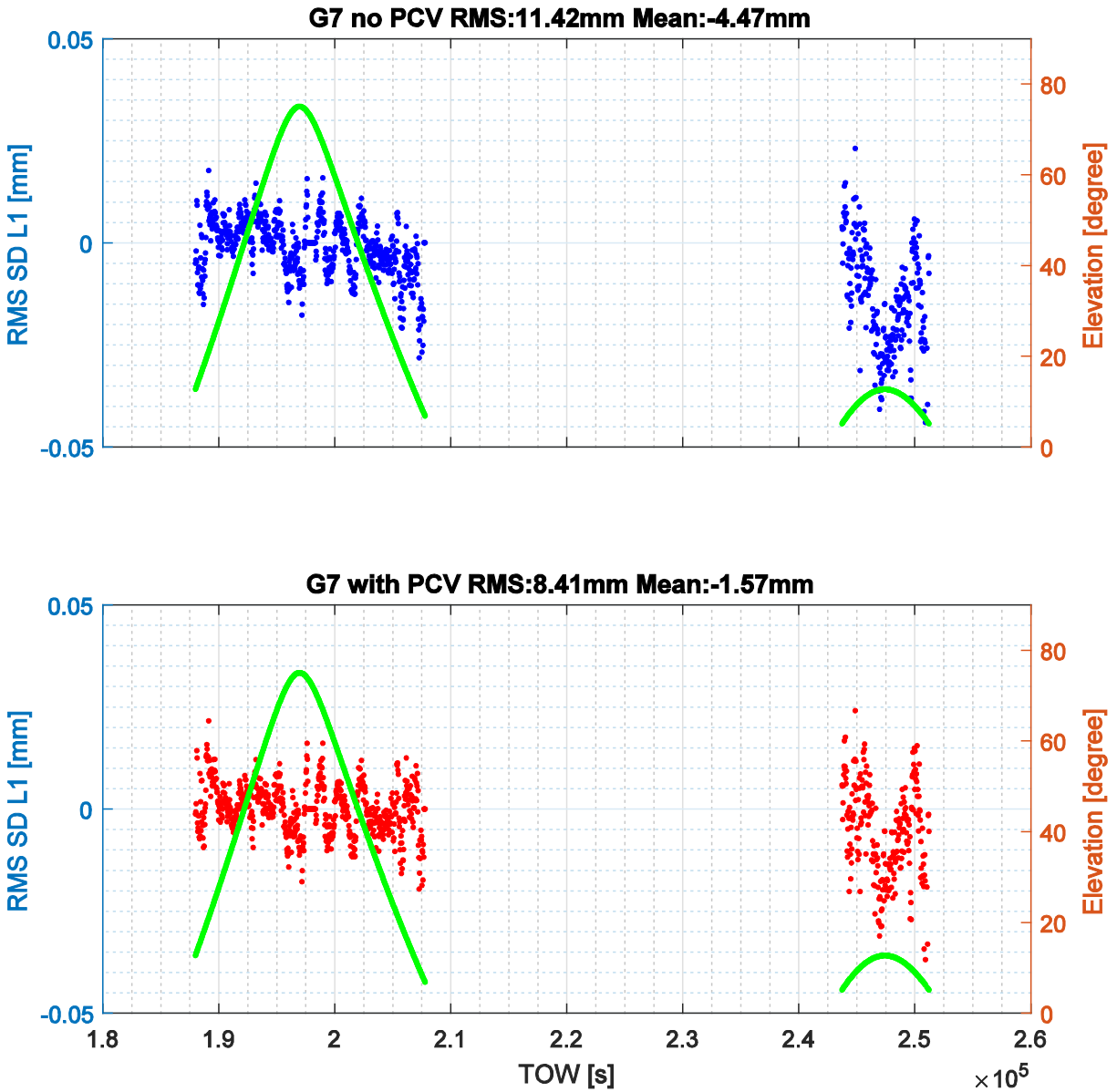


Figure 86 SD carrier-phase residuals by RTK processing of satellite G07 for DOY188

## 5.5 Conclusions

On one side, the estimated PCV for the Trimble Bullet III antenna is less than 1 cm and for most directions it is within  $\pm 6$  mm. Even though this amounts to 3 times the carrier phase noise level of the u-blox receiver, no significant improvement of the kinematic positions has been seen. On the other side, using the antenna PCV does reduce some systematic trends and biases/offsets in the SD carrier-phase residuals.

In a typical scenario of RTK application, the rover antenna is moving and may rotate. This makes it more difficult to apply the azimuth- and elevation-dependent PCV corrections to the rover antenna. Our analysis indicates that the Trimble Bullet III antenna's PCV is small enough that we

can ignore its influence on a short baseline RTK positioning application. Nevertheless, one can still benefit from applying the low-cost antenna PCV corrections for a reference station.

## Chapter 6 C/N<sub>0</sub>- and elevation-based observation weighting model

The realistic stochastic model (namely the covariance matrix) will directly affect the estimated parameters in a least squares and a Kalman filter. Moreover, the covariance matrices of the estimated parameters describing the precision of the estimators directly depend on the stochastic model of the observations (Amiri-Simkooei 2007).

### 6.1 Existing observation weighting approaches

The proper weighting of the observations, i.e., to use an optimal stochastic model in the GNSS data processing, is a key to improve the performance of GNSS positioning.

Recall that the stochastic model of the GNSS observations is defined in (2-16) as

$$P = \sigma_0^2 * Q_L^{-1}$$

where  $P$  is the weight matrix,  $\sigma_0^2$  is the variance of unit weight and  $Q_L$  is the co-variance matrix of the carrier phase observations at zero difference level. Thus, the variance  $\sigma_{L^i}^2$  of a zero differenced GNSS carrier phase of satellite  $i$ , is computed as

$$\sigma_{L^i}^2 = \frac{\sigma_0^2}{P_i} = \sigma_0^2 \cdot w_i \quad (6-1)$$

where  $P_i$  is the element  $i$  of the weight matrix  $P$ . Then the weight function  $w_i$  is defined as

$$w_i = \frac{1}{P_i} \quad (6-2)$$

Various studies on different weighting approaches have been conducted and these weighting functions can be categorized into 4 classes:

#### Class I, Equal weight

The weight matrix is an identity matrix with all diagonal elements to be 1:

$$w_i = 1 \quad (6-3)$$

#### Class II, Elevation based weighting

Elevation-based Weighting (EBW) approaches use, e.g., the cosecant of the satellite elevation angle proposed in (Collins and Langley 1999), which is derived from the Tropospheric Mapping Function (TMF), assuming the statistical variance of the GNSS signal noise is proportional to the squared value of the TMF (like  $1.001/\sqrt{0.002001 + \sin^2 e_l}$  proposed by (Black and Eisner 1984). In addition, the cosecant function is a first-order approximation to the TMF. Similar weighting

functions like the square of a cosecant of the elevation angle were evaluated in (Vermeer 1997) and it is implemented in the Bernese GPS software (Rothacher and Beutler, The role of GPS in the study of global change 1998):

$$w(el) = \frac{1}{\sin^2 el} \quad (6-4)$$

Even though in DD processing over short baselines the tropospheric errors cancel out, the induced noise remains in the measurements. Therefore, the use of a TMF-derived weighting function is justified.

(Euler and Goad 1991) applied an exponential weighting function to approximate the elevation dependent uncertainty in the code measurements:

$$w(el) = a_0 + a_1 e^{-\frac{el}{el_0}} \quad (6-5)$$

where  $a_0$  and  $a_1$  are empirical coefficients and  $el_0$  is a scale value for the elevation angle in degrees and  $el$  is the satellite elevation angle. They expected this function to model the increased uncertainty of the measurements at lower elevation, due to higher likelihood of encountering multipath and lower  $C/N_0$  values. In this paper, it was proven that comparing to equal weighting, using the proposed function significantly improves the precision of estimated wide-lane ambiguities, especially for measurements below 15° elevation angle.

### Class III, $C/N_0$ based weighting

$C/N_0$ -based weighting using formula (2-47) was also investigated by (Collins and Langley 1999) and they agreed in theory that it is potentially more powerful than the elevation-based approach. However, due to the limitation in the accuracy of  $C/N_0$  the receiver could measure by that time, their analysis suggested that the  $C/N_0$ -based weighting is almost numerically equivalent to the EBW approaches. However, (Brunner, Hartinger and Troyer 1999) and (Hartinger and Brunner 1999) have shown that the SIGMA- $\epsilon$  and SIGMA- $\Delta$  have good performances in mitigating the type II multipath error (mainly the diffraction signals). The SIGMA- $\epsilon$  is given as

$$w(C/N_0) = K \cdot 10^{-0.1 \cdot C/N_0} \quad (6-6)$$

where  $K$  is a scale factor related to the variance of the observations.

The SIGMA- $\Delta$  model is given as

$$w(C/N_0) = K \cdot 10^{-0.1 \left( \frac{C}{N_0} - \alpha \cdot \Delta \right)} \quad (6-7)$$

where  $K$  and  $\alpha$  are scale factors, and  $\Delta$  is computed from

$$\Delta = C/N_{0 \text{ template}} - C/N_0 \quad (6-8)$$

$C/N_0$  *template* is obtained by modeling the elevation-dependent  $C/N_0$  trend mostly due to the receiver antenna's gain/radiation pattern.

(Luo 2013) proposed another  $C/N_0$ -based weight function as

$$w(C/N_0) = [a + (1 - a) \cdot \left( \frac{C/N_0 - C/N_0^{min}}{C/N_0^{max} - C/N_0^{min}} \right)]^2 \quad (6-9)$$

where 0.1 is taken for coefficient  $a$  as the author suggested. It's called Luo model in later comparison.

#### Class IV, $C/N_0$ - and elevation-based weighting

This type of combination is given in (A. M. Herrera, et al. 2016) but without detailed explanationsd:

$$w(el, C/N_0) = \frac{1}{\sin^2 el} \cdot 10^{-\frac{(C/N_0 - s1)}{a}} \cdot \left( \left( \frac{A}{10^{-\frac{s0 - s1}{a}}} - 1 \right) \frac{C/N_0 - s1}{s0 - s1} + 1 \right) \quad (6-10)$$

And any  $C/N_0$  larger than the threshold  $s1$  is assigned with weight 1. The coefficients  $A = 30$ ,  $s0 = 10$ ,  $s1 = 50$  and  $a = 20$  suggested in the paper, are used in later comparison. We call it goGPS model in this thesis.

The four classes of weight functions are summarized in Table 15. Class I of equal weighting of all measurements is idea for independent measurements with white noise. Class II EBW, accounts for tropospheric error whereas, Class III  $C/N_0$ -based weighting function is intended to dilute the multipath-induced errors in the processing. EBW also partially accounts for the multipath, considering the fact that satellites of low elevation angles are more likely to be contaminated by multipath. Class IV is the weight function combining the dependence on elevation and  $C/N_0$ , with the expectation to model both tropospheric and multipath effects on the measurement uncertainties.

Table 15 Different weight functions

Weight function type	Noise	w
Class I	Equal weight	$I$

Class II	Tropospheric error	$w(el)$
Class III	Multipath	$w(C/N_0)$
Class IV	Trop. + Multipath	$w(el, C/N_0)$

---

## 6.2 Proposed mixed weighting function

A Mixed Weighting Function (MWF) is proposed in this thesis, where the weight function is defined as a multiplication of an elevation-dependent function and a  $C/N_0$ -dependent function:

$$w(el, C/N_0) = (a + b/\sin^2 el) \cdot 10^5 \cdot 10^{-0.1(\frac{C}{N_0} - G_r)} \quad (6-11)$$

where the  $G_r$  is the receiver antenna gain pattern. The argument for this MWF is that the elevation-based function accounts for the troposphere-induced noise (not the deterministic part of error, but the stochastic part of uncertainty) and the  $C/N_0$ -based function is expected to account for the multipath-induced uncertainties in the observations. The coefficients  $a$  and  $b$  take 0.5 as their value in this thesis. To avoid down weighting of good observations with high  $C/N_0$  values, any observation with  $C/N_0$  larger than 50 dBHz is assigned with the weight 1. Besides, a  $C/N_0$  mask is set at 34 dBHz to block the weak signals.

There are two assumptions behind the MWF. The first assumption is that code and carrier phase measurements have larger standard deviations at lower satellite elevation, reflected by the  $a + b/\sin^2 el$  term in the MWF formula. This assumption is proven correct by (Amiri-Simkooei and Tiberius 2007) where the author quantified the standard deviation of phase residuals in a short baseline for both original residuals and the one with multipath removed (by harmonic estimation). The results clearly showed that regardless of multipath effect, phase measurements (both L1 and L2) from low elevations have larger noises than those from high elevations. A compiled table for L1 carrier phase measurements is shown in following

Table 16.



Table 16 Estimated standard deviation of L1 phases in a short baseline for high-elevation and low-elevation satellites. Compiled from (Amiri-Simkooei and Tiberius 2007)

Receiver (Trimble)	Statistics : Standard Deviation [mm]			
	Low Elevation		High Elevation	
	Original	Multipath Removed	Original	Multipath Removed
<b>4000ssi</b>	1.31	0.72	0.83	0.44
<b>4700</b>	2.58	1.67	1.67	1.44
<b>R7</b>	4.44	2.64	2.09	1.63

The second assumption is that a lower  $C/N_0$  (after removing the contribution from receiver antenna gain  $G_r$ ) indicates a larger standard deviation for the code and phase measurements at the same observation epoch, reflected by the  $10^{-0.1(\frac{C}{N_0} - G_r)}$  term. This assumption is justified by all the previous studies on the relation between  $C/N_0$  and GNSS measurement qualities.

This MWF is used to weight the measurements from both the rover and the reference station in an RTK processing. Given the DD carrier phase measurements of one epoch:

$$[L_{rb}^{ij} \dots L_{rb}^{ik}]^T$$

The covariance matrix of these DD measurements writes as

$$\begin{bmatrix} (\sigma_r^i)^2 + (\sigma_b^i)^2 + (\sigma_r^j)^2 + (\sigma_b^j)^2 & \dots & (\sigma_r^i)^2 + (\sigma_b^i)^2 \\ \vdots & \ddots & \vdots \\ (\sigma_r^i)^2 + (\sigma_b^i)^2 & \dots & (\sigma_r^i)^2 + (\sigma_b^i)^2 + (\sigma_r^k)^2 + (\sigma_b^k)^2 \end{bmatrix} \quad (6-12)$$

where  $(\sigma_r^i)^2$  is the variance of the carrier-phase measurement of satellite  $i$  measured by rover receiver  $r$ ;  $b$  denotes the reference receiver; The variances of the DD measurements, in the diagonal of the covariance matrix, equal to the sum of the variances of all four measurements involved. The variance sum of the pivot/reference satellite (serving as the common satellite to form double differences) measured by the rover and the references station lies in the non-diagonal entries of the covariance matrix of the DD measurements. The covariance matrix for code measurements is scaled by the scale factor determined in Chapter 3.

The above determined covariance matrix is used as  $Q$  in a LSA:

$$\hat{X} = (A^T Q^{-1} A)^{-1} A^T Q^{-1} Y$$

or as  $R$ , the measurement noise model, in a Kalman filter:

$$K = PH(H^T PH + R)^{-1}$$

where  $K$  is the Kalman gain,  $P$  is the covariance matrix of the state vector and  $H$  is the matrix of partial derivatives connecting the state vector to the measurements.

### 6.3 Comparing different weighting approaches

To compare how the different weighting approaches improve the results, the satellite elevations and  $C/N_0$  values of satellite G27 measured by the u-blox 5T receiver module in the ZB test are used as input to the different weighting functions. And the corresponding sigma (standard deviation or square root of the variance) is computed as

$$\sigma = \sigma_0 \cdot \sqrt{w(e\ell, C/N_0)} \quad (6-13)$$

where  $\sigma_0 = 0.00021\text{m}$  is the standard deviation of unit weight for carrier-phase measurements derived in Chapter 3.

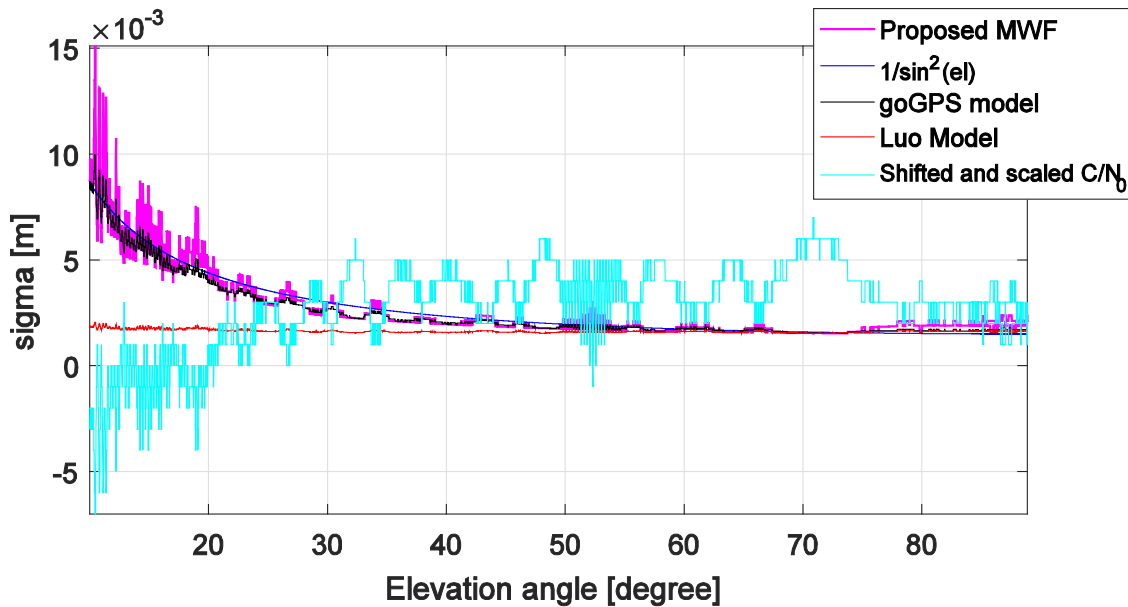


Figure 87 Comparing the proposed MWF to the elevation-based model, the goGPS model, and Luo Model

In Figure 87, the sigma computed by (6-13) is plotted in vertical axis for the different weighting model with the elevation angles as the horizontal axis. The proposed MWF is compared to the EBW, the goGPS model and the Luo model. A good weighting model is expected to satisfy the following two aspects:

- Giving higher weights (thus smaller sigma) to the measurements at high elevations and lower weight at low elevations
- Giving higher weights (thus smaller sigma) to the measurements with high  $C/N_0$  values (antenna gain pattern effect compensated) and lower weight for measurements with low  $C/N_0$

Figure 87 and the zoom in to the Luo model in Figure 88 show that the Luo model does interact with the  $C/N_0$  variations but does not account the elevation change in the measurements. Thus the measurements at low elevations are overweighed (given too much weight).

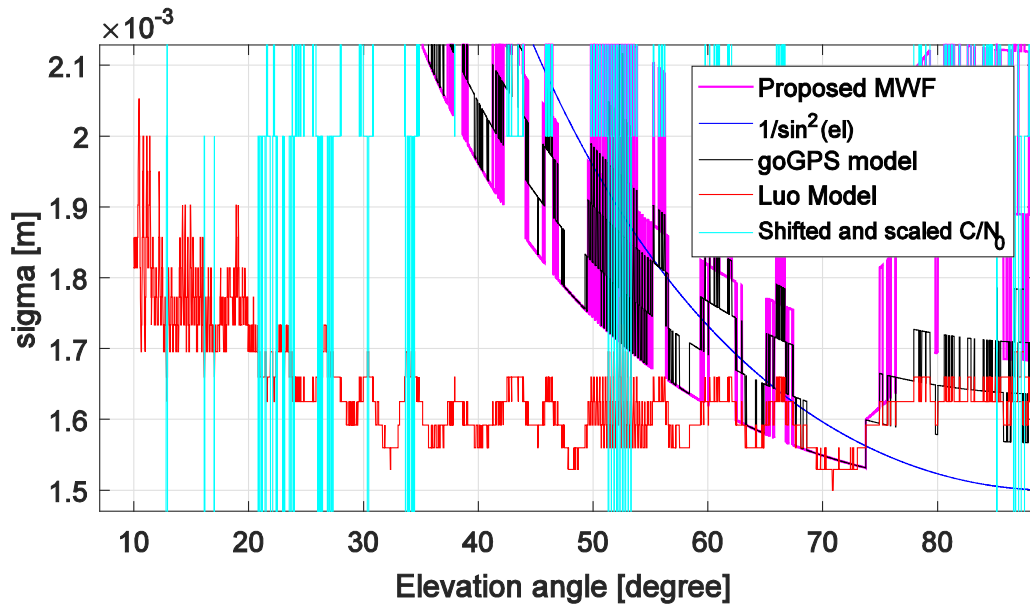


Figure 88 Zoom into the Luo Model

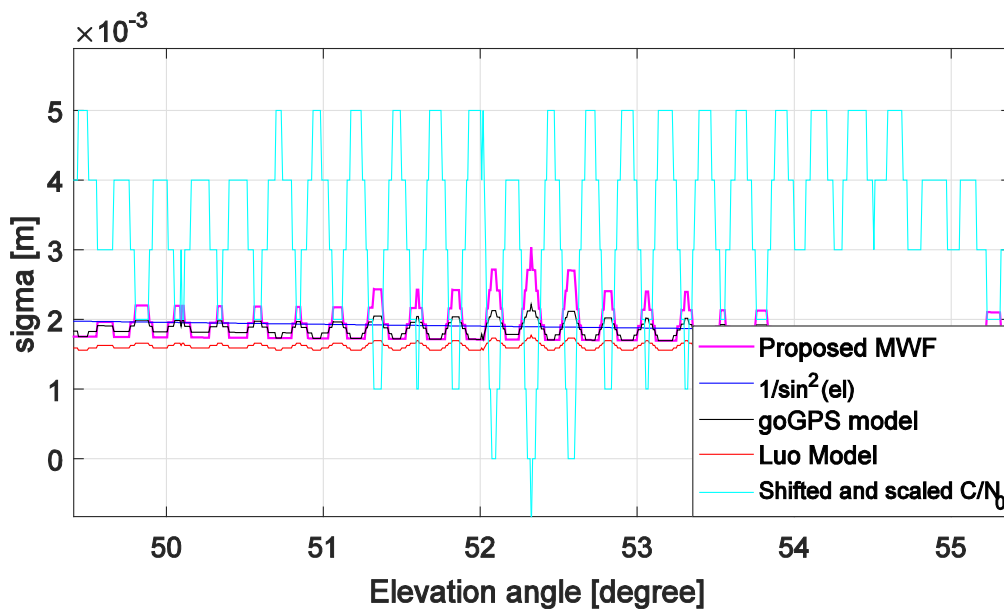


Figure 89 Zoom into elevation-based weighting

The elevation-based weighting model does not account for the  $C/N_0$  variations at all. One can see in Figure 89 that a strong oscillation exists in the  $C/N_0$  values at elevation  $50^\circ$  to  $55^\circ$ , except for the EBW model, the rest (the MWF, the goGPS model and the Luo model) all account for this oscillation and adjust their given weights accordingly but with different scale. The goGPS model shows similar performance as the proposed MWF model, but the latter one better accounts for the  $C/N_0$  variations. This is seen from the larger scale of changes in the computed sigma with respect to multipath indicated by the  $C/N_0$  oscillations.

Then the proposed MWF is compared to the SIGMA- $\epsilon$  and SIGMA- $\Delta$  models in Figure 90. The SIGMA- $\Delta$  underweights the measurements in the low elevation as one see the most left side of the graph, which makes these measurements almost useless in the processing.

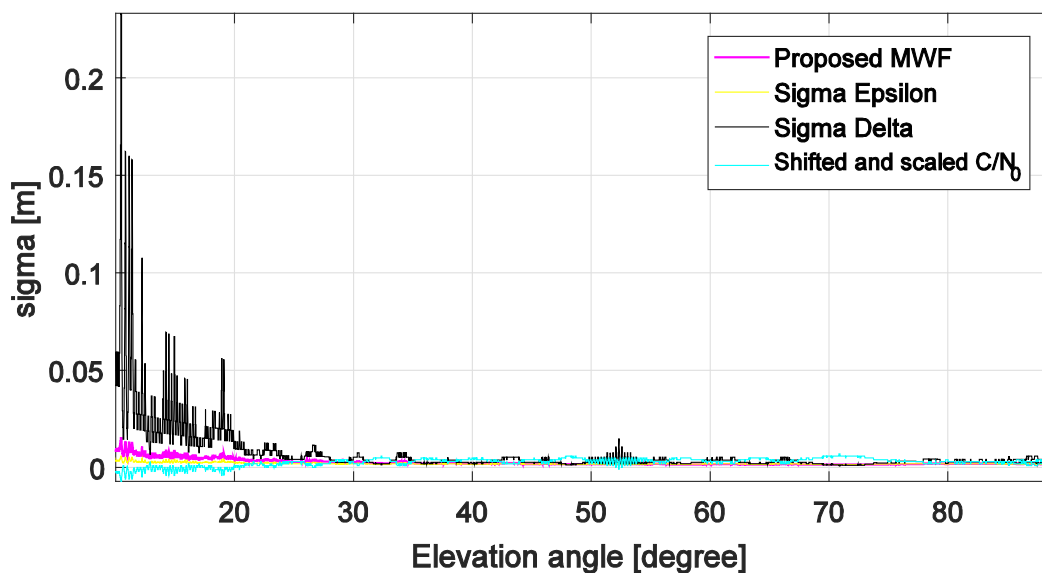


Figure 90 Comparing the proposed MWF to Sigma Epsilon and Sigma Delta

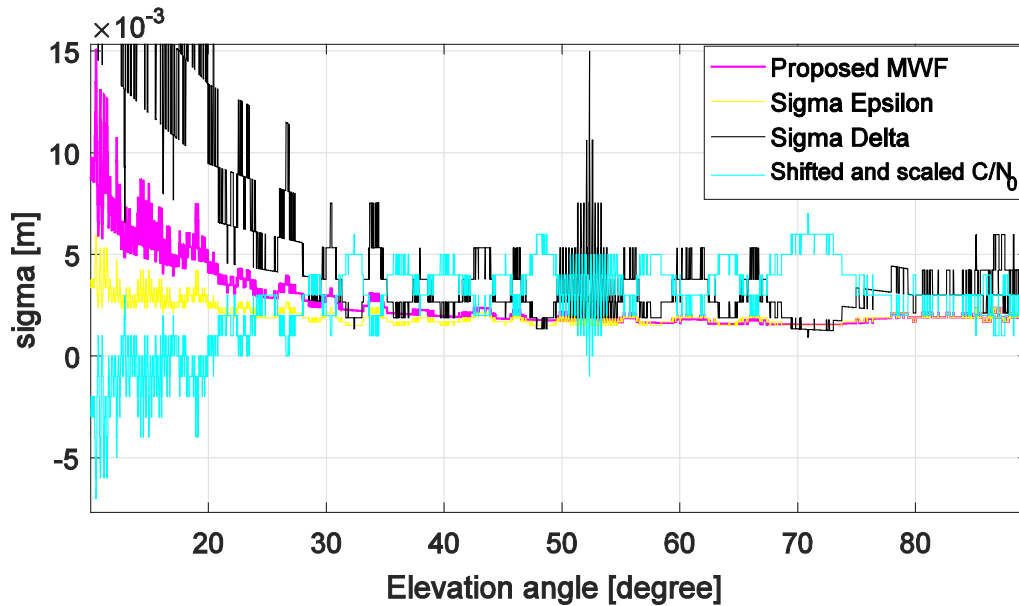


Figure 91 Zoom in to Sigma Epsilon and MWF Model

In Figure 91, the graph is zoomed in to see more details on the MWF and Sigma Epsilon Model. The Sigma- $\epsilon$  weights the measurements similarly to the MWF in the high elevation part (above 45°) but gives higher weight (thus smaller computed sigma) in the low elevation part.

#### 6.4 Benefits of applying MWF in RTK positioning

A 3.8 km baseline between the station RG01 (treated as a rover) and RD01 (treated as a reference) from the X-Sense project is processed by applying the MWF and a traditional EBW with the weight function  $0.5+0.5/\sin^2(e)$ . The computed kinematic positions of the rover station RG01 are compared to the true positions. A 5-degree elevation mask and a 35 dBHz  $C/N_0$  mask are used to exclude measurements with potentially higher noises for the RTK processing shown in Figure 92.

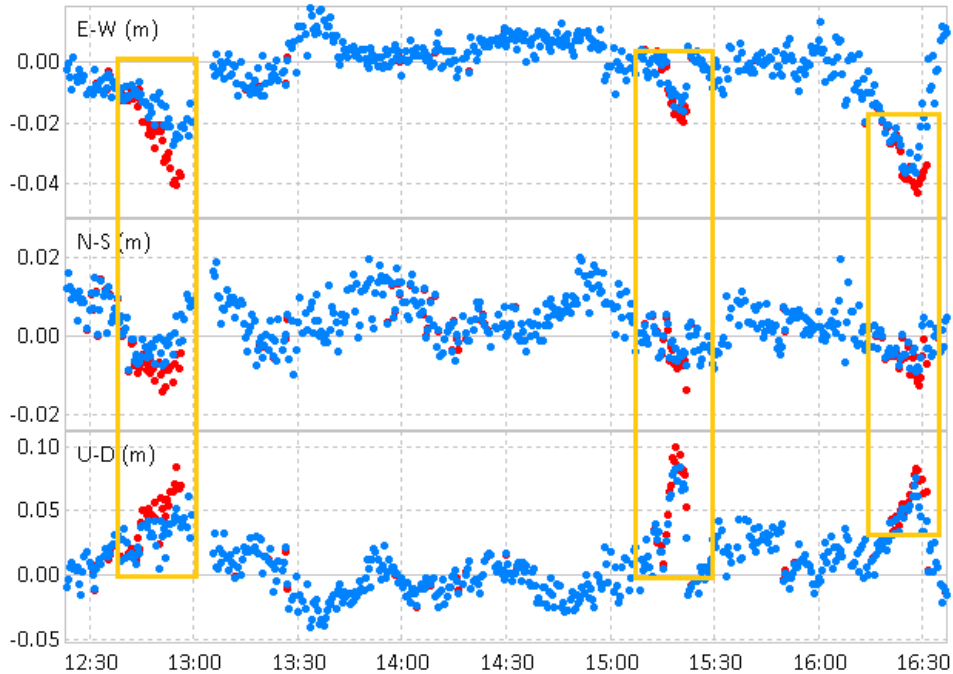


Figure 92 Differences of the kinematic positions against the true positions; Red points – Positions computed with EBW to the true positions; Blue points – Positions computed with MWF (only fixed solutions are plotted here)

Figure 92 shows, in the three areas marked by orange rectangles, that the deviations of the computed fixed positions from the true position are significantly reduced after applying the MWF. The maximum deviation in the three marked areas are summarized in Table 17 for the kinematic positions computed with the EBW and with the proposed MWF. Up to 1.7 cm reduction in the position deviations is seen in the Up coordinate component in the second marked area. The rate of ambiguity fixed solutions (using LAMBDA method, with 4 as the threshold value for ratio test (Verhagen and Li 2012)) increases slightly from 98.1% to 98.3% after applying the MWF.

Table 17 Maximum deviation of the kinematic positions from the true position

Maximum Deviation	East		North		Up	
	EBW	MWF	EBW	MWF	EBW	MWF
Marked area I	4.0cm	2.7cm	1.4cm	0.9cm	8.0cm	6.0cm
Marked area II	1.9cm	1.6cm	1.4cm	0.8cm	10cm	8.3cm
Marked area III	4.3cm	3.6cm	1.3cm	0.9cm	8.3cm	7.6cm

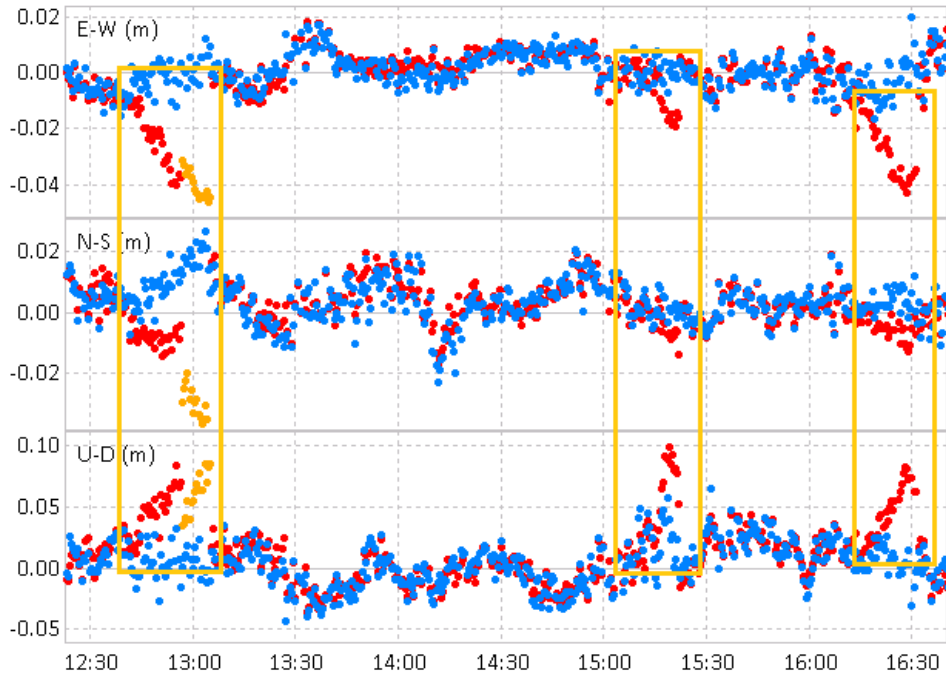


Figure 93 Differences of the kinematic positions against the true positions (computed with 15 degree elevation mask) ; red points – positions computed with EBW to the true positions; blue points – Positions computed with MWF; orange points – the float solutions with EBW

When the elevation mask is increased to 15 degrees, as usually recommended for RTK GNSS surveying (see (Sickle 2015) and (Donahue, Wentzel and Berg July 2013)), the improvement in the accuracy of the computed kinematic positions by using MWF is even more prominent as shown in Figure 93. The rate of ambiguity-fixed solution increases slightly from 95.5% to 95.6%. However, one can see that the carrier-phase ambiguities, which could not be fixed when using the EBW (shown as orange points), are successfully fixed to integers and produce more accurate fixed solutions (shown as blue points). The maximum deviation in the kinematic positions are dramatically reduced after applying the MWF (see Table 18). Up to 4.4 cm reduction is seen in the Up component.

Table 18 Maximum deviation of the kinematic positions from the true position (15-degree elevation mask)

Maximum Deviation	East		North		Up	
	EBW	MWF	EBW	MWF	EBW	MWF
Marked area I	4.6cm	1.6cm	4.4cm	2.7cm	8.6cm	3.5cm
Marked area II	1.9cm	1.3cm	1.4cm	0.8cm	10cm	6.5cm
Marked area III	4.3cm	1.6cm	1.3cm	1.1cm	8.3cm	3.9cm

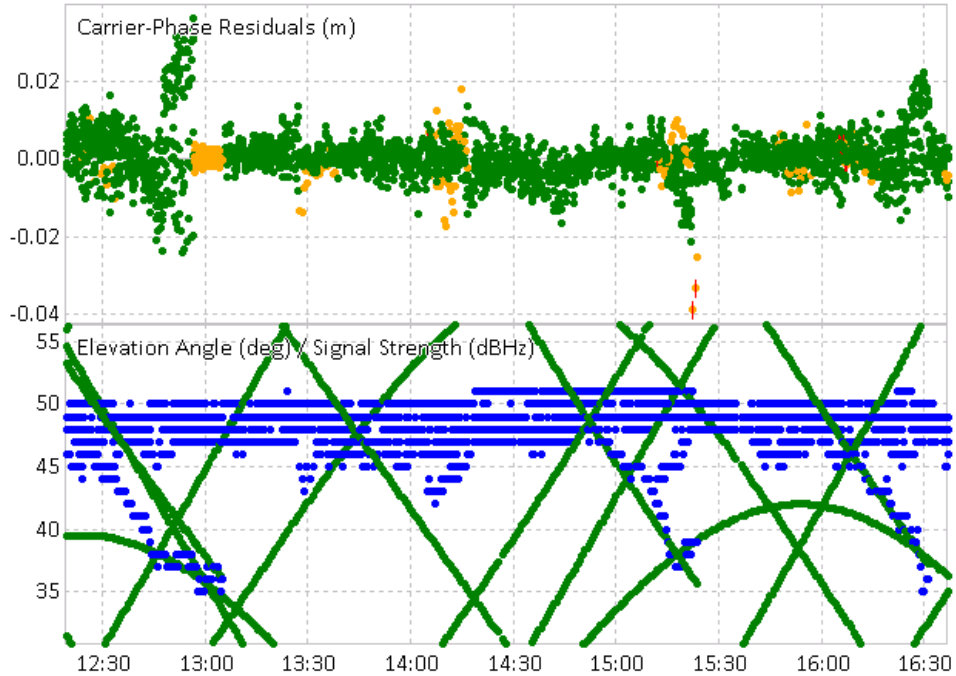


Figure 94 SD carrier-phase residuals (when using EBW)

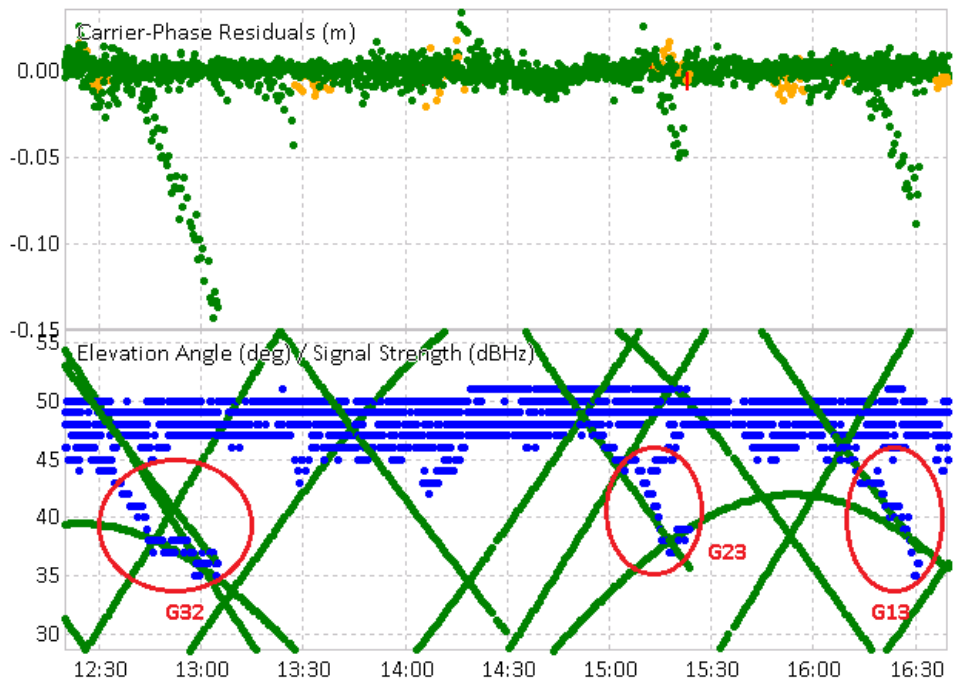


Figure 95 SD carrier-phase residuals (when using MWF)

The plot of the SD carrier-phase residuals along with the elevation angle and the  $C/N_0$  values in Figure 94 and Figure 95 explains what happens in the three marked areas: the typical multipath type II exists in the observations of the satellites G32, G23 and G13. The EBW could not identify nor mitigate the multipath errors in the carrier-phase measurements, thus the errors are



absorbed by all the computed SD residuals as seen in Figure 94. In contrast, the proposed MWF has successfully detected these type II multipath errors and down-weighted the contaminated measurements. Thus the SD residuals of the multipath contaminated carrier-phase measurements are much bigger than those of the clean measurements as seen in Figure 95.

## Chapter 7 RTK positioning with Dual GNSS constellations

As more satellites from new GNSS, like the Chinese BeiDou and the European Galileo, are becoming available for navigation and positioning, a joint multi-constellation GNSS positioning is an obvious trend given the benefits of increased satellite dilution of precision, increased availability and reliability.

### 7.1 GPS+BeiDou

It is difficult to see the improvement in kinematic positioning accuracy brought by adding the BeiDou system for a static station with open sky, because the RTK positioning with GPS only provides already sufficiently high accuracy at the centimeter level and the number of the GPS satellites is still much higher than that of other systems that are working towards completion of their full constellations. Nevertheless, RTK positioning with additional constellations does increase the reliability of the centimeter-level accurate positions in terms of increasing the integer ambiguity fixing rate. To show this benefit, the RTK solution processed with the single-epoch ambiguity fixing strategy is presented here with two data sets: one collected in Switzerland on the roof of HPV building by Javad SIGM3 receivers and Javad GRNT-G3T antennas; the other collected in Xian China by Trimble NETR9 receivers and TRM57971 antennas. Single-epoch ambiguity fixing strategy forces the RTK processing to do instantaneous ambiguity fixing with only the observations of the current epoch.

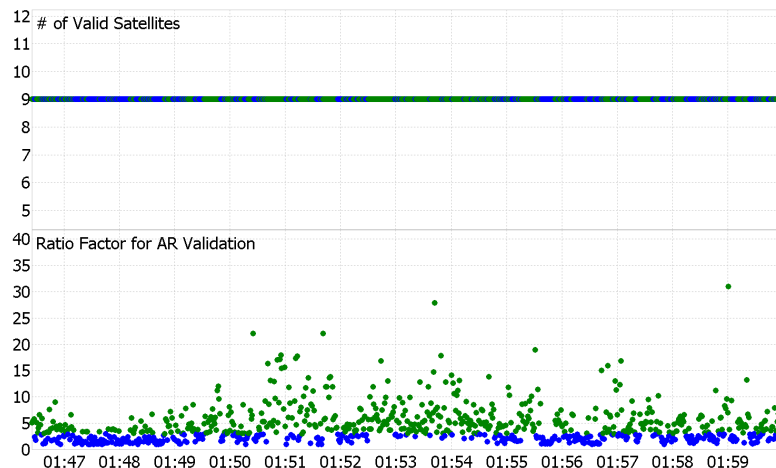


Figure 96 GPS only ratio of fixed solutions: 59.3%; HPV roof; 17/04/2014

Figure 96 shows that with GPS only, the number of valid satellites is 9 and the ratio of fixed solutions is only 59.3% in the overall solutions processed with Single-epoch ambiguity fixing strategy. By adding the BeiDou constellation into the processing, the number of valid satellites is increased from 9 to 11 in that data set, and the ratio of fixed solutions increases to 72.8% (see

Figure 97). Besides, the ratio factor for Ambiguity Resolution (AR) validation (see F-ratio test in (Wang, Stewart and Tsakiri 2000) or (Teunissen 1993) has most values below 5 when using only GPS. After using additional satellites from BeiDou system, the ratio factor for AR validation has more values above 5. A higher ratio factor indicates a higher confidence in a correct ambiguity-fixing.

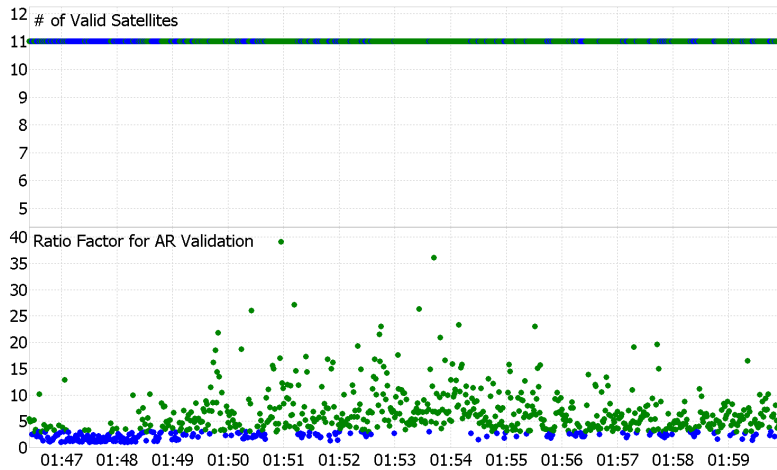


Figure 97 GPS+BDS ratio of fixed solutions: 72.8%; HPV roof; 17/04/2014

For the second data set collected in Xian China, the number of valid satellites is significantly increased because of good converge with the BeiDou system in Asia. The ratio of fixed solutions increases from 74% with GPS only to 97.8% with GPS+BeiDou (see Figure 98 and Figure 99).

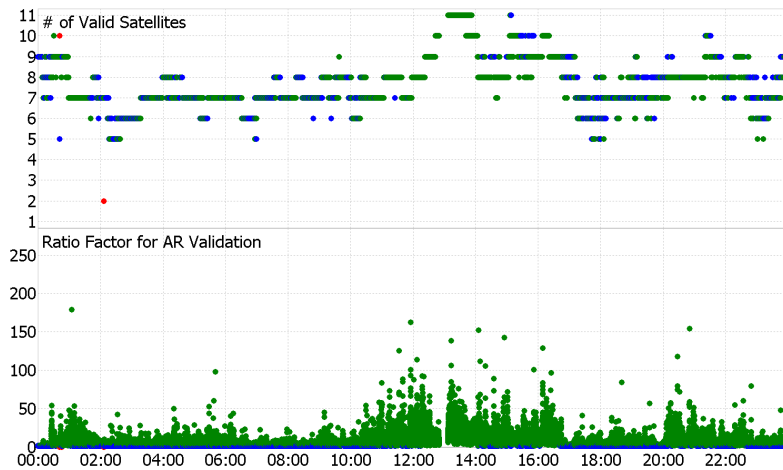


Figure 98 GPS Only, ratio of fixed solutions: 74.0%, XIAN-CHINA; 18/03/2014

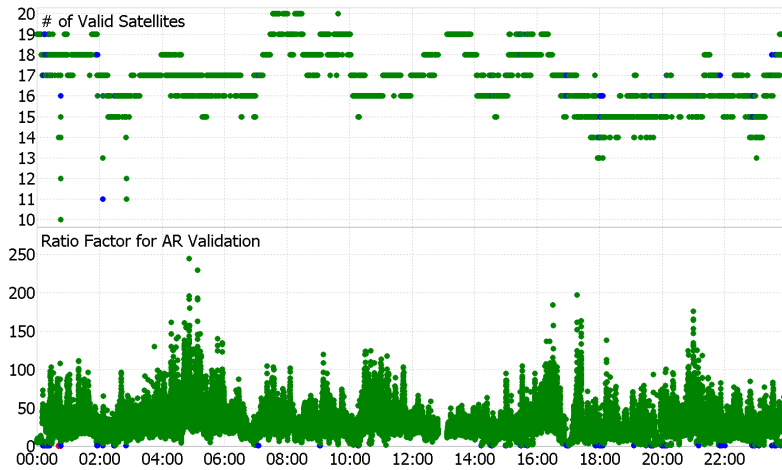


Figure 99 BDS+GPS, ratio of fixed solutions: 97.8%; XIAN-CHINA ;18/03/2014

Besides the increased ratio of fixed solutions, the accuracy of the kinematic coordinates computed with the single-epoch ambiguity fixing strategy is also significantly improved after adding BeiDou into the processing for the data set collected in Xian. Using GPS only, the kinematic positions can differ from the real positions by up to 3 meters in East and North, and up to 5 meters in the Up component (see Figure 100). After adding BeiDou into the processing, the deviations are at centimeter level as one can see in Figure 101.

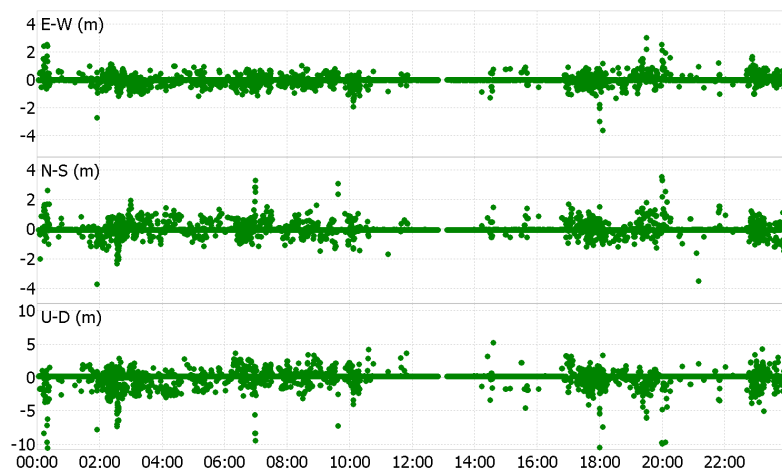


Figure 100 Deviation from the real positions; GPS only; XIAN

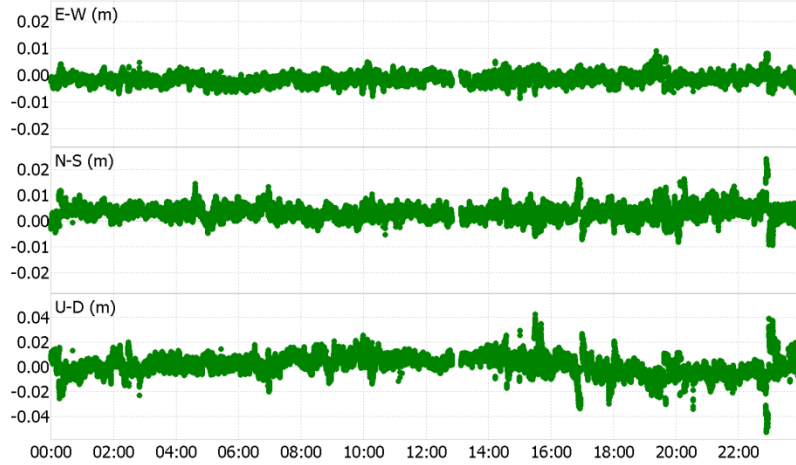


Figure 101 Deviation from the real positions; BDS+GPS; XIAN

## 7.2 GPS+GLONASS

The advantage of using GLONASS as a second system is the larger number of valid satellites currently visible in Europe comparing to BeiDou or Galileo. As the BeiDou and Galileo systems are completing their full constellations, the situation will soon change. The number of satellites increases from 10, when using only GPS, to 17 after adding GLONASS to the data set used in this chapter.

The disadvantage of adding GLONASS to the RTK processing is that one has to handle two additional issues: an additional SD reference ambiguity term (beside the usual DD ambiguity term) and the Inter-Frequency Biases (IFB) (Takac 2009). Both are due to the Frequency Division Multi Access based signal structure of GLONASS.

### The additional SD reference ambiguity term

According to (GLONASS-ICD 1998), the nominal values of the GLONASS L1 carrier frequencies are defined as

$$f_{k_{L_1}} = f_{0_{L_1}} + k\Delta f_{L_1} \quad (7-1)$$

where  $k = -7, \dots, 6$  is the frequency number;  $f_{0_{L_1}} = 1602$  MHz is the GLONASS L1 frequency;  $\Delta f_{L_1} = 562.5$  kHz is the frequency separation for the L1 sub-bands.

Therefore, the DD carrier-phase observation equation of two GLONASS satellites  $p$  and  $q$  reads:

$$L_{rb}^{pq} = \rho_{rb}^{pq} + (\lambda^p n_{rb}^p - \lambda^q n_{rb}^q) + e_{ifb}^{pq} + \epsilon \quad (7-2)$$

where  $r$  and  $b$  stand for rover and base receivers;  $L_{rb}^{pq}$  is the DD carrier-phase measurements between two satellites and two receivers;  $\rho_{rb}^{pq}$  is the DD geometric distance;  $e_{ifb}^{pq}$  is the DD

inter-frequency bias;  $\epsilon$  denotes the remaining errors.  $\lambda^p$  and  $\lambda^q$  are the wavelengths of satellite  $p$  and  $q$ , respectively.

The wavelengths of two satellites are not equal as

$$\begin{aligned}\lambda^p &= \frac{c}{f_{pL1}} = \frac{c}{(f_{0L1} + p\Delta f_{L1})} \\ \lambda^q &= \frac{c}{f_{qL1}} = \frac{c}{(f_{0L1} + q\Delta f_{L1})}\end{aligned}\quad (7-3)$$

where  $c$  is the speed of light.

Assuming that satellite  $p$  has the highest elevation angle, it is used as reference satellite to form double differences. One has

$$\lambda^p = \lambda^q + (k^p - k^q) \cdot \Delta f_{L1} \quad (7-4)$$

Formula (7-2) then develops into

$$\begin{aligned}L_{rb}^{pq} &= \rho_{rb}^{pq} + \lambda^q \cdot (n_{rb}^p - n_{rb}^q) + (k^p - k^q) \cdot \Delta f_{L1} \cdot n_{rb}^p + e_{ifb}^{pq} + \epsilon \\ &= \rho_{rb}^{pq} + \lambda^q n_{rb}^{pq} + \Delta \lambda^{pq} \cdot n_{rb}^p + e_{ifb}^{pq} + \epsilon\end{aligned}\quad (7-5)$$

Formula (7-5) shows clearly that apart from the usual DD ambiguity term  $n_{rb}^{pq}$  there is an additional SD ambiguity term of the reference satellite  $n_{rb}^p$  that has to be solved along with other unknown parameters. However, for SD-based RTK processing, like in the case of RTKLIB, the ambiguities are stored internally as SD ambiguities per satellite, so that this is not a big issue.

### The inter-frequency biases

The second issue, the IFB, that can reach up to several decimeters, is the real problem when using the GLONASS system for positioning purposes. (Wanninger 2012) shows that the IFB can be modeled as a linear function of the frequencies and is stable over time for the geodetic-grade receivers.

(Sleewaegen, et al. 2012) has well explained that the inter-frequency bias  $e_{ifb}$  consists of a dominating part, the Digital Signal Processing (DSP) induced code-phase bias, and a minor part induced by the analog RF filter at the millimeter-level. Ignoring the minor part, the IFB of satellite  $p$  reads

$$e_{ifb}^p = \delta t_{CP} \cdot \Delta f_{L1} \cdot k^p \quad (7-6)$$

where  $\delta t_{CP}$  is the aggregated code-phase bias, which can be computed from

$$\delta t_{CP} = \delta t_C - \delta t_P - \delta t_{PPS} \quad (7-7)$$

The  $\delta t_C$  is the delay between the code generator and the correlator in the tracking channel of a GNSS receiver and  $\delta t_P$  is the delay between the phase generator and the correlator. The  $\delta t_{PPS}$

denotes the offset time to the pulse-per-second strobe. These values are known by the GNSS receiver manufacturers from their firmware parameters. This means that corrections can be applied directly to the carrier-phase, or indirectly to the code measurements, e.g., the u-blox M8P and M8T modules have internally compensated the GLONASS inter-frequency channel delays in the code pseudorange measurement already (u-blox AG 2014).

### **GPS+GLONASS RTK**

To further explore the benefits of using additional GNSS constellations besides GPS, a kinematic track was measured with an u-blox M8P rover and reference pair. The rover was mounted on a bike and travelled along the route shown in Figure 102. Besides the onboard RTK solution by the u-blox M8P receiver, the raw GNSS data from both, the rover and the reference were logged and streamed to parallel running RKT processing engines. To exclude the influence due to wireless communication losses, the logged raw data were processed, but with exactly the same configuration and processing strategy as in the RTK processing model. The processed kinematic solution using GPS only, GPS + GLONASS (GLONASS ambiguities kept float) and GPS + GLONASS (both ambiguities fixed) are presented. In the processing with GPS + GLONASS (GLONASS ambiguities kept float), only the GPS carrier phase ambiguities were fixed and the GLONASS carrier phase ambiguities kept as float values. At the end, the onboard RTK solution by u-blox M8P is also presented. One should not directly compare the overall performance of the onboard RTK solution to the post-processed RTK solution due to the effects of wireless communication losses. Luckily, the most interesting part of the track, along the path beside the forest where heavy multipath errors exist and some satellites are blocked (due to the 20 meters tall trees), had no problems with the data communication between rover and receiver. Thus, the comparison of the u-blox M8P onboard solution using GPS and GLONASS (GLONASS ambiguities kept float) to other solution is meaningful. Moreover, the post-processed GPS+GLONASS (GLONASS ambiguities kept float) shall represent the best performance the u-blox M8P onboard solution can achieve.





Figure 102 The bike route measured by the RTK positioning using GPS + GLONASS (both ambiguities fixed)

The ground track (horizontal components of the kinematic coordinates plotted in local north and east) of all 4 solutions are plotted in Figure 103 to Figure 106, where green points stand for the ambiguity-fixed solutions and the yellow points are float solutions.

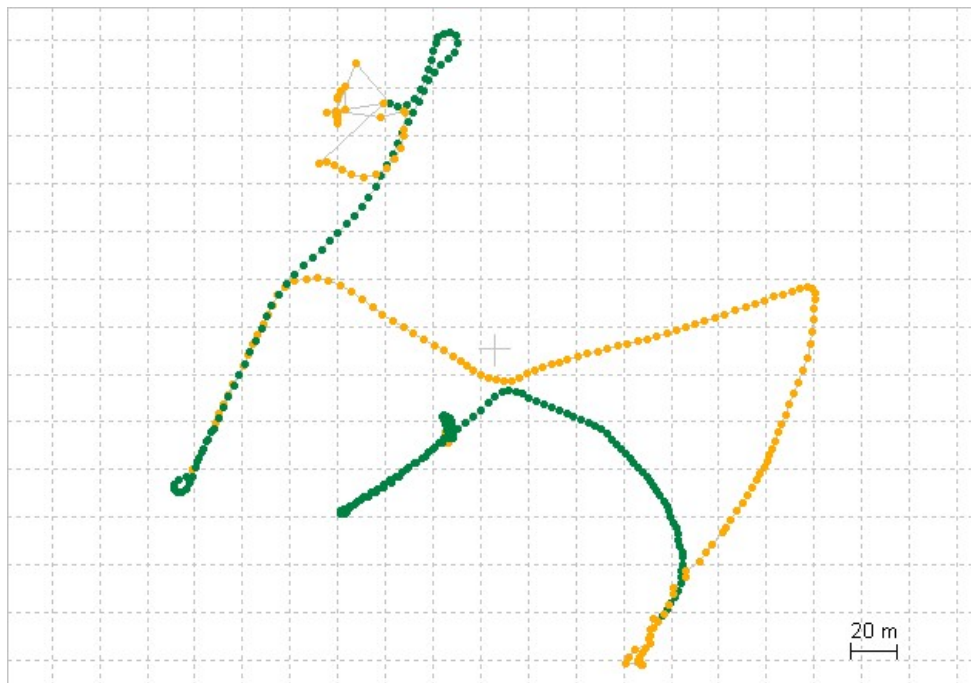




Figure 103 GPS only RTK solution (Horizontal components; Green – Ambiguity-fixed solutions; Yellow – Float solutions)

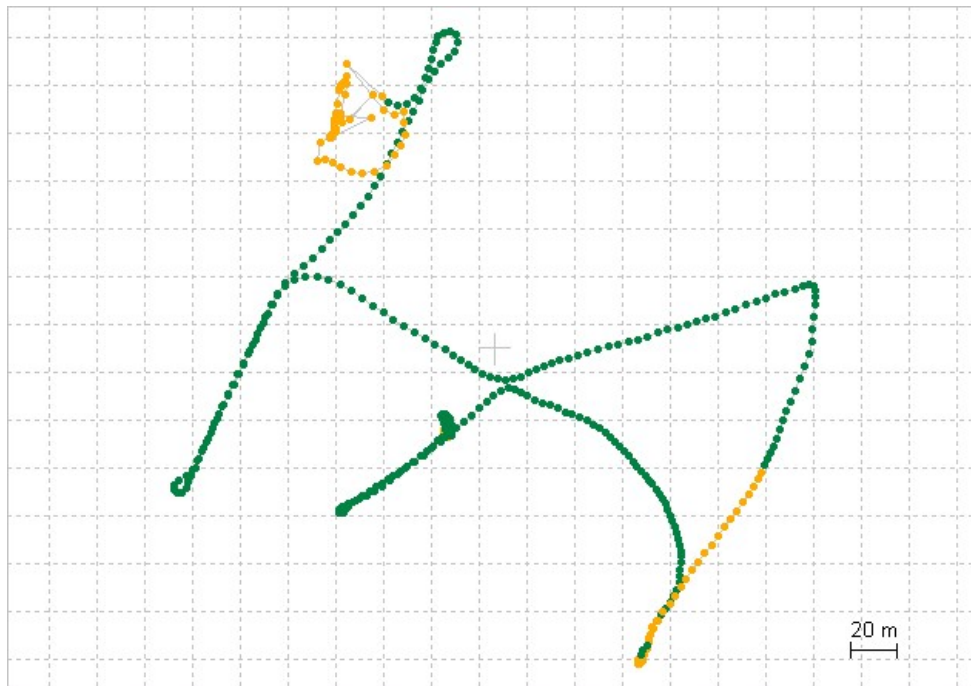


Figure 104 GPS + GLONASS (GLNOASS ambiguities kept float) RTK solution (Horizontal components; Green – Ambiguity-fixed solutions; Yellow – Float solutions)

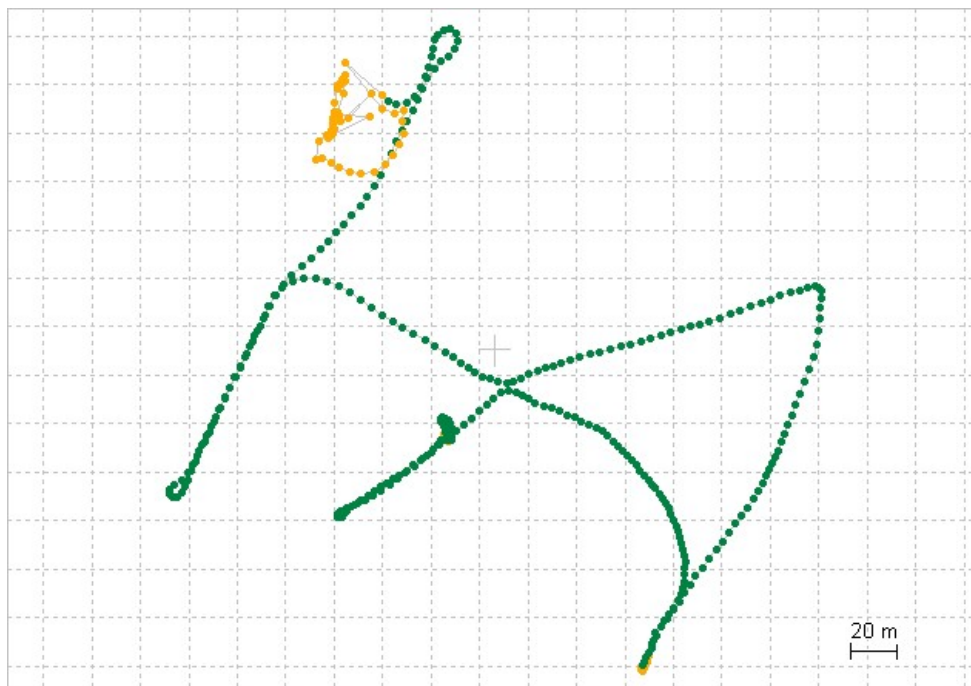


Figure 105 GPS + GLONASS (both ambiguities fixed) solution (Horizontal components; Green – Ambiguity-fixed solutions; Yellow – Float solutions)

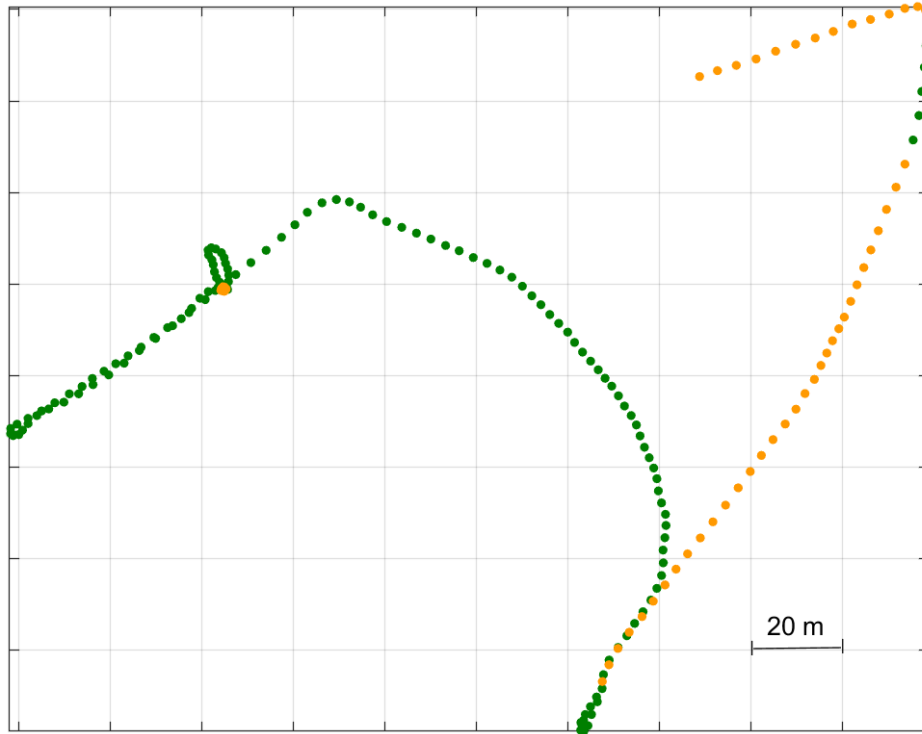


Figure 106 u-blox M8P (firmware 3.01HPG 1.11) onboard solution (Horizontal components; Green – Ambiguity-fixed solutions; Yellow – Float solutions)

The ratios of the fixed solutions to the total number of solutions in each data set are summarized in Figure 107.

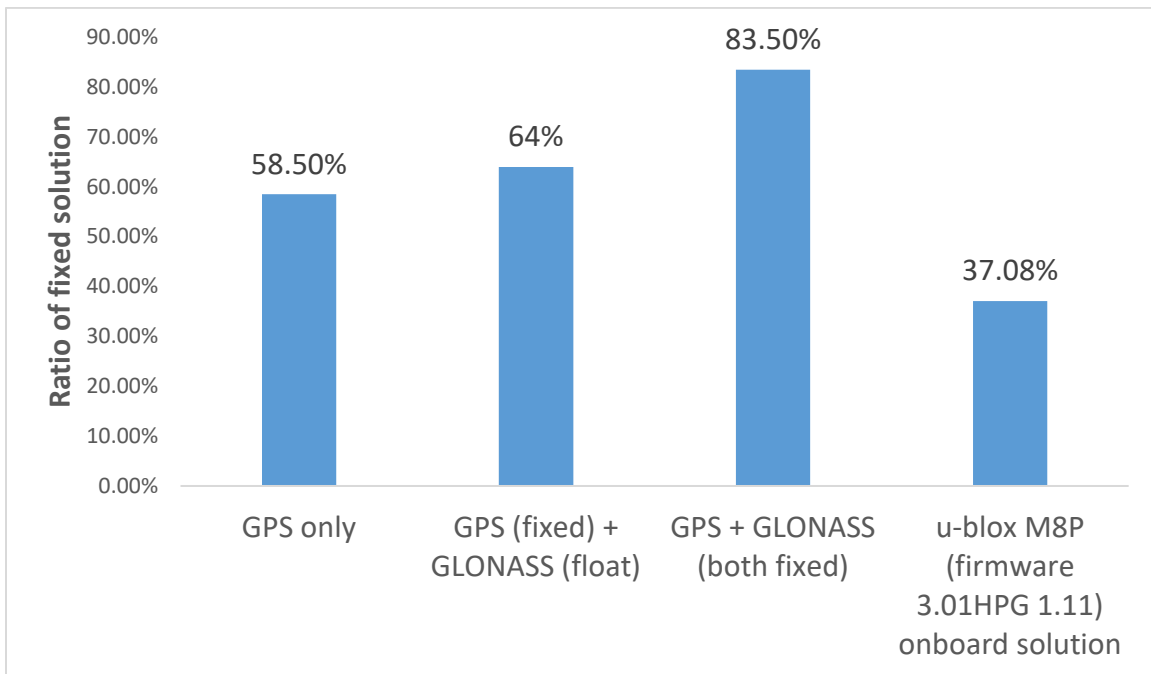


Figure 107 Ratio of the fixed solutions to the total number of solutions

From the above results, one can conclude that by using a second GNSS constellation like GLONASS, the ratio of fixed solutions is significantly increased, which leads to a higher ratio of centimeter-level positions. In a path where tall trees cause heavy multipath and obstruction to the satellite signals, it is not possible to get a fixed solution using GPS only or GPS + GLONASS (GLONASS ambiguities kept float). By taking GLONASS signals and attempting to solve the GLONASS carrier phase ambiguities along with GPS, more fixed solutions are achieved.

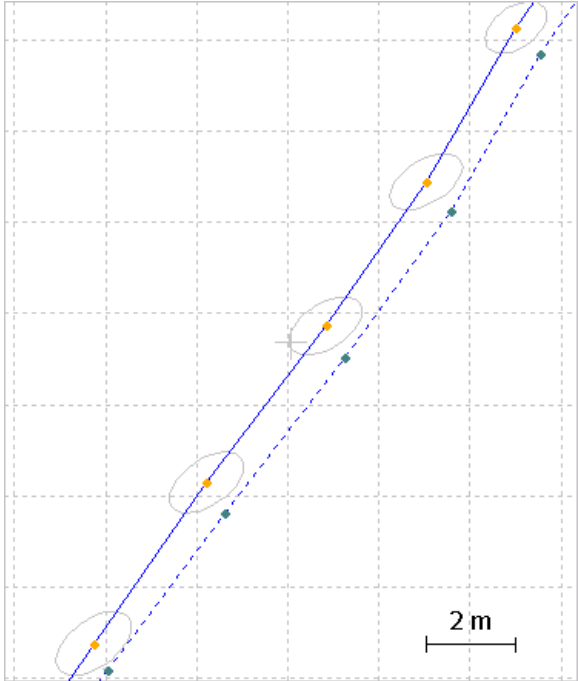


Figure 108 Zoom in on the path beside the trees; Yellow points – float solutions computed with GPS only; Green point – fixed solutions computed with GPS+GLONASS (both fixed); Grey ellipse – error ellipse

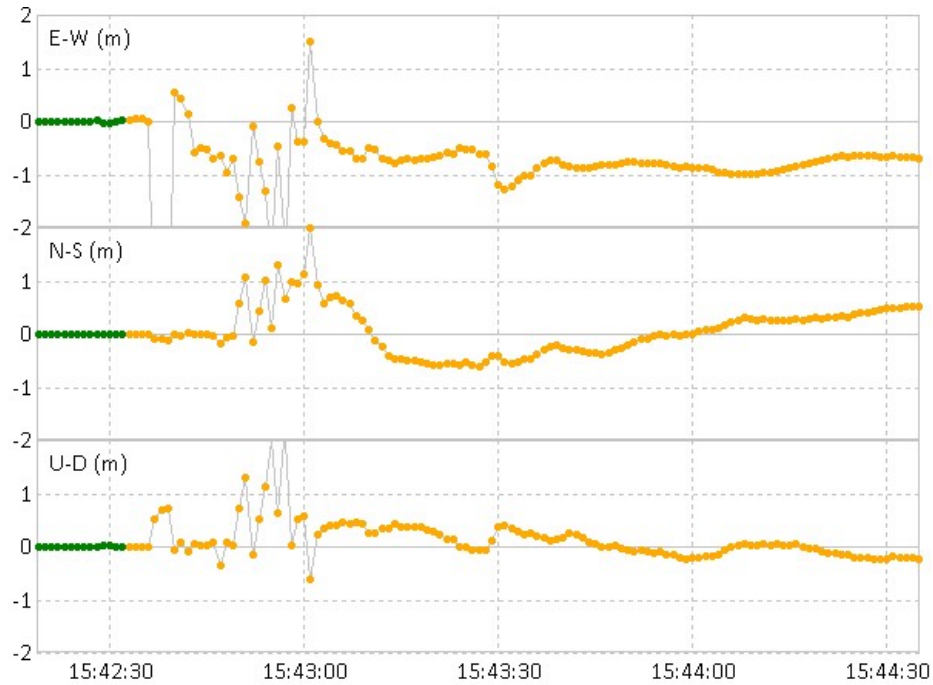


Figure 109 Coordinate differences in topocentric East, North and Up component between the GPS only solution and the GPS+GLONASS(both fixed) solution for the track beside trees

As one can see in Figure 108, the float solutions and the fixed solutions for the same bike track along the path beside trees can differ at the meter level (see Figure 109). The formal errors (standard deviations) of the float solutions are at the sub-meter level shown as the grey error ellipses in the ground track plot, while the formal errors of the GPS+GLONASS fixed solutions are at the centimeter level, which is too small to be seen in the same plot. Th

# Chapter 8 Conclusions and Outlook

## 8.1 Conclusions

The goal of this thesis is to improve the performance of single-frequency RTK GNSS positioning. Firstly, the author has investigated the dominating errors in single-frequency RTK GNSS positioning using low-cost receivers and antennas. Then, these errors have been quantified, modeled, or diluted through observation weighting and finally the RTK performance has been improved by using an additional GNSS constellation.

First, the performances of low-cost single-frequency receivers were investigated and quantified. In low-cost receivers like u-blox LEA 5T and 6T, the receiver clock adjustments (to align the receiver clock to GPS time within 1ms) are seen and these clock adjustments are compensated in the code measurements but not in the carrier-phase measurements. In the newer u-blox M8 GNSS modules, this issue does not exist anymore. There is an offset between the  $C/N_0$  output by the low-cost receiver and the high-end receiver, but the deterministic trend is consistent. The precisions of the code and carrier-phase measurements are estimated through a variance component estimation and then they are used to construct the complete stochastic model together with the observation weighting function.

The relation between multipath and  $C/N_0$  is explained and it is demonstrated that by a Fourier transform and a wavelet analysis of the  $C/N_0$  time series, one can find the multipath frequency that is common to the multipath-induced oscillations in both, the  $C/N_0$  and carrier-phase measurements.

The author proposes an approach to model the low-cost antenna  $C/N_0$  pattern using a geostationary satellite. This empirically modelled antenna  $C/N_0$  pattern accounts for the  $C/N_0$  variations due to the antenna gain change with respect to elevation. The Trimble Bullet antenna gain varies up to 6 dB from zenith to the horizontal plane.

The PCV of the low-cost Trimble Bullet III antenna is estimated. The maximum PCV value is 1 cm and 97% of the values are within  $\pm 6$  mm. By applying the PCV correction to the RTK processing, the carrier-phase residuals are improved in terms of reduced mean and RMS. In their time series plots, it is seen that clear systematic errors in the residuals are removed by PCV corrections.

A MWF based on both,  $C/N_0$  and elevation, is proposed and compared to other weighting functions. The MWF has the advantage to account for both, the elevation-dependent noise increase due to troposphere and the  $C/N_0$ -related multipath errors. The RTK positions computed with the proposed MWF are compared to those of the elevation-based weighting function; a clear accuracy improvement is seen in terms of reduced maximum position deviation as well as a slight increase in the rate of fixed solutions. Through the plot of the SD carrier phase residuals,

it is seen that the MWF could well detect type II multipath (the GNSS receiver observes only the indirect signals) and dilutes its effect on the processing by down-weighting.

RTK positioning of static stations with a single-epoch ambiguity-fixing strategy is used to demonstrate the benefits of using the GPS+BeiDou dual constellation. The ratio of fixed solution is increased comparing to using a GPS only solution. Then, the RTK positioning of a moving rover using GPS+GLONASS demonstrates that the ratio of fixed solutions is increased from 58.5% (u-blox M8P onboard solution using GPS only) to 83.5%. The most promising improvement is in the track, where multipath and obstructions are strong: using GPS only could achieve only float solutions but using GPS+GLONASS ambiguity-fixing can be achieved.

## 8.2 Outlook

To further enhance the performance of single-frequency RTK GNSS positioning in terms of accuracy and reliability, the author proposes the following for future work:

- To better understand where and when the positioning accuracy drops in a kinematic track, a system comparing the RTK GNSS positions to a ground truth measured by a system like GNSS time-synchronized robotic total station or Laser Tracker shall be developed. Such a system will help to quantify and document the multipath environment. The time synchronization of the ground-truth measurements with the GNSS positions is very important. For example, when using the robotic total station like Leica TPS1200 or TS60 as the ground truth tracking system, the Network Time Protocol (NTP) synchronized laptop UTC time is used as timestamp for the positions tracked by total station. Even though the laptop time is NTP synchronized through an internet time server, it still differs from the UTC time of a u-blox GPS receiver by about 0.22 seconds (see Figure 110). The cable delay and the u-blox receiver internal time delay (the delay between the measurement epoch and the epoch when UTC time message is output) will lead to about 0.15 seconds in total, thus the NTP synchronized laptop time still has a time error of 70ms. Considering the unknown delay between the measurement epoch at the total station and the epoch when the data arrives at the laptop, it is justified to say that time differences at 100ms level exist between a laptop timed total station position and a GPS timed GPS position. When the rover antenna moves at a pedestrian speed of 1 m/s, the 100ms time error will lead to a 10 cm position error already. If the antenna is mounted on top of a vehicle, the induced error will be much larger and one cannot verify the centimeter-level RTK positioning accuracy at all. Therefore, having a ground-truth tracking system with good time synchronization to GPS time is critical.

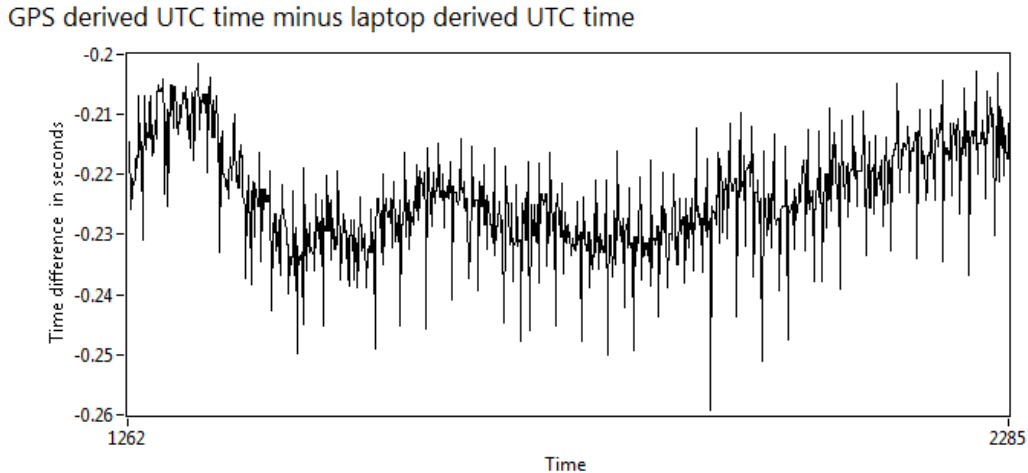


Figure 110 The time difference between a NTP synchronized laptop UTC time and the UTC time from a u-blox LEA 6T (5Hz update rate); Vertical axis is the time difference in seconds and the horizontal axis is elapsed time in seconds

- For a moving GNSS rover, it is difficult to model and quantify the multipath errors. However, the multipath-contaminated satellite signals possess some features, as described in Chapter 2.5, like the correlation to  $C/N_0$  variations. If the above proposed ground truth tracking system is available, one can collect enough data sets with quantified position errors, code and carrier phase residuals due to multipath. Together with the correlation with  $C/N_0$  features and the site specific features of multipath, it should be possible to label the collected data set. One can then apply machine learning techniques to train a good model to detect and model the code and carrier phase multipath in RTK GNSS positioning.
- Pure GNSS positioning techniques are heavily constrained to the conditions of good line-of-sight to GNSS satellites. And for RTK GNSS positioning techniques, getting the raw GNSS data or corrections from a GNSS reference station relies on a wireless communication technique, like radio or Wi-Fi, which is inherently unstable and again limited by distance and obstructions. To overcome these problems, an integration of RTK GNSS positioning with other navigation sensors is a promising approach. The author proposed a vision enhanced RTK technique where the machine vision is tightly coupled to the RTK GNSS technique. From one side, machine vision works well in a challenging environment for GNSS and is not constrained by line-of-sight to the satellites. On the other side, in open sky when RTK GNSS positioning works well, the derived high-precision solution is used to calibrate the error accumulated in proportional to the traveling distance in machine vision based navigation. The author is developing this technique together with his team in the startup company Fixposition AG.

## Appendix A Mathematical derivation of phase wind-up

If we denote the horizontal signal as

$$E_h = E \cos(\omega t + \delta) \quad (8-1)$$

where  $E$  is the magnitude of the electric field,  $\omega$  is the angular velocity or angular frequency,  $\delta$  is the initial phase. Then the vertical signal for a RHCP shall be

$$E_v = E \cos\left(\omega t + \delta - \frac{\pi}{2}\right) = E \sin(\omega t + \delta) \quad (8-2)$$

Using the unit vectors  $\vec{h}$  and  $\vec{v}$  to represent the H-V wave plane, the combined electric field is the vector sum of above two signals:

$$\vec{E}_s = E \cos(\omega t + \delta) \vec{h} + E \sin(\omega t + \delta) \vec{v} \quad (8-3)$$

Therefore, the generated circularly polarized signal has an angular frequency  $\omega$ , and more important, a constant electric magnitude  $E = \sqrt{(E \cos(\omega t + \delta))^2 + (E \sin(\omega t + \delta))^2}$ . This feature is the main advantage of circular polarization: the electric field can be seen as a rotating vector of constant length, so that turning the receiving antenna around its boresight axis will not affect the magnitude of the received signal (W. Gosling 1998). That is why the GNSS carrier is circularly polarized: to render it immune to fading caused by receiver antenna misalignment or by Faraday rotation <sup>14</sup> (Tetewsky and Mullen 1996).

Even though rotating the antenna around the boresight axis does not change the amplitude of GNSS signal, it does introduce a phase shift: the PWD bias. To derive the expression for the PWD bias, we illustrate in Figure 111 how the incident signal is projected into the plane of receiving antenna, which can be easily understood from a coordinate transformation point of view, inspired by (Wu, et al. 1993).

---

<sup>14</sup> Faraday rotation: a change in carrier polarization direction caused by the combination of the Earth's magnetic field and ionospheric plasma



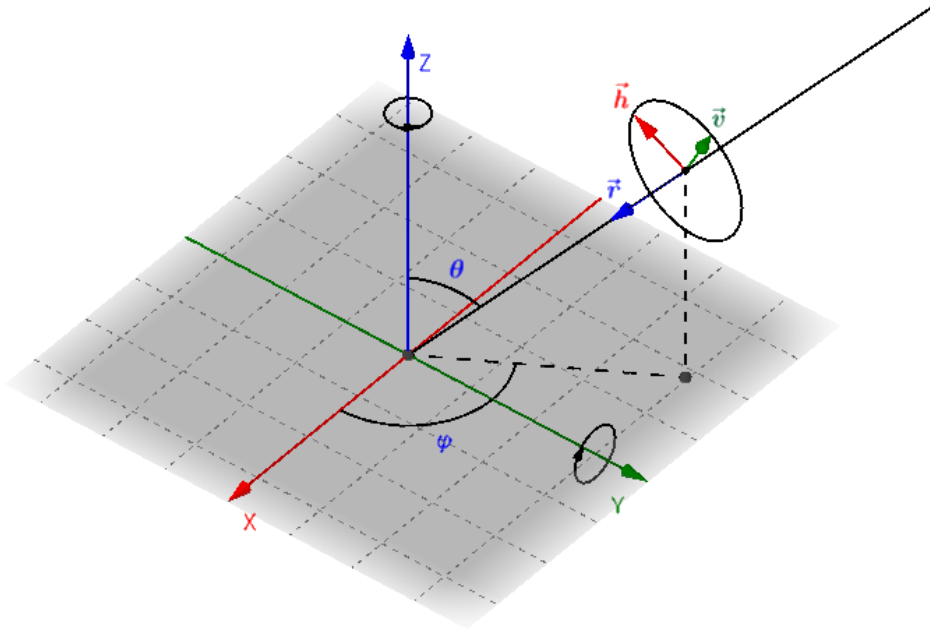


Figure 111 A RHCP GNSS signal in the coordinate system of the receiving antenna

There are two Cartesian coordinate systems in the above figure: one is defined in the receiving antenna body frame, with the antenna boresight axis as  $Z$  axis, the two cross dipoles as the  $X$  and  $Y$  axes forming a right-handed coordinate system; the other is the local coordinate system of the signal where the unit vector  $\vec{r}$  represents the propagation direction of the incident signal transmitted by a GNSS satellite, the unit vectors  $\vec{h}$  and  $\vec{v}$  represent the horizontal and vertical components in the RHCP GNSS signal plane. Rewriting formula (8-3) as a complex expression, we have:

$$\vec{E}_s = \text{Re}[E \cdot (\vec{h} - i\vec{v}) \cdot e^{i(\omega t + \delta)}] = \text{Re}[E \cdot \vec{P}_{RHCP} \cdot e^{i(\omega t + \delta)}] \quad (8-4)$$

$\vec{P}_{RHCP} = \vec{h} - i\vec{v}$  is the polarization vector of a RHCP signal (Tetewsky and Mullen 1996) (Yadava 2011). Then the electric field  $\vec{E}_r$  measured by the receiving antenna, is proportional to its own polarization vector  $(\vec{X} - i\vec{Y})$  and that of the incident signal<sup>15</sup>:

$$\vec{E}_r = \text{Re}[(\vec{X} - i\vec{Y}) \cdot (\vec{h} - i\vec{v}) \cdot E e^{i\omega t}] \quad (8-5)$$

But  $\vec{h} - i\vec{v}$  must be expressed in the coordinate system of the receiving antenna, which is done by a three-dimensional coordinate system transformation (Xu and Xu 2016).

<sup>15</sup> Because the present analysis concentrates on phase changes caused by antenna rotation, we ignore the initial phase term  $\delta$  in  $E e^{i(\omega t + \delta)}$ , which counts for the distance between receiver and satellite.

$$\begin{bmatrix} x_s \\ y_s \\ z_s \end{bmatrix} = c + \mu \cdot R \cdot \begin{bmatrix} X_s \\ Y_s \\ Z_s \end{bmatrix} \quad (8-6)$$

where  $c$  is the translation vector,  $\mu$  is the scale matrix,  $R$  is the rotation matrix;  $x_s$ ,  $y_s$  and  $z_s$  are the incident vector elements in the signal coordinate system (or the coordinate system of the transmitting antenna);  $X_s$ ,  $Y_s$  and  $Z_s$ , are their coordinates, represented in the coordinate system of the receiving antenna. Given the incident carrier is measured at the origin of the receiving antenna coordinate system,  $c$  equals to a zero vector and the  $\mu$  is an identity matrix. As you see in Figure 111, we make firstly a counter-clockwise rotation around  $\vec{Z}$  by angle  $\varphi$  and then a clockwise rotation around  $\vec{Y}$  by angle  $(\pi - \theta)$ . The rotation matrix  $R$  is the product of the two basic rotation matrices.

$$\begin{aligned} R &= R_y(-(\pi - \theta))R_z(\varphi) \\ &= \begin{bmatrix} \cos(-(\pi - \theta)) & 0 & -\sin(-(\pi - \theta)) \\ 0 & 1 & 0 \\ \sin(-(\pi - \theta)) & 0 & \cos(-(\pi - \theta)) \end{bmatrix} \cdot \begin{bmatrix} \cos(\varphi) & \sin(\varphi) & 0 \\ -\sin(\varphi) & \cos(\varphi) & 0 \\ 0 & 0 & 1 \end{bmatrix} \\ &= \begin{bmatrix} -\cos(\theta) & 0 & \sin(\theta) \\ 0 & 1 & 0 \\ -\sin(\theta) & 0 & -\cos(\theta) \end{bmatrix} \cdot \begin{bmatrix} \cos(\varphi) & \sin(\varphi) & 0 \\ -\sin(\varphi) & \cos(\varphi) & 0 \\ 0 & 0 & 1 \end{bmatrix} \\ &= \begin{bmatrix} -\cos\theta\cos\varphi & -\cos\theta\sin\varphi & \sin\theta \\ -\sin\varphi & \cos\varphi & 0 \\ -\sin\theta\cos\varphi & -\sin\theta\sin\varphi & -\cos\theta \end{bmatrix} \end{aligned} \quad (8-7)$$

where  $\theta$  is the depression angle and  $\varphi$  is the azimuth angle of the incident carrier. Applying the above rotation matrix to  $(\vec{X}, \vec{Y}, \vec{Z})$ , where  $\vec{X}, \vec{Y}, \vec{Z}$  represents the incident signal's vector projection on the receiving antenna's coordinate system's three axes, we have:

$$\begin{aligned} \vec{h} &= -\vec{X}\cos\theta\cos\varphi - \vec{Y}\cos\theta\sin\varphi + \vec{Z}\sin\theta \\ \vec{v} &= -\vec{X}\sin\varphi + \vec{Y}\cos\varphi \end{aligned} \quad (8-8)$$

So put (8-8) into (8-5), we get :

$$\begin{aligned} E_r &= Re\{Ee^{i\omega t} \cdot [(-\vec{X}\cos\theta\cos\varphi - \vec{Y}\cos\theta\sin\varphi + \vec{Z}\sin\theta) - (-\vec{X}\sin\varphi + \vec{Y}\cos\varphi)i] \cdot (\vec{X} - \vec{Y}i)\} \\ E_r &= Re\{Ee^{i\omega t} \cdot [-\vec{X}(\cos\theta\cos\varphi - i\sin\varphi) - \vec{Y}(\cos\theta\sin\varphi + i\cos\varphi) + \vec{Z}\sin\theta] \cdot (\vec{X} - \vec{Y}i)\} \end{aligned} \quad (8-9)$$

As  $\vec{X}, \vec{Y}$ , and  $\vec{Z}$  are unit orthogonal vectors, we have:

$$\begin{aligned}
E_r &= \text{Re}\{Ee^{i\omega t} \cdot [-(\cos\theta\cos\varphi - i\sin\varphi) + i(\cos\theta\sin\varphi + i\cos\varphi)]\} \\
&= \text{Re}\{Ee^{i\omega t} \cdot [-(\cos\theta\cos\varphi + \cos\varphi) + i(\cos\theta\sin\varphi + \sin\varphi)]\} \\
&= \text{Re}\{-Ee^{i\omega t} \cdot (1 + \cos\theta)(\cos\varphi - i\sin\varphi)\}
\end{aligned} \tag{8-10}$$

The above equation can be rewritten as:

$$E_r = \text{Re}\{-Ee^{i\omega t} \cdot e^{-i\varphi} \cdot (1 + \cos\theta)\} = E(1 + \cos\theta)\text{Re}\{-e^{i(\omega t - \varphi)}\} \tag{8-11}$$

Equation (8-11) clearly shows that the measured phase of the incident carrier is solely depending on the relative azimuth angle  $\varphi$  between the receiving antenna and the transmitting antenna, whereas the amplitude is scaled by  $(1 + \cos\theta)$ , related to only the depression angle  $\theta$ . So whenever there is a relative rotation between the receiving and transmitting antennas, the changed azimuth angle  $\varphi$  goes into the phase term directly, causing a phase bias called phase wind up. Please notice that, when the receiving antenna rotates counter-clockwise, namely in the same rotation direction of the incident carrier, the azimuth angle  $\varphi$  increases, leading to a decrease in carrier-phase measurements, and vice versa when rotating clockwise. If this rotation is continuous, the changing of azimuth angle is  $\varphi = \alpha t$  which enters the frequency term:

$$\vec{E}_r = E(1 + \cos\theta)\text{Re}\{-e^{i(\omega t - \alpha t)}\} = E(1 + \cos\theta)\text{Re}\{-e^{i(\omega - \alpha)t}\} \tag{8-12}$$

From the above equation, we can see that a continuous rotation of the antenna changes also the frequency of the GNSS signal observed by the receiver. Also indicated by the above equation is that the PWD effect is only on carrier-phases but not in code pseudoranges.

The PWD effect has to be corrected in PPP (Cosentino, et al. 2006). RTKLIB adapts the formulas from (Wu, et al. 1993) to correct the PWD errors in carrier phases.

In contrast, for an RTK system, especially when the baseline length is short, the PWD effect is negligible. (Kim, Serrano and Richard 2006) explained that in case the antenna's spin axis is aligned with the boresight, PWD is removed by double-differencing or absorbed along with the clock estimation (García-Fernández, Markgraf and Montenbruck 2008) because the phase shift is common to all satellite signals. However, in case the spin axis is not aligned with the antenna boresight, the receiver channels see the same steady phase wind-up term but each channel has a different amount of spin modulation. This additional spin modulation is determined by the satellite elevation angle and, therefore, cannot be cancelled by double-differencing operation. This is an interesting field worthy of further study, but it is out of the scope of this thesis.

## Appendix B Proof of the first and second derivative of carrier-phase multipath error over the phase shift in NLOS signal.

Here a proof of the first derivative in formula (2-54) and the second derivative in (2-56) is given.

$$\theta_M = \arctan \frac{\alpha \sin \theta}{1 + \alpha \cos \theta}$$

Given:

$$\frac{d \arctan x}{dx} = \frac{1}{1 + x^2}$$

Thus:

$$\frac{d\theta_M}{d\theta} = \frac{1}{1 + \left(\frac{\alpha \sin \theta}{1 + \alpha \cos \theta}\right)^2} \cdot \frac{d\left(\frac{\alpha \sin \theta}{1 + \alpha \cos \theta}\right)}{d\theta}$$

Given:

$$\frac{d(f(x)g(x))}{dx} = \frac{df(x)}{dx}g(x) + \frac{dg(x)}{dx}f(x)$$

Thus:

$$\begin{aligned} \frac{d\left(\frac{\alpha \sin \theta}{1 + \alpha \cos \theta}\right)}{d\theta} &= \frac{\alpha \cos \theta}{1 + \alpha \cos \theta} + \alpha \sin \theta \frac{-(-\alpha \sin \theta)}{(1 + \alpha \cos \theta)^2} \\ &= \frac{\alpha \cos \theta + \alpha^2 \cos^2 \theta + \alpha^2 \sin^2 \theta}{(1 + \alpha \cos \theta)^2} \\ &= \frac{\alpha \cos \theta + \alpha^2}{(1 + \alpha \cos \theta)^2} \end{aligned}$$

Thus:

$$\begin{aligned} \frac{d\theta_M}{d\theta} &= \frac{1}{1 + \left(\frac{\alpha \sin \theta}{1 + \alpha \cos \theta}\right)^2} \cdot \frac{\alpha \cos \theta + \alpha^2}{(1 + \alpha \cos \theta)^2} \\ &= \frac{\alpha \cos \theta + \alpha^2}{(1 + \alpha \cos \theta)^2 + \alpha^2 \sin^2 \theta} \end{aligned}$$

Proof of first derivative done.

$$\begin{aligned}
\frac{d^2\theta_M}{d\theta^2} &= \frac{d\left(\frac{\alpha\cos\theta + \alpha^2}{(1 + \alpha\cos\theta)^2 + \alpha^2\sin^2\theta}\right)}{d\theta} \\
&= \frac{d\left(\frac{\alpha\cos\theta + \alpha^2}{1 + 2\alpha\cos\theta + \alpha^2}\right)}{d\theta} \\
&= \frac{-\alpha\sin\theta}{1 + 2\alpha\cos\theta + \alpha^2} + (\alpha\cos\theta + \alpha^2) \frac{-1 \cdot (-2\alpha\sin\theta)}{(1 + 2\alpha\cos\theta + \alpha^2)^2} \\
&= \frac{-\alpha\sin\theta - 2\alpha^2\cos\theta\sin\theta - \alpha^3\sin\theta}{(1 + 2\alpha\cos\theta + \alpha^2)^2} + \frac{2\alpha^2\cos\theta\sin\theta + 2\alpha^3\sin\theta}{(1 + 2\alpha\cos\theta + \alpha^2)^2} \\
&= \frac{\alpha\sin\theta(\alpha^2 - 1)}{(1 + 2\alpha\cos\theta + \alpha^2)^2}
\end{aligned}$$

Proof of second derivative done.

## Appendix C u-blox Evaluation kit to u-blox modules mapping list

Evaluation Kits	u-blox GNSS modules
EVK-5T	LEA-5T
EVK-6T	LEA-6T
EVK-M8	LEA-M8T
C94-M8P	NEO-M8P

Table 19 Antenna Technical / Performance specifications

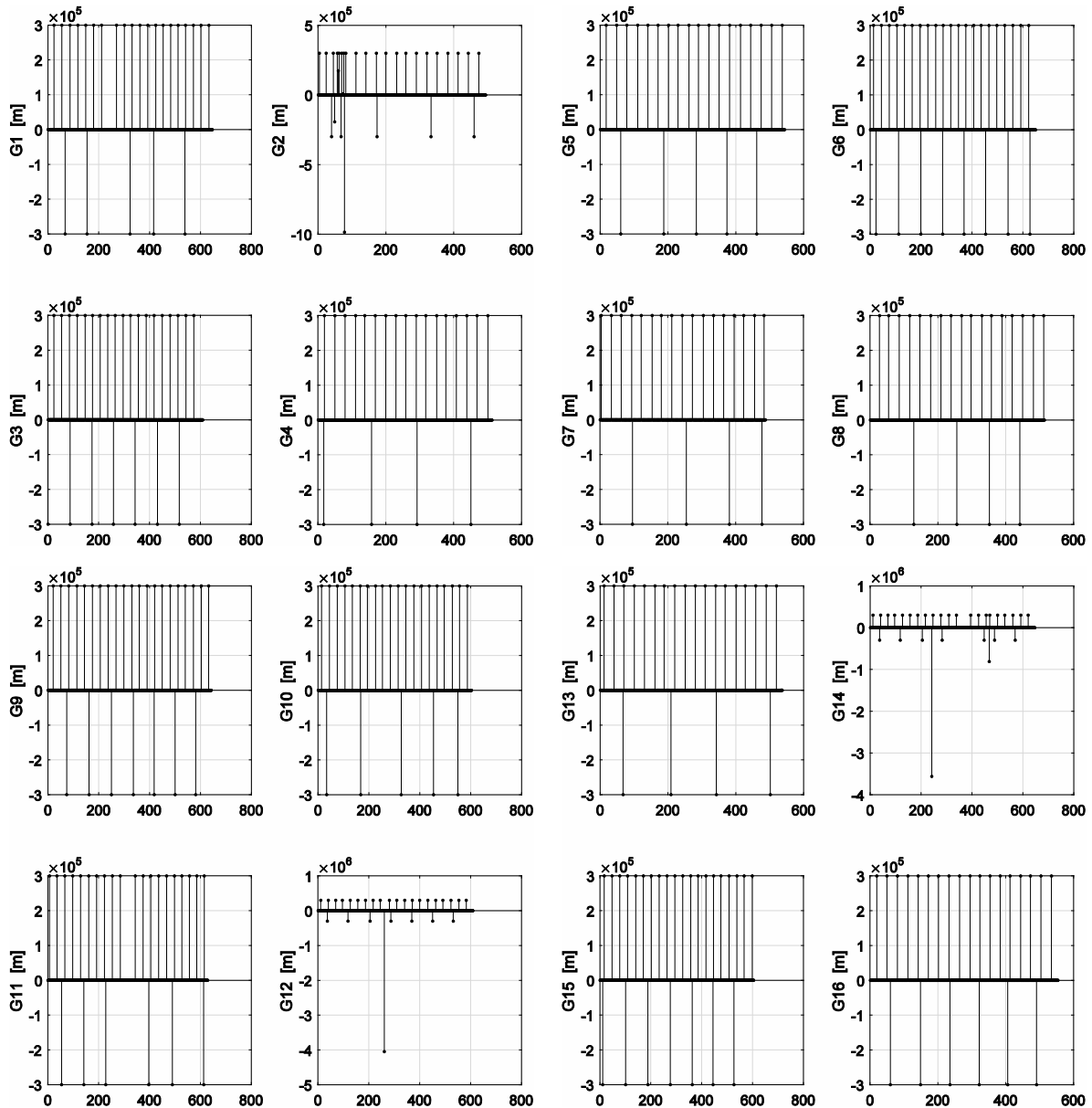
Trimble Bullet™ III GPS Antenna	value
P/N	57861-00
Prime Power	3.3 V DV ( $\pm 10\%$ )
Gain	28 dB $\pm$ 3dB
Noise	3.0 dB (omni-directional)
Frequency	GPS L1 1575.42 $\pm$ 1.023 MHz

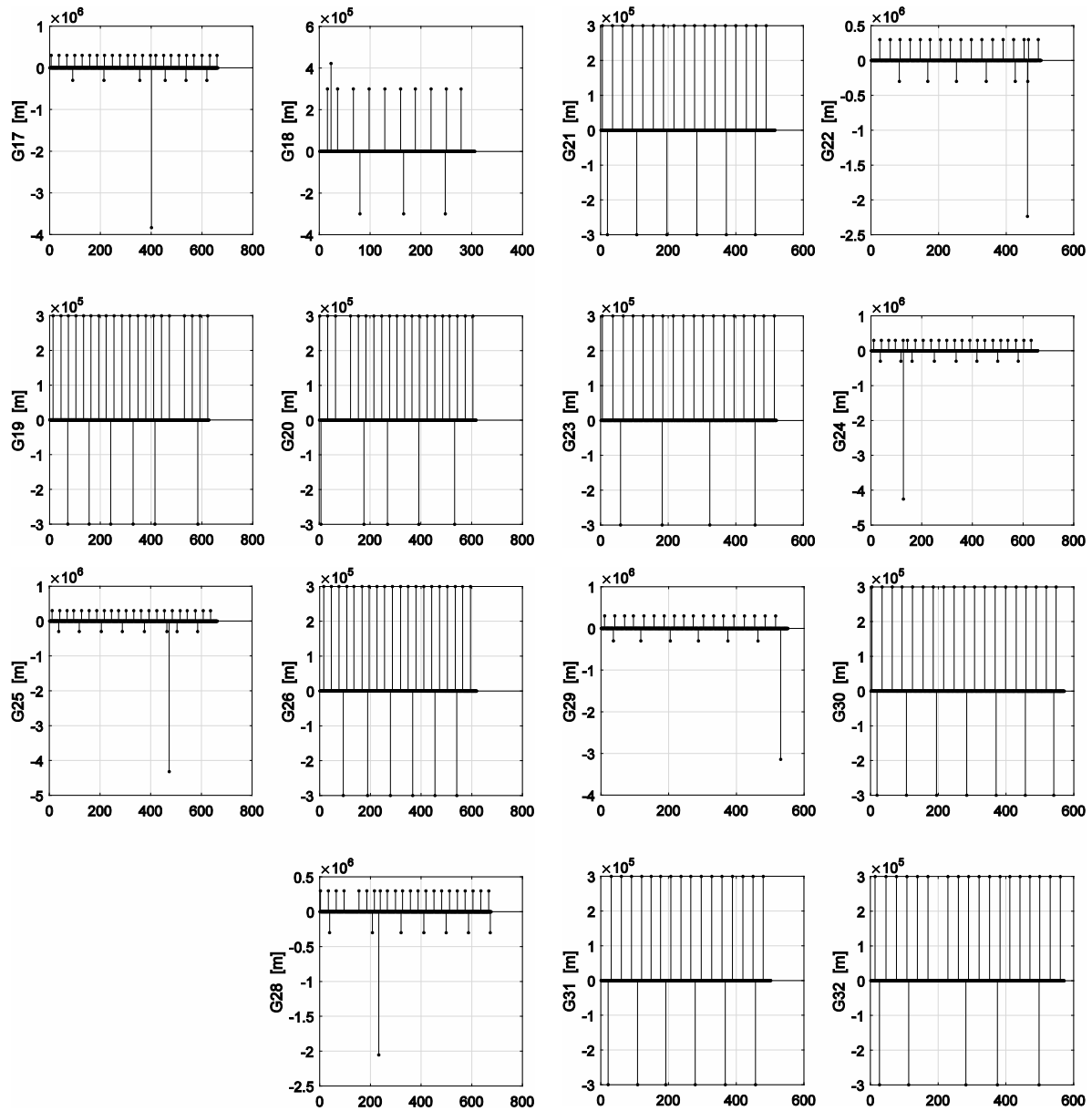
## Appendix D CPGF linear combination jumps

The images below are the SD (between two receivers) CPGF linear combination (see(3-6)) changes between two adjacent measurement epochs:

$$dL_{CPGF,SD}(t_{i+1}) = L_{CPGF,SD}(t_{i+1}) - L_{CPGF,SD}(t_i)$$

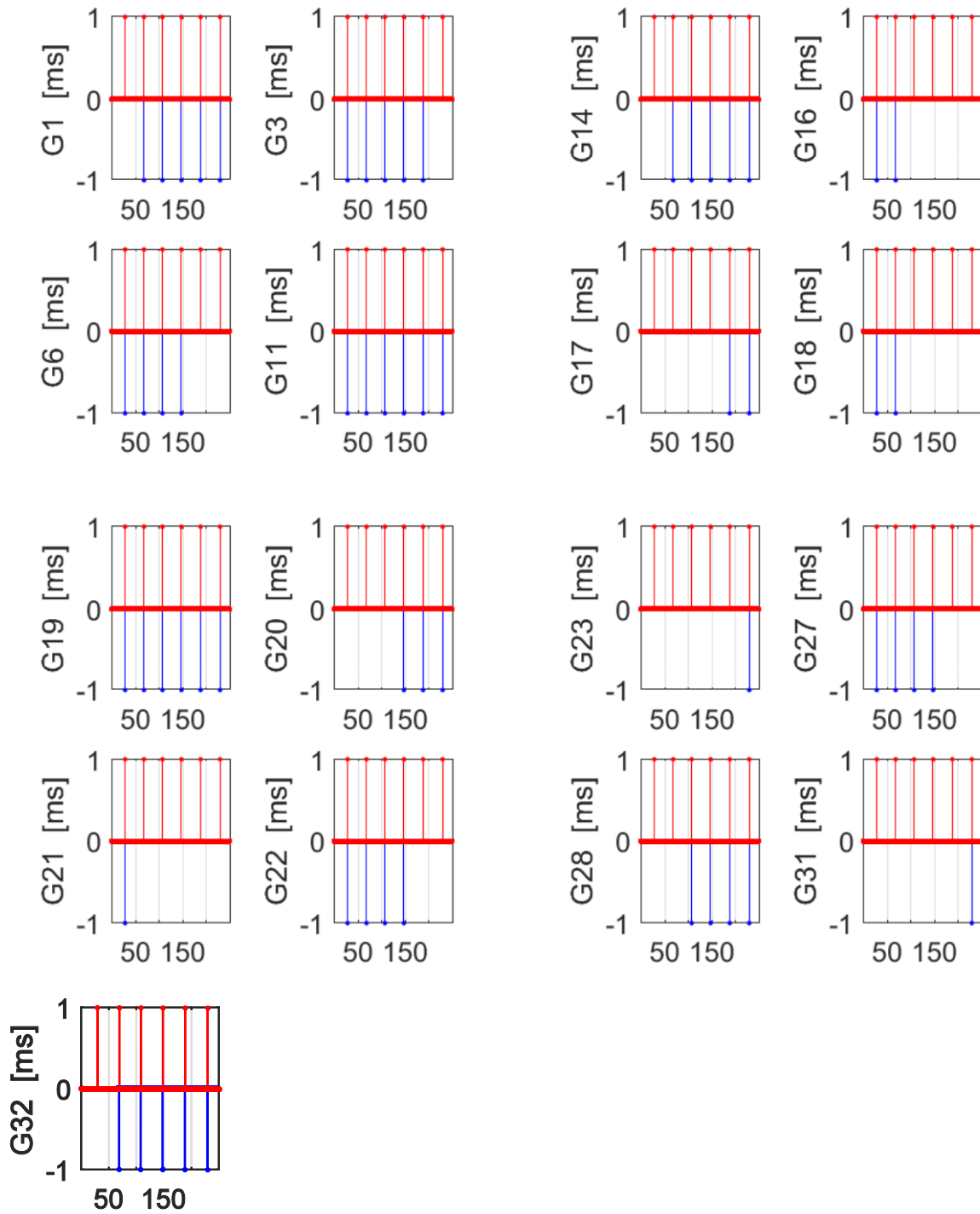
The GNSS data processed are from GNSS station RG01 and RD01 of the X-Sense project on 13/01/2013, with 30 s sampling interval of 24 hours of observations. Both stations use u-blox LEA-6T as receiver modules.



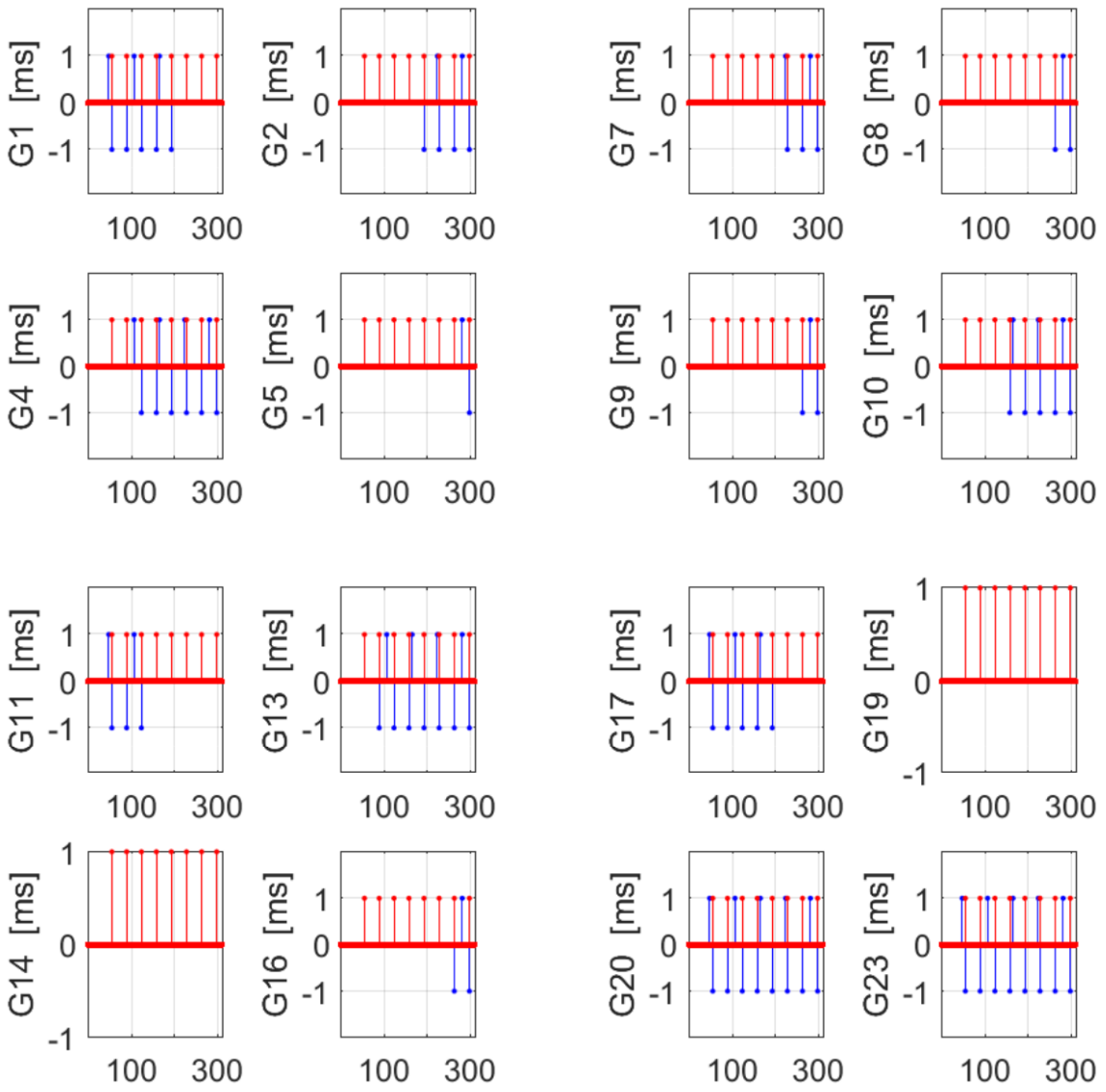


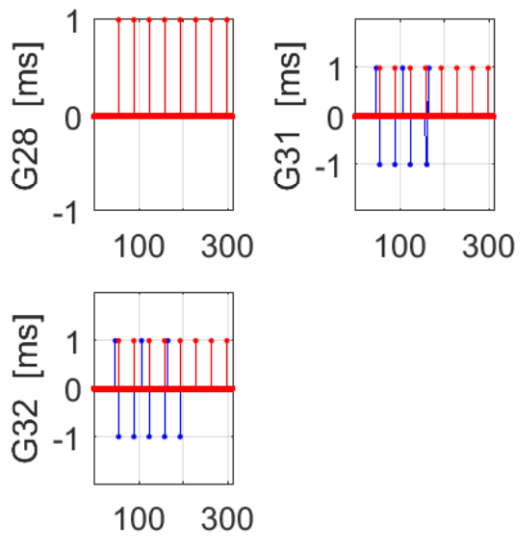
In the ZB of a ublox 5T receiver and a Javad sigma receiver, the CPGF linear combination jumps occur whenever the ublox 5T receiver makes the 1 ms clock offset adjustment.





The CPGF linear combination jumps converted to light travel time in millisecond (blue) and the receiver clock jumps (red), horizontal axis is the GPS time of week in minute





## Appendix E Statistics of the DD code and carrier phase residuals in a zero baseline test with two u-blox M8P receiver modules and one Trimble Bullet III antenna

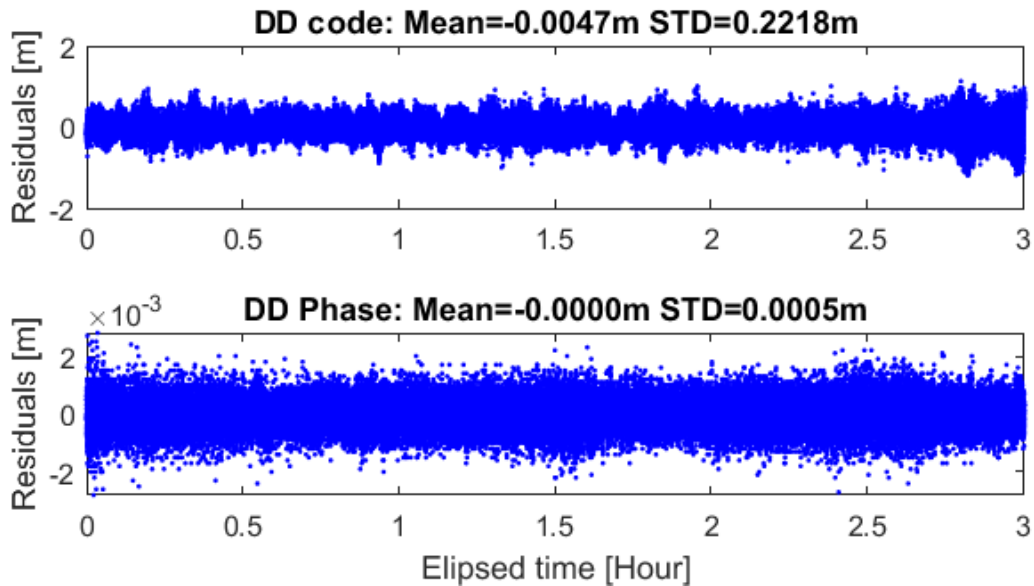


Figure 112 Time series of the DD code and phase residuals (zero baseline of two u-blox M8P receivers with Trimble Bullet antenna)

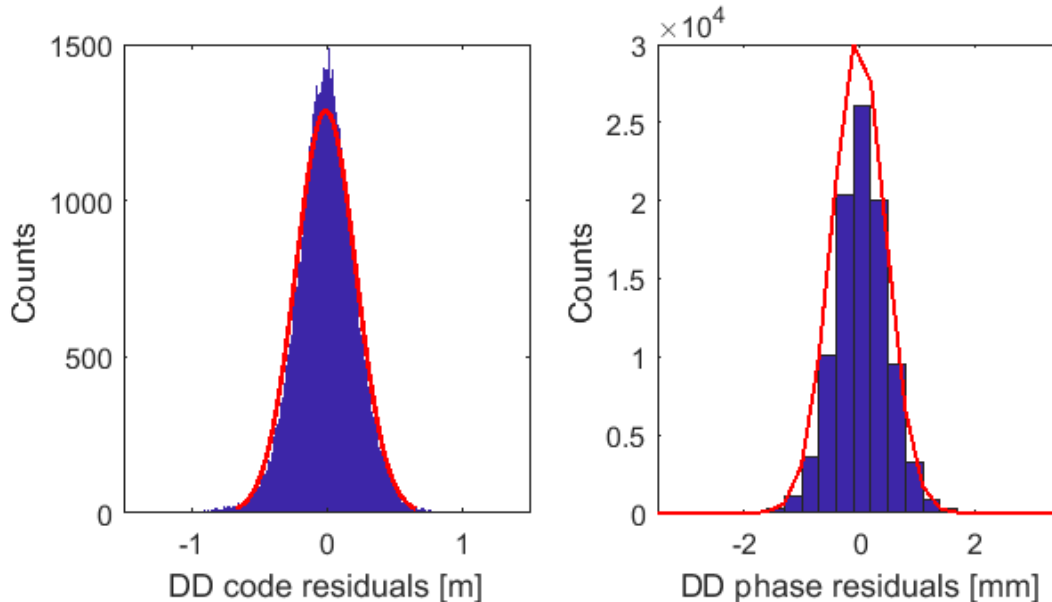


Figure 113 The histogram and normal distribution fit (red line) of the DD code and phase residuals (zero baseline of two u-blox M8P receivers)

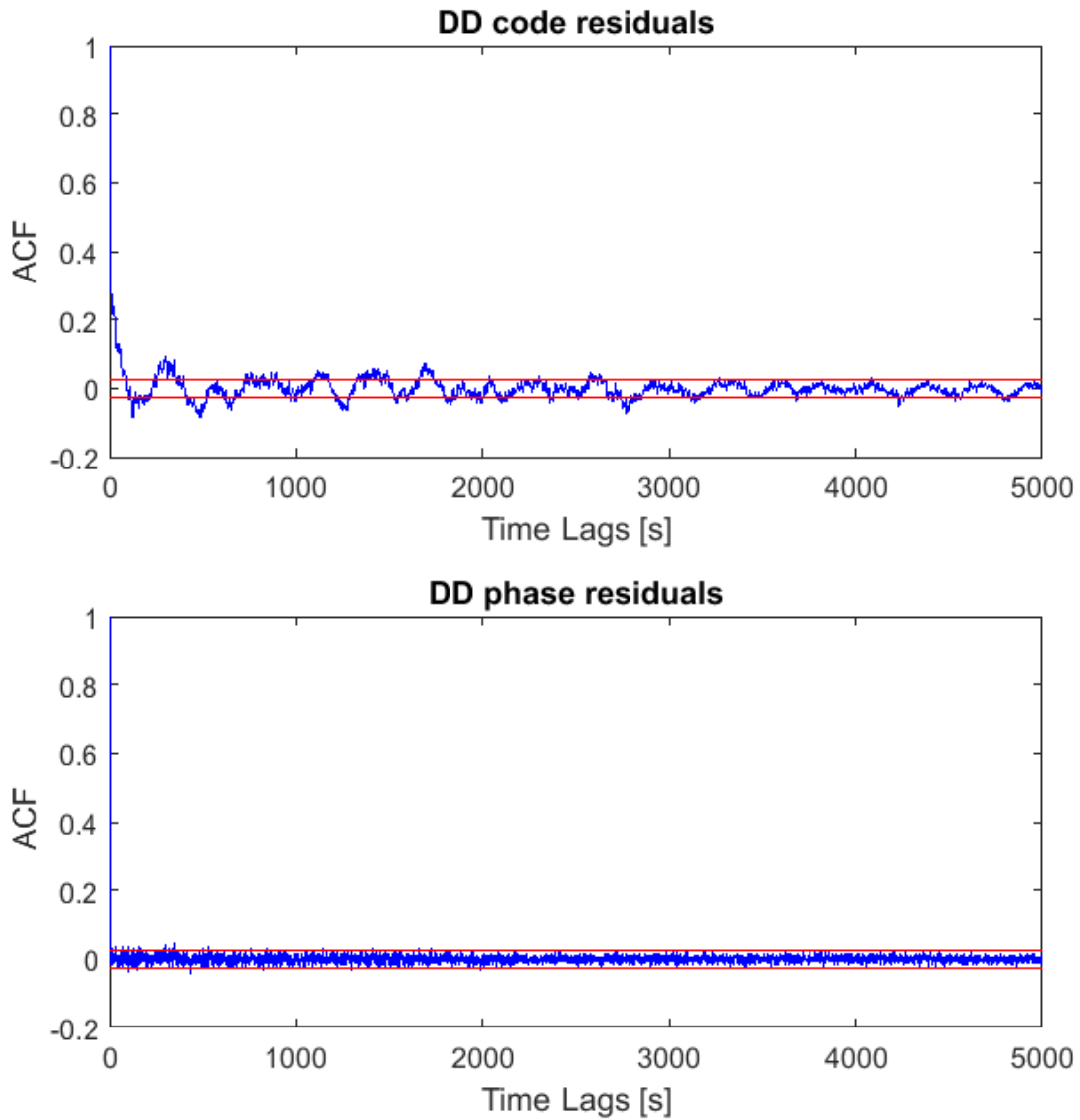
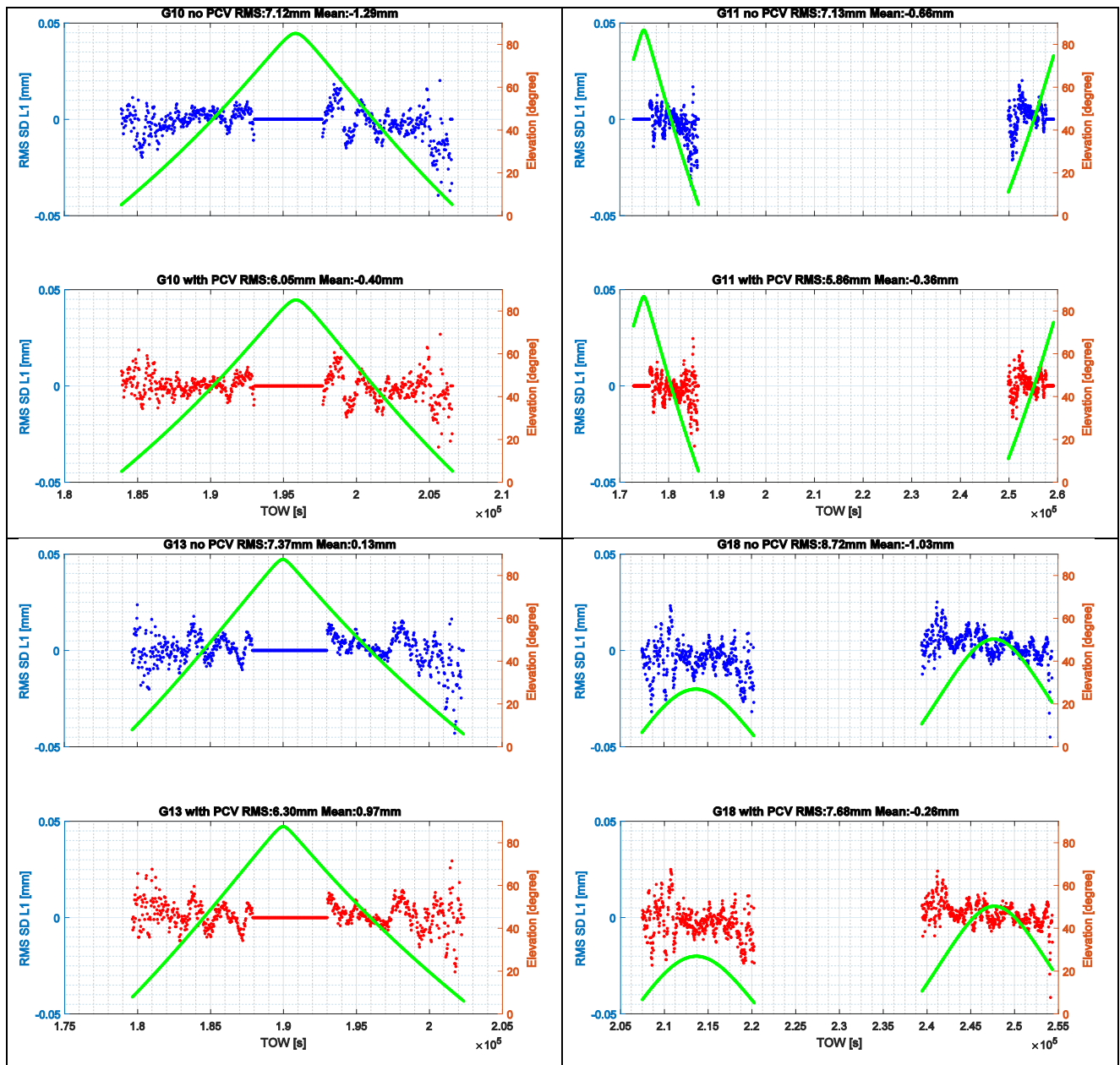
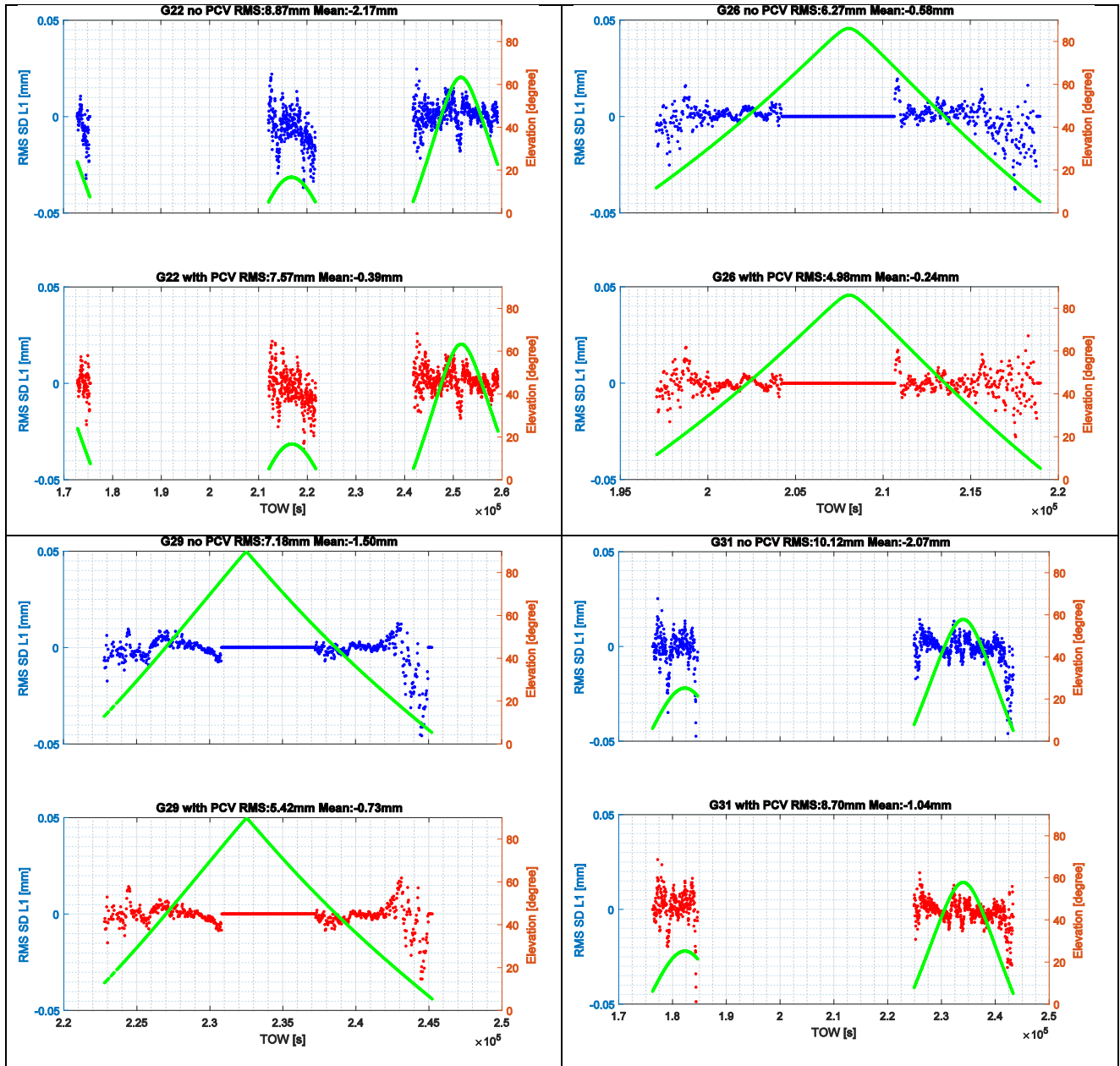


Figure 114 The sampled autocorrelation of the zero baseline DD code (top) and phase residuals (bottom); Red lines are the upper and lower bounds with 95% confidence (zero baseline of two u-blox M8P receivers)

# Appendix F Plots of SD carrier-phase residuals for the RTK processing with and without the estimated rover antenna PCV corrections

Those SD carrier-phase residuals having an RMS reduction more than 1 mm by PCV corrections, are plotted in the following figures (except for satellites G02 and G07 which are already given in Chapter 5.4).





## Appendix G From the X-Sense project to the low-cost RTK GNSS receiver prototype

From a wireless connected, near real-time low-cost RTK GPS positioning system with a distributed data acquisition and centralized data processing architecture, to a fully functional low-cost RTK GNSS receiver prototype.

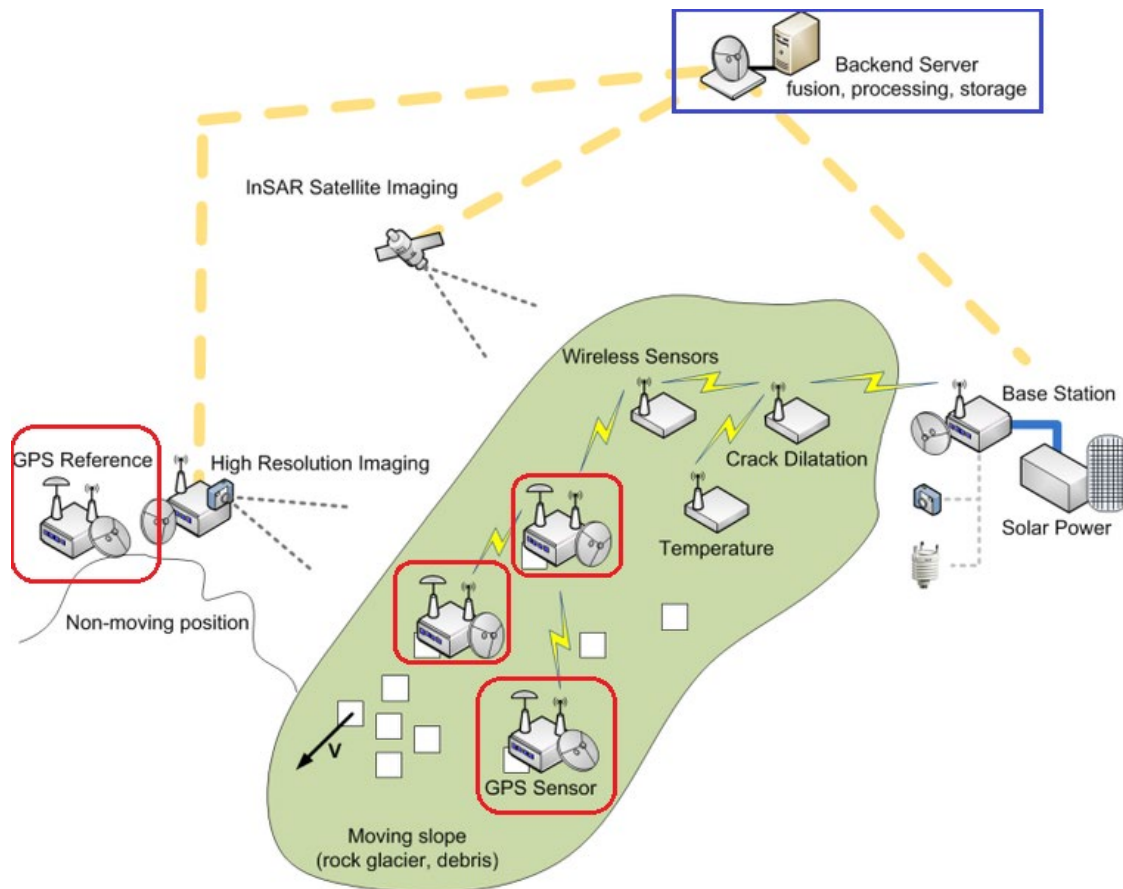


Figure 115 Near real-time low-cost RTK GPS positioning system in the X-Sense project: distributed data acquisition and centralized data processing architecture, connected by wireless network (@ <http://www.permasense.ch/de/projects/x-sense.html>)

The GPS data acquisition nodes (including GPS reference station and rover stations on moving targets) are highlighted by red squares. The data processing service is highlighted by a blue square, which is in fact subdivided into two parts:

- the backend server, including data streaming, processing and storage based on the Global Sensor Network (GSN) middleware (for details refer to (Salehi 2010)), operated by the



Computer Engineering Group at the Computer Engineering and Networks Laboratory, ETH Zurich

- and the GPS data processing server operated by the Mathematical and Physical Geodesy Group at the Institute of Photogrammetry and Geodesy, ETH Zurich. The processing center uses software developed based on RTKLIB to compute real-time (with respect to the incoming data stream) kinematic positions by Zhenzhong Su and Bernese GNSS Software to compute daily static positions by Dr. Philippe Limpach. The computed kinematic and static positions are uploaded back to the database in the backend server.

The raw GPS data are collected in real-time by the ublox LEA-6T modules which are integrated into the GPS nodes. Then, the raw GPS data are transferred, first through the wireless sensor network and then through the cable connected network, to the backend server. Due to the power duty cycle (designed to balance the power consumption and maximization of the sensor observational time span) in the wireless sensor nodes, the raw GPS data are transmitted with latency of some seconds up to hours. The backend server will then stream the raw GPS data to the data processing server to have a near real-time positioning of those GPS nodes.

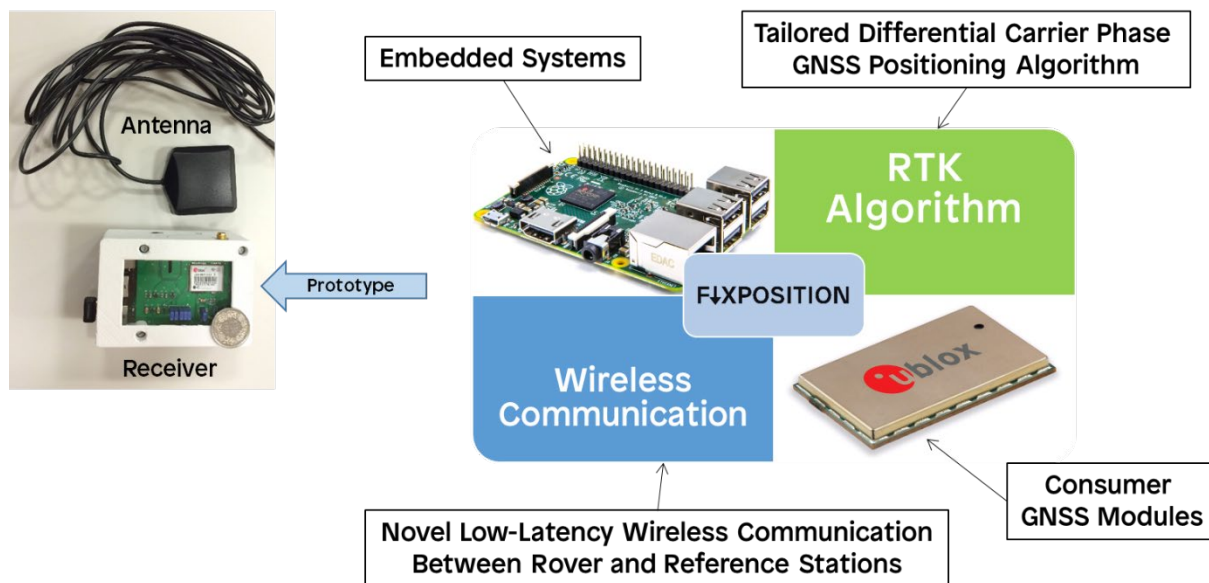


Figure 116 Low-cost RTK GNSS receiver (Functional prototype)

After the X-Sense project, a low-cost RTK GNSS receiver prototype which integrated the wireless communication module, GNSS data acquisition module and processing unit into one device has been further developed. The fully functional prototype consists of an embedded system, the tailored RTK positioning software, the wireless communication module and the consumer GNSS modules.

## References

- Aminian, B. 2011. *Investigation of GPS Observations for indoor/INS integration*. Master thesis, Alberta: Department of Geomatics Engineering, University of Calgary.
- Amiri-Simkooei, A. R. 2007. *Least-squares variance component estimation: theory and GPS applications*. PhD Thesis, Delft, Netherlands: Netherlands Geodetic Commission, 21-22.
- Amiri-Simkooei, A. R., and C. C. J. M. Tiberius. 2007. "Assessing receiver noise using GPS short baseline time series." *GPS Solutions* 21-35.
- Aparicio, M., P. Brodie, L. Doyle, J. Rajan, and P. Torriero. 1996. "GPS satellite and Payload." In *Global positioning system, theory and applications I*, by J. Spilker, P. Axelrad, P. Enge B. Parkinson, 209-244.
- Axelrad, P., C. Comp, and P. MacDoran. 1994. "Use of Signal-To-Noise Ratio for Multipath Error Correction in GPS Differential Phase Measurements: Methodology and Experimental Results." *Proc. ION GPS-94* 655–666.
- Axelrad, P., K. Larson, and B. Jones. 2005. "Use of the correct satellite repeat period to characterize and reduce site-specific multipath errors." *ION GNSS 18th International Technical Meeting of the Satellite Division* 2638-2648.
- Badke, B. 2009. "Carrier-to-Noise Density and AI for INS/GPS Integration." Edited by Mark Petovello. (Gibbons Media & Research LLC) 20-23.
- BDS-ICD. 2013. "BeiDou navigation satellite system signal in space."
- Beyerle, G. 2009. "Carrier phase wind-up in GPS reflectometry." *GPS Solutions* (Springer-Verlag) 191-198. doi:10.1007/s10291-008-0112-1.
- Bilich, A., and K. M. Larson. 2007. "Mapping the GPS multipath environment using the signal-to-noise ratio (SNR)." *Radio Science* 42 (6). doi:10.1029/2007RS003652.
- Bilich, A., K. M. Larson, and P. Axelrad. 2008. "Modeling GPS phase multipath with SNR: Case study from the Salar de Uyuni, Boliva." *Journal of Geophysical Research: Solid Earth* 113 (B4). doi:10.1029/2007JB005194.
- Black, H. D., and A. Eisner. 1984. "Correcting satellite doppler data for troospheric effects." *Journal of Geophysical Research* 89: 2616-2626.
- Bossler, J. D., J. R. Jensen, R. B. McMaster, and C. Rizos. 2002. *Manual of Geospatial Science and Technology*. Taylor & Francis.

- Braasch, M. S. 1996. *Multipath effects*. Vol. I, chap. 14 in *Global Positioning System: Theory and Applications*, by James J. Spilker Jr., Penina Axelrad, Bradford W. Parkinson and Per Enge, 547-568. American Institute of Aeronautics and Astronautics.
- Brunner, F. K., H. Hartinger, and L. Troyer. 1999. "GPS signal diffraction modelling: the stochastic SIGMA- $\Delta$  model." *Journal of Geodesy* (Springer-Verlag) 259-267.
- Cannon, H. L. 1964. "Modulation of Signals Received from a Cw Transmitting Turnstile Antenna Due to Its Rotation." *IEEE Transactions on Space Electronics and Telemetry* (IEEE) 10 (2): 70 - 78. doi:10.1109/TSET.1964.4337570.
- Carcanague, S. 2012. "Real-Time Geometry-Based Cycle Slip Resolution Technique for Single-Frequency PPP and RTK." *ION GNSS 2012, 25th International Technical Meeting of The Satel-lite Division of the Institute of Navigation*. Nashville, United States: ION GNSS 2012. 1136-1148.
- Carcanague, S., O. Julien, W. Vigneau, and C. Macabiau. 2013. "Finding the Right Algorithm: Low-Cost, Single-Frequency GPS/GLONASS RTK for Road Users." *Inside GNSS*, NOVEMBER/DECEMBER: 70-80.
- Chassagne, O. 2012. "One centimeter accuracy with PPP." *InsideGNSS*, 49-54.
- Chui, C. K., and G. Chen. 2009. *Kalman Filtering with Real-Time Applications*. 4th Edition. Springer-Verlag Berlin Heidelberg. doi:10.1007/978-3-540-87849-0.
- Collins, J. P., and R. B. Langley. 1999. "Possible weighting schemes for GPS carrier phase observations in the presence of multipath." Contract report No. DAAH04-96-C-0086/TCN98151 for the United States Army Corps of Engineers Topographic Engineering Center. <http://gge.unb.ca/Personnel/Langley/Langley.html>.
- Comp, C. J., and P. Axelrad. 1998. "Adaptive SNR-based carrier phase multipath mitigation technique." *IEEE Transactions on Aerospace and Electronic Systems* 34 (1): 264-276.
- Cosentino, R. J., D. W. Diggle, M. U. de Haag, C. J. Hegarty, D. Milbert, and J. Nagle. 2006. "Differential GPS." In *Understanding GPS principles and applications*, by Elliott D. Kaplan and Christopher J. Hegarty, 449-450. ARTECH HOUSE, INC.
- Dach, R., U. Hugentobler, P. Fridez, and M. Meindl. 2007. *Bernese GPS Software Version 5.0*. Software manual, Bern: Astronomical Institute, University of Bern.
- Daubechies, I. 1990. "The wavelet transform, time-frequency localization and signal analysis." *IEEE transactions on information theory* 36 (5): 961-1005.
- de Bakker, P. F., H. van de Marel, and C. C. J. M. Tiberius. 2009. "Geometry-free undifferenced, single and double differenced analysis of single frequency GPS, EGNOS and GIOVE-A/B measurements." *GPS Solutions* 305–314.

- Dierendonck, A. J. V. 1995. "GPS Receivers." In *Global positioning system theory and applications, Volume I*, by B. Parkinson, J. Spilker Jr., P. Axelrad and P. Enge. CA: The American Institute of Aeronautics and Astronautics Inc.
- Donahue, B., J. Wentzel, and R. E. Berg. July 2013. *Guidelines for RTK/RTN GNSS Surveying in Canada*. National Resources Canada.
- Dorsey, A. J., W.A. Marquis, P. M. Fyfe, E. D. Kaplan, and L. F. Wiederholt. 2006. "GPS system segments." In *Understanding GPS principles and applications*, by Elliott D. Kaplan and Christopher J. Hegarty. ARTECH HOUSE, INC.
- Elsobeiey, M., and S. Al-Harbi. 2016. "Performance of real-time Precise Point Positioning using IGS real-time service." *GPS Solutions* 565–571.
- Euler, H. J., and C. C. Goad. 1991. "On optimal filtering of GPS dual frequency observations without using orbit information." *Bulletin Géodésique* 130-143.
- Falletti, E, M. Pini, and L. L Presti. 2010. "Carrier-to-noise algorithms." *Inside GNSS*, January/February 2010: 20-27.
- Falletti, E., M. Pini, and L. L. Presti. 2011. "Low complexity carrier-to-noise ratio estimator for GNSS digital receivers." *IEEE transactions on aerospace and electronic systems* 47 (1): 420-437.
- Galileo-ICD. 2015. "European GNSS (Galileo) Open Service."
- García-Fernández, M., M. Markgraf, and O. Montenbruck. 2008. "Spin rate estimation of sounding rockets using GPS wind-up." *GPS Solutions* 12 (3): 155-161. doi:10.1007/s10291-007-0074-8.
- Geiger, A. 1988. "Modeling of phase center variation and its influence on GPS-positioning." Edited by Prof. Dr. Erwin Groten and Dr. Ing. Robert Strauß. *GPS-Techniques Applied to Geodesy and Surveying*. Springer, Berlin, Heidelberg. 210-222. doi:10.1007/BFb0011339.
- Georgiadou, Y., and A. Kleusberg. 1988. "On carrier signal multipath effects in relative GPS positioning." *Manuscripta geodaetica* 13 (3): 172-179.
- Gibbs, B. P. 2011. *Advanced Kalman filtering, least-squares and modeling : a practical handbook*. Hoboken, N.J. : Wiley. doi:10.1002/9780470890042 .
- Glabsch, J., O. Heunecke, S. Pink, and S. Schubäck. 2010. "Nutzung von Low-Cost GNSS Empfängern für ingenieurgeodätische Überwachungsaufgaben." *GNSS 2010 - Vermessung und Navigation im 21. Jahrhundert. DVW-Schriftenreihe*. Augsburg: Wissner-Verlag. 113-129.
- Gleason, S., and D. Gebre-Egziabher. 2009. *GNSS applications and methods*. Artech House.

- GLONASS-ICD. 1998. "GLONASS interface control document." Interface control document.
- GLONASS-ICD. 2008. "Navigational radiosignal in bands L1, L2." GLONASS Interface Control Document Edition 5.1.
- Gopi, S. 2005. *Global Positioning System: Principles And Applications*. Tata McGraw-Hill.
- Gosling, W. 1998. *Radio antennas and propagation*. Elsevier Ltd.
- Gourevitch, S. 1996. "Measuring GPS receiver performance: a new approach." *GPS World*, 56–62.
- GPS-ICD. 2012. "Navstar GPS space segment/navigation user segment interfaces." Navstar GPS space Segment/Navigation User Interfacaces.
- Grewal, M. S., A. P. Andrews, and C. G. Bartone. 2013. *Global navigation satellite systems, inertial navigation, and integration*. John Wiley & Sons.
- Grewal, M. S., and A. P. Andrews. 2015. "Nonlinear approximation." In *Kalman Filtering: Theory and Practice with MATLAB*, by Mohinder S. Grewal. Wiley-IEEE Press.
- Gurtner, W. 2007. *RINEX: The Receiver Independent Exchange Format Version 2.10*. Astronomical Institute, University of Berne.
- Häberling, S. 2015. *Theoretical and Practical Aspects of High-Rate GNSS Geodetic Observations*. PhD Thesis, Zurich: ETH Zurich.
- Hartinger, H., and F. K. Brunner. 1999. "Variances of GPS phase observations: the SIGMA- $\epsilon$  model." *GPS solutions* 35-43.
- Hegarty, C. J., and E. Chatre. 2008. "Evolution of the Global Navigation SatelliteSystem (GNSS)." *Proceedings of the IEEE* 1902 - 1917. doi:10.1109/JPROC.2008.2006090.
- Helmert, F. R. 1907. "Die Ausgleichsrechnung nach der Methode der kleinsten." Leipzig.
- Herrera, A. M., H. F. Suhandri, E. Realini, M. Reguzzoni, and M. C. de Lacy. 2016. "goGPS: open-source MATLAB software." *GPS Solutions* 595-603.
- Heunecke, O., J. Glabsch, and S. Schuhbäck. 2011. "Landslide monitoring using low cost GNSS equipment - Experiences from two alpine testing sites." *Journal of Civil Engineering and Architecture* 660-669.
- Hofmann-Wellenhof, B., H. Lichtenegger, and E. Wasle. 2008. *GNSS - Global Navigation Satellite Systems GPS, GLONASS, Galileo, and more*. Wien: SpringerWienNewYork. doi:10.1007/978-3-211-73017-1.
- Ingenieurbüro M. Gysling Steuer- und Regeltechnik. 1998. "User's Manual MCS7000 Series Rev 3.1." User's Manual, Zurich.

- Jin, X. X., and C. D. de Jong. 1996. "Relationship between satellite elevation and precision of GPS code observations." *J Navig* 253-265.
- Joseph, A. 2010. "Measuring GNSS Signal Strength." *GNSS Solutions, InsideGNSS*, November/December: 20-25.
- Kelly, J. T. 2006. "PPS versus SPS – why military applications require military GPS." *GPS World*, 28-35.
- Kim, D., L. Serrano, and L. Richard. 2006. "Phase wind-up analysis: assessing real-time kinematic performance." *Innovation, GPS World*, September: 58-64.
- Koch, K. R. 1999. *Parameter Estimation and Hypothesis Testing in Linear Models*. Berlin, Germany: Springer-Verlag.
- Kútik, O., and M. Orejas. 2012. "Evaluation of C/N0 estimators performance for GNSS receivers." *The 14th International Association of Institutes of Navigation*. Cairo, Egypt.
- Langley, B. R. 1997. "GPS Receiver System Noise." *Innovation, GPS WORLD*, June: 40-45.
- Larson, K. M., and E. E. Small. 2016. "Estimation of Snow Depth Using L1 GPS Signal-to-Noise Ratio Data." *IEEE JOURNAL OF SELECTED TOPICS IN APPLIED EARTH OBSERVATIONS AND REMOTE SENSING* (IEEE) 9 (10): 4802 - 4808. doi:10.1109/JSTARS.2015.2508673.
- Leica Geosystems AG. 2008. "Leica GPS1200+ Series technical data." Product data sheet, Heerbrugg, Switzerland.
- Limpach, P., A. Geiger, and Z. Su. 2013. "Permanent monitoring of alpine slope instabilities with L1-GPS." *Geophysical Research Abstracts*. EGU General Assembly 2013.
- Liu, J., J. Huang, H. Tian, and C. Liu. 2008. *Research on GPS Receiver Antenna Gain and Signal Carrier-to-Noise Ratio*. Vol. 132, in *VI Hotine-Marussi Symposium on Theoretical and Computational Geodesy*, by P. Xu and A. Dermanis J. Liu, 189-194. Berlin Heidelberg: International Association of Geodesy Symposia, Springer-Verlag. doi:10.1007/978-3-540-74584-6\_30.
- Luo, X. 2013. *GPS Stochastic Modelling: Signal Quality Measures and ARMA Processes*. Springer Science & Business Media. doi:10.1007/978-3-642-34836-5.
- Marini, J. W. 1972. "A Test of the Effect of Satellite Spin on Two-Way Doppler Range-Rate Measurements." *IEEE Transactions on Aerospace and Electronic Systems* (IEEE) AES-8 (3): 269 - 272. doi:10.1109/TAES.1972.309508.
- Marini, J. W. 1971. "The effect of satellite spin on two-way Doppler range-rate measurements." *IEEE Trans. Aerospace and Electronic Systems* (IEEE) AES-7 (2): 316-320. doi:10.1109/TAES.1971.310370.



- Meyers, S. D., B. G. Kelly, and J. J. O'Brien. 1993. "An introduction to wavelet analysis in oceanography and meteorology: With application to the dispersion of Yanai waves," *Monthly weather review* 2858-2866.
- Misiti, M., Y. Misiti, G. Oppenheim, and J. M. Poggi. 2009. *Wavelet Toolbox™ 4 User's Guide*. User's Guidance, MathWorks, Inc.
- Misra, P., and P. Enge. 2011. *Global positioning system : signals, measurements, and performance*. Revised 2nd ed. Lincoln : Ganga-Jamuna Press.
- Montenbruck, O., P. Steigenberger, and A. Hauschild. 2015. "Broadcast versus precise ephemerides: a multi-GNSS perspective." *GPS Solutions* 19 (2): 321-333. doi:10.1007/s10291-014-0390-8.
- Muthuraman, K., and D. Borio. 2010. "C/N0 estimation for modernized GNSS signals: theoretical bounds and a novel iterative." *Navigation: Journal of The Institute of Navigation* 57 (4): 309-323.
- Odijk, D. 2014. "Multi-GNSS Precise Positioning: New Solutions, New Challenges." *InsideGNSS*, November/December: 32-33.
- Odolinski, R., and D. Odijk. 2014. "Combined GPS and BeiDou Instantaneous RTK Positioning." *NAVIGATION: Journal of The Institute of Navigation* 135-148.
- Odolinski, R., and P. J. G. Teunissen. 2017. "Low-cost, high-precision, single-frequency GPS-BDS RTK positioning." *GPS Solutions* 1315-1330. doi:https://doi.org/10.1007/s10291-017-0613-x.
- Panther, G. 2012. "Patch antennas for the new GNSS." *GPS World*, 52-58.
- Pesyna, K. M., R. Heath, and T. E. Humphreys. 2014. "Centimeter positioning with a smartphone-quality GNSS antenna." *Proceedings of the ION GNSS 2014*. Tampa. 1568–1577.
- Qian, K., J. Wang, and B. Hu. 2016. "A posteriori estimation of stochastic model for multi-sensor integrated inertial kinematic positioning and navigation on basis of variance component estimation." *The Journal of Global Positioning Systems*. doi:10.1186/s41445-016-0005-5.
- Rost, C., and L. Wanninger. 2009. "Carrier phase multipath mitigation based on GNSS signal quality measurements." *Journal of applied geodesy*.
- Rothacher, M., and D. Willi. 2017. "GNSS attitude determination with non-synchronized receivers and short baselines onboard a spacecraft." *GPS Solutions* 1605-1617.
- Rothacher, M., and G. Beutler. 1998. "The role of GPS in the study of global change." *Physics and Chemistry of The Earth* 1029-1040.

- Rothacher, M., and G. Mader. 2002. "Receiver and Satellite Antenna Phase Center Offsets and Variations." Position paper of the Antenna session in IGS Workshop, Ottawa.
- Rothacher, M., and R. Schmid. 2010. *ANTEX: The Antenna Exchange Format, Version 1.4*. IGS GNSS product convention, Forschungseinrichtung Satellitengeodäsie, TU München: [www.igs.org](http://www.igs.org).
- Rothacher, M., S. Schaer, L. Mervart, and G. Beutler. 1995. "Determination of antenna phase center variations using GPS data." In: *Gendt G, Dick G (eds): Proceedings of the IGS Workshop on Special Topics and New Directions*. Potsdam, Germany. 205–220.
- Salehi, A. 2010. *Design and Implementation of an Efficient Data Stream*. PhD thesis, Lausanne: ÉCOLE POLYTECHNIQUE FÉDÉRALE DE LAUSANNE.
- Schmid, R., M. Rothacher, D. Thaller, and P. Steigenberger. 2005. "Absolute phase center corrections of satellite and receiver antennas." *GPS solutions* 9 (4): 283-293. doi:10.1007/s10291-005-0134-x.
- Schmid, R., R. Dach, X. Collilieux, A. Jäggi, M. Schmitz, and F. Dilssner. 2016. "Absolute IGS antenna phase center model igs08.atx: status and potential improvements." *Journal of Geodesy* 343–364.
- Schmidt, S. F. 1981. "The Kalman Filter: Its Recognition and Development for Aerospace Applications." *J. Guidance and Control* 4-7.
- Sickle, J. V. 2015. *GPS for land surveyors, Fourth edition*. CRC Press, Taylor & Francis Group.
- Singh, R. P., and S. D. Sapre. 2007. *Communication systems : analog & digital*. Second Edition. New Delhi: Tata McGraw-Hill.
- Sleewaegen, J. M., A. Simsky, W. D. Wilde, F. Boon, and T. Willems. 2012. "Demystifying GLONASS inter-frequency carrier phase biases." *InsideGNSS*, May/June: 57-61.
- Spilker Jr, J. J. 1996. "GPS Navigation Data." In *Global Positioning System: Theory and applications Volume I*, by Bradford W. Parkinson, James J. Spilker Jr., Penina Axelrad and Per Enge, 138. American Institute of Aeronautics and Astronautics, Inc.
- Steigenberger, P., U. Hugentobler, A. Hauschild, and O. Montenbruck. 2013. "Orbit and clock analysis of Compass GEO and IGSO satellites." *Journal of Geodesy* 515-525. doi:10.1007/s00190-013-0625-4.
- Takac, F. 2009. "GLONASS inter-frequency biases and ambiguity resolution." *GNSS Solutions, InsideGNSS*, March/April: 24-28.
- Takasu, T. 2013. "RTKLIB ver. 2.4.2 Manual." Software Manual. [http://www.rtklib.com/rtklib\\_document.htm](http://www.rtklib.com/rtklib_document.htm).



- Takasu, T. 2009. *RTKLIB: Open Source Program Package for RTK-GPS*. Tokyo, Japan,, November 2. [http://gpspp.sakura.ne.jp/paper2005/foss4g\\_2009\\_rtklib.pdf](http://gpspp.sakura.ne.jp/paper2005/foss4g_2009_rtklib.pdf).
- Tetewsky, A. K., and F. E. Mullen. 1996. "Carrier Phase Wrap-Up Induced by Rotating GPS Antennas." *Proceedings of the 52nd Annual Meeting of The Institute of Navigation*. Proceedings of the 52nd Annual Meeting of The Institute of Navigation, Cambridge, MA. 21 - 28.
- Teunissen, P. J. G. 1997. "A canonical theory for short GPS baselines. Part I: The baseline precision." *Journal of Geodesy* 320-336.
- Teunissen, P. J. G. 2003. *Adjustment theory*. Delft University Press.
- Teunissen, P. J. G. 1988. "Towards a least-squares framework for adjusting and testing of both functional and stochastic model." Internal research memo Geodetic Computing Centre, Delft.
- Teunissen, P. J. G., and A. R. Amiri-Simkooei. 2008. "Least-squares variance component estimation." *Journal of Geodesy* 65-82. doi:DOI 10.1007/s00190-007-0157-x.
- Teunissen, P. J. G. 1993. "Least-squares estimation of the integer GPS ambiguities." *Invited Lecture, Section IV, theory and methodology, IAG general meeting*. Beijing, China.
- Theus, M., and S. Urbanek. 2008. *Interactive Graphics for Data Analysis: Principles and Examples*. CRC Press.
- Townsend, B., J. Wiebe, and A. Jakab. 2000. "Results and analysis of using the MEDLL receiver as a multipath meter." *ION national technical meeting*. Anaheim, Californiare. 73-79.
- u-blox AG. 2011. "LEA-5 u-blox 5 GPS modules Data Sheet (GPS.G5-MS5-07026-B4)." Product data sheet.
- u-blox AG. 2010. "LEA-6 ublox 6 GPS Modules Data Sheet (GPS.G6-HW-09004-D)." Product data sheet.
- u-blox AG. 2016. *NEO/LEA-M8T, u-blox M8 concurrent GNSS timing modules, Data sheet (UBX-15025193 - R03)*. Product data sheet, u-blox AG.
- u-blox AG. 2014. *u-blox M8 receiver description including protocol specification (UBX-13003221-R08)*. Product specification, u-blox AG.
- Verhagen, S., and B. Li. 2012. *LAMBDA software package, Matlab implementation, Version 3.0*. Perth, Australia: Delft University of Technology and Curtin University.
- Vermeer, M. 1997. "The precision of geodetic GPS and one way to improve it." *Journal of Geodesy* 240-245.

- Wang, J. 1997. *Filtermethoden zur fehlertoleranten kinematischen Positionsbestimmung*. PhD dissertation, UniBw München: Schriftenreihe Studiengang.
- Wang, J., M. P. Stewart, and M. Tsakiri. 2000. "A comparative study of the integer ambiguity validation procedures." *Earth Planets Space* 813–817.
- Wang, J., N. Gopaul, and J. Guo. 2010. "Adaptive Kalman filtering based on posteriori variance-covariance components estimation." *The International Association of Chinese Professionals in Global Positioning Systems 2010 Technical Forum*. Shanghai: CPGPS.
- Wanninger, L. 2012. "Carrier-phase inter-frequency biases of GLONASS receivers." *Journal of Geodesy* 139-148.
- Ward, P. W., J. W. Betz, and C. J. Hegarty. 2006. "Satellite signal acquisition, tracking and data demodulation." In *Understanding GPS principles and applications second edition*, by Christopher J. Hegarty Elliott D. Kaplan. Norwood, MA: ARTECH HOUSE , INC.
- Weston, N. D., and V. Schwieger. 2014. *Cost effective GNSS positioning techniques*. FIG Commission 5 Publication, Copenhagen: The International Federation of Surveyors (FIG).
- Wieser, A., and F. K. Brunner. 2000. "An extended weight model for GPS phase observations." *Earth, planets and space* 52 (10): 777-782.
- Willi, D., M. Meindl, H. Xu, and M. Rothacher. 2017. "GNSS Antenna Phase Center Variation Calibration for Attitude Determination on Short Baselines." *Proceedings of ION GNSS+ (submitted)*. Portland, Oregon, USA.
- Wu, J. T., S. C. Wu, G. A. Hajj, W. I. Bertiger, and S. M. Lichten. 1993. "Effects of antenna orientation on GPS carrier phase." *manuscripta geodaetica* (Springer-Verlag) 91-98.
- Xsens Technologies B.V. 2010. "MTi and MTx User Manual and Technical Documentation, Document MT0100P." Product manual.
- Xu, G., and Y. Xu. 2016. *GPS: Theory, Algorithms and Applications*. Springer. doi: 10.1007/978-3-662-50367-6.
- Xu, P. . 2013. "The effect of incorrect weights on estimating the variance of unit weight." *Stud Geophys Geod* (Springer Netherlands) 57 (3): 339–352. doi:<https://doi.org/10.1007/s11200-012-0665-x>.
- Yadava, R. L. 2011. *Antenna and wave propagation*. New Delhi : PHI Learning Private Limited.
- Yavuz, E., O. Baykal, and N. Ersoy. 2011. "Comparison of variance component estimation methods for horizontal control networks." *International Journal of the Physical Sciences* 1317-1324.

- Zhang, L. 2016. *Qualitätssteigerung von Low-Cost-GPS Zeitreihen für Monitoring Applikationen durch zeitlich-räumliche Korrelationsanalyse*. PhD thesis, München: Deutsche Geodätische Kommission.
- Zhang, L., and V. Schwieger. 2013. "Monitoring mit Low-cost GPS Empfängern - Chancen und Grenzen." *DVW-Seminar*. Augsburg: Wissner Verlag.
- Zhang, L., M. Stange, and V. Schwieger. 2012. "Automatic Low-cost GPS Monitoring System Using WLAN Communication." *FIG Working Week*. Rom.